Understanding Angular Momentum Evolution of Solar-age Stars with *K2* Data

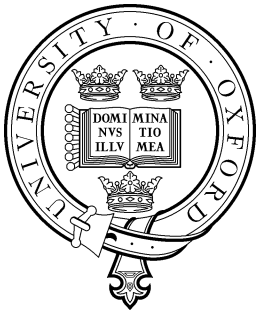

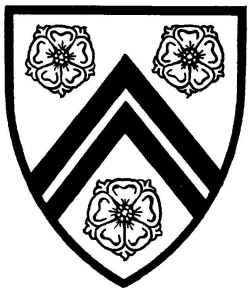

1Lt Rebecca A. Esselstein

New College

University of Oxford

A thesis submitted for the degree of

Doctor of Philosophy

Trinity 2018

To my parents, for their love and support;
to Chadley, my best friend;
and to Dr. Brown, Dr. Della-Rose, and Dr. Varble,
without whom I would never have found myself in Oxford.

Abstract

Gyrochronology, which describes the empirical relationship among stellar mass, rotation period, and age, is a potentially powerful tool for determining the ages of stars, upon which the understanding of stellar evolutionary models hangs. Well-calibrated with open clusters up to the age of $\sim$2.5 Gyr, predictions from gyrochronology are in conflict with asteroseismic observations of older stars, and the underlying physics are poorly understood. The solar-age, open cluster M67, recently observed by the NASA *K2* mission, offers the opportunity to test both gyrochronology and more physically-motivated angular momentum evolution models. Here, we seek to gain insight into the angular momentum evolution of solar-age stars through the analysis of *K2* data. Using our own pipeline, we extract and process *K2* light curves that encompass the inner and outer portions of M67. We describe various rotation period detection methods, focusing on the Lomb-Scargle periodogram, autocorrelation function (ACF), and Gaussian processes (GPs), before presenting our own preliminary results. Observed scatter between colour and period, combined with disagreement from the first published sets of *K2* M67 periods, prompted a comprehensive round of sinusoidal injection tests to probe our absolute detection limits with *K2* data using two different light curve preparation pipelines. Finding low sensitivity for 25 d, 0.1% amplitude signals and lingering systematics on the order of 25 d and greater, we use a combination of the Lomb-Scargle, ACF, and GP methods to determine our 'final' M67 rotation periods from *K2* data. We find agreement between tidal synchronization theory and observed rotation periods for our M67 binaries. While angular momentum evolution models may perform slightly better than gyrochronology, we cannot make any conclusive statements regarding the validity of either due to the inherent scatter and small sample size. Future work at refining detection methods is needed, along with complementary data from upcoming missions such as LSST and *PLATO*.

Acknowledgements

I would like to thank, above all, Suzanne. I can't tell you how grateful I am that you were willing to take on a student in the U.S. Air Force with a background in engineering, strict three-year timeline, and no foreseeable future in academia. Thanks for those hours spent in your office, going over code, putting me on track, and patiently listening to my questions and confusions. Your dedication to your family, students, and research is inspirational, and you have exemplified what it means to have a work-life balance and still do good science. Thanks for supporting me when I rowed with the Blues, decided to do an ultramarathon just weeks before my thesis was due, and wanted to travel around Europe. I've learned so much, not only from your mentorship and guidance, but from these and other experiences I've had while at Oxford. My confidence has really grown these last three years; I can't thank you enough.

I would like to thank Bob for organizing the *K2* M67 Study collaboration, and specifically the rotation team — Søren, Jen, Andrew, and Jeff — for your expertise, cooperation, mentorship, and insight. And I can't forget to thank Dan!

I'm grateful to the department, especially Ashling and Garret, for being flexible with my Air Force requirements and timeline, and to Pat, for acting as my secondary supervisor. Jonathan, you're my hero. Special thanks to Ben, Vinesh, Ruth, Hannu, and Ed for being great friends, assuaging my fears, and answering my dumb questions. I would also like to give a shout-out to my entire year group, particularly Catherine, Sam, Sergio, Ellen, Naomi, and Paul, for putting up with me and my rowing talk.

I'm indebted to the U.S. Air Force, for permitting me to do a three-year DPhil instead of a two-year Masters, to the Rhodes Trust for funding me, and to New College for providing a warm, supportive space for its members. Thanks to all the senior Air Force officers at Oxford, my mentors from USAFA, and my program manager for their invaluable guidance and advice. From Rhodes House, I would like to thank the miracle-worker that is Mary, and all the lovely porters, for making me feel like a true part of the Rhodes community. John, thanks for all the Swedish fish, trips to the base, and for being the first British person to welcome me to the country.

I couldn't have gotten through Oxford without my friends. Caroline, Tory, Stephen, Harriet, and Jeremy — thanks for joining me in navigating the Air Force as UK grad students, all the wonderful conversations, and for being the people who understand both the military and Oxford. Tory, thanks for all the teas, joining me on my ice-climbing adventure, and inspiring me to do crazy things like running 100 km. Laurel, Tanja, Isa, Abi, Jenna, Claz, Sarah, Hannah, Sanja, Andrea, and Emmie — thanks for the hot chocolate & grapes, Nutella & waffles, dinners, work days, brunches, Iceland, and coffees. Much love to my NCBC family, particularly Howard, Charlie, Jo, my Purple Boat crews, and my W1 crews. And thanks to Barrie Jon, Piers, Jo, Caitlin, and Ben, my fantastic S&C team, for not judging me when I had to sleep in.

Last, but certainly not least, I want to thank my family. Mom and Dad, you have supported me in everything I have done. I don't know how I got so lucky to have you as parents, and I love you so much. Matt, Katie, Hil, and Andrew — you are the best siblings a person could ask for; I can't imagine growing up with anyone else.

Declaration

The work in this thesis is based on research I carried out at the University of Oxford between Michaelmas Term 2015 and Trinity Term 2018.

Chapter 4 is primarily taken from my first-author, peer-reviewed paper (see below), as are small portions of Chapter 1, Chapter 2, and Chapter 3. While I was the main author, these sections include edits and comments made by my coauthors. In Chapter 2, Section 2.5, I adapted into my own words the 'CfA' pipeline and *Kepler* PDC-MAP paragraphs from our paper, written by Andrew Vanderburg and Jeff Smith, respectively.

The code to extract the superstamp light curves in Chapter 2 comes from the Cambridge Astronomy Survey Unit. The idea for the normalization of the Lomb-Scargle periodogram in Chapter 4 to remove artificial power belongs to Suzanne Aigrain, who wrote the original code to apply the Lomb-Scargle to our test light curves and compute the results. I made necessary modifications, applied it to the whole test set, and am in general solely responsible for the injection tests presented in that chapter. The Gaussian process (GP) technique described in Chapter 3 and employed in Chapter 5, utilizing a kernel composed of a mixture of simple harmonic oscillators, was conceived by Dan Foreman-Mackey. He invited me to the Flatiron Institute in January 2018 to work on the basic kernel together, but I implemented the realizations of it in this thesis. Suzanne Aigrain also had the idea for the GP periodogram presented in Chapter 5, which I then tested.

The views expressed in this thesis are those of the author and do not reflect the official policy or position of the United States Air Force, Department of Defense, or the U.S. Government.

Rebecca Esselstein

(*August 2018*)

First-author, Peer Reviewed Publication:

The K2 M67 Study: Establishing the Limits of Stellar Rotation Period Measurements in M67 with K2 Campaign 5 Data. **Rebecca Esselstein, Suzanne Aigrain, Andrew Vanderburg, Jeffrey C. Smith, Søren Meibom, Jennifer Van Saders, Robert Mathieu**. The Astrophysical Journal, Volume 859, Issue 2, p.167–198. doi: 10.3847/1538-4357/aac20e.

Contents

List of Figures

List of Tables

List of Acronyms

- **ACF**: Autocorrelation function.
- **BLM**: M67 binary likely member.
- **BM**: M67 binary member.
- **BPSD**: Bayesian period signal detetion.
- **C##**: *K2* Campaign ##.
- **CAL**: *Kepler* pixel-level calibration.
- **CMD**: Colour-magnitude diagram.
- **CPD**: Colour-period diagram.
- **DSS**: Digitized Sky Survey.
- **DVA**: Differential velocity aberration.
- **EPD**: External parameter decorrelation.
- **FFI**: Full frame image.
- **FT**: Fourier transform.
- **GP**: Gaussian process.
- **H-R**: Hertzsrpung-Russell.
- **MAD**: Median of absolute deviations.
- **MAP**: Maximum *a posteriori*.
- **MAST**: Mikulski Archive for Space Telescopes.
- **MCMC**: Markov chain Monte Carlo.
- **MSL**: Minimum string length.
- **PA**: *Kepler* photometric analysis.
- **PBM**: M67 possible binary member.
- **PCA**: Principle component analysis.
- **PDC**: Pre-search data conditioning.
- **PDM**: Phase dispersion minimization.
- **PLD**: Pixel-level decorrelation.
- **PMS**: Pre-main sequence.
- **PRF**: Pixel response function.
- **PSD**: Power spectral density.
- **PSF**: Point spread function.
- **SAP**: Simple aperture photometry.
- **SHO**: Simple harmonic oscillator.
- **SM**: M67 single member.
- **SNR**: Signal-to-noise ratio.
- **SS**: Superstamp.
- **SSM**: Star spot model.
- **TFA**: Trend filtering algorithm.
- **TPF**: Target pixel file.
- **WPS**: Wavelet power spectrum.

Chapter 1

Introduction

For my part, I know nothing with any certainty,
but the sight of the stars makes me dream.

Vincent van Gogh

When I was eight-years-old, I could not decide whether I wanted to be a chemist, paleontologist, or astronaut when I grew up. The next year, we did a unit on space in school, learning all about the Solar System, stars, and galaxies. Suddenly, I had my answer. I plastered my bedroom ceiling with glow-in-the-dark stars and planets, tacked any and all newspaper clippings that had to do with space on my wall, and conducted space missions in my closet. Every major decision in my life has been fueled by this passion, from going to the United States Air Force Academy and studying astronautical engineering to finding myself at Oxford, with the privilege of completing a thesis in astrophysics, before I head off to pilot training for the Air Force.

'I have loved the stars too fondly to be fearful of the night,' from Sarah Williams' 'The Old Astronomer to His Pupil,' is my favorite line from poetry. The more I have learned about stars throughout the course of this thesis, the more I have loved them. They are the beautiful, complex building blocks of the universe, bright enough to tantalize and inspire us humans who are confined to the Earth, but just distant

Sections of this Chapter have been published as Esselstein et al. (2018).

enough to puzzle, and at times frustrate, us with their secrets, slowly revealed but also deepened through the progression of technology. This thesis is dedicated to the effort of unlocking one of those secrets, even if only in a minor way, and in the broadest sense that 'secret' is how we determine a given star's age. Specifically, we explore angular momentum evolution as a potential key.

The angular momentum evolution of young, pre-main sequence stars is complex, but the higher activity levels for these stars allow for the relatively easy acquisition of indicators and proxies, such as the rotational modulation of stellar flux, to be measured and quantified. Quieter, older main-sequence stars, however, offer another sort of challenge, and the translation of stellar rotation periods, for example, to angular momentum evolution over this phase of a star's life is difficult to constrain. Because of the Sun, we can gain some insight into this process by comparing solar observations with those from stars of similar age and composition. This thesis contributes to that task through the processing and analysis of photometric data obtained for the solar-age, open cluster M67 through the NASA *K2* mission.

In this chapter, we set the background and context in which we tackle the problem of the angular momentum evolution of middle-aged, main-sequence stars. We start with a discussion on various age-dating methods in Section 1.1, diving more specifically into stellar spin-down, or 'gyrochronlogy.' We then take a look at angular momentum transport and evolution, and their implications for gyrochronology, in Section 1.2. We introduce M67 in Section 1.3. After providing a brief history of the acquisition of stellar rotation periods in Section 1.4, we focus on the *Kepler* and *K2* missions in Section 1.5. Then we move on to techniques for extracting and processing light curves in Section 1.6, and we give an overview of rotation detection methods in Section 1.7. Finally, in Section 1.8, we outline the structure of this thesis in light of the stage that we will have set.

1.1 Age-Dating of Stars

Alongside mass, the most fundamental stellar parameter is age. From a star's age, we can gain significant insight into astronomical phenomena including, but not limited to, the generation and degradation of protoplanetary and debris disks around protostars, planetary formation, star system dynamics, and even the evolution of the Milky Way (Soderblom, 2010). Furthermore, stellar evolution models obviously have a functional dependence on time. While certainly not applicable in all cases, if we know a given star's age, we can generally combine that knowledge with its mass to infer its composition and its physical state according to the Vogt-Russel theorem, especially for stars along the main sequence (Kaehler, 1978; Endal & Sofia, 1981; Soderblom, 2010). Therefore, obtaining the ages of stars is not only desirable but also critical to our understanding of one of the most basic components in the macro structure of the universe.

Age-dating stars, particularly field stars, however, is a complicated task that often depends on non-negligible assumptions or very precise measurements of various quantities, such as distance, chemical abundances, and photometric intensity. The review by Soderblom (2010) provides a list of major age-dating techniques, though some are more or less suitable depending on the evolutionary state of the stars in question, or whether the stars are field stars or members of a cluster or association. In this section, we briefly acknowledge those methods less applicable to this thesis, such as kinematics, lithium depletion, and nucleocosmochronometry, while spending more time on those more relevant to older, main sequence stars. These include isochrone fitting, asteroseismology, chromospheric activity, and stellar spin-down. The last of these has evolved into the field known as 'gyrochronology,' which we will discuss more extensively in Section 1.2, after we provide a comparison of the relative performance of these four techniques in Section 1.1.8.

1.1.1 Kinematics

The term 'kinematics' generally refers to the motion of stars around the galactic centre, including both in bulk and random. Using kinematics as an age-dating method involves taking radial velocity, proper motion, and space motion measurements to trace the movement of stellar associations in time (Blaauw, 1964). The work of von Hoerner (1960) first acknowledged the use of kinematics as an effective method for age-dating young associations by noting the dependency of various kinematic properties on age (Mayor, 1974). In particular, ages are derived from the expansion of these associations, though depending on the approach one takes, these ages tend to be younger than those found by other age-dating methods (Maeder, 1972; Soderblom, 2010). Because the kinematic properties of associations change relatively rapidly (on the order of about 2×10^8 yr; Mayor 1974), this method is best suited to very young stars. However, one may still be able to glean some indication of age for groups of field stars by measuring their kinematic properties in relation to each other.

1.1.2 Lithium Depletion

Young clusters of stars may form with a certain abundance of lithium in the photospheres of member stars, which is subsequently depleted during the fully convective, pre-main sequence (PMS) phase of a star's life. Higher mass stars deplete lithium faster than lower mass stars, however, so a comparison between the relative measurements of lithium in coeval stars of different masses can help put a constraint on the cluster's age (Bildsten et al., 1997). Burke et al. (2004) explored the practicality of this so-called 'lithium depletion boundary,' and found that, while an effective technique, it is subject to uncertainties from bolometric corrections, insufficient understanding of the physics involved, and stellar rotation considerations. Despite this, lithium depletion has been successfully utilized for clusters ranging from 20 to 200 Myr of age (Burke et al., 2004), such as in the cases of NGC 2547 (35 Myr; Jeffries & Oliveira

2005), IC 4665 (28 Myr; Manzi et al. 2008), and NGC 1960 (22 Myr; Jeffries et al. 2013). In a comparison between kinematics and lithium depletion to find the age of a 21 Myr association, Binks & Jeffries (2014) found the latter to be more precise.

1.1.3 Nucleocosmochronometry

The rapid nucleosynthesis and subsequent slow degradation of various radioactive isotopes of heavy elements with known half lives can be used to measure stellar ages if detected in the photospheres of stars. This technique is known as 'nucleocosmochronometry,' and it evolved from the discovery that isotopes of heavy elements such as thorium and uranium can be synthesized by rapid neutron capture, otherwise known as the 'r-process' (Burbidge et al., 1957). The r-process is most likely initiated by the extreme conditions of supernovae, meaning that these isotopes form quickly as they are scattered into the interstellar medium to be recycled into stars (Hoyle & Fowler, 1960). The best isotopes to use for very old stars (i.e. approaching the age of the galaxy) are ^{232}Th, ^{238}U, and ^{235}U, with half lives of 1.405×10^{10}, 4.47×10^{9}, and 7.038×10^{8} yr, respectively (Cowan et al., 1991). Alternatively, isotopes with half lives on the order of $\sim 10^{7}$ yr can be used for younger objects (Cowan et al., 1987). Unlike kinematics and lithium depletion, this method can be used on individual stars, but only down to a precision of about 2 Gyr; uncertainty in the measurement could improve, however, if applied to an old cluster of coeval stars (Ludwig et al., 2010).

1.1.4 Isochrone Fitting

Isochrone fitting is one of the most widely used age-dating techniques. Observed stars are plotted on the Hertzsprung-Russell (H-R) diagram, or a colour-magnitude diagram (CMD), in relation to evolutionary tracks fixed at certain ages and calculated over a range of masses. Stellar luminosities and effective temperatures change over time, so a star's proximity to an isochrone can indicate age (Lachaume et al., 1999).

The tracks themselves are derived from evolutionary models that take into account parameters such as mass, metallicity, opacity, and reddening to return luminosities and effective temperatures at different ages.

The literature is rich with isochrones derived from different evolutionary models across a diverse assortment of parameters, including mass, metallicity, and age, among many others. For example, the Vandenberg (1985) isochrones, computed for masses of 0.4 – 4.0 $M_\odot$ down to ages of ∼0.2 Gyr, across a wide range of [Fe/H] and α-element abundances, led to the foundational work of Edvardsson et al. (1993) on understanding our galaxy's evolution through the age determination of 200 F and G stars along the Galactic disk. The combined work of Bressan et al. (1993), Fagotto et al. (1994a,b), and Bertelli et al. (1994) produced the classic Padova isochrones, incorporating masses ranging from 0.6 to 120 $M_\odot$ and metallicities of $Z = 0.0004$ to $Z = 0.05$. More recent isochrone datasets include: the popular Girardi et al. (2000) isochrones, calculated for 0.15 – 7 $M_\odot$ and $Z = 0.0004 - 0.03$, and extended by Marigo et al. (2008) to the thermally pulsating asymptotic giant branch (TP-AGB); the Y^2 isochrones (Yi et al., 2001; Yi et al., 2001), computed from the PMS to the helium core flash for 0.4 – 5.0 $M_\odot$ and $Z = 0.00001 - 0.08$; the publicly-available MIST framework for computing isochrones, scaled using the Sun for masses of 0.1 – 300 $M_\odot$ at the PMS up to the end of hydrogen burning for solar-like metallicities (Dotter, 2016), and up to helium core burning for metal-poor stars (Choi et al., 2016); the YaPSI grid of Spada et al. (2017), ranging from 1 Myr – 20 Gyr for 0.15 – 5.0 $M_\odot$ and [Fe/H] = -0.15 to +0.3; and PARSEC (Bressan et al., 2012), publicly-available code from which tracks can be computed for 0.1 – 12 $M_\odot$ from the PMS to TP-AGB.

The use of isochrone fitting to determine stellar ages has been very successful, aided in part by the bulk of astrometric and photometric data acquired by the *Hipparcos* mission (Perryman et al., 1997) (although significant gains will also undoubtedly be made by the unfolding *Gaia* mission; Gaia Collaboration et al. 2018). Feltzing

et al. (2001) and Ibukiyama & Arimoto (2002) found ages for several thousand *Hipparcos* stars within the solar neighbourhood, and isochrones have also been used to constrain the ages of planet host stars. For example, using *Hipparcos* data, Laws et al. (2003) estimated the ages of 30 stars that had either known giant planet or brown dwarf companions.

Clusters are especially well-suited to isochrone fitting because of the relatively large samples of coeval stars spanning a range of masses and evolutionary states. Liu & Chaboyer (2000) looked at the old open cluster NGC 188 and found an approximate age of 6.5 Gyr, while Oliveira et al. (2013) used isochrones to determine the metallicities of nine open clusters, using age as a free parameter. Figure 1.1, taken from Figure 3 of Liu & Chaboyer (2000), gives an example of plotting isochrones, developed by one of the collaborators of that work, with members of NGC 188. Both panels in the figure show isochrones for 5, 6, and 7 Gyr for two different CMDs ($B-V$ vs. V and $V-I$ vs. V). The respective reddening for each CMD is provided, as well as the difference between the apparent and absolute magnitudes.

While a 6.5 Gyr age for NGC 188 seems to be reasonable given the comparison with the isochrones, Figure 1.1 indirectly highlights some of the shortcomings of the isochrone method. First, it is particularly dependent on the evolutionary tracks applied, including the parameters and uncertainties therein. Differences between models aside, isochrones will overlap in various regions of the H-R diagram depending on the mass-age combination, so one needs to have a general idea of the evolutionary state of the stars in question to choose the more probable isochrone. And while getting the ages from clusters is relatively straightforward thanks to the shear number of data points, applying the same technique to individual, main sequence field stars is much more uncertain — one can fit anything to a single point — and requires high-precision photometric, metallicity, and distance measurements (Lachaume et al., 1999; Pont & Eyer, 2004; Barnes, 2007). It is not surprising, then, that isochrone

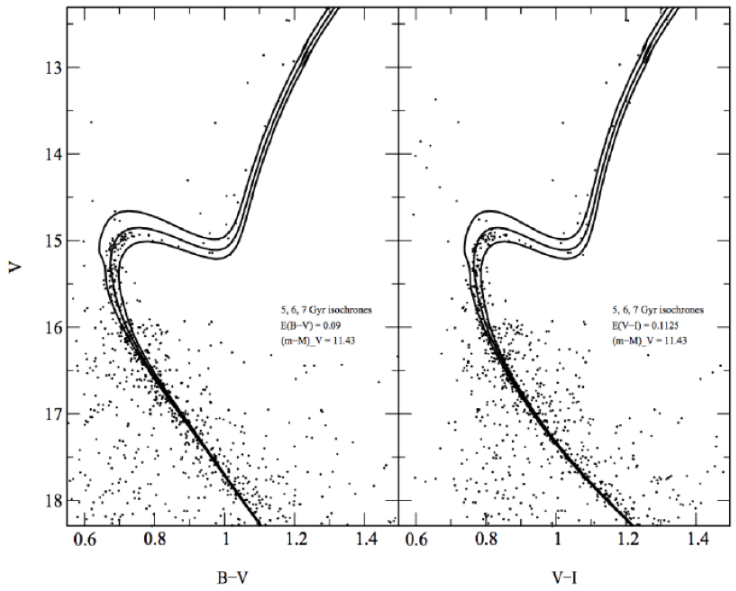

Figure 1.1: Example isochrones and NGC 188 data plotted on two CMDs, taken from Liu & Chaboyer (2000).

age precision can range anywhere from 20 – 50% for main-sequence stars (Soderblom, 2010). Furthermore, isochrones have uncertainties in both the x- and y-directions (colour and magnitude, respectively), which necessitate a slightly more sophisticated approach (e.g. the method of Naylor & Jeffries 2006) than simple least squares fitting.

The work of Lachaume et al. (1999) compared five different age-dating methods — isochrones, metallicity, kinematics, chromospheric activity, and rotation (the latter two will be discussed below) — for a set of main sequence B through K stars, and found that isochrones are good for putting upper and lower bounds on ages, but often need to be combined with other techniques in order to get a more precise measurement, especially for cooler stars. In addition, Lachaume et al. (1999) discovered that there is a tendency to underestimate isochrone age uncertainties based on insufficient understanding of the uncertainties inherent in evolutionary model parameters. To achieve better results, however, some studies have tried weighting likelihoods for

goodness of fit or taking a more Bayesian approach, and with some success (Pont & Eyer, 2004; Jørgensen & Lindegren, 2005; Monteiro et al., 2010).

1.1.5 Asteroseismology

Asteroseismology is the study of stellar oscillations, the frequencies of which can be used to determine interior density and sound speed, which, when combined with evolutionary models, return fundamental stellar parameters. These include mass, $\log g$, and age. The review from Brown & Gilliland (1994) provides an overview of the key terminology and method. The two overarching frequency mode categories are the so-called 'p-mode' and 'g-mode' frequencies, named based on their respective restoring forces, i.e. pressure gradients and buoyancy. Oscillations can be measured either from photometric data, as they cause observed flux to change at high frequencies, or from the Doppler shifts associated with the pulsation of stellar plasma (Brown & Gilliland, 1994). For deriving stellar ages from solar-like stars, typically only p-mode frequencies come into play; g-mode oscillations are more difficult to detect.

Each frequency is parameterized by a radial order n, which is the number of nodes between the center of the star and the surface; the angular degree l, or the frequency's wavenumber multiplied with the stellar radius (i.e. the number of nodes on the surface); and the azimuthal order m, a description of l in relation to the star's equator (Brown & Gilliland, 1994). These parameters are intrinsically linked with the large separation, Δv_o, and the small separation, δv_o. The former characterizes the time for sound to travel through the star (Brown & Gilliland, 1994):

$$\Delta\, v_o = (2 \int_0^{R_*} \frac{dr}{c})^{-1} \tag{1.1}$$

Here, R_* is the stellar radius and c is the speed of sound in the star. Equation 1.1 is ultimately related to the density and internal structure of the star (Cox, 1980;

Gough, 1990; Brown & Gilliland, 1994). The small separation, on the other hand, hints at the star's evolutionary state, since it is particularly affected by gradients in the sound speed (Brown & Gilliland, 1994). Observed frequency modes that have the same l and come from neighboring nodes, n, are separated by Δv_o. Alternatively, modes which share n and are either both even or both odd in l exhibit δv_o spacing. Finally, modes with the same l and n, but different m, are distinguishable due to rotational splitting, i.e. the Doppler shifts arising from rotation (Aerts et al., 2010; Nielsen et al., 2014).[1]

Together, the large and small separations can be used to return many fundamental stellar properties. Ulrich (1986) created stellar evolutionary models that related asteroseismic frequencies to stellar mass, metallicity, and convective mixing length. The work of Christensen-Dalsgaard (1988) built off this idea, even creating an 'oscillation H-R diagram' based on the evolutionary tracks for stars ranging from 0.7 – 1.5 $\mathrm{M}_\odot$ and computed as a function of Δv_o and δv_o from p-mode frequencies. A combination of high precision observations (Gough, 1987) and improvements made to model parameters (Brown et al., 1994) can greatly minimize measurement uncertainties from stellar properties derived from asteroseismology. In fact, asteroseismology has proven to be one of the best techniques for constraining stellar properties, thanks in large part to space-based missions such as *MOST*, *CoRoT*, and *Kepler* (Gilliland et al., 2010), which will be discussed in later sections. High-precision photometric data from *Kepler* has greatly opened up the number of asteroseismic, solar-like targets available to the community (Gilliland et al., 2010), and even the follow-on mission *K2* (also discussed in more detail below, as it is a key component of this thesis) allows for frequency measurements up to at least 2 500 μHz (Chaplin et al., 2015). Asteroseismology has been used to determine ages for planet-host stars (Silva

[1]Rotational splitting from modes with different n, which penetrate to different stellar depths, can be used to measure internal rotation at varying radii (see e.g. Schou et al., 1998; Nielsen et al., 2014)

Aguirre et al., 2015), evolved subgiants (Metcalfe et al., 2010), and main sequence stars (Chaplin et al., 2014), typically achieving precision levels of 10% (Soderblom, 2010), and, in some cases, reaching down to 2.5% (Mathur et al., 2012).

1.1.6 Chromospheric Activity

Chromospheric activity, often interpreted as the strength of Ca II H and K transition lines (and less commonly as Hα emission), was first considered as a potential age indicator by Wilson (1963), who found that the H-K intensities for cool, main-sequence stars were higher in the Pleiades than the older Hyades, Praesepe, and Coma clusters. A follow-on study by Wilson & Skumanich (1964) found that of 17 stars with strong H-K lines out of a sample of 114 main-sequence stars, 15 were close to the zero-age main sequence, supporting the idea that chromospheric activity decreases with age. Kraft (1967) then suggested that chromospheric activity was also correlated with rotation period in cool stars. The connection with rotation is particularly important to this thesis and is explored more fully below (in Section 1.1.7), but it is difficult to talk about chromospheric activity without alluding to rotational effects. Stellar rotation is intrinsically linked with a star's surface magnetic activity via the Rossby number, or the ratio of the observed rotation period to the convective turnover time, τ_c (Noyes, 1983). The indirect dependence of chromospheric activity on the Rossby number implies that convection zone depth is an important factor in emission strength due to the role it plays in creating the stellar dynamo; indeed, Noyes et al. (1984) confirmed that H-K emission depends not only on rotation period, but also spectral type. Further studies have attempted to better understand the expression of chromospheric activity through stellar evolution models, particularly with respect to convection zone parameters (Gilliland, 1985) and stellar dynamo numbers, the latter expressed as the ratio between magnetic activity cycles and rotation period (Baliunas et al., 1996).

The relationship between chromospheric activity and age, however, was further

solidified by the foundational work of Skumanich (1972). He discovered that R'_{HK} (the ratio between H-K emission and stellar flux; Noyes et al. 1984) is roughly proportional to $t^{-1/2}$, where t is the age of the star, providing the first functional connection between chromospheric activity and age (and, critically, rotation). Eventually, Soderblom et al. (1991) confirmed that the relationship between chromospheric activity and age was deterministic rather than merely statistical, properly opening the door for its application as an age-dating method. Effective applications of these observations include those of Mamajek & Hillenbrand (2008), who made improvements to determining ages from R'_{HK} (and also rotation via the Rossby number). In addition, after Gizis et al. (2002) looked at the relationship between Hα and age, Lyra & Porto de Mello (2005) calibrated Hα with age for 175 stars in the solar neighborhood.

There are limits to using chromospheric activity to discern stellar ages. The first indication of this came from Vaughan & Preston (1980), who discovered a gap, now known as the 'Vaughan-Preston' gap, in chromospheric emission for a sample of 185 F and G stars. They hypothesized, barring a bias in the sample selection, that this gap was related to the age of the stars, i.e. that stars were less active by about 1 Gyr of age (Vaughan & Preston, 1980). In addition, Pace & Pasquini (2004) looked at 35 stars from five clusters: Hyades, Praesepe, IC 4651, NGC 3680, and M67. There was a significant difference in chromospheric activity between the $\sim$0.6 Gyr Hyades and Praesepe clusters and the $\sim$1.7 Gyr IC 4651 and NGC 3680 clusters, as expected, but there was very little difference between the latter pair and the much older, solar-age M67. This indicates that chromospheric activity does not change substantially beyond about 1 – 2 Gyr (Pace & Pasquini, 2004; Pace, 2013), except potentially in very specific cases (Zhao et al., 2011). Despite these limitations, several studies have found that chromospheric ages, when applicable, tend to be more accurate than those derived from isochrone fitting (Lachaume et al., 1999; Pont & Eyer, 2004). Precisions for chromospheric ages hover around 0.2 dex, or about 60% (Mamajek & Hillenbrand,

2008; Soderblom, 2010)

1.1.7 Stellar Spin-down, or 'Gyrochronology'

As mentioned before, Skumanich (1972) discovered that the chromospheric emission, which results from stellar rotation, is proportional to $t^{-1/2}$. This, in turn, implies that rotation has a similar functional dependence on age, since chromospheric activity and rotation are correlated (but only if τ_c does not significantly change on the main sequence). Rotation period also appears to depend on spectral type, as observed in the Hyades, where there is a noticeable trend between colour and period for stars cooler than about mid-F (Radick et al., 1987; Delorme et al., 2011). Kawaler (1988) concluded that by ∼600 Myr, a star's initial angular momentum no longer plays a significant role in determining its rotation period, and another mechanism, possibly stellar winds coupled with magnetic fields, 'brakes' the rotation of a star as it ages (see Section 1.2 below). Kawaler (1989) then acknowledged the potential use of stellar spin-down, a direct observable independent of distance, as an age estimator, if rotation periods could be properly calibrated with age and spectral type. Barnes (2003) developed the first semi-empirical model for deriving ages from the colours and rotation periods of FGK dwarfs based on the rotation periods of a large sample of stars from clusters with ages of ∼30 Myr to 600 Myr, as well as old Mt. Wilson field stars. Figure 1.2, taken from Figure 2 of Barnes (2003), illustrates the dependence of the observed rotation period on age, which appears to become a single relation by the age of the Hyades. In doing so, Barnes (2003) coined the term 'gyrochronology' to describe the relationship between age, colour (mass), and rotation period.

The traditional gyrochronology model comes from the work of Barnes (2007), and it separates the age and mass dependencies based on the general formulation:

$$P = g(t)f(B-V) \tag{1.2}$$

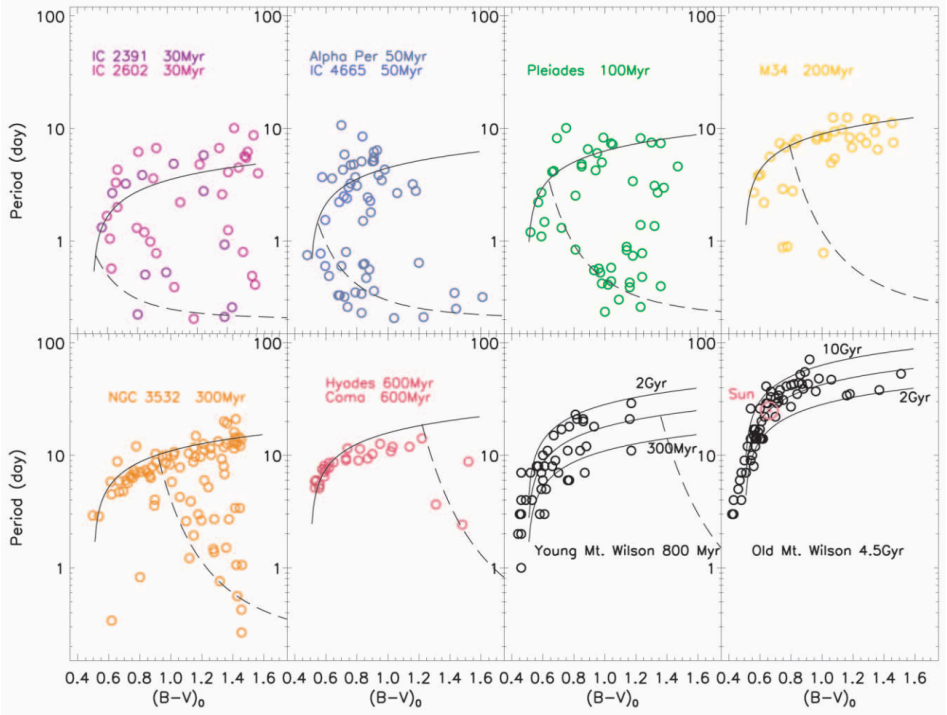

Figure 1.2: Illustration of the apparent age-colour-period dependence for a range of young open clusters and field stars taken from Figure 2 of Barnes (2003).

where P is the rotation period, $g(t)$ is the age dependency, and $f(B-V)$ is the mass dependency, in this case represented as a function of $B-V$ colour. To determine the mass dependency, Barnes (2007) analyzed cluster data where the initial angular momentum distribution no longer affects observed rotation periods, i.e. the differences in rotation periods for stars of a given mass from one cluster to another are due to age alone. Barnes (2007) initially defined the time dependency based on the Skumanich relation of $t^{-1/2}$ and settled on the following form for $f(B-V)$:

$$f(B-V) = a(B-V-0.4)^b \tag{1.3}$$

where a and b are parameters that are best fit to the data, which they determined to be $a = 0.7725 \pm 0.011$ and $b = 0.601 \pm 0.024$. With respect to the time dependence, $g(t)$, Barnes (2007) use the general form:

$$g(t) = t^n \tag{1.4}$$

where the exponent n is calibrated using Equations 1.2 and 1.3 with data from the Sun, and t is in Myr. They find a value of $n = 0.5189 \pm 0.0070$, closely following the Skumanich relation but more empirically fit.

If the value of 0.4 in $f(B-V)$ is changed to a free parameter c, the traditional gyrochronology relation takes the form:

$$P = t^n \left(a[(B-V)_o - c]^b\right) \tag{1.5}$$

where $(B-V)_o$ is the intrinsic colour. This yields a 'gyro-age,' in Myr, of:

$$t = \left(\frac{P}{a[(B-V)_o - c]^b}\right)^{\frac{1}{n}} \tag{1.6}$$

Others have built off this model, determining their own values for a, b, c, and

Table 1.1: Summary of Standard Gyrochronology Model Parameters

Study	a	b	c	n
B2007	0.7725 ± 0.011	0.601 ± 0.024	0.4	0.5189 ± 0.0070
MH2008	0.407 ± 0.0021	0.325 ± 0.024	0.495 ± 0.010	0.566 ± 0.008
M2009	0.770 ± 0.005	0.553 ± 0.052	0.472 ± 0.027	0.5189 ± 0.0070
A2015	$0.40^{+0.3}_{-0.05}$	$0.31^{+0.05}_{-0.02}$	0.45	$0.55^{+0.02}_{-0.09}$

n thanks to the availability of thousands of open cluster member rotation periods enabled by large field-of-view (FOV) CCD cameras on ∼1 m class telescopes (see Section 1.4). Studies utilizing the prescription of Equation 1.5 include those of Mamajek & Hillenbrand (2008) and Meibom et al. (2009). The former incorporated chromospheric activity via the Rossby number, Ro, in addition to gyrochronology using Mt. Wilson stars, while the latter used high-precision data from a 5-month observation of the ∼150 Myr M35 cluster to make slight adjustments to the parameters in Equation 1.5. A summary of the three different sets of model parameters can be seen in Table 1.1, where 'B2007' refers to Barnes (2007), 'MH2008' refers to Mamajek & Hillenbrand (2008), and 'M2009' refers to Meibom et al. (2009). Also included are the parameters derived by Angus et al. (2015) ('A2015') using Markov Chain Monte Carlo (MCMC) methods, who compared this traditional gyrochronology relationship, derived from clusters, with ages from an asteroseismic sample of field stars from *Kepler*; the main conclusions of this work are discussed in Section 1.2. Angus et al. (2015) did not include c as a free parameter, and Meibom et al. (2009) used the time dependence originally found by Barnes (2007).

Others have attempted to determine their own gyrochronology relations separate from the Barnes (2007) model. For example, Collier Cameron et al. (2009) looked at FGK data from the ∼600 Myr Coma Berenices cluster, and, finding a close relationship between rotation period and $J - K$ colour, developed their own formula that could reproduce the rotation period of the Sun. They still relied on a power law for

the age dependency, however, finding $n = 0.56$. Their final gyro-age formula is:

$$t = 591\left[\frac{P}{9.30 + 10.39(J - K - 0.504)}\right]^{\frac{1}{0.56}} \tag{1.7}$$

Equation 1.7 has a similar form to that of Equation 1.6, and it was likewise determined through empirical fitting. Thus, the coefficients represent the best-fit result and are not necessarily physically motivated.

Another deviation from the standard model is that of Barnes (2010). The biggest change from Barnes (2007) was the incorporation of the convective turnover timescale, τ_c, as well as an explicit, empirical dependence on two parameters, k_C and k_I, which reflect the bimodality of the period distribution of low-mass stars at young ages (see Figure 1.2). The gyro-age from Barnes (2010) is determined by:

$$t = \frac{\tau_c}{k_C}\ln\left(\frac{P}{P_o}\right) + \frac{k_I}{\tau_c}(P^2 - P_o^2) \tag{1.8}$$

where P_o is the initial period. Barnes (2010) adopt values of $k_C = 0.646$, $k_I = 452$ and $P_o = 1.1\,\mathrm{d}$. While including the convective turnover timescale indirectly integrates some physical baseline into Equation 1.8, it requires theoretical estimates of τ_c, and the formula is still fundamentally based on empirical observations. Importantly, however, Equation 1.8 implies that the dependence on age and mass is not separable.

The aforementioned studies primarily base their calibrations on young open clusters, typically neglecting anything older than about 600 Myr (the exception being a sample of old Mt. Wilson field stars used in Barnes 2003 and Barnes 2007). This changed with the work of Meibom et al. (2011), who applied the gyrochronology relations of Barnes (2010), given above, to the 1 Gyr cluster NGC 6811 using different values for P_o. They found that the observed relationship between age, period, and colour extended beyond the 600 Myr Hyades to this cluster. Meibom et al. (2015)

went a step further, this time testing gyrochronology with the 2.5 Gyr NGC 6819 using both Equation 1.8 and the standard models from Barnes (2007) and Mamajek & Hillenbrand (2008). They found excellent agreement between the model from Barnes (2010), and reproduced a period-age-mass (*P-t-M*) surface illustrating how NGC 6811, NGC 6819, and the Sun all fall along predicted gyrochronology relations. The *P-t-M* surface is reproduced in Figure 1.4 in Section 1.2. Barnes (2010) quote age uncertainties of approximately 13% from their gyrochronology model.

The extension of gyrochronology out to ages of 2.5 Gyr encourages the use of this technique as an age-dating method, although testing gyrochronology on a cluster of solar-age stars is even more desirable, since we have the best datapoint for comparison — the Sun. The Sun's rotation period of ∼26.2 d has been well-established, using, for example, spectroscopic measurements from Mt. Wilson to find its average equatorial velocity (Howard & Harvey, 1970). The solar amplitude varies with its 11-year activity cycle, but time series of total irradiance have been documented over the years (see e.g. Fröhlich & Lean, 1998; Fröhlich, 2000, 2006), thanks in large part to data from the *SOHO* mission ('Solar and Heliospheric Observatory'; Domingo et al. 1995). The average amplitude is on the order of ∼0.1%, which can be seen in Figure 2 of Aigrain et al. (2015b) — reproduced below in Figure 1.3 — who use solar data to simulate light curves for a blind rotation period recovery exercise; we will discuss aspects of this work in more detail in Chapter 5.

Despite gyrochronology's success in being able to reproduce both cluster data and the Sun's rotation period given its age, the fact that Collier Cameron et al. (2009) and the studies represented in Table 1.1 found different fits to their distinct datasets highlights the empirical nature of gyrochronology, a shortcoming which could have an effect on its overall applicability. Epstein & Pinsonneault (2014) derived rotation periods using both angular momentum evolution models (see Section 1.2) and the standard gyrochronology relationship from Equation 1.5. They found that there appeared

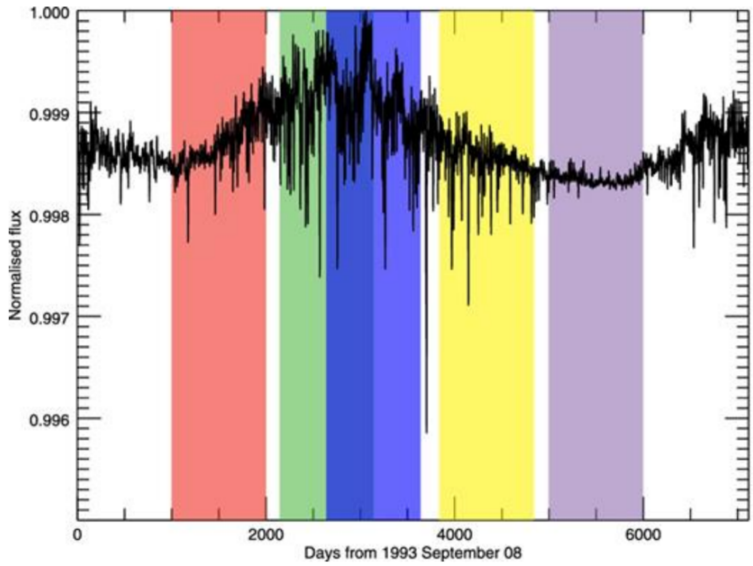

Figure 1.3: Figure 2 from Aigrain et al. (2015b), demonstrating the normalized irradiance of the Sun for a recent solar cycle. The colored regions represent sections used to simulate light curves in that work.

to be a systematic offset between the more theoretical and traditional gyrochronology methods, a potentially troubling conclusion. However, they also concluded that the use of rotation periods as an age-indicator could be the most precise approach for main-sequence stars when properly applied. The limitations of gyrochronology in light of angular momentum evolution is discussed in Section 1.2.

1.1.8 Comparison of Age-dating Techniques

We now briefly the summarize relative performances of isochrone fitting, asteroseismology, chromospheric activity, and gyrochronology as age-dating methods for main-sequence, solar-like stars. The precisions of each technique are given in Table 1.2. Isochrone fitting is effective for large groups of stars, but becomes much less certain for individual field stars in the absence of tightly-constrained estimates of mass, dis-

Table 1.2: Precisions for Different Age-Dating Methods

Technique	Precision (%)	Technique	Precision (%)
Isochrone fitting	∼20 – 50	Chromospheric Activity	∼60 (0.2 dex)
Asteroseismology	∼10	Gyrochronology	∼13

tance, etc. Ages from chromospheric activity are typically more reliable than those from isochrones, but they are limited to ages of less than 1 Gyr and are less precise. Asteroseismology is the most precise, but requires months to years of high-precision monitoring to return useful data for solar-like stars (Soderblom, 2010). Finally, while gyrochronology is reasonably precise, it suffers from its empirically-based roots and inconsistencies with other methods (see the following section for more details). Ultimately, combinations of these techniques, when available and applicable, should be used to constrain ages, as was done by Lachaume et al. (1999).

1.2 Angular Momentum Loss and Gyrochronology

The primary weakness of gyrochronology is that, as an age-dating technique, it is largely empirical. To fully take advantage of this method's strengths while acknowledging its limitations, we need to have an understanding of the physical processes which produce the observed relationships between age, mass, and rotation period. This is best understood in the context of angular momentum evolution, which encompasses both internal angular momentum transport and, more importantly to this thesis, angular momentum loss.

1.2.1 Angular Momentum Transport in Stars

We will now look briefly at how angular momentum is transported within the interiors of stars. Examples of reviews on the subject include those of Fricke & Kippenhahn (1972) and Maeder & Meynet (2000), and they both highlight turbulent flow or

instabilities, magnetic fields arising from convection, and meridional circulation as some of the primary mechanisms for internal angular momentum transport. One of the landmark models incorporating both turbulent flow and meridional circulation comes from the work of Zahn (1992). Meridional circulation arises from the differences in heating at the poles compared to the equator, resulting in the transport of matter from the poles to the equator (Maeder & Meynet, 2000). Departing from the more simplistic meridional circulation models of Mestel (1953), Zahn (1992) postulated that meridional circulation and horizontal turbulent transport via shear instabilities are limited by the presence of a stellar wind, such that both mechanisms become more important when the winds exist. However, the horizontal transport through shear directly interferes with that of the longitudinal meridional circulation (Zahn, 1992).

In addition to meridional circulation, magnetic fields play a substantial role in angular momentum transport. A classical work describing the generation and behavior of stellar magnetic fields is that of Parker (1979), and a popular basis model for angular momentum transport by magnetic fields is given by Spruit (1999) and Spruit (2002). The so-called 'Tayler-Spruit' mechanism, updated and modified by the work of Denissenkov & Pinsonneault (2007), basically describes how angular momentum gets transferred through the displacement of fluid from magnetic fields made unstable by differential rotation (Denissenkov & Pinsonneault, 2007). The model incorporated by Denissenkov (2010) also included the effects of magnetic fields on stellar rotation rate proposed by Charbonneau & MacGregor (1992) and Charbonneau & MacGregor (1993), since magnetic fields contribute to the spin-down of stars (see the following discussion on angular momentum loss). Denissenkov (2010) then modified this model in an attempt to explain the amount of lithium that can be observed in the Sun.

Another important mechanism is internal gravity waves, measured as g-mode oscillations in asteroseismic studies (Charbonnel & Talon, 2005). Charbonnel & Talon

(2005) introduced this mechanism as a way of both explaining the co-rotation of the Sun's core with its envelope and observed lithium abundances. While the core is rotating faster than the envelope, waves produced in the convection zone cause a shear layer to develop at the tachocline, and further propagation of the waves allows for the angular momentum to be readily transported into the slower-rotating envelope, spinning it up while slowing down the core until they rotate together (Charbonnel & Talon, 2005). Charbonnel et al. (2013) combined internal gravity modes with meridional circulation and turbulence to predict the rotation profiles for $0.6 - 2.0\,M_{\odot}$.

The interactions of the different types of angular momentum transport mechanisms can have a substantial and complex impact on the rotation of solar-like stars. Many have attempted to model the angular momentum transport within stars as part of larger stellar evolutionary models or to predict rotational velocities of stars using different combinations of these mechanisms (see e.g. Endal & Sofia, 1979; Chaboyer et al., 1995a,b; Krishnamurthi et al., 1997). However, while the internal transport of angular momentum is important to consider, we now look more specifically at how angular momentum is lost, as that has the biggest effect on gyrochronology models for older, main sequence stars.

1.2.2 Angular Momentum Loss

Schatzman (1962) proposed the mechanism for angular momentum loss in solar-type stars, suggesting that ejected matter in the form of stellar winds co-rotating with magnetic fields out to sufficiently large radii can bleed a disproportionate amount of angular momentum relative to the amount of mass lost. This mechanism depends on surface activity, which is in turn dependent on the presence and size of the underlying convection zone (Schatzman, 1962); the larger the convective zone, the easier it is for the star to lose angular momentum and spin down. Weber & Davis (1967) modeled the stellar wind itself, analyzing the effect that wind velocity and magnetic field

strength, particularly in the azimuthal direction, had on angular momentum loss. They used the Sun as a test case and demonstrated that this mechanism can lead to significant angular momentum loss for solar-like stars due to the induced torque (Weber & Davis, 1967):

$$\frac{dJ}{dt} = \frac{2}{3}\Omega\, r_a^2\, \frac{dM}{dt} \tag{1.9}$$

where J is angular momentum, Ω is the angular velocity of the roots of the magnetic force lines (i.e. the angular velocity of the star; Belcher & MacGregor 1976), r_a is the radius at which the Alfvénic Mach number is equal to one, and M is the mass of the star. Belcher & MacGregor (1976) built off this model, exploring the Sun's probable period of rapid rotation in the first half billion years of its life. As briefly mentioned above, Charbonneau & MacGregor (1992) and Charbonneau & MacGregor (1993) use angular momentum transport via magnetic fields to model both the spin-up and spin-down of the Sun, respectively.

The concept of magnetically-coupled stellar winds as the mechanism for 'braking' the rotation of a star implies that lower mass stars ($\sim$K spectral type) should spin down more quickly than their higher mass counterparts (up to about mid-F; Radick et al. 1987). This is not necessarily the case, however, as the internal structure of the star plays a large role in the early phases of angular momentum evolution. For example, Soderblom et al. (1993a) determined that the presence of ultra-fast rotators (UFRs) in a sample of Pleiades predominantly came from K dwarfs, and there have been many attempts to explain this and similarly observed phenomena. As a PMS, solar-like star contracts onto the radiative track following the convective Hayashi phase, the star's angular velocity increases as the moment of inertia decreases (Stauffer et al., 1984). At the same time, however, the star is losing angular momentum through the solar wind mechanism. While the star is contracting, there is effectively no net decrease in angular velocity, even while angular momentum is being lost, and the

timescale of this phase is longer for stars less massive than the Sun (Stauffer et al., 1984). The difference between the angular velocity of the core and that of the envelope adds another layer to the problem. If the core is uncoupled from the envelope (i.e. they are not rotating together), then the transfer or angular momentum from the core to the envelope will help the envelope maintain its angular velocity — or at least have a more gradual spin-down — until they have re-coupled (Endal & Sofia, 1981; MacGregor & Brenner, 1991; Soderblom et al., 1993b). It should be noted that accretion disks can prevent the spin-up of a PMS star, but only on a timescale up to the disk's lifetime of about 10 Myr (Edwards et al., 1993).

Once the core and envelope have re-coupled, the larger convective zones of lower mass stars increase the efficiency of wind braking. This is why, by the age of the Hyades, stars later than mid-F appear to follow the same general angular momentum loss rate, dependent only upon mass (Radick et al., 1987; Delorme et al., 2011). Kawaler (1988) derived a relatively simple equation for the angular momentum loss of stars that have reached the point where they no longer 'remember' their initial angular momentum (on the order of 10^8 yr) and can follow the Skumanich relation:

$$\frac{dJ}{dt} = -K_w \Omega^3 \Big(\frac{R}{\mathrm{R}_\odot}\Big)^{\frac{1}{2}} \Big(\frac{M}{\mathrm{M}_\odot}\Big)^{-\frac{1}{2}} \tag{1.10}$$

where K_w is a factor that represents uncertainties regarding the formation of stellar magnetic fields and winds. While Equation 1.10 does factor in important wind parameters, it is largely empirical, relying heavily on the Skumanich relation for stars beyond about 100 Myr of age. Kawaler (1988) does provide a more generalized version of Equation 1.10, but uses the one provided to demonstrate its validity. This has motivated more recent studies (Matt et al., 2015; Gallet & Bouvier, 2015) to create more physically-motivated models for angular momentum loss.

The work of Matt et al. (2015) builds off the steady-state stellar wind braking model developed by Matt et al. (2012) and relates the torque produced by the stellar

wind to the Rossby number, *Ro*. This model is built on the idea of 'saturation,' or when indicators for magnetic activity no longer correlate with *Ro* (Matt et al., 2015), which occurs at a transition point defined as (Matt et al., 2015):

$$\chi \equiv \frac{Ro_\odot}{Ro_{sat}} \equiv \frac{\Omega_{sat}\tau_c}{\Omega_\odot \tau_{c\odot}} \tag{1.11}$$

where $Ro_\odot$ is the Sun's Rossby number; Ro_{sat} is the saturation Rossby number for a given star; Ω_{sat} is the angular velocity at saturation; τ_c is the convective turnover timescale; and $\Omega_\odot$ and $\tau_{c\odot}$ are the solar angular velocity and convective timescale, respectively. This implies that saturation occurs when $Ro \leq Ro_\odot/\chi$ (Matt et al., 2015). Saturation only comes into play when solar-like stars are very young and rapidly rotating. After saturation, spin-down is chiefly dependent on τ_c, meaning low-mass stars are able to spin-down as quickly as necessary (Matt et al., 2015). To test their model, Matt et al. (2015) created a synthetic cluster with a range of masses and initial rotation period rates and let it evolve up to about 4 Gyr. By comparing the rotation periods of their synthetic cluster with those measured by *Kepler* (see e.g. McQuillan et al., 2014), they were able to determine that most of the stars with measurable periods in the original *Kepler* field are younger than about 4 Gyr (although selection bias excludes older, less active stars without measured periods).

The angular momentum evolution model from Gallet & Bouvier (2015) focused on stars of 0.5 – 0.8 $M_\odot$ such that, for the convective zone of the star:

$$\frac{dJ}{dt} = -\Gamma_{wind} + \Gamma_{c-e} - \Gamma_{rad} \tag{1.12}$$

where each Γ term represents a torque: Γ_{wind} is the torque due to the stellar wind, proportional to the angular velocity, mass loss rate, and the Alfvén radius, r_a; Γ_{c-e} is the torque resulting from the re-coupling between the core and the envelope; and Γ_{rad} results from the formation of the radiative core. Gallet & Bouvier (2015) also produce

a corresponding equation for the angular momentum evolution of the core, but we have only included the one for the envelope because it is generally the external stellar rotation that we measure (unless using asteroseismic methods). Gallet & Bouvier (2015) confirmed that the Skumanich relation is generally valid for solar-like stars beyond about 0.5 Gyr, although for stars approaching $0.5\,M_{\odot}$, the timescale can be up to 3 Gyr, depending on how quickly the core and envelope re-couple.

1.2.3 Implications for Gyrochronology

While angular momentum evolution models have become more sophisticated since Kawaler (1988), they have so far either generally followed the Skumanich relation or have drawn conclusions regarding its validity for sufficiently-aged, solar-like stars. This falls in line with the minor differences in parameter values for the more basic gyrochronology relations of Barnes (2007), Mamajek & Hillenbrand (2008), and Meibom et al. (2009), all of which have n values (the exponent which controls the age dependence in gyrochronology; see Table 1.1) near the Skumanich value of 0.5. However, this may not be the case for the whole duration of the main sequence. The first clue came from Angus et al. (2015), who fit the same basic gyrochronology model to a sample of *Kepler* stars with asteroseismic ages, several field stars, and two open clusters. They could not find model parameters that successfully fit each group of target stars simultaneously, though they admit that this could be a result of not taking certain complexities, such as metallicity, into account (Angus et al., 2015). On the surface, it appears that a discrepancy could exist not only between certain gyrochronology and asteroseismic ages, but also between field stars and cluster members, indicating that standard gyrochronology models may be inherently flawed.

Additionally, van Saders et al. (2016) found that gyrochronology systematically overestimated the rotation periods for older, main-sequence stars whose ages had been found using asteroseismology. Figure 1 from that paper, reproduced in Figure 1.4,

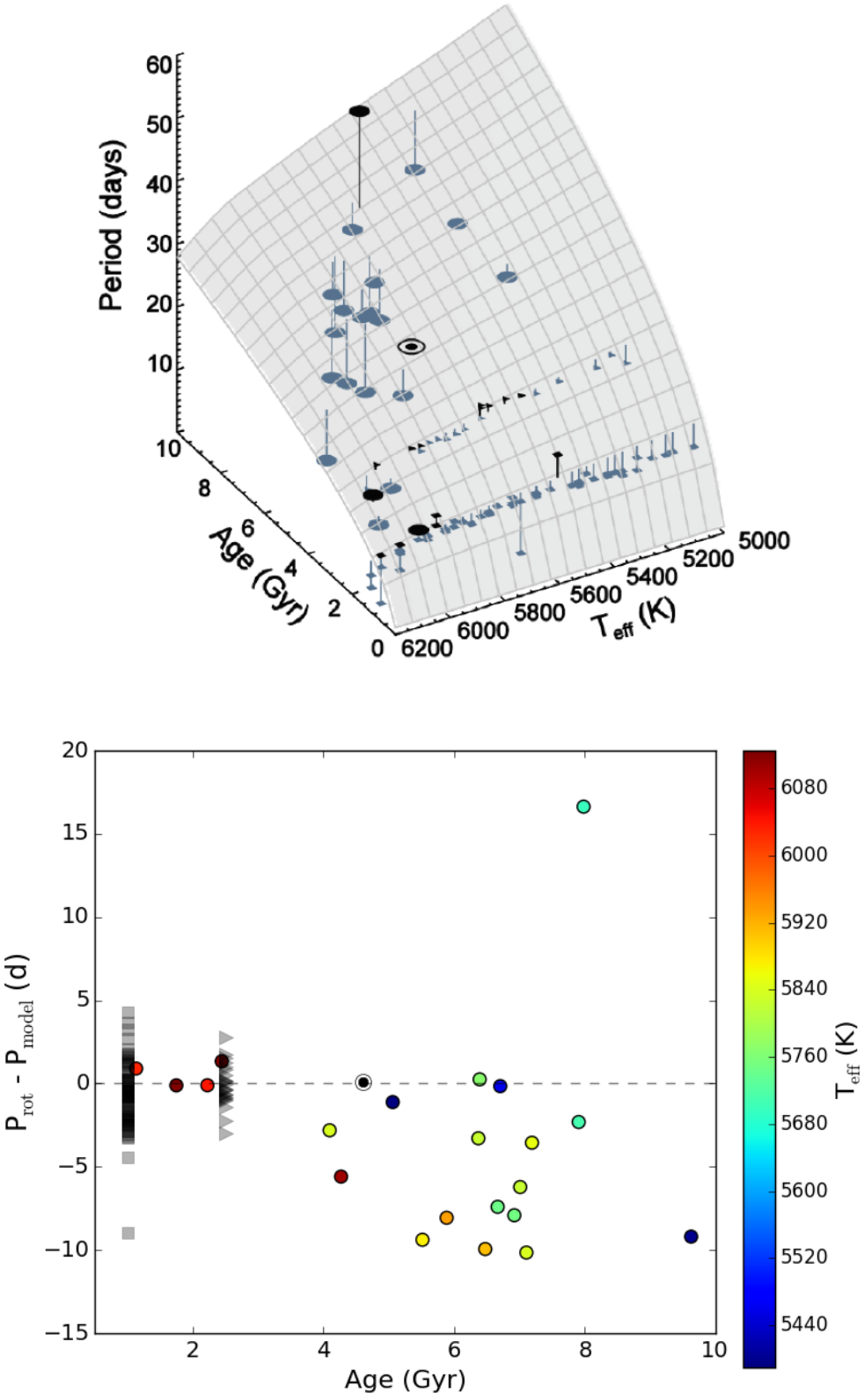

Figure 1.4: Figure 1 (top) from van Saders et al. (2016) illustrating the *P-t-M* surface from Meibom et al. (2015) with targets from the asteroseismic sample (circles), the 1 Gyr NGC 6811 (squares), the 2.5 Gyr NGC 6819 (triangles), and the Sun overplotted. The bottom plot reproduces the figure in 2D, displaying the difference between the modeled and measured rotation periods at a given age. Here, effective temperatures are given for the asteroseismic sample only.

puts the asteroseismic targets on the *P-t-M* surface from Meibom et al. (2015). This suggests that at some point during the main sequence, the magnetic wind braking becomes less efficient. van Saders et al. (2016) claim this happens when the Rossby number reaches a critical point, $Ro_{crit} = 2.16$, such that the period has become too long relative to the convective turnover timescale to effectively generate the surface activity and torque necessary to reproduce the spin-down required by gyrochronology. An important prediction from this is that higher mass stars reach Ro_{crit} faster (van Saders et al., 2016), since their convective turnover timescales are shorter. As a result, higher mass stars in particular do not follow gyrochronology relations for ages around 4 Gyr and older, and it is unlikely that the time dependence is a simple power law. By slowing down the angular momentum loss once Ro_{crit} is reached, however, van Saders et al. (2016) were able to reproduce both the rotation period trends predicted by gyrochronology for younger stars and the older asteroseismic sample.

If the 'weakened magnetic braking' theory of van Saders et al. (2016) is correct, it indicates that gyrochronology is only suitable up to about the age of the Sun, where the transition to Ro_{crit} is likely to occur for solar-like stars. Furthermore, it adds to the understanding of the physics involved, which gyrochronology on its own generally lacks. This new model, however, still needs more testing, preferably on a sample of stars that are roughly solar-age and encompass a sufficiently wide range of masses.

1.3 M67: The Old Open Cluster

The best candidate for testing both the weakened magnetic braking theory of van Saders et al. (2016) and gyrochronology at the solar age is the old open cluster M67, a.k.a. the 'King Cobra Cluster.' An image of M67 provided by NASA is given in Figure 1.5.[2] M67 is estimated to be $\sim$4.0 – 4.3 Gyr old, and roughly $800 - 900$ pc from the Sun (Carraro et al., 1994; Balaguer-Núñez et al., 2007; Geller et al., 2015).

[2]https://apod.nasa.gov/apod/ap070809.html

Figure 1.5: Picture of M67 from the 9 August 2007 NASA 'Astronomy Picture of the Day,' processed by Noel Carboni and Greg Parker.

Calculated metallicity values from the literature show that [Fe/H] ranges from about -0.1 to 0.1, with average values lying around -0.01 (Fan et al., 1996; Balaguer-Núñez et al., 2007; Taylor, 2007; Jacobson et al., 2011, the most recent of which reports -0.01 ± 0.05). Thus, the stars of M67 bear remarkable similarities to the Sun in both age and composition, making them a perfect platform for comparison.

The cluster has been surveyed many times in the past (see e.g. Johnson & Sandage, 1955; Eggen & Sandage, 1964; Racine, 1971; Montgomery et al., 1993), each iteration following improvements made to photometric observations. Members have been catalogued several times based on proper motion (Sanders, 1977; Loktin, 2005; Yadav et al., 2008) and radial velocities (Mathieu et al., 1986; Yadav et al., 2008; Pasquini et al., 2008; Geller et al., 2015, hereafter 'G15'). G15 report 1,278 candidate members, making M67 the richest, relatively nearby, solar-age open cluster. The CMD for M67

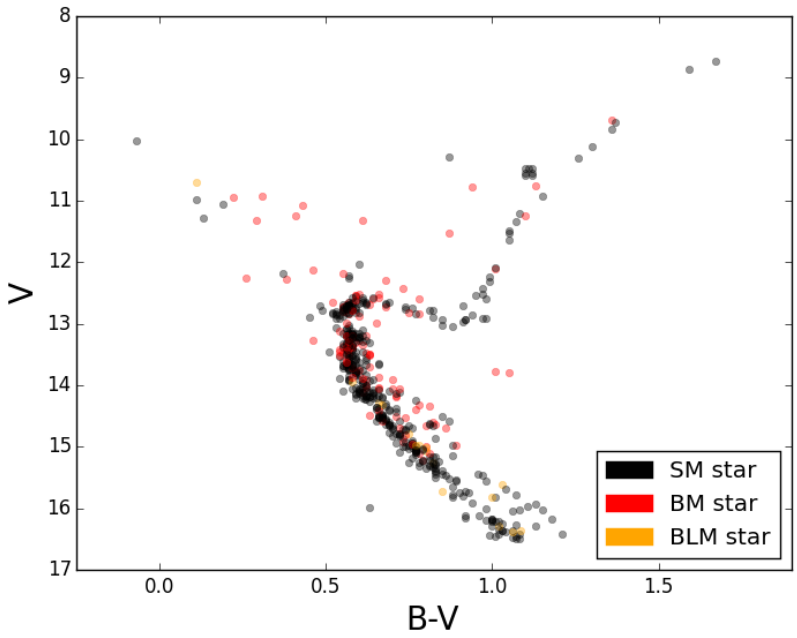

Figure 1.6: CMD from Geller et al. (2015), with single members ('SM') in black, binary members ('BM') in red, and binary likely members ('BLM') in yellow.

from G15 can be seen in Figure 1.6, where the membership type (i.e. single member, binary member, or binary likely member) is indicated by the colour of each point, as classified by G15. Of the 1,278 candidate members, G15 have only confirmed 562.

M67 has been the target of a wide range of astrophysical studies. Gilliland & Brown (1988) used M67 first as a testing ground for processing CCD photometry on large, dense groups of stars before Gilliland & Brown (1992) looked at the p-mode oscillations of member blue stragglers to back out important information regarding the stars' formation history and structure. Gilliland et al. (1993) attempted a more complete asteroseismic study on M67, finding evidence of oscillations for a substantial percentage of member stars. Janes & Smith (1984) discovered the homogeneity in composition for member giants. Mathieu & Latham (1986) looked at how spectroscopic binaries and blue stragglers were concentrated spatially within the cluster itself, and Mathieu & Mazeh (1988) used M67 to trial the use of binary circularization

timescales as age indicators. VandenBerg et al. (2007) and Magic et al. (2010) applied isochrones to M67 in an effort to understand the constraints on solar metallicity and the shape of the cluster's CMD, specifically with respect to the main sequence turn-off. The photometric precision offered by the *K2* mission (see Section 1.5) has more recently prompted the '*K2* M67 Study,' a collaboration dedicated to a wide range of topics, including a few of those mentioned above (see e.g. Leiner et al., 2016; Stello et al., 2016; Sandquist et al., 2018). However, until the *K2* mission, rotation period measurements of M67 — necessary for testing out gyrochronology — were nonexistent due to the lack of sufficient precision to detect the low-amplitude modulation of solar-age stars. We will return to this advancement in Section 1.5, and it forms the foundation for this thesis.

1.4 Brief History of Rotation Period Measurements

M67 provides the unique opportunity to test both gyrochronology and the weakened magnetic braking theory of van Saders et al. (2016) through the measurement of member rotation periods. Stellar rotation periods, in one form or another, have been measured and recorded since the early 1900s. Before high-precision photometry allowed for the direct measurement of rotation periods, the determination of rotational velocities from spectral line broadening dominated the effort for much of the twentieth century. Rotational velocities are usually denoted as $v \sin i$, and they provide a lower limit to a star's rotation period, since the inclination (and radius) of the star is uncertain unless the star is a member of an eclipsing binary.

Early discussions on how line widths can be translated into the corresponding $v \sin i$ measurement can be found in Shajn & Struve (1929) and Elvey (1930); the latter specifically looks at one of the more common lines for $v \sin i$, namely Mg II 4481. Since then, many studies have produced $v \sin i$ for thousands of stars, lead-

ing to significant advancements in the understanding of stellar evolution. The Mt. Wilson observatory contributed heavily to $v \sin i$ measurements, releasing over 23 000 measurements for 7 200 stars observed between 1901 and 1952 (Abt, 1970, 1973). The cumulative work of Slettebak (1954), Slettebak (1955), and Slettebak & Howard (1955) found the rotational velocities of hundreds of stars for spectral types ranging from early G to B using the Mg II 4481, Fe I 4071, and He I 4471 lines, concluding in the process that there is an observed relationship between stellar rotation and location on the H-R diagram. This body of work also offered evidence that rotation period increases from A to G on the main sequence, and that stars later than F5 appear to have little rotation, in general agreement with a contemporary study by Herbig & Spalding (1955). Abt & Hunter Jr (1962) focused specifically on clusters and associations, looking at members from I Lacerta, I Orion, α Persei, and the Pleiades. They found that the different groups of stars had their own dependencies on luminosity separate from one another, and that there appeared to be an inverse correlation between the number of spectroscopic binaries present in each group with the average rotational velocity, presumably due to how the total angular momentum is distributed between the orbit and each component's rotation period (Abt & Hunter Jr, 1962). A review of the rotational velocities of low mass stars, both PMS and along the main sequence, is given by Stauffer & Hartmann (1986), coming at a time when $v \sin i$ measurements started to be replaced with rotation periods through photometric means. However, rotational velocities are still important today, as they offer a critical point of comparison for directly observed rotation periods (see e.g. Nielsen et al., 2013b).

By the early 1980s, advances in photometric observations had allowed for the measurement of stellar rotation periods without any dependence on either stellar radius or orbital inclination. This was done through photoelectric photometry. Used even as early as 1955 to obtain the CMD for the old open cluster M67 (Johnson &

Sandage, 1955), photomultiplier tubes amplified the incoming signal from the star within a narrow wavelength band to measure flux. The critical Ca H and K emission surveys of stars in the solar neighborhood conducted at the Mt. Wilson observatory were obtained through photoelectric photometers (Wilson, 1968, 1978; Vaughan et al., 1978), and an example of using photoelectric photometry for the acquisition of rotation periods can be found in Dorren & Guinan (1982). Often, to produce target light curves, data acquired from photoelectric means required differential photometry, where both the target and several comparison stars are observed within a survey. A light curve is created by comparing the changes in intensity from the target relative to the comparison stars, and the latter relative to each other, over time. Rotation periods can then be determined from spot modulation in the light curve.

Variations of differential, photoelectric photometry were utilized extensively on open clusters during this time. To avoid having to assume that the comparison stars were not variable, studies such as Radick et al. (1982) used the average intensity of cluster members as their point of comparison for individual targets to find several rotation periods in the Pleiades and Hyades. A follow-up study of the Hyades from Radick et al. (1983a) found an inverse relationship between brightness and variability, a similar conclusion to that of Radick et al. (1983b), who looked specifically at chromospheric emission and its relationship to the amplitude of variability. Lockwood et al. (1984) and Radick et al. (1987) compared the majority of a sample of Hyads with corresponding measurements from Mt. Wilson observations, including Ca H and K intensities. This study was particularly important for confirming that later, main-sequence stars typically exhibit lower amplitude variability in their light curves, and that the Hyades follows the Rossby relation between rotation period and chromospheric activity.

The advent of CCD photometry, however, revolutionized the field by allowing for long-term, simultaneous, high-precision monitoring of stellar fields. The combined

work of Prosser et al. (1993a), Prosser et al. (1993b), and Prosser et al. (1995) used CCD photometry to precisely measure the rotation periods of tens of stars in open clusters, including α Persei and the Pleiades, as well as a field T Tauri star. The last of these studies was able to correlate rotation period with X-ray activity, finding a break beyond periods of about 7 d. A more ambitious undertaking that took advantage of the power of CCD photometry was that of the Monitor project (Aigrain et al., 2007; Irwin et al., 2007b), which used 2 m and 4 m telescopes to acquire light curves for over 10 000 stars. The Monitor project systematically measured hundreds of rotation periods of low mass stars from several open clusters across a range of ages, including NGC 2362 (5 Myr; Irwin et al. 2008a), NGC 2547 ($\sim$39 Myr; Irwin et al. 2008b), M50 (130 Myr; Irwin et al. 2009), NGC 2516 (150 Myr; Irwin et al. 2007a), and M34 (200 Myr; Irwin et al. 2006). Other important rotation period measurements studies using CCD photometry include the 5-month re-observation of M34 by Meibom et al. (2011) on a 0.9 m telescope, in which two distinct sequences were found for young, low mass stars. A similar approach to M35 was taken by Meibom et al. (2009), where a clear relationship between period and mass at 150 Myr was again revealed by the 300 measured periods, leading to the calibration of gyrochronology relations previously described. In addition, Hartman et al. (2009) investigated the relationship between variability, colour, and period from the 575 periods of solar-like stars in the $\sim$550 Myr M37, using a combination of CCD photometry and $v \sin i$ measurements to provide important test points for gyrochronology.

The search for planets outside our Solar System prompted other large-scale photometric studies whose data could be used for other astrophysical pursuits, including stellar rotation and angular momentum studies, when CCD photometry enabled the first detection of an exoplanet transiting in front of its star (Charbonneau et al., 2000). These dedicated programs include the Hungarian Automated Telescope network (HATnet) (Bakos et al., 2004) and SuperWASP (Pollacco et al., 2006), where

'WASP' stands for 'Wide Angle Search for Planets.' While important for exoplanet discovery, these platforms enabled advancements in the understanding of angular momentum evolution. Hartman et al. (2010) used HATnet data to determine the rotation periods of over 350 solar-like Pleiades stars which could be compared to periods from M35 to acquire a spin-down timescale for young, low-mass stars. Collier Cameron et al. (2009) and Delorme et al. (2011) both analyzed SuperWASP data, finding tight relationships between colour and period for the ∼600 Myr Coma Berenices, Praesepe, and Hyades clusters. These ground-based programs, along with the independent open cluster studies mentioned above, enriched the literature with thousands of rotation periods acquired from high-precision CCD photometry.

The potential of CCD photometry has not been limited to ground-based observations, however. Space-based platforms have caused the field to explode due to the precision achievable without atmospheric interference. These started with *MOST*, a microsatellite launched in June 2003 and initially dedicated to asteroseismic studies ('MOST' stands for 'Microvariability & Oscillations of STars') of solar-like stars, pulsators, and Wolf-Rayet stars (Walker et al., 2003; Matthews, 2007). While not specifically used for rotation purposes, *MOST* used two CCDs in conjunction with a 150 mm aperture to acquire asteroseismic data (Walker et al., 2003) and eventually even light curves for planetary searches (see e.g. Miller-Ricci et al., 2008b,a), providing a glimpse of the true potential of space-based photometry. Three and a half years later saw the launch of the *CoRoT* mission, a French-funded satellite originally dedicated to both asteroseismology and the discovery of exoplanets through the simultaneous observation of 12 000 stars using a 27 cm telescope (Michel et al., 2008; Baglinl et al., 2009). The *CoRoT* mission has been successful both in finding planets (see e.g. Barge et al., 2008; Alonso et al., 2008; Bouchy et al., 2008; Aigrain et al., 2008; Moutou et al., 2008; Deleuil et al., 2008; Rauer et al., 2009, etc.), rotation studies (see e.g. Affer et al., 2013; Stauffer et al., 2014), and asteroseismology (see

e.g. Appourchaux et al., 2008; Bruntt, 2009; Hernández et al., 2009; Kallinger et al., 2010).

While *MOST* and *CoRoT* ushered in the era of wide-field, space-based photometry for the purpose of hunting exoplanets, the NASA *Kepler* mission has set the new standard. Launched in 2009, the mission sought to discover Earth-like, habitable planets while simultaneously monitoring over 150 000 stars (Jenkins et al., 2010), reaching precision down to 84 ppm for 6.5-hour combined differential photometric precision (CDPP) (Borucki et al., 2010; Koch et al., 2010; Christiansen et al., 2012). The data from this mission, and its secondary mission *K2*, have produced spectacular results, detecting thousands of exoplanet candidates and producing light curves well-suited for variability and asteroseismic studies in the process. Both the *Kepler* and *K2* missions will be discussed in more detail below. While designed for a different purpose, i.e. understanding the structure and history of the Milky Way, the European Space Agency's *Gaia* mission surpasses *Kepler* in scope, providing astrometric and spectral data for ∼1 billion[3] stars, including rotational velocities (Katz et al., 2004; Gaia Collaboration et al., 2016). *Gaia* Data Release 2 (DR2) has recently become available, and rotation periods for nearly 150 000 stars have already been identified (Lanzafame et al., 2018). DR2 has also catalogued 1526 members for M67 (Gaia Collaboration et al., 2018). Finally, the follow-on mission to *Kepler* and *K2*, the Transiting Exoplanet Survey Satellite (*TESS*), will survey nearly the entire sky, accumulating anywhere from ∼27 – 350 days of observation for each target (Ricker et al., 2014). *TESS* was launched in the spring of 2018 and has begun preliminary operations.

[3]http://sci.esa.int/gaia/47354-fact-sheet/

1.5 *Kepler* and *K2*

As briefly mentioned above, the advent of NASA's *Kepler* mission revolutionized both the exoplanet and stellar variability fields of study. With respect to its principal mission, *Kepler* discovered almost 4,500 exoplanet candidates, over half of which were later confirmed using a combination of detailed light curve analysis and ground-based follow-up (Thompson et al., 2017). However, *Kepler* has proven to be invaluable for research into stellar variability, thanks to its unprecedented levels of photometric precision. Key *Kepler* large-scale rotation period studies include those of McQuillan et al. (2013), Reinhold et al. (2013), McQuillan et al. (2013) (letter), McQuillan et al. (2014), Nielsen et al. (2013a), García et al. (2014), and Reinhold & Gizon (2015). These studies measured the rotation periods of tens of thousands of *Kepler* field stars (there were very few clusters in the original *Kepler* FOV), including planet-host stars. Along with the ground-based studies mentioned above, they helped bring to light a number of interesting trends, including, for example, the bimodal period distribution shown by late K and M-dwarfs, and the correlation between stellar temperature, rotation period, and the spread therein, which may be related to differential rotation, active region evolution, or a combination of the two. The measurement of FGK dwarf rotation periods in the 1 Gyr NGC 6811 (Meibom et al., 2011) and 2.5 Gyr NGC 6819 (Meibom et al., 2015) was a result of the '*Kepler* Cluster Study,' extending for the first time the gyrochronology *P-t-M* surface beyond ∼600 Myr. *Kepler* data has also been utilized for asteroseismic age determination (García et al., 2014; Angus et al., 2015; van Saders et al., 2016), and these studies have called into question the behavior of stars at older ages and the applicability of gyrochronology further along the main sequence, as previously mentioned.

While M67 does have great scientific potential in removing some of the ambiguity in this regard, there are intrinsic difficulties in finding rotational modulation among its members, the most obvious being the generally low amplitude of variability in

middle-aged, solar-like stars (Mamajek & Hillenbrand, 2008; Radick et al., 1995, 1998; Hempelmann et al., 1996; Baliunas et al., 1998), which is only on the order of a few tenths of a percent. This necessitates high-precision observations of the cluster beyond that of ground-based platforms. The best chance for such observations come from *K2*, the second of phase of the original *Kepler* mission initiated after two of the spacecraft's reaction wheels ceased to operate in 2013. Unlike the ∼360 d observation windows from *Kepler*, *K2* campaigns last approximately 75 d and focus on regions around the Ecliptic, using a combination of thruster firings and solar pressure to retain a large degree of pointing stability. While this ingenious solution from Ball Aerospace engineers allows the *Kepler* spacecraft to continue to provide invaluable science, it does mean that *K2* data suffer from reduced precision relative to the original mission, as well as a characteristic 'sawtooth' pattern on 6-hr timescales (Vanderburg & Johnson, 2014; Vanderburg et al., 2016). The loss in precision also comes from aperture losses and differences in sensitivity within and among pixels as the target rolls across the spacecraft's boresight (Howell et al., 2014). For example, while the precision for *Kepler* at $K_p = 10$ was 10 ppm on 6-hr CDPP timescales, the early *K2* precision was about 80 ppm at $V = 12$ for the same timescale, and 400 ppm for the 30-minute, long-cadence data (Christiansen et al., 2012; Vanderburg & Johnson, 2014).

The reduced photometric precision spurred the development of various pipelines to address the unique systematic features inherent in *K2* data, and with resounding success. These include K2VARCAT (Armstrong et al., 2014, 2016), the approach of Huang et al. (2015), PSF-fitting (Libralato et al., 2016), K2P^2 (Lund et al., 2015), and EVEREST (Luger et al., 2016). The two most important pipelines for this thesis, however, are the *K2* Systematics Correction (K2SC) pipeline (Aigrain et al., 2015a, 2016) and K2SFF (Vanderburg & Johnson, 2014; Vanderburg et al., 2016) combined with the *Kepler* single-scale PDC-MAP (see Section 2.5 in Chapter 2).

We will discuss these various photometric and detrending techniques in the following section. A number of these detrending pipelines — including K2SC and K2SFF — have achieved photometric precision within a factor of two or better of *Kepler* for stars fainter than $K_p = 12.5$, while nearly matching the original precision for brighter stars. As a result, *K2* has already been successful in producing high-quality results for other (albeit younger) open clusters, particularly the Pleiades (Rebull et al., 2016a,b; Stauffer et al., 2016) and Hyades (Douglas et al., 2016). Stauffer et al. (2016) found in the Pleiades evidence supporting the break in angular momentum loss from magnetized winds at F5, and they illustrate how the shape of the sequence of slow-rotating stars could imply age. With respect to the Hyades, Douglas et al. (2016) suggest that magnetic braking is more effective than what previous literature had claimed. Importantly, the first M67 rotation periods have been acquired and published through the analysis of *K2* Campaign 5 data (Barnes et al., 2016; Gonzalez, 2016b,a). We address these results in Chapters 3 and 4.

1.6 Photometric and Detrending Techniques

As previously mentioned, the *Kepler* spacecraft takes advantage of CCDs to simultaneously observe over 150 000 stars. There are several families of photometric techniques, post CCD pixel-level calibration (dark current, flat field frames, bias frames, etc.), that can then be applied to extract light curves from the raw data. Aperture photometry comprises the first category; Da Costa (1992) and Mighell (1999) both provide concise reviews on the subject. According to Da Costa (1992), there are three main steps to aperture photometry: determining the center of the target image, estimating background intensity, and then determining the amount of flux coming from the actual target. The first step can be done in several ways. Da Costa (1992) gives as examples the marginal sum technique (Auer & Van Altena, 1978;

Stetson, 1979), in which the intensity is marginalized over the X- and Y-pixels and then fit to a Gaussian, and centroid determination, in which intensity centroids are computed after determining the mean intensity of target pixels. We can estimate the background by finding the mean, median, or mode (or all three together) of all the pixels and iteratively removing those with intensities above a certain threshold from the calculated value (Da Costa, 1992). Finally, an aperture, whose shape takes the form of either a pixellated or 'soft-edged' circle, is placed over the target. The size of the aperture's radius depends on the brightness of the star; brighter stars require larger apertures to optimize the amount of measured flux while fainter stars typically have smaller apertures to avoid background contamination. Examples of pixellated apertures applied to *K2* data can be found in Armstrong et al. (2014) and Armstrong et al. (2016), while circular apertures are utilized by Vanderburg & Johnson (2014), Aigrain et al. (2015a), Huang et al. (2015), and Vanderburg et al. (2016). The apertures can also be 'fixed' or 'moving,' meaning they do not change pixel location from frame to frame in the case of the former, or they move with the image centroid in the case of the latter. Vanderburg & Johnson (2014) and Armstrong et al. (2014) use fixed apertures, while Aigrain et al. (2015a) use moving apertures. The intensities of the pixels within the aperture are then summed and the background is subtracted to provide a flux value at each frame. We make use of the technique from Aigrain et al. (2015a) in this thesis, and we will discuss it in more detail in Chapter 2.

The next major category for the photometric extraction of light curves is the fitting of the point spread function (PSF). A detector's PSF describes the shape of its response to incoming light, which can be estimated as coming from a point source. Da Costa (1992) also provides a review on PSF-fitting. Assuming that all the pixels in a given frame vary by a scaling ratio, fitting a PSF to each successive frame reveals the relative intensities of each target, though this leads to uncertainty when converting to proper magnitudes (Da Costa, 1992). PSF-fitting is much easier to accomplish

using space-based observatories because no accounting has to be made for seeing. Early programs for PSF-fitting include the well-used DAOPHOT (Stetson, 1987), the STARMAN pipeline for photometric observations of the globular cluster NGC 6752 (Penny & Dickens, 1986), and the program DoPHOT (Mateo & Schechter, 1989). More recently, Anderson & King (2000) and Anderson et al. (2006) have modified the traditional approach to PSF-fitting by using what they call an 'effective' PSF. Instead of trying to fit the actual PSF of the instrument, one can instead model an effective PSF that describes how much light from a star should fall within a given pixel based on that pixel's location on the detector (Anderson & King, 2000). Libralato et al. (2016) built off both of those works to produce light curves from *K2* data.

Difference imaging makes up the final family of photometric extraction techniques. The idea, originally conceived by Crotts (1992) for the purpose of detecting microlensing events, suggests that if each CCD image of a given field in an observing campaign is subtracted from a template image with a high signal-to-noise ratio, one can construct light curves of variable targets based on the differences in measured intensities. Tomaney & Crotts (1996) dubbed this approach 'difference image photometry,' and fully implemented the idea of Crotts (1992) for the first time. While this method is particularly useful for crowded fields, it requires matching the PSF intensities of each target image with that of the template, which is a difficult task (Tomaney & Crotts, 1996). This PSF matching has to be done in order to correct for differences in seeing when observing from the ground, and Alard & Lupton (1998) created a pipeline which optimized this process. Microlensing collaborations, such as the Probing Lensing Anomalies NETwork, or PLANET (see e.g. Albrow et al., 1998, 2009, and references therein), have utilized difference imaging with success, but the basic technique can be applied to variability studies, as well.

The term 'detrending' refers to the identification and removal of artificial features or trends in the extracted light curves generally known as 'systematics.' Systematics

have to be corrected, or at least understood to an extent, before one can properly analyze a light curve. Systematics often arise from the small movement of the target across a pixel on the detector, since one part of a given pixel may be more sensitive to incoming light than another. Inter-pixel variations, or flat-field residuals, have a similar effect. Intra- and inter-pixel variations comprise what is known as position-dependent systematics, which are often corrected by modeling the correlation of intensity with X- and Y-pixel location. This approach has been widely used for the infrared space telescope *Spitzer*. For example, Charbonneau et al. (2005) employed this technique while measuring the photometric emission of the planet orbiting TrES-1. Some studies measure the correlation by fitting a polynomial to a function that describes flux as a result of X- and Y-pixel position. Knutson et al. (2008), Machalek et al. (2008), and Shporer et al. (2014) apply quadratic fits, utilizing MCMC to determine the best-fit parameters for the coefficients, in order to find exoplanet thermal emission from the light curves. This approach requires accurate image centroids.

Ballard et al. (2010) presented a different method for modeling systematics, described as a 'point-by-point correction.' Binning the flux of a light curve, they derived the value of a weighted sensitivity function for each binned 'point' by weighting the flux of the un-binned points based on the X- and Y-pixel distance from the point in question. Avoiding astrophysical variations (from, for example, a transit signal) with a mask, the correction is completed by dividing each point by the corresponding value in the normalized sensitivity function (Ballard et al., 2010). Stevenson et al. (2012) built on the work of Ballard et al. (2010) to create a computationally faster algorithm. In their analysis of the transiting exoplanet HD 149026b, Stevenson et al. (2012) perform what they dub 'bi-linear interpolated sensitivity mapping,' or 'BLISS.' In this method, the pixel surface is mapped in such a way that 'knots' of data are identified (as opposed to simple bins), although their positions are also modeled with weighted flux values. Applications and variations of the method of Ballard et al. (2010) and

BLISS can be found in Cowan et al. (2012), Lewis et al. (2013), Lanotte et al. (2014), and Zellem et al. (2014).

Pixel-level decorrelation, or 'PLD,' is another novel approach to systematic correction originally developed by Deming et al. (2015) for *Spitzer* data. Because variations in flux within a given pixel are proxies for position effects, one can directly use intensities as opposed to relying on accurate centroid determinations (Deming et al., 2015; Luger et al., 2016). PLD works by normalizing intensities within a specified aperture and then using them as the basis for a least squares fit, effectively avoiding the astrophysical signal while isolating the systematic trends (Luger et al., 2016). Luger et al. (2016) use PLD to model light curves from *K2* data, adding a principal component analysis (PCA; see below and Chapter 2 for more details) to the method of Deming et al. (2015) in order to put limits on the fit. While not ideal for a crowded field (Luger et al., 2016, 2017), PLD automatically corrects for differences in sensitivity between pixels, is analytic in nature, and is computationally inexpensive.

Many other systematic correction techniques are available in the literature, and we list a few more of them here. The trend filtering algorithm (TFA) of Kovács et al. (2005) and the external parameter decorrelation (EPD) of Bakos et al. (2007) and Bakos et al. (2010) have been used by, for example, the *K2* pipeline of Huang et al. (2015). The former performs the correction by calculating the linear combination of a set of template light curves that represent the common trends existent in the dataset and subtracting it from each light curve. This approach is similar to that of the PCA we use in this thesis. On the other hand, EPD cross-correlates any departures from the median intensity of each light curve with a variety of factors, including pixel location (Bakos et al., 2007). In the K2VARCAT pipeline, a surface made up of the centroids of pixel locations based on the measured flux is created, and dividing the binned median flux along the surface corrects the light curve. Finally, the Astrophysically Robust Correction (ARC; Roberts et al. 2013) and ARC2 (Aigrain

et al., 2017) model common-mode trends with co-trending basis vectors which implement Bayesian-like inference to remove systematics without affecting astrophysical variability in *Kepler* data. ARC and ARC2 are similar to the systematics removal pipeline designed specifically for the *Kepler* mission and addressed by Stumpe et al. (2012), Stumpe et al. (2014), and Smith et al. (2012). We discuss the *Kepler* pipeline in more detail in Chapter 2, along with the K2SFF and K2SC pipelines, developed specifically for *K2* data and applied in this thesis.

1.7 Rotation Detection Techniques

With respect to actually measuring the rotation periods themselves, the literature is filled with a wide variety of different approaches and tactics. Chapter 3 is dedicated to a more in-depth discussion of the techniques relevant to this thesis, so we will limit this section to a brief overview of three broad 'categories' of period detection methods and their respective pros and cons. We define these categories as Fourier-based, statistic-based, and Bayesian.

For our purposes, a Fourier-based method constructs a periodogram based on the Fourier transform (FT) of the data. This reveals the dominant frequency modes in a light curve, which, for a periodic signal, should indicate the value of the period. Wehlau & Leung (1964) present a detailed description of how this works, as well as some of the problems that may arise when using this approach. For example, competing peaks in the periodogram resulting from different sources (i.e. those not related to a periodic, astrophysical signal but lingering systematic trends) may lessen the significance of the real peak, leading to false detections (Wehlau & Leung, 1964). In addition, FT periodograms can be computationally slow, though one can implement different strategies to speed up the process (see e.g. Fitch, 1967). However, these periodograms do not need evenly-spaced data (they actually benefit from irregular

sampling), and in some cases, do not even require the computation of the FT. The best example is the Lomb-Scargle periodogram (Lomb, 1976; Scargle, 1982), which is *equivalent* to the Fourier-based method but merely calculates the least squares fit of a sinusoidal model. We discuss this special periodogram in more detail in Chapter 3.

Statistic-based methods hearken from the traditional approach of testing a range of periods to see which one can produce the least amount of scatter with respect to the mean flux of a given light curve (Stellingwerf, 1978). Lafler & Kinman (1965) famously automated this process, setting the foundation for rotation detection techniques which require the computation and minimization of a statistic that expresses how well a period fits the data. Examples of statistic-based methods include phase dispersion minimization (Stellingwerf, 1978) and minimum string length (Burke et al., 1970; Dworetsky, 1983), which both use phase curves to compute their respective statistics; these are described in Chapter 3. The primary advantages of statistic-based methods is that they are computationally very quick, can be utilized on irregularly sampled data, and do not require a functional form in modeling the light curve. In general they do not, however, have a way of deciphering between the true period or its harmonic, for example, and may pick the latter over the former. The autocorrelation function (also discussed in Chapter 3) is technically statistic-based, as well, but it requires evenly-sampled data and, for periodic signals, provides a clue to the difference between the actual period and its half harmonic.

The third main category of rotation detection methods presented in this thesis is the Bayesian approach. This involves applying Bayes' Theorem (see Chapter 3) in order to determine the probability distribution of a set of parameters (e.g. the period of a signal) with respect to the data. The parameter set that maximizes the likelihood that the data can be explained by those parameters is chosen. This was first utilized for the purpose of detecting rotation period searches in light curves by Gregory & Loredo (1992), and Gaussian processes (GPs) take it a step further;

more detail regarding both of these approaches is given in Chapter 3. The Bayesian approach allows for many different models to be tested, and it only depends on specifying a range of test periods as opposed to a fixed set (Gregory & Loredo, 1992). In addition, this method leads to the determination of period uncertainties and does not require regularly sampled data (Gregory & Loredo, 1992). Just as with the other category of methods, however, lingering systematic features can 'fool' this method, and, depending on the type of Bayesian approach used, can be very computationally slow. Furthermore, human decision-making is involved in the decision of which models to test directly with Bayesian inference or, in the case of GPs, how the covariance between data points is to be modeled.

1.8 Thesis Structure

Age-dating a field star on the main sequence is a difficult task, as few observable characteristics change noticeably throughout this lengthy, stable phase of a star's life. As a relatively nearby, solar-age cluster, M67 offers the perfect opportunity to determine if established gyrochronology relations, which offer rotation as a convenient indicator of maturity and hold fast up to at least 2.5 Gyr (Meibom et al., 2015), still apply for older, main-sequence stars. Alternatively, the cluster provides a rich testing ground for more complex theories regarding the angular momentum evolution of stars with slightly greater masses than the Sun. Asteroseismology has given evidence that, as they begin to evolve onto the subgiant branch, these stars are rotating faster than what gyrochronology would predict, suggesting that at some point during the main sequence, the magnetic field strength decreases, reducing the efficiency of the angular momentum loss in those stars (van Saders et al., 2016). This anomalous rotation further highlights the empirical nature of gyrochronology, urging the need for a more physical understanding behind the angular momentum evolution of main-sequence

stars.

It is clear, then, that acquiring a set of accurate rotation periods from M67 is highly desirable. We can now attempt this thanks to the relatively high-precision data from the space-based *K2* mission and its observation campaigns conducted along the Ecliptic. This thesis, which details the steps taken in pursuit of this goal and the subsequent implications the periods themselves have for the angular momentum evolution of solar-age stars, is structured as follows: In Chapter 2, we outline our method for the extraction and correction of *K2* light curves. We explore rotation detection techniques in Chapter 3, determining our own preliminary set of M67 rotation periods. This set of rotation periods, however, showed considerable scatter, and we found general disagreement with the published values of Barnes et al. (2016). These disconcerting results, combined with the even greater scatter found in the follow-on periods by Gonzalez (2016a), motivated a comprehensive round of sinusoidal injection tests to probe our best-case sensitivity limits in finding solar-like signals from a single campaign of *K2* data, presented in Chapter 4. Based on what we learned from the sinusoidal injection tests, we use smaller, more realistic injections with realistic star spot model signals from Aigrain et al. (2015b) to develop in Chapter 5 an algorithm that combines several rotation detection techniques to find periods from both single and multiple campaigns of *K2* data. Here, we present a list of 'final' rotation periods, which we then analyze in the context of gyrochronology and angular momentum evolution models, as well as tidal evolution theory for a sample of binaries, in Chapter 6. Finally, our main conclusions are summarized in Chapter 7.

Chapter 2

Light Curve Extraction and Detrending

Calvin and Hobbes by Bill Watterson

2.1 Introduction

Critically, M67 was first observed during *K2* Campaign 5 (C05), which took place from April to July 2015.[1] The typical series of 'postage stamp' images, known as target pixel files (TPFs), account for individual stars on the outer edges of the cluster, while a larger 'superstamp' encompasses the crowded regions of the centre. M67

Sections of this Chapter have been published as Esselstein et al. (2018).

[1] https://keplerscience.arc.nasa.gov/k2-fields.html

was very recently re-observed during Campaign 16 (C16; discussed in Chapter 5), and again for a final time in Campaign 18 (C18; just completed at the time of this writing), but we focus here on the C05 light curves to illustrate how we extract and process the light curves from this important cluster. In addition, this chapter documents our attempts to maximize light curve precision in the face of the systematic features inherent in *K2*. Section 2.2 focuses on the light curve extraction methods we employed to produce light curve files. These include the standard *Kepler* processing pipeline, as well as the manual construction of the M67 superstamp followed up by source identification, astrometric solution determination, and target matching. Section 2.3 details the removal of systematics from individual stars, presenting an overview of K2SC and how it works to correct position-related artifacts (though for a more in-depth description, the reader is referred to Aigrain et al. 2016). This section also outlines our approach to remove long-term, common-mode trends in the *K2* M67 data that could interfere with the accurate determination of rotation periods from the cluster. The whole process for extraction, detrending, and common-mode systematic removal to produce light curves ready for analysis is hereafter referred to as the 'Oxford' pipeline. Estimates of final light curve precision from C05 are given in Section 2.4. Finally, Section 2.5 provides a brief, analogous description of K2SFF combined with *Kepler* PDC-MAP, known collectively as the 'CfA' pipeline, before we comment on the quality of the light curves produced by both the Oxford and CfA pipelines in Section 2.6.

2.2 Light Curve Extraction

The Oxford pipeline ultimately produces two sets of light curves for M67. The first is derived from the *Kepler* pipeline using simple aperture photometry, and is known as the 'SAP' dataset. While the *Kepler* spacecraft has a sizable field-of-view of 116

square degrees,[2] telemetry limitations restrict data to individual 'postage stamps' of each target, the sizes of which are determined based on each star's brightness. Falling into this category, the SAP stars constitute the outer edges of M67, and their raw light curves are available directly from the Mikulski Archive for Space Telescopes (MAST). The second set, known collectively as the 'superstamp,' is a bit more complicated, as the crowded inner regions of the cluster would make obtaining individual postage stamps for each member star both gruelingly difficult and inefficient. Therefore, we essentially stitch together a bunch of indiscriminate (i.e. they may contain more than one star) postage stamps covering the cluster's centre and identify individual targets from this larger image. The extraction process for each dataset will now be described in more detail.

2.2.1 *Kepler* Simple Aperture Photometry

The raw (i.e. not yet corrected for star-by-star and common-mode systematics) SAP light curves are a mid-level product of the overarching *Kepler* pipeline at the Science Operations Center (SOC) at NASA Ames, which consists of three main parts in producing usable flux time series: pixel-level calibration (CAL), photometric analysis (PA), and pre-search data conditioning (PDC).[3] A schematic provided by the NASA *Kepler* & *K2* Science Center is given below in Figure 2.1. Each target is observed and then downloaded as either 'long cadence' , with the total exposure lasting approximately 30 min, or 'short cadence,' where the final exposure time is roughly 1 min.[4] We only use the long-cadence data for our light curves. The CAL step then implements the standard pixel calibrations to create the TPFs, accounting for CCD channel-specific bias, thermally-induced dark current, and inter-pixel differences (i.e. the flat field calibration) (Quintana et al., 2010). In addition, CAL corrects for the

[2]https://keplerscience.arc.nasa.gov/the-kepler-space-telescope.html#field-of-view
[3]https://keplerscience.arc.nasa.gov/pipeline.html
[4]https://keplerscience.arc.nasa.gov/data-products.html

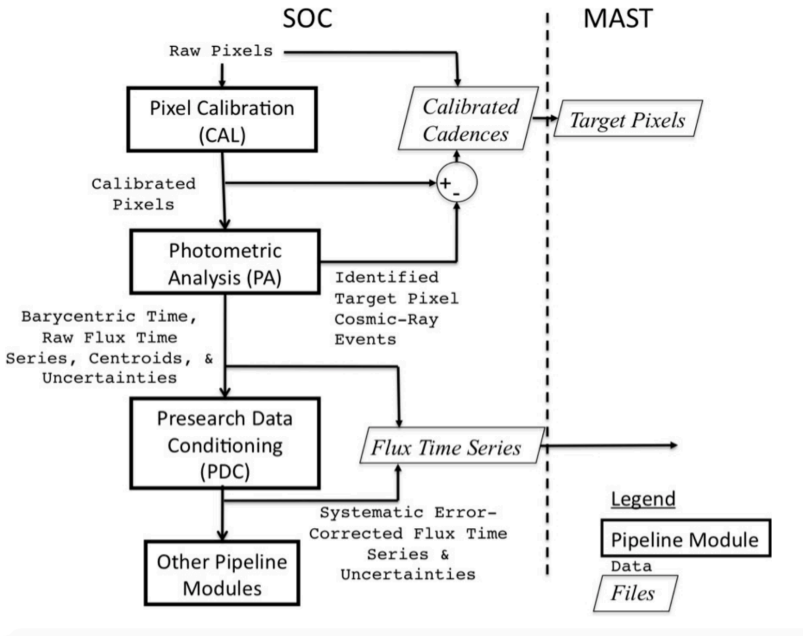

Figure 2.1: Schematic of the data extraction and processing steps within the *Kepler* pipeline (image publicly available from the online NASA *Kepler* & *K2* Science Center).

smear that results from the lack of a shutter on the *Kepler* photometer during CCD read-out, under- or overshooting distortions, and any nonlinear departure from the modeled gain (Quintana et al., 2010).

After CAL, the pixel data are ready for PA, which includes the actual application of simple aperture photometry. Before this step, however, PA searches for abnormalities around each target star within each cadence, such as anomalously increased flux levels known as 'Argabrightening events' and cosmic ray hits (Twicken et al., 2010). Then PA models and removes the background for each target. At this point, each pixel is modeled by the *Kepler* pixel response function (PRF) (Bryson et al., 2010), which takes into account the effects of differential velocity aberration (DVA), spacecraft jitter, differences in sensitivity within a given pixel, and *Kepler*'s point spread function (PSF) (Smith et al., 2016). The PRF is used to create a model full frame image (FFI) for each CCD channel at every cadence, and for each target, a second FFI

is constructed with the pixels from the target's respective postage stamp removed, allowing the signal-to-noise ratio (SNR) for the target to be computed (Smith et al., 2016). At first, only one pixel from the target is used to determine the SNR, but additional pixels are included in the calculation until the optimum SNR is reached (Smith et al., 2016; Van Cleve et al., 2016). This process of maximizing SNR by including the appropriate pixels is what constitutes simple aperture photometry (Smith et al., 2016), and the sum of the pixels within the apertures yields the flux for each cadence (Twicken et al., 2010). This procedure was optimized, however, by using actual data instead of just the modeled FFI to calculate the SNR (Smith et al., 2016). After creating the apertures, the centroids from each cadence are determined by weighting the flux within the aperture, the target's final brightness is computed, and a barycentric timestamp correction is applied (Twicken et al., 2010). The final outputs of PA are the raw versions of the SAP light curves, which are made available on MAST (see Figure 2.1). These light curve files also contain predicted positions based on the global astrometric solution used for spacecraft pointing, which are later needed for detrending. Over 25 000 SAP light curves were extracted from C05, although we are interested in the 1877 of those that fall on CCD module 6, which contains M67.

After PA, there is the additional PDC step in the *Kepler* pipeline, which prepares the light curves for planetary transit searches (the primary mission of *Kepler*) by attempting to remove common-mode systematics while preserving astrophysical signals. However, PDC does not account for the *K2* sawtooth, and it comes at the cost of reduced amplitudes for astrophysical signals with timescales greater than about 15 d (Stumpe et al., 2012; Smith et al., 2012; Stumpe et al., 2014; Gilliland et al., 2015). This a problem for an in-depth study of rotation in M67, where we expect to find periods around 25 – 30 d. While the PDC versions of the light curves are also available on MAST, we do not use them, as they are not optimal for our purposes.

2.2.2 The Superstamp

Our second set of M67 light curves contains those stars in the crowded, inner regions of the cluster where it would be impractical to develop individual postage stamps for every star of interest. Rather, we use a specially designated set of TPFs with data covering the entire cluster centre at every cadence. This 'stitching' together of calibrated postage stamps creates the 'superstamp,' though individual targets are not yet identified. As a result, acquiring the light curves for these stars is a bit more complicated than simply downloading the raw flux from MAST. Instead, we employ a slightly modified version of the technique presented in Aigrain et al. (2015a).

Somewhat similar to the production of the SAP light curves, this process involves creating a new FFI for the CCD channel(s) on which the superstamp falls. In C05, M67 falls across two channels of CCD module 6 (6.1 and 6.2), so we must reconstruct two separate FFIs for every cadence. Before we can do this, however, we must gather some preliminary information. After using one of the superstamp TPFs to record the observation times and which cadences may be corrupt (i.e. due to cosmic rays, saturation events, missing data, or thruster firings), we determine the pixel location of each TPF on the specific CCD module channel. Then, using a previously calibrated FFI from the same campaign with an astrometric solution from `astrometry.net` (Lang et al., 2010), we create a template FFI for each channel of our superstamp data, setting every pixel value to zero. The FFI template is then ready to be filled in with data from the superstamp TPFs.

For each cadence and channel, we place the corresponding data from each TPF in the proper locations on the template FFI based on the preliminary astrometric solution, creating a frame with data for the superstamp only. Figure 2.2 provides example FFIs from C05, covering both channels 6.1 and 6.2, at a single cadence. The regions filled in with superstamp data are highlighted by the purple rectangles. We do not create FFIs for poor quality cadences that have been flagged due to possible cor-

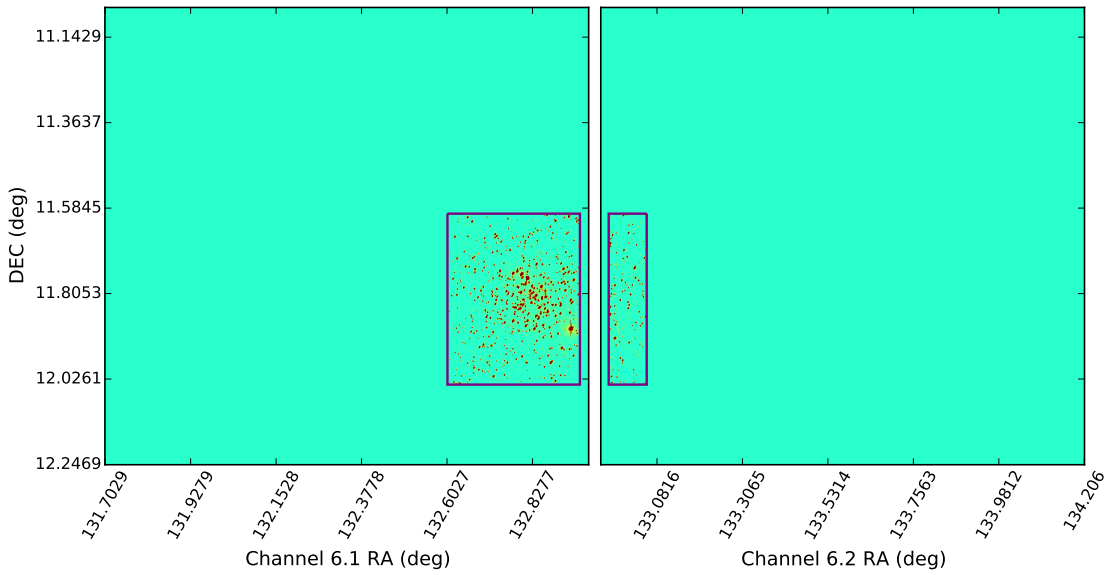

Figure 2.2: Example superstamp FFIs from Campaign 5 for channels 6.1 (left) and 6.2 (right) at a single cadence. The superstamp regions where data have been filled in are highlighted by purple rectangles.

ruption. With the new FFIs constructed, we generate a confidence map with a binary mask that shows where we have data from the TPFs and where we do not (or where a pixel did not have a finite value). We can then begin the process of source identification and light curve extraction, using the publicly available `CASUTools` routines `nebuliser`, `imcore`, and `wcsfit` (Irwin et al., 2004).

The addition of `nebuliser` is an upgrade to the method outlined in Aigrain et al. (2015a). It accounts for variable background modeling and removal for every FFI through the use of sliding, iterative mean and median filters, which we apply, in practice, to both the X- and Y-axes at the same time.[5] We specify median and mean pixel windows of 45 and 15 pixels, respectively, because the median is more robust to outliers than the mean, and remove the background through subtraction. The implementation of the `nebuliser` routine is important due to the crowded, unresolved areas in the centre of M67, and an example of its effect is given in Figure 2.3. The left panel displays the original image at a given cadence from the FFI of a single

[5]http://casu.ast.cam.ac.uk/surveys-projects/software-release/background-filtering

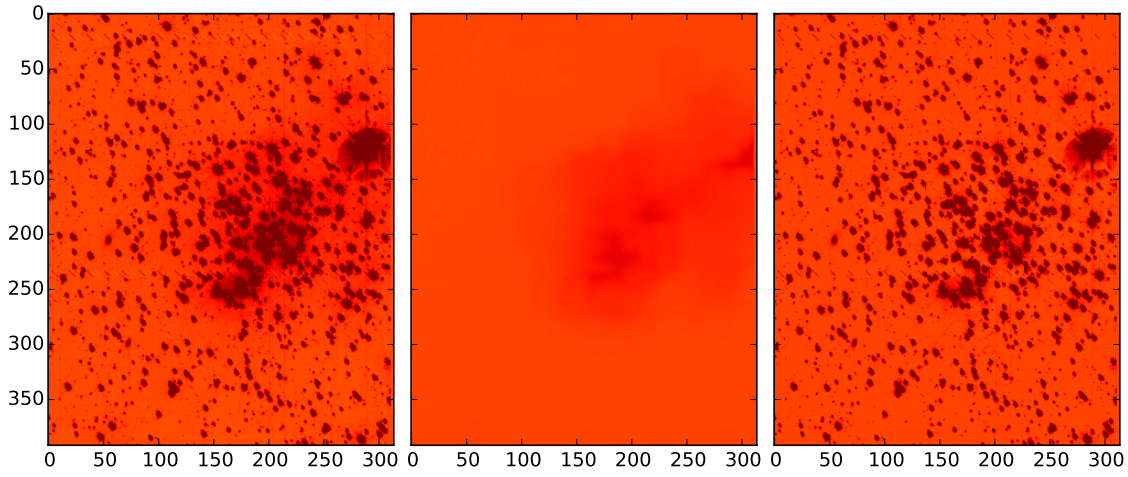

Figure 2.3: Example effect of background removal using `nebuliser` on the first extension of a given C05 cadence. From left to right are the original image, the modeled background from `nebuliser`, and the corrected image.

extension. The middle illustrates the modeled background from `nebuliser`, and the far right panel shows the corrected image.

After `nebuliser`, we run `imcore`, which uses the confidence map and several rounds of k-sigma clipping to filter out the remaining background and detect individual sources within the superstamp.[6] This produces a catalog of potential objects for each frame. We also generate a master catalog using the first 20 FFIs, stacking them into one image and running through the same steps listed above to best identify the true sources within M67. We then cross-match the master catalog with 2MASS using `wcsfit` to acquire a more precise astrometric solution. Next, we extract light curves for every listed star at every cadence by placing a circular aperture at each star's sky position (as recorded in the master catalog). We use six different aperture sizes as a way to offer flexibility based on an individual star's brightness; larger apertures are more optimal for brighter stars, while smaller apertures reduce the amount of background noise which could contaminate the flux received from fainter stars. In

[6]http://casu.ast.cam.ac.uk/surveys-projects/software-release/imcore

addition, with a crowded cluster, we have to be wary of possible light from neighboring stars spilling into a particular target's aperture, especially since the *Kepler* pixels are relatively large. Therefore, we use apertures with the following radii: 1, 2, $2\sqrt{2}$, 4, $4\sqrt{2}$, and 8 pixels. As a point of reference, the full width at half maximum for *K2* images is ∼1.5 pixels (Aigrain et al., 2015a). Ultimately, from the *K2* C05 data, we produce six different light curve versions for 1342 stars identified from the master image.

Once the light curves are extracted, we apply a zero-point correction for the six different apertures of all targets in each frame in a preliminary attempt to remove some of the systematics, especially those resulting from aperture losses. We first normalize each light curve by dividing the flux array by its median value. Next, we calculate each light curve's basic scatter using the following equation:

$$s_i = 1.48 * \text{median}(|f\text{norm}_i - 1|) \tag{2.1}$$

where $f\text{norm}_i$ is the normalized flux array of object i. We use 1.48 as a scaling factor that, under the assumption of a Gaussian distribution of $f\text{norm}_i$, makes the scatter equivalent to the standard deviation. We then assign a weight to each object, using the inverse square scatter, and compute the zero-point based on the weighted, normalized flux. The zero-point flux for each object from a given aperture is then, simply, the zero-point subtracted from the normalized flux. We save this flux in a new light curve, along with the relative X- and Y-pixel locations of each target. These have similarly been normalized for each object by computing the median and then subtracting it from the original value for each object in each frame.

At this point, we have superstamp (SS) light curves, but we have not yet matched each object with an actual star, identified in *K2* data with an EPIC number. We need to convert our astrometric solutions from pixels to RA and DEC so that we can match it to a catalog of M67 EPICs. For our light curves, we use a master target list built

off Geller et al. (2015) and compiled under the direction of Robert Mathieu of the University of Wisconsin for the *K2* C05 target proposal as a way of maximizing the number of M67 members which fell on silicon when the final pointing for the campaign was chosen. This catalog contains 12 935 candidate members of M67. Of these, 12 521 are drawn from the *Kepler* EPIC database, 266 come from the 2MASS calibration field (see e.g. Sarajedini et al., 2009), and the last 148 targets make up those missing from the EPIC database around $K_p \sim 19$ (Gilliland & Mathieu, private communication). Cluster membership probabilities for stars brighter than $K_p = 15$ are based on radial velocity and proper motion, as explained in Geller et al. (2015). For completeness, the catalog keeps those stars with probabilities of 20% or greater. For fainter stars, the master list includes all potential members based on photometric membership, unless otherwise contradicted by known radial velocities or proper motions. After we convert pixel locations to RA and DEC using the World Coordinate System module from `astropy`, we utilize the software `TOPCAT` to cross-match objects from our SS light curve file to *K2* EPICs from the master target list. Of the 1342 objects identified in the C05 superstamp, 976 have EPIC numbers from this master list (henceforth known as the 'Mathieu catalog', this is not to be confused with the one developed in light curve extraction). We restrict the SS dataset to include only these matched objects.

2.3 Systematics Correction

At this stage, the fully-extracted SAP and SS light curves still suffer heavily from systematics, the most dominant of which in *K2* data are those due to the spacecraft's pointing variations. These systematics fall into two primary categories, one accounting for the short-term features which affect each star individually, the other comprised of long-term trends which are common to a majority of the light curves.

The former include the 6-hour sawtooth pattern previously mentioned, while the latter are products of DVA, which causes stars to drift across any given pixel, leading to aperture losses and producing systematic features where the pixel has regions of varying sensitivity. The next step in the Oxford pipeline is to correct these systematics, first detrending each star on an individual basis before applying a common-mode correction to all the light curves in a given set.

2.3.1 Individual Stellar Detrending

We accomplish the star-by-star detrending using K2SC. We here give an overview of how this method works, but it is fully described in Aigrain et al. (2016). K2SC models each light curve as the sum of two unknown functions, one which depends on the star's pixel location on the CCD and represents the pointing systematics, and one which depends on time and represents the star's intrinsic variations, as well as any residual systematics not captured by the position-dependent component. The model is formulated as an additive Gaussian process (GP), which allows us to require that each function has a certain degree of smoothness without having to specify its exact form. GPs will be discussed in more detail in Chapter 3, but for now, it is enough to know that using an additive GP also enables us to separate the time- and position-dependent components. Removing the former from the original light curve is helpful for looking for planetary transits, while subtracting the latter, which is dominated by the $\sim$6-hour drift of the spacecraft, leaves us with a light curve corrected for position-dependent systematics only, minimizing the impact on any astrophysical variability. K2SC also flags significant outliers in the data, which we subsequently remove since the rotational signals we are interested in should be relatively smooth.

2.3.2 Common-Mode Systematics Removal

While K2SC is effective at removing positional systematics occurring on short timescales, visual inspection of the light curves post-K2SC reveals significant, residual long-term trends in both the SAP and SS datasets. As these trends are primarily caused by DVA (as previously mentioned), they are present in the *K2* M67 light curves regardless of the extraction or detrending techniques used. For example, two dominant trends were noticed by Barnes et al. (2016) during their period search in M67, though they used the PDC versions of the *K2* C05 light curves available from MAST. To remove these trends, Barnes et al. (2016) applied a principal component analysis (PCA). We use this approach, as well. The PCA produces a set of principal components (PCs), which describe the trends that explain a given percentage of the total variance in a set of light curves. Each light curve can be modeled as a linear combination of each PC according to the following relationship:

$$LC_{ij} = \sum_{k=1}^{K} \omega_{ik} PC_{jk} + \varepsilon_{ij} \tag{2.2}$$

where LC_{ij} is the flux of the light curve of star i at observation j out of N stars in a set and M observations (i.e. cadences); ω_{ik} is the weight of the k^{th} principal component PC_{jk} for the i^{th} star, out of a total of K calculated PCs; and ε_{ij} describes everything else that comprises the light curve (i.e. the astrophysical signal and noise). Subtracting the first term in Equation 2.2 removes the long-term trends.

To calculate the PCs, we first normalize each light curve by dividing by its median. We then construct an NxM matrix, where each row is the logarithm of the normalized light curve, which produces better results than the standard re-scaling of each light curve to have a zero mean and unit variance. We compute the singular value decomposition (SVD) of the matrix, returning the eigenvectors, which are the PCs; the associated eigenvalues, which tell us what fraction of the total variance of

the dataset is explained by each trend; and a matrix of coefficients relating each light curve to each PC (i.e. ω_{ik}). The most dominant trends in the data are represented by the first few PCs.

Because the M67 members fall on two different output channels of a single CCD and are read by a different set of electronics, light curves extracted from the different channels may potentially have different systematic trends. However, we found no significant difference between the sets of PCs calculated from an entire set, or from each output channel in turn. On the other hand, there were much more significant differences between the PCs extracted from the SAP and SS sets, as illustrated in Figure 2.4, so these were processed separately. Therefore, we processed all the SAP and SS stars, respectively, at the same time, regardless of actual cluster membership.

If PCA is applied blindly, however, large-amplitude features in individual light curves can dominate the PCs, skewing the correction and introducing these features in the corrected light curves of other stars. Luckily, this can be diagnosed easily because the linear combination of PCs becomes dominated by a single star. Two problematic stars were identified in this way in the SAP set, and were subsequently excluded from the PC estimation: EPIC 211391083 (an eclipsing binary) and EPIC 211327533 (whose light curve contains a large discontinuity). We also excluded the first 85 cadences ($\sim$1.8 d) from the light curves before evaluating the PCs, as the systematics are particularly pronounced in the early phase of the campaign as the spacecraft settles into its thermal environment. When these cadences were included, the PCA correction was of significantly lower quality, perhaps because the assumption of linearity is not as appropriate for the very beginning of the campaign.

Usually, a threshold in the fraction of explained variance (i.e. the eigenvalue) associated with each PC is used to decide how many PCs to include in the correction. We experimented with different values for this threshold, and settled on 2.5% and 7.5% for the SAP and SS sets, respectively, which correspond to two PCs in both

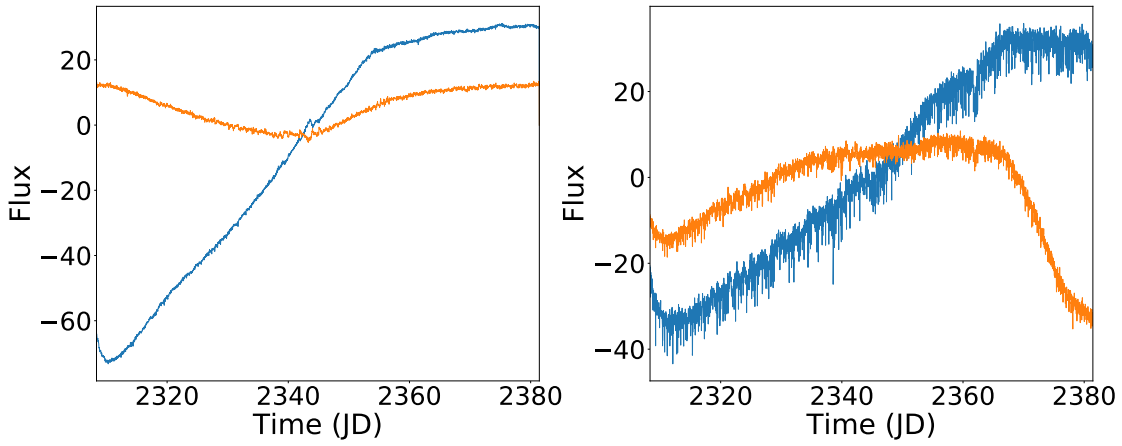

Figure 2.4: Principal components used to correct long-term systematics in the SAP (left) and superstamp (right) datasets as part of the Oxford pipeline. The primary PCs are in blue, while the secondary PCs are in orange.

cases. While we did test a range of thresholds for each dataset, too high a threshold only produced one PC, which was not sufficient enough to explain all of the dominant, common modes seen in the light curves when examined by eye, while too low produced three or more, in which case the extra PCs were superfluous or could potentially introduce unwanted features in the data. The resulting PCs from our choice of thresholds were somewhat similar in shape between the SAP and SS light curves, showing that these are the dominant modes in the *K2* data. A range of thresholds can produce the same 2 PCs, but the ones we chose were the on the lower end of those ranges for both datasets. The final sets of PCs used for the SAP and SS are shown in the left and right panels of Figure 2.4, respectively. The PCs that explain the largest percentage of light curve variance are in blue, while the secondary PCs are in orange. The SS PCs appear noisier than the SAP PCs because their amplitudes are much smaller relative to the noise than the SAP PCs; the most dominant SAP PC accounts for roughly 84% of the total variance of the light curves, while the first PC of the SS set only accounts for about 43%.

To illustrate the effectiveness of our systematic corrections, Figure 2.5 displays

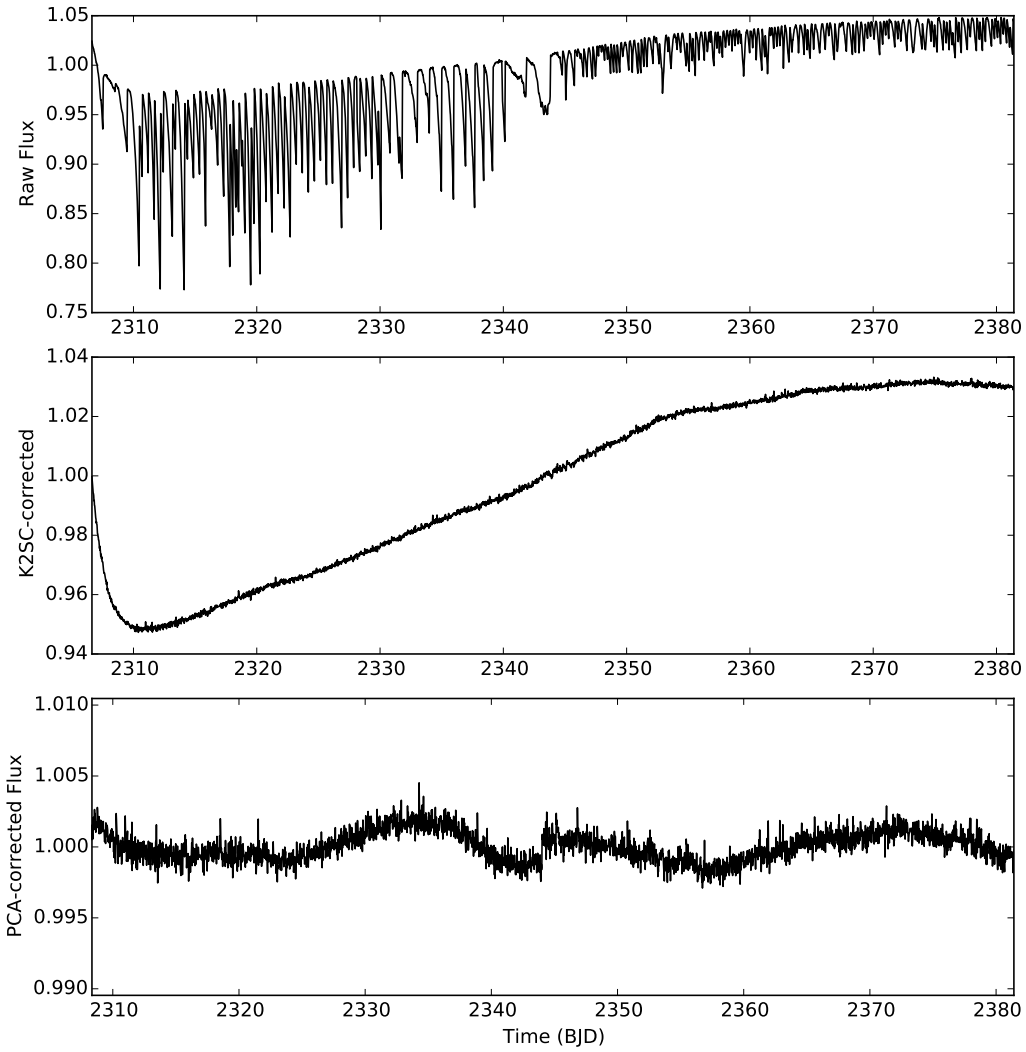

Figure 2.5: Example SAP light curve from EPIC 211410992 at each of the three different stages of the Oxford pipeline: raw flux from extraction (top), K2SC-corrected flux (middle), and final flux after the application of the PCA (bottom)

the light curve for a sample SAP star (EPIC 211410922) after each of the three main stages of the Oxford pipeline. The top panel shows the raw flux post-extraction but before any of the systematics have been removed. The raw light curve is clearly riddled with high frequency systematics, but these features disappear after the application of K2SC, shown in the middle panel. However, while K2SC cleans up the raw light curve considerably, there is still an obvious long-term trend in the data lasting the duration of the whole campaign and which matches the primary SAP PC from the top panel of Figure 2.4. This trend is removed after the PCA, as evident in the bottom panel of Figure 2.5, producing the final, usable version of the light curve.

2.4 Light Curve Precision

After the application of K2SC and the PCA, the light curves are now ready for analysis. As a first check on the effectiveness of our pipeline, we calculate the scatter using a variation of the median of absolute deviations, or MAD (Hoaglin et al., 1983):

$$\mathrm{MAD} = 1.48 * \mathrm{median}(|f_i - m_f|) \tag{2.3}$$

where f_i is the flux of a specific light curve at each cadence i, and m_f is the median flux. Technically, the median term itself is the MAD scatter; we include the factor of 1.48 as before in Equation 2.1. The median MAD scatter at $K_p = 12$ for the C05 SAP sample is 544 ppm. To compute the MAD scatter for the SS dataset, we first had to choose the optimum aperture for each star. We applied Equation 2.3 to each of the six SS apertures for a given SS target, and the aperture with the lowest scatter was selected. Almost 65% of the SS sample had optimum aperture radii of one pixel, and ∼19% used the 2-pixel radius aperture. The remaining four apertures were each selected for less than 10% of SS stars. The median MAD scatter at $K_p = 12$ for the C05 SS based on optimal apertures is 203 ppm.

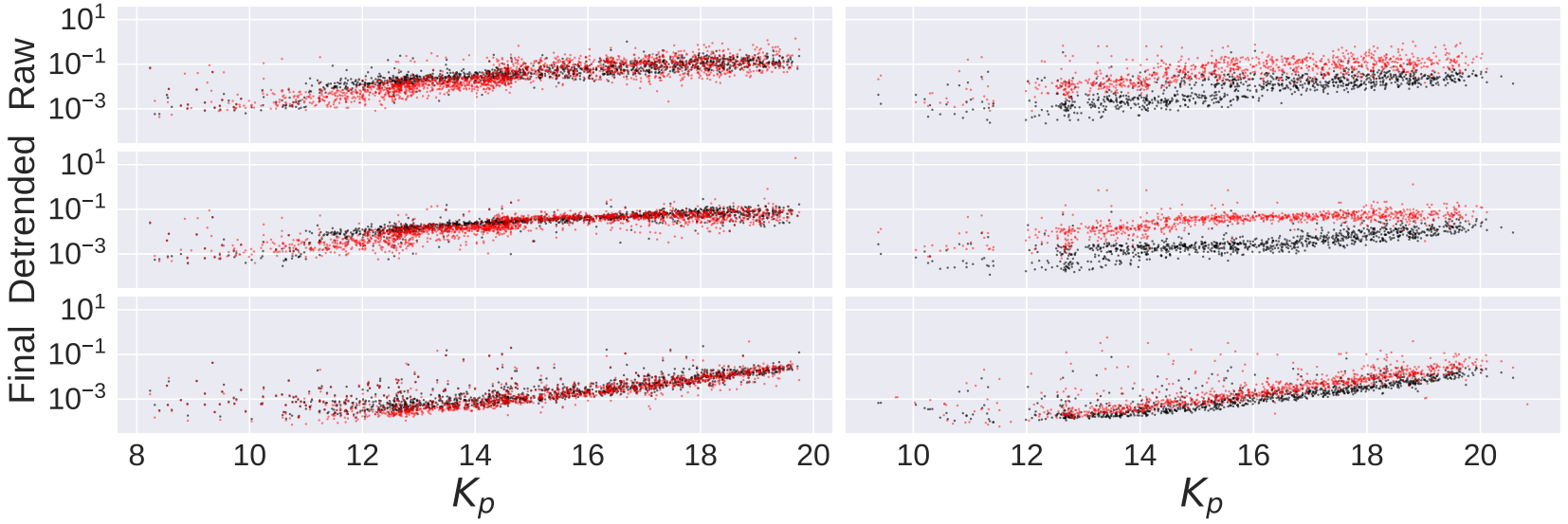

Figure 2.6: MAD scatter versus K_p magnitude for the SAP (left column) and SS (right column) samples. The results of the Oxford and CfA pipelines are shown in black and red, respectively. From top to bottom, we plot the MAD scatter in the raw light curves, after star-by-star systematics correction, and after common-mode systematics correction.

The discrepancy between the SAP and SS datasets processed with the Oxford pipeline is most likely due to the differences in light curve extraction, with the SS having a lower starting point with respect to noise levels. Despite this, the magnitude distributions between the two datasets are very similar, as shown by the black data points in the two bottom panels of Figure 2.6. The left-hand column of Figure 2.6 shows the SAP MAD scatter at the various stages of the pipeline, while the right-hand side gives the SS scatter. The rows, from top to bottom, show the raw scatter post-extraction, after star-by-star detrending, and, finally, following the application of the common-mode trend removal, echoing the changes in the example from Figure 2.5. The red data points provide the MAD scatter for the same stars extracted and processed from the CfA pipeline, briefly outlined below in Section 2.5. The Oxford and CfA precisions are properly compared in Section 2.6.

2.5 The 'CfA' Pipeline

The CfA pipeline acts as a point of comparison when probing the quantitative limits of a period search in M67 (Chapter 4), and it offers another set of light curves from which we can attempt to detect rotation periods (Chapters 3, 5). The CfA pipeline is so-named because it is originally the product of a collaboration, led by current NASA Sagan Fellow Andrew Vanderburg, between the Harvard Center for Astrophysics and NASA Ames. Like the Oxford pipeline, the CfA pipeline involves an extraction step, star-by-star correction for position-related systematics, and common-mode trend removal. We do not execute these steps ourselves, but since we use the output light curves from this pipeline, it is important to have an understanding of how they have been processed and prepared. While other *K2* pipelines have been successful in various contexts, we did not include them in this study for a variety of reasons. The EVEREST pipeline, for example, does not perform optimally with a crowded field

(Luger et al., 2016, 2017). The *K2* light curves from K2VARCAT (Armstrong et al., 2014, 2016) only encompass Campaigns 0 – 4. Alternatively, Cody et al. (2018) have recently released a procedure for extracting superstamp data similar to Aigrain et al. (2015a). Though a future comparison of our results with light curves from both Cody et al. (2018) and the PSF photometry Libralato et al. (2016) — applied to M67 by Nardiello et al. (2016) — would be interesting, we either did not yet have access to them (in the case of the former), or we were unaware of their existence (in the case of the latter) when we began the study in Chapter 4.

The CfA pipeline extracts all targets — whether they belong to the superstamp or individual TPFs — using the same method, following the techniques outlined in Vanderburg & Johnson (2014) and Vanderburg et al. (2016). This involves taking the post-CAL TPFs for the individual postage stamps and the superstamp and, rather than creating FFIs as is done in the *Kepler* SAP pipeline and the Oxford superstamp construction, directly utilizing the astrometric solution from the World Coordinate System to identify targets and place stationary apertures. While the Oxford pipeline uses 6 set aperture sizes, the CfA pipeline uses 20, summing up the pixels at every cadence to create 20 different versions of each light curve. Half of the CfA apertures are based on the *Kepler* pipeline PRF, while the remainder range in size from 1.5 to 13 pixels. However, for the *K2* M67 light curves, only those apertures with radii of less than 3 pixels are considered to avoid potential contamination from other stars in the crowded field.

To correct the 6-hour, position-dependent systematics, the CfA pipeline again follows the method prescribed by Vanderburg & Johnson (2014) and Vanderburg et al. (2016), iteratively modeling and dividing out any correlation between the spacecraft's roll angle and the observed flux while avoiding any data points that could result from flares, transits, or other real astrophysical events. The flux is first broken up into smaller bins so one-dimensional approximations for the low-frequency variations can

be made, and each bin is then corrected separately in turn. This procedure effectively removes the short-term systematics from the *K2* light curves while generally preserving astrophysical signals and transit events.

Of the remaining aperture sizes, the version of the light curve with the best photometric precision post-detrending is chosen to undergo the last step in the CfA pipeline, which corrects for the same long-term, common-mode trends seen in the Oxford light curves pre-PCA. Again, DVA is primarily responsible for these trends. The CfA strategy for tackling the common-mode systematics involves putting *Kepler* PDC-MAP to work, where 'PDC' is the pre-search data conditioning we briefly described above, and 'MAP' refers to the technique known as 'maximum *a posteriori*' (Smith et al., 2012; Stumpe et al., 2014). In essence, PDC-MAP is a much more sophisticated version of PCA, using Bayesian MAP to determine the preliminary fit parameters for a co-trending basis vector set created from a sample of stars. These parameters are a starting point for maximizing the Bayesian posterior probability distribution (PDF). Once the best-fit parameters that describe the long-term trends are found, the trends can be removed.

There are two different versions of PDC-MAP which can be utilized. The first, known as 'single-scale,' restricts the fitting to a single band-pass and imposes a strict limit on the values which can be taken by the fit coefficients (Smith et al., 2012). While this may mean that some systematic features are not completely removed from the light curves, the astrophysical signals remain largely intact. The second version, 'multi-scale,' splits each light curve up into several bands using a discrete wavelet transform as a way to individually correct a variety of systematic trends (Stumpe et al., 2014). While this is more effective than single-scale PDC-MAP in completely removing systematic effects — making it ideal for planetary transit searches — it comes at the cost of longer astrophysical signals, such as those coming from the rotational modulation which we would expect to see in M67. Therefore, where we use

the CfA light curves, we use the light curves from single-scale PDC-MAP.

2.6 Discussion

Armed now with two versions each of the SAP and SS light curves courtesy of the Oxford and CfA pipelines, we can begin to understand our ability to find rotation periods in M67 from *K2* data. Because we will explore this topic in more depth in Chapter 4, we limit the discussion here to a preliminary comparison between the light curve precisions from the two pipelines. Continuing the discourse on MAD scatter that began with the Oxford pipeline, the final median scatter values for the C05 CfA SAP and SS datasets at $K_p = 12$ are 321 ppm and 275 ppm, respectively. The smaller margin between the CfA SAP and SS final values compared to that of the Oxford pipeline stems from the fact that the two CfA datasets are extracted and processed in the same way.

The CfA pipeline performs slightly better than the Oxford pipeline for the SAP set. This can be seen in Figure 2.6, which clearly shows that the final SAP MAD scatter obtained by the CfA pipeline is lower than that of the Oxford pipeline over the entire magnitude range for this sample, despite the similar starting points in the raw light curves. This is likely due to the sophistication of single scale PDC-MAP compared to the relatively crude PCA following star-by-star detrending.

By contrast, while the two pipelines produce very different values for the raw SS light curves, their final MAD scatter values are comparable. The light curve extraction step used by the Oxford pipeline for the superstamp already minimizes the pointing-related systematics in the raw light curves, at least for the fainter stars. In fact, there are a number of instances among the fainter stars where the CfA pipeline leads to final MAD scatter values on the order of 1%, whereas the corresponding scatter from the Oxford pipeline is much lower. In these cases, the Oxford pipeline

generally tends to correct the systematics better, especially where the stars are have greater variability. The change in MAD scatter following the star-by-star systematic correction is relatively minor, as neither pipeline shows significant improvement after this step. However, the CfA SS light curves experience a drastic reduction in MAD scatter over the whole magnitude range following the common-mode systematic correction. The effect is apparent in the Oxford pipeline, as well, particularly for bright stars. Ultimately, the final SS MAD scatter for the CfA pipeline is very similar to that of the Oxford pipeline (275 ppm versus 203 ppm, respectively), although the the former is slightly better for brighter stars.

Regardless of the minor differences in performance between the two pipelines, the final MAD scatter values should give us increased confidence that the light curves from both pipelines are relatively robust. In addition, they indicate that there is no obvious effect in either sample that is not handled reasonably well by either pipeline. With two datasets of high-quality light curves encompassing both the outer edges of the cluster and its crowded inner regions, processed using two different pipelines, we can embark on the tedious process of determining rotation periods for M67 members.

Chapter 3

Tools for Rotation Period Detection

As far as the laws of mathematics refer to reality, they are not certain, and as far as they are certain, they do not refer to reality.

Albert Einstein

3.1 Introduction

After extracting and correcting the *K2* M67 light curves, the natural next step is to look for rotation periods. Technically, Barnes et al. (2016) and Gonzalez (2016a) have already accomplished this using C05 data. However, their studies were either very limited in scope or showed too much scatter to be considered very meaningful, though we will discuss these problems in more detail in Chapter 4. For now, we focus our attention on how to determine rotation periods from photometric data (we have not yet had a chance to look at $v \sin i$ data) using some relatively common techniques.

There are many different ways to detect rotation periods from stellar light curves. Some, such as the Lomb-Scargle periodogram, specify an exact form of the light curve and find the best-fit parameters of that model. Others are a bit more flexible,

Sections of this Chapter have been published as Esselstein et al. (2018).

such as the wavelet power spectrum (WPS), while others still compute a statistic which is either optimized or used to pinpoint the best period, never defining an exact functional form for the light curve. Examples of these include the autocorrelation function (ACF), phase dispersion minimization (PDM), and minimum string length (MSL). Finally, more sophisticated approaches employ Bayesian inference, generally taking the form of what is referred to as Bayesian period signal detection (BPSD), or more specifically as Gaussian processes (GPs), to find the most probable set of parameters that describe a dataset.

We only utilize the Lomb-Scargle, ACF, and GP in our work, but it is useful to understand some of the other methods, especially those that have previously been used to find rotation periods in M67. This chapter, therefore, is dedicated to explaining some of the most common techniques for rotation period detection. We first briefly consider MLS, PDM, BPSD, and WPS in Section 3.2 before examining the Lomb-Scargle and ACF in Section 3.3. We then provide an overview of GPs and our specific implementation in Section 3.4. Finally, we present our first set of rotation periods derived for M67 from C05 data, found using a combination of the Lomb-Scargle and ACF but prior to a full application of the GP. This is accompanied by a discussion of how these results, in light of the published rotation periods from Barnes et al. (2016) in particular, motivated a more careful, detailed study of our ability to actually recover solar-like signals from one campaign of *K2* data; this work is outlined in Chapter 4. Informed by the conclusions from Chapter 4, we will then compare our three methods of choice and ultimately use a combination of them to produce our own set of rotation periods from *K2* light curves in Chapter 5.

3.2 Some Common Rotation Detection Techniques

Many methods exist for finding rotation periods besides the Lomb-Scargle, ACF, and GP, but we will restrict this portion of our discussion to three additional techniques used by the published M67 rotation studies — MSL, PDM, and BPSD — and the WPS, another fairly popular approach. Both MSL and PDM make use of the phase curves produced by the trial periods to find the best one, avoiding the need to specify an exact form for the data. MSL measures the distances between data points phase-folded on the trial period, forming a set of 'strings' whose combined lengths form the basis of the statistic that needs to be minimized (Burke et al., 1970; Dworetsky, 1983). PDM, on the other hand, finds the period which minimizes the variance of the dataset (Stellingwerf, 1978). Here, the data are phase-folded onto each trial period, binned into M subsets, and the statistic Θ is subsequently computed by (Stellingwerf, 1978):

$$\Theta = \frac{s^2}{\sigma^2} \tag{3.1}$$

where σ^2 is the variance of the dataset as a whole, and s^2 is the combined variance based on M subsets of the data. The former is calculated in the following manner:

$$\sigma^2 = \frac{\sum_{i=1}^{N}(x_i - \bar{x})^2}{N-1} \tag{3.2}$$

where x_i is the value of a dataset at observation i out of N data points, and $\bar{x}$ is the mean value of the dataset. The calculation of s^2 is conducted in an analogous fashion:

$$s^2 = \frac{\sum_{j=1}^{M}(n_j - 1)s_j^2}{\sum_{j=1}^{M} n_j - M} \tag{3.3}$$

where n_j is the number of data points in each subset j, and s_j^2 is computed in the

exact manner as Equation 3.2, but just for that subset of data. The period which minimizes Θ is selected (Stellingwerf, 1978). Both Barnes et al. (2016) and Gonzalez (2016a) employed PDM in their respective searches for M67 rotation periods, and the former also used MLS.

As their final choice of rotation detection method, Barnes et al. (2016) utilize BPSD, which tests the probability distributions of different models, both periodic and non-periodic, with Bayesian inference to decide upon the most probable period (Gregory & Loredo, 1992). While this is similar to the approach we take with the GP (see Section 3.4), the two methods are fundamentally different. The BPSD does not assume that each point in the dataset is drawn from a multivariate Gaussian distribution, and while the GP generates a family of possible functions to the dataset based on the chosen covariance function, BPSD tests separate models picked beforehand.

Finally, we briefly examine the WPS, another relatively popular technique which is fully described in Torrence & Compo (1998). Essentially, the WPS uses a wavelet transform to measure the power of a time series at various frequencies, or periods, with the Morlet wavelet being one of the more common wavelets. The Morlet wavelet convolves a Gaussian and a sinusoid, allowing the frequency to be varied, and when computed over each point in the time series gives the WPS (Mathur et al., 2010b; García et al., 2014). Torrence & Compo (1998) define the Morelet wavelet function as:

$$\psi_0(\eta) = \pi^{-\frac{1}{4}} e^{i\omega_0\eta} e^{\frac{-\eta^2}{2}} \tag{3.4}$$

where ψ_0 is the actual wavelet, η is a non-dimensional parameter specified by the user, and ω_0 is the frequency for which the WPS is being calculated. The Morlet wavelet has been used to measure the surface rotation of solar-like stars (Ceillier et al., 2014) and stellar parameters from oscillations (Mathur et al., 2010a,b). In addition, García et al. (2014) used the Morlet wavelet to measure the rotation periods of *Kepler* stars,

and van Saders et al. (2016) used a version of the WPS, along with the ACF, to compute the rotation periods of the asteroseismic samples used in that study.

3.3 The Lomb-Scargle Periodogram and Autocorrelation Function

We now turn to the two traditional methods employed in this thesis. The Lomb-Scargle periodogram (Scargle, 1982) is one of the most common techniques used in rotation period searches. The standard periodogram for a dataset X with N data points is defined as (Scargle, 1982):

$$P_X(\omega) = \frac{1}{N}\left|FT_X(\omega)\right|^2 = \frac{1}{N}\left[\left(\sum_j X_j \cos\omega t_j\right)^2 + \left(\sum_j X_j \sin\omega t_j\right)^2\right] \tag{3.5}$$

where ω is the angular frequency and $FT_X(\omega)$ is the discrete Fourier Transform (DFT) of X. This version of the periodogram often suffers from 'spectral leakage' (e.g. aliasing) and high noise levels that make the statistical interpretation ambiguous (Scargle, 1982). However, Scargle (1982) demonstrated that $P_X(\omega)$ can be redefined as:

$$P_X(\omega) = \frac{1}{2}\left\{\frac{\left[\sum_j X_j \cos\omega(t_j-\tau)\right]^2}{\sum_j \cos^2\omega(t_j-\tau)} + \frac{\left[\sum_j X_j \sin\omega(t_j-\tau)\right]^2}{\sum_j \sin^2\omega(t_j-\tau)}\right\} \tag{3.6}$$

where τ is found from:

$$\tan(2\omega\tau) = \frac{\sum_j \sin 2\omega t_j}{\sum_j \cos 2\omega t_j} \tag{3.7}$$

This version of $P_X(\omega)$ is less prone both to leakage and high noise levels due to effective statistical redistribution (Scargle, 1982).

Scargle (1982) proved that Equation 3.6 is equivalent to the least squares fitting of the following general sinusoidal model, as implemented by Lomb (1976):

$$X_f(t) = A\cos(t-\tau) + B\sin(t-\tau) \tag{3.8}$$

Zechmeister & Kürster (2009) generalized Equation 3.8 further with the addition of an offset, c. Here, we utilize the following sinusoidal model, as was done in the Monitor project (see e.g. Irwin et al., 2006, 2007, 2008b):

$$m(t) = m_{\rm dc} + \alpha\sin(\omega t + \phi) \tag{3.9}$$

where $m_{\rm dc}$ is the light curve's vertical offset, α is the amplitude, ϕ is the phase, and ω is the angular frequency. For each value of ω (or period, $P = 2\pi/\omega$), this model can be expressed as a linear basis model with three basis functions: a constant, a sine term, and a cosine term, each with period P. Thus, for each trial period, we can solve for the values of $m_{\rm dc}$, α, and ϕ that minimize the sum of the squared residuals, or χ^2 (in space data, the relative measurement uncertainties can be treated as approximately constant for a given star, so the two are equivalent). We evaluate the relative reduction in χ^2 with respect to a constant model, $S = (\chi^2(0) - \chi^2(P))/\chi^2(0)$, as a function of period P, to construct a periodogram.

The effectiveness of the Lomb-Scargle has been demonstrated many times over, with the Monitor project being a prime example. Despite this success, periodic signals in light curves are not sinusoidal; they evolve over time as star spots appear and disappear, often on opposing hemispheres, and can be subject to several layers of rotational modulation due to differential rotation. As a result, the Lomb-Scargle often leads to periodic measurements at half the true period, and at times, may simply be too inflexible to pick up on the complexities of the actual signal, producing inaccurate periods.

While the Lomb-Scargle periodogram finds the best-fit sinusoid for a given dataset, the ACF is a comparison of the dataset with itself shifted to different candidate periods. The ACF is computed by 'sliding' the dataset over itself at a range of intervals, or lags, and determining at which lag the shifted dataset most resembles the original, indicated by the maximum value of the 'ACF coefficient.' In this way, the ACF looks for periodicity without having to specify an exact form, making it a more flexible tool for measuring real rotational modulation than the Lomb-Scargle. The ACF at lag k is calculated using the following equation, as implemented in McQuillan et al. (2013):

$$r_k = \frac{\sum_{i=1}^{N-1}(x_i - \bar{x})(x_{i+k} - \bar{x})}{\sum_{i=1}^{N}(x_i - \bar{x})^2} \tag{3.10}$$

where $\bar{x}$ is the mean value of the dataset x, and N is the total number of data points. In order for the ACF to work, x must be interpolated to a regular grid prior to computation. In practice, we employ the fast Fourier transform (FFT) to decrease computation time because the discrete correlation of two functions translates to the product of the FT of one function and the complex conjugate of the FT of the other (Press et al., 1992). We first fit the data to a linear model and then subtract the fit, giving x'. We then compute the FFT of $x' - \bar{x}'$. The inverse of the product of the FFT and its conjugate is then equivalent to the ACF (since an autocorrelation is a correlation of a function with itself). Using the FFT speeds up the calculation of the ACF given by Equation 3.10, but gives the same result. We then smooth the ACF by convolving it with a Gaussian kernel. For a periodic signal, the ACF produces a plot of successive maxima that decay over time. The rotation period of the light curve is then typically designated by the lag corresponding to the highest peak after $k = 0$.

We have described a relatively simple approach to the ACF, wherein we merely select the highest peak. There are ways of making a more informed decision regarding the correct peak (or, rather, a peak that actually represents real periodicity), depen-

dent, for example, on relative peak height and the effective temperature of the star (McQuillan et al., 2014). Another approach involves assigning a weight to the output based not only on the maximum peak height, but also the decay rate of the peaks and how well the ACF can be fit to a damped oscillator (Angus et al., 2017). We do not employ these contingents ourselves because, apart from our use of the simple ACF in Section 3.5, we use a combination of methods to determine our final *K2* M67 rotation periods (see Chapter 5).

The ACF has successfully measured stellar rotation periods from *Kepler* data, including for 737 exoplanet host stars (McQuillan et al., 2013) and 34,030 *Kepler* main-sequence stars in McQuillan et al. (2014). The insightful work from van Saders et al. (2016) employed the ACF for *Kepler* asteroseismic targets, as well. The ACF was also one of the four methods used by Barnes et al. (2016) to find rotation periods in M67 from *K2* C05 data.

Figure 3.1 provides example ACF plots and Lomb-Scargle periodograms for three different light curves processed with the Oxford pipeline. Each plot in this figure displays the systematics-corrected light curve in the top panel, and, in the bottom panel, the standard Lomb-Scargle periodogram in black with the ACF in blue. The periods found by the Lomb-Scargle and ACF are indicated by the location of the red and green lines, respectively. Plot (a) in Figure 3.1 is an example of a light curve (EPIC 211307159) with obvious rotational modulation, and as a result, the ACF takes the clean shape of a series of peaks whose heights generally decrease with increasing lag. In addition, the Lomb-Scargle produces a prominent, narrow peak at the correct period. Although the light curve does evolve over the course of the campaign, the periodic signal is strong, and both the ACF and Lomb-Scargle find periods of 10.6 d. Plot (b) demonstrates the 'harmonic case' with EPIC 211320437. The light curve in this plot likely has a period of approximately 15 d, but the period could easily be mistaken for 7 – 8 d. While a relatively strong peak does exist at the true period,

the Lomb-Scargle is 'fooled' by the harmonic signal. The ACF, however, is flexible enough to account for this. Often, the ACF peak at the true period will be higher, even if only slightly, than that of the half-period harmonic. This is what we see in plot (b), with the ACF settling on 14.8 d.

The light curve in plot (c), however, is more ambiguous than either plot (a) or (b); there appears to be some variability in the light curve (EPIC 211439059), but it is difficult to determine if this is the result of lingering systematics or a real astrophysical signal. If it is the latter, and if it is in any way periodic, then the signal has a long period, making the measurement more uncertain given the observation time. Thus, the greatest peak in Lomb-Scargle periodogram is very broad, and the ACF does not show any convincing periodicity. At a glance, the periods selected by the two methods, 33.3 d and 35.8 d, respectively, would be disregarded.

3.4 Gaussian Processes

Gaussian processes, or GPs, are a powerful tool for modeling datasets whose exact generative functions are unknown, making them particularly attractive for finding rotation periods in *K2* M67 light curves. A GP produces a family of possible functions that can describe the data based on the modeled covariance of each observed data point. The form of the covariance can be specified by the user to provide a set of informative parameters which give insights into the nature of the dataset, such as evolutionary timescales or inherent periodicity. We give a relatively brief overview on GPs here, but the more interested reader is referred to Rasmussen & Williams (2006).

A GP essentially extends a multivariate Gaussian distribution to an infinite number of random variables, as shown below[1]:

[1]https://github.com/LSSTC-DSFP/LSSTC-DSFP-Sessions/blob/master/Session4/Day2/GPLecture1.ipynb

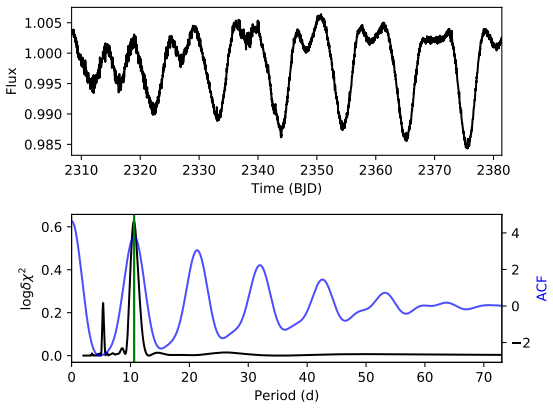

(a)

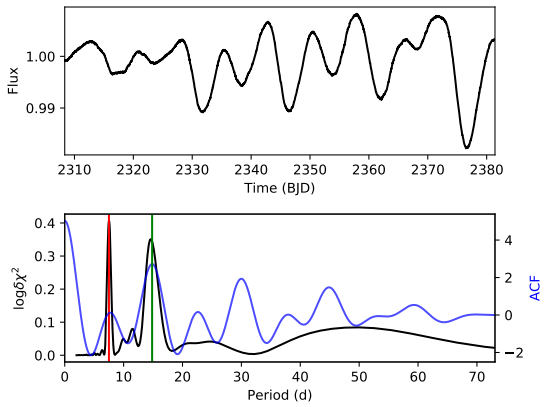

(b)

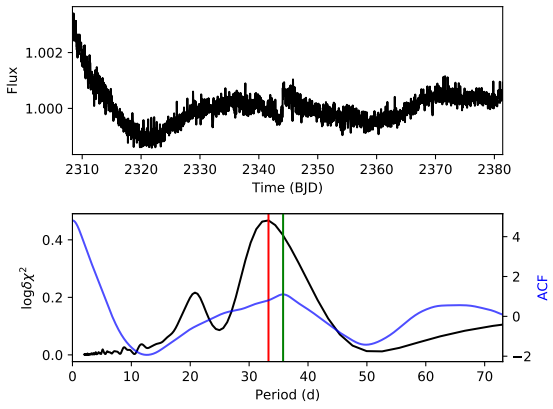

(c)

Figure 3.1: Sets of plots depicting examples of light curves where the Lomb-Scargle and ACF results are clear (a), are harmonics of each other (b), and are more ambiguous in the absence of a trustworthy periodic signal (c). The corrected and normalized flux is given in the top panel of each set of plots, while the Lomb-Scargle periodogram (black) and the ACF (blue) are given in the bottom panel. The red line indicates the location of the Lomb-Scargle period, while the green line indicates the location of the ACF period.

$$\bar{y} \sim \mathcal{N}(\bar{m},\, K) \tag{3.11}$$

where $\bar{y} = (y_1, y_2, ..., y_N)^T$ is a collection of random variables with N points, $\bar{m}$ is the associated mean vector, and K is an NxN positive, semi-definite covariance matrix with elements $K_{ij} = \mathrm{cov}(y_i, y_j)$. The covariance matrix is generated by a function known as a kernel, the choice of which depends on the nature of the dataset, as well as an educated guess; we will eventually discuss the choice of kernel, but for now we focus on the general application of a GP. By using a GP, we inherently assume that each data point is drawn from a Gaussian distribution.

More formally, for a one-dimensional dataset (such as a flux time series), Equation 3.11 can be written as the following[2]:

$$y(x) \sim \mathcal{GP}(m(x), k(x, x')) \tag{3.12}$$

where $y(x)$ is the underlying, unknown function that has produced the observed data points, $m(x)$ is the mean function that gives the expected value of y at any point x, and $k(x, x')$ is the covariance of two data points generated by the kernel, equivalent to K_{ij} above. Because the parameters of any kernel, known as the 'hyperparameters,' can take an infinite number of values, an infinite number of functions could ultimately describe $y(x)$. Obviously, some functions will do a better job than others, so we will now outline how to determine the most probable set of hyperparameters for a given choice of kernel. Being able to do this means that we never have to know the exact form of $y(x)$ itself; all we need are the maximum likelihood hyperparameters. Technically, the hyperparameters include those of the mean function, as well, but we care more about those associated with the kernel.

Picking the set of hyperparameters that most accurately reproduces the observ-

[2]https://github.com/LSSTC-DSFP/LSSTC-DSFP-Sessions/blob/master/Session4/Day2/GPLecture1.ipynb

ables from $y(x)$ involves implementing Bayesian inference through Bayes' theorem:

$$p(\theta|y) = \frac{p(y|\theta)p(\theta)}{p(y)} \tag{3.13}$$

where θ represents the hyperparameters, and y is the collection of observed values from the dataset. The two terms in the numerator of the right-hand side of Equation 3.13 are the likelihood and prior distributions, respectively, and the denominator is the marginal distribution of y, i.e. the probability of observing y in the absence of any other information. In practice, $p(y)$ is merely a normalization factor, so we are more interested in the numerator. The prior is our estimate of the true probability distribution for a set of parameters before any computation has been made and without any knowledge of the data. If nothing is known about the prior, one can use a uniform distribution for all parameters. The likelihood, on the other hand, is given by the following equation (see e.g. Rajpaul et al., 2015):

$$\ln p(y|\theta) = \ln \mathcal{L} = -\frac{1}{2} r^T K^{-1} r^T - \frac{1}{2}\ln(\det K) - \frac{N}{2}\ln(2\pi) \tag{3.14}$$

where $r = y(x) - m(x)$ for non-zero mean functions. We present the natural logarithm of the likelihood because it is easier to work with than the likelihood itself.

The left-hand side of Equation 3.13 is known as the posterior distribution, which describes the probability of the hyperparameters given the data. Our goal is to find the set of hyperparameters that maximize the posterior, which should help us identify the best-fit model for the dataset. First, we must 'condition' the GP. This means using the observed data, or a subset of it, as a training set to produce the family of functions which could possibly reproduce and explain the data.[3] In doing this, we create what is known as the conditional, or predictive, distribution, which helps us predict the value of $y(x)$ at new input values x_*[4]:

[3] https://github.com/LSSTC-DSFP/LSSTC-DSFP-Sessions/blob/master/Session4/Day2/GPLecture1.ipynb
[4] https://github.com/LSSTC-DSFP/LSSTC-DSFP-Sessions/blob/master/Session4/Day2/GPLecture1.ipynb

$$p(y_*|y,k) = \mathcal{N}(K_*^T K^{-1} y,\ K_{**} - K_*^T K^{-1} K_*) \tag{3.15}$$

where k is the kernel function, with hyperparameters θ, that describes the covariance matrix K; $K_{**} = k(x_*, x'_*)$; and $K_* = k(x, x'_*)$. We can then 'train' the GP by minimizing the negative log likelihood given by Equation 3.14, which ultimately determines the best-fit parameters for the kernel.[5] The parameters from the maximum likelihood may only come from a local minimum as opposed to the global, however, so we can use a Markov chain Monte Carlo (MCMC) to fully explore the parameter space. This has the added benefit of providing uncertainties on the parameters.

We have explained how we can use a GP to model a dataset and produce a set of informative parameters which describe the covariance between data points, but we have not yet talked about the choice of kernel. There are many different kernels available for use, but the decision of which one to apply is based on the kind of information we are trying to glean from the data, as well as an educated guess as to the nature of the data itself. One of the most common and simplest kernels is the squared exponential, and it takes the form:

$$k_{SE}(x, x') = h^2 \exp[-\frac{(x - x')^2}{2L^2}] \tag{3.16}$$

where h is the parameter for the function's amplitude, and L is the length scale, which describes the correlation of points which are far away from each other, essentially explaining how quickly the function evolves over time (Angus et al., 2017). A large value for L corresponds to slow evolution because the points are more correlated, while a small value means that the function evolves very quickly (Angus et al., 2017). The squared exponential kernel is fairly flexible, but with only two parameters, it may not be adequate enough to model periodic rotation, as is our goal for the M67 light

[5] https://github.com/LSSTC-DSFP/LSSTC-DSFP-Sessions/blob/master/Session4/Day2/GPLecture1.ipynb

curves. Luckily, one can combine kernels in a variety of ways, including addition and multiplication. For periodic functions, a common kernel is the product of a squared exponential with a periodic term:

$$k_{QP}(x, x') = k_{SE} \exp[-\frac{\sin^2(\frac{\pi[x-x']}{P})}{2L_P^2}] \tag{3.17}$$

where P is the period and L_P is the length scale of periodic variations, similar to L from Equation 3.16. In this case, L_P describes the correlation of points located a period from one another (Angus et al., 2017). This could help model, for example, the variations in the shape of a light curve as star spots evolve, changing size and shape over the course of their lifetimes. This kernel is known as the quasi-periodic kernel, and it is flexible enough to account for both periodicity and other features in the data.

Often, it is prudent to account for white noise. Assuming constant white noise, this simply means we add a white noise term to the kernel we already have, such as the quasi-periodic kernel:

$$k(x, x') = k(x_i, x_j) = k_{QP}(x_i, x_j) + \sigma^2 \delta_{ij} \tag{3.18}$$

where σ^2 is the estimated white noise variance, and δ_{ij} is the Kronecker delta function. We can estimate the white noise variance as:

$$\sigma^2 \approx \text{median}(|\text{diff}(y)|) \tag{3.19}$$

where $\text{diff}(y)$ is the first order difference of the observed data points. The white noise term can be adapted to account for non-constant variance, but the version presented in Equation 3.19 is a decent approximation in the absence of other information.

There are several, powerful GP tools which can be applied to astrophysical data and which are available for public use. Typically, the inversion and determinant

calculations of the kernel K render a computational requirement of $\mathcal{O}(N^3)$. In spite of this, the `python` package `george` (Ambikasaran et al., 2016), wrapped around `C++` and originally developed to cope with *Kepler* data, is fairly quick for reasonably-sized datasets. Ambikasaran et al. (2016) employ a factorization technique which reduces the requirement to $\mathcal{O}(N \ln^2 N)$. In addition, `george` implements a wide variety of kernels, including the squared exponential and several periodic kernels, which can be combined to form quasi-periodic kernels. Many studies have made use of `george` in a range of different capacities, from modeling the transits or out-of-eclipse variations of exoplanets and eclipsing binaries (Berta-Thompson et al., 2015; Stevenson et al., 2016; Pepper et al., 2017; Gillen et al., 2017), to attempting to recover stellar rotation periods (Mancini et al., 2015; Vanderburg et al., 2015; Angus et al., 2017), to even modeling the emission spectrum of the interstellar medium (Tchernyshyov et al., 2015).

Despite the utility of `george`, it is still too slow for large-scale *K2* rotation studies. On the other hand, the `python` package `celerite` (Foreman-Mackey et al., 2017), also wrapped around `C++`, uses a clever technique to reduce the computation requirement to scale as $\mathcal{O}(N)$. Foreman-Mackey et al. (2017) define the general `celerite` kernel:

$$k(\tau_{nm}) = \sigma_n^2 \delta_{nm} + \sum_{j=1}^{J} \left[a_j \exp(-c_j \tau_{nm}) \cos(d_j \tau_{nm}) + b_j \exp(-c_j \tau_{nm}) \sin(d_j \tau_{nm}) \right] \quad (3.20)$$

where $\tau_{nm} = |t_n - t_m|$, and a_j, b_j, c_j, and d_j are hyperparameters. The power spectral density (PSD), found by taking the FT of Equation 3.20, is then (Foreman-Mackey et al., 2017):

$$S(\omega) = \sum_{j=1}^{J} \sqrt{\frac{2}{\pi}} \frac{(a_j c_j + b_j d_j)(c_j^2 + d_j^2) + (a_j c_j - b_j d_j)\omega^2}{\omega^4 + 2(c_j^2 - d_j^2)\omega^2 + (c_j^2 + d_j^2)^2} \quad (3.21)$$

We cannot implement a quasi-periodic kernel like that of Equation 3.17 in `celerite`

because it may cause Equation 3.21 to become negative, which does not allow the GP to compute (Foreman-Mackey et al., 2017). Instead, we use a mixture of single harmonic oscillators (SHOs). The differential equation describing the dynamics of a single SHO is given by (Foreman-Mackey et al., 2017):

$$\epsilon(t) = y(t)\Big[\frac{\mathrm{d}^2}{\mathrm{d}t^2} + \frac{\omega_0}{Q}\frac{\mathrm{d}}{\mathrm{d}t} + \omega_0^2\Big] \tag{3.22}$$

where $\epsilon(t)$ is the driving force (usually just modeled as white noise), ω_0 is the undamped frequency, Q is a quality factor related to the damping of the system, and $y(t)$ describes the 'position' of the oscillator at any given point in time. We can then translate this into a `celerite` kernel whose PSD takes the form (Foreman-Mackey et al., 2017; Anderson et al., 1990):

$$S(\omega) = \sum_{j=1}^{J} \sqrt{\frac{2}{\pi}} \frac{S_j \omega_j^4}{(\omega^2 - \omega_j)^2 + \frac{\omega_j^2 \omega^2}{Q_j^2}} \tag{3.23}$$

where J is the number of SHO terms used, S_j is the value of the PSD of a given SHO at its respective undamped frequency ω_j, Q_j is the SHO's quality factor, and ω is just a frequency array. When $Q > 1/2$, Equations 3.21 and 3.23 are equivalent if (Foreman-Mackey et al., 2017):

$$\begin{aligned} a_j &= S_j \omega_j Q_j \\ b_j &= \frac{S_j \omega_j Q_j}{\sqrt{4Q_j^2 - 1}} \\ c_j &= \frac{\omega_j}{2Q_j} \\ d_j &= \frac{\omega_j}{2Q_j}\sqrt{4Q_j^2 - 1} \end{aligned} \tag{3.24}$$

In practice, we mix two SHOs that have an amplitude, $\sqrt{a}$ (same as a_j, except we use $a = a_1 = a_2$), in common, but otherwise are separately controlled by their quality factors Q_1 and Q_2, respectively, as well as their undamped frequencies ω_1 and ω_2.

The undamped frequencies are dependent both on the values of Q_1 and Q_2 and their respective periods, P_1 and $P_2 = P_1/2$ (the latter included to incorporate harmonic measurements), such that:

$$\omega_1 = \frac{4\pi(Q_1 + Q_2)}{P\sqrt{4(Q_1 + Q_2)^2 - 1}}, \tag{3.25}$$

$$\omega_2 = \frac{4\pi\, Q_2}{P_2\sqrt{4Q_2^2 - 1}} \tag{3.26}$$

We define ω_1 and ω_2 based off the fact that, if b_j in Equation 3.20 is zero, Equation 3.21 simplifies to an oscillator with period $P_j = 2\pi/d_j$, with d_j as defined by Equation 3.24 (Foreman-Mackey et al., 2017). We add the quality factors for ω_1 to ensure that the 'true' period, P_1, is always preferred as the output of the GP (Foreman-Mackey, private communication). Despite this, we will discuss how to deal with a real harmonic case, where the actual period is $P_1/2$, momentarily.

We can describe the value of the PSD of each SHO at their respective undamped frequencies as the following:

$$S_1 = \frac{a}{\omega_1 Q_1} = \frac{aP_1\sqrt{4(Q_1 + Q_2)^2 - 1}}{4\pi(Q_1 + Q_2)Q_1}, \tag{3.27}$$

$$S_2 = \frac{ma}{\omega_2 Q_2} = \frac{maP_2\sqrt{4Q_2^2 - 1}}{4\pi\, Q_2^2} \tag{3.28}$$

where m in Equation 3.28 is a mixing parameter that explains the relative significance of the peak from the half-period SHO relative to the 'true' period SHO in the combined PSD. We can compute the PSD for our kernel by plugging in Equations 3.25 through 3.28 into Equation 3.23; the inverse FT produces the kernel itself, to which we add a white noise term. We give a few examples of PSDs computed from the mixture of SHOs kernel at different initial values of Q_1 and Q_2 for a test light curve we want

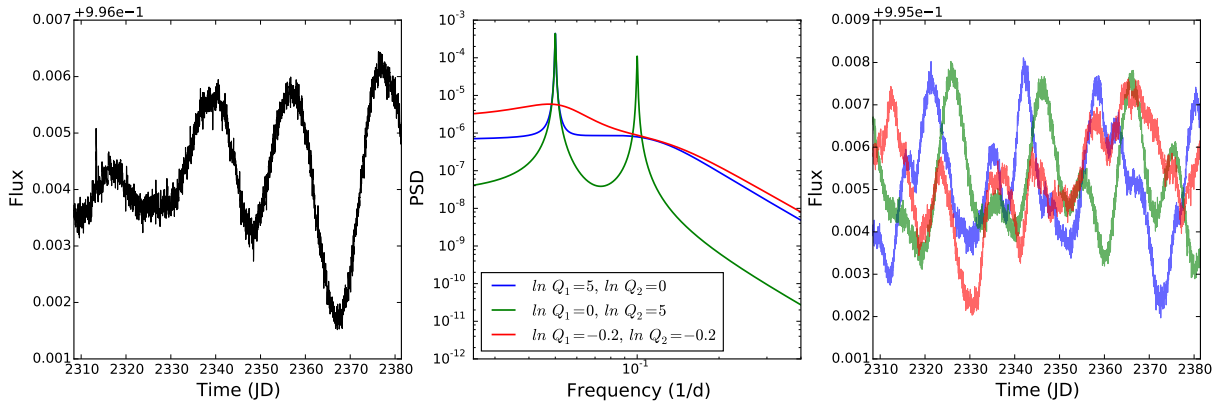

Figure 3.2: Example PSDs (middle) and random samples (right) drawn from the prior distributions of the GP computed for the test light curve (left) with different values for Q_1 and Q_2.

to model with the GP in Figure 3.2. In blue is the case where $Q_1 > Q_2$, and both are greater than zero. Green illustrates the same, except with $Q_2 > Q_1$, which leads to the additional peak at 10 d. The peak has flattened out in the red case, where $\ln Q_1 = \ln Q_2 = -0.2$, approaching the periodicity limit of $1/\sqrt{2}$, which is where a peak is no longer observed in the PSD. The far right panel displays a random sample for each case drawn from its respective prior distribution. At this point, we have not yet optimized the hyperparameters.

As briefly alluded to above, when we compute the GP, we first have to initialize it with a guess for each of the following hyperparameters: a, m, Q_1, Q_2, and $P = P_1$. Working with the natural logarithm of each parameter, we typically set $\ln a_0$ to be the variance of the data, $\ln m_0 = 0$, $\ln Q_{1,0} = 7.5$, and $\ln Q_{2,0} = 0$ (though the latter two are subject to change). We initialize with a high $Q_{1,0}$ because we are making an assumption *a priori* that there is some periodicity in the light curve. Given the computational efficiency of `celerite`, we run the GP several times using the first few peaks from the normalized Lomb-Scargle periodogram and the ACF as initial guesses for P. In the end, we choose the value for P that produced the greatest log likelihood.

We also set bounds on the natural logarithm of each hyperparameter. This pre-

vents the GP from exploring nonsensical parameters during conditioning. The period must fall between 0.05 d and 40 d (since we will not be able to see two complete cycles for a 40 d period in one campaign of data), while $\ln a$ and $\ln m$ must fall between -15 and 15. The minimum value that the quality factors can take, if there is periodicity in the light curves, is $1/\sqrt{2}$ (Foreman-Mackey et al., 2017). Generally, the greater the value of Q_j, the greater the probability that the light curves do have inherent periodicity, and the stronger the peaks in the PSD at ω_1 and ω_2. The lower bound for both $\ln Q_1$ and $\ln Q_2$ is $\ln(1/\sqrt{2})$, but the upper bounds are 20 and 15, respectively. We choose a higher upper bound for $\ln Q_1$ for a similar reason as to give Q_1 more room to reach a value representing strong periodicity. If, however, the final value of Q_2 is greater than its lower bound and also greater than Q_1, the output period P should be halved.

In Figure 3.3, we show the same light curves from Figure 3.1, but this time we present the relevant information from the GP. In the top panel of each respective plot, we show the systematics-corrected flux in black overlaid in red with the predicted mean from the best-fit model generated by the GP. In the bottom panels, we illustrate in blue the PSD computed using the initial guesses for each hyperparameter, prior to optimization. The final PSD is given in black. We mark the location of the best-fit period with a vertical red line. The first plot belongs to EPIC 211307159. Like the Lomb-Scargle and the ACF, the GP finds a value of 10.6 d, reinforced by the strong peak in both the initial and final PSD. The middle plot corresponds to harmonic case of EPIC 211320437. Like the ACF, the GP finds a period of 15.2 d, much closer to the apparent truth. The initial PSD, likely computed from the input Lomb-Scargle value, produces a peak at half the true period (double the frequency), but the harmonic peak has shrunk in the final PSD in favour of the longer period. Finally, we again included the ambiguous example of EPIC 211439059. Like the other two methods, the output of the GP is not as trustworthy. The GP finds a period of

22.3 d, which does not appear to be accurate from either the actual light curve or the predicted mean. Furthermore, the peak of this star's PSD is several orders smaller than that of the other two (units are absolute). The GP, then, is not infallible.

As previously mentioned, we can use the MCMC to fully explore the parameter space of the GP and get uncertainties on our period. We employ the python package `emcee` (Foreman-Mackey et al., 2013) to run the MCMC, using a standard walker sampler. We run a relatively short burn-in of 200 steps using 36 walkers for each of the five parameters from our kernel before running a production chain with 1000 steps. We can then produce a 'corner' plot that shows the probability distributions of each parameter in relation to the others. We can also measure the uncertainty of a given parameter based on its marginal distribution. Example of corner plots for EPICs 211307159 and 211439059 are given in Figure 3.4 below. All the parameters are in log space. The output period from the MCMC was 10.6 ± 1.0 d for EPIC 211307159, whose corner plot shows reasonably well-behaved distributions for all six parameters. In contrast, the corner plot for EPIC 211439059 has a multi-modal distribution in m; approaches the parameter bounds for a, Q_1, and Q_2; and has a broader distribution in P than EPIC 211307159. The MCMC again finds a period of 22.3 d for this ambiguous case, with slightly larger uncertainties of $+1.3$ d and -1.21 d.

3.5 Preliminary Results and Discussion

We now switch gears away from the GP and back to the Lomb-Scargle and ACF. In the early summer of 2016, we determined our own, preliminary set of M67 rotation periods using just the standard Lomb-Scargle periodogram and the ACF, which we first applied to all 976 stars in the SS sample. We then looked through the systematics-corrected light curves, visually inspecting each one by eye and deciding if the variability of a given light curve matched either the corresponding Lomb-Scargle

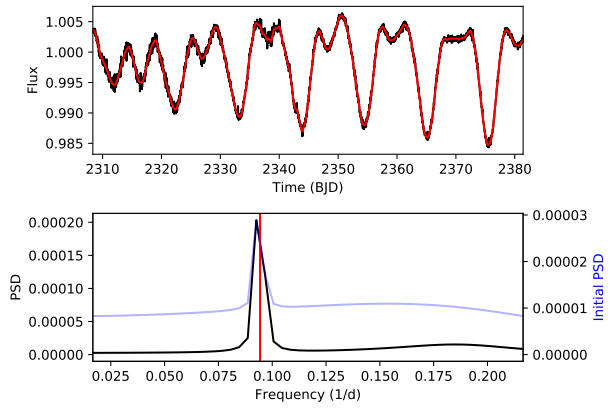

(a)

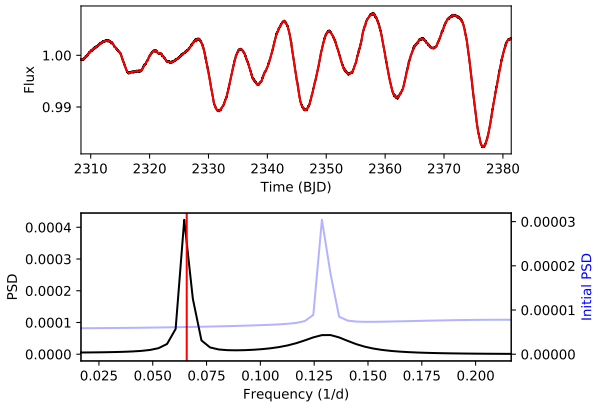

(b)

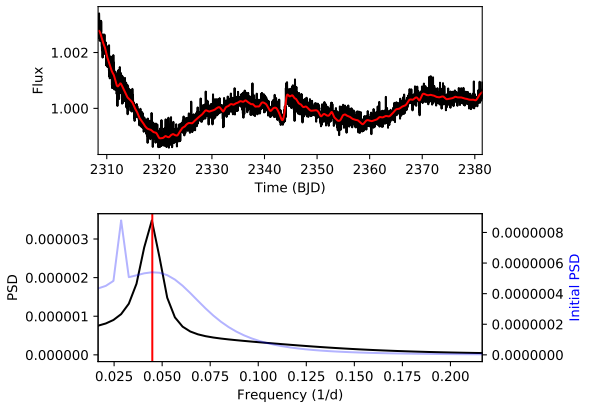

(c)

Figure 3.3: Same example light curves from Figure 3.1 except measured with the GP. The flux from the systematics-corrected and normalized light curve is given in black in each top panel, while the predicted mean from the best-fit model output by the GP is given in red. The bottom panels show the PSD as a result of the initial guess for the period (in blue) and the output PSD (in black), with a red line depicting the location of the determined period.

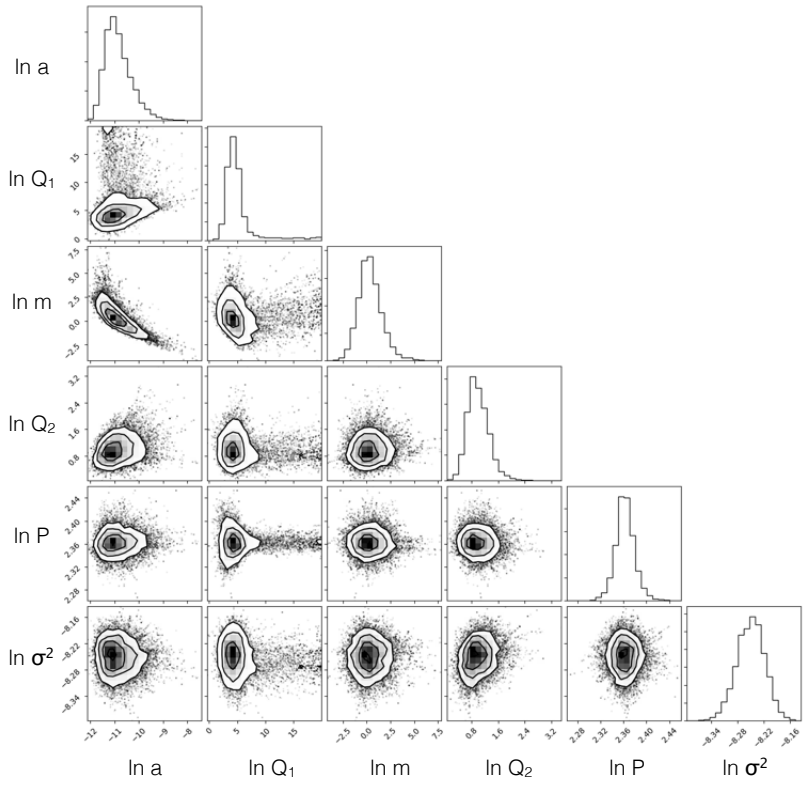

(a)

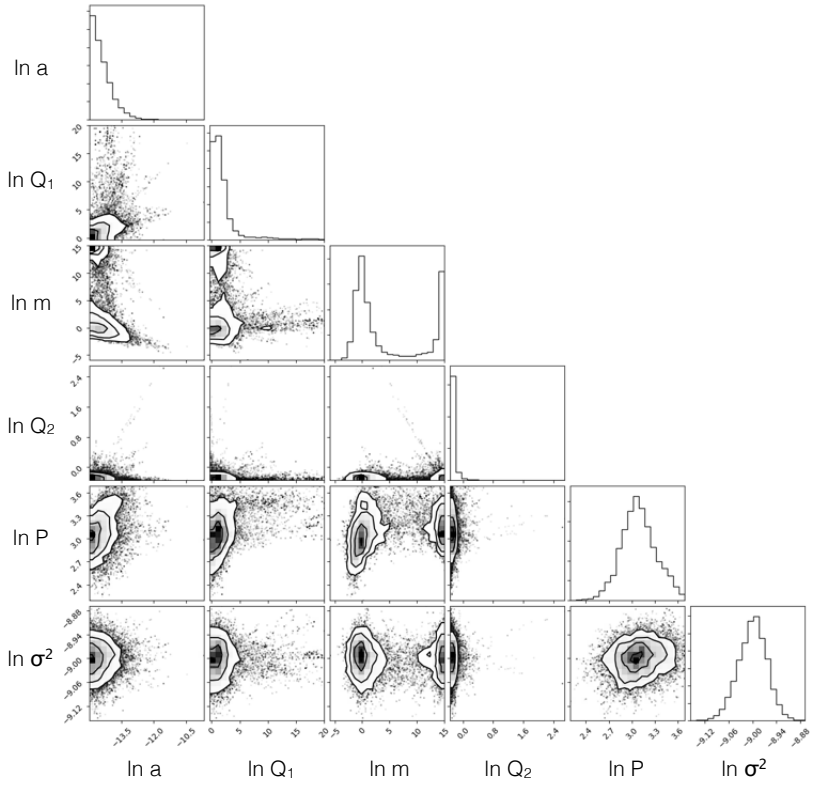

(b)

Figure 3.4: Example corner plots from the MCMC for EPIC 211307159 (a) and EPIC 211439059 (b). These plots were generated using the `corner` package developed by Dan Foreman-Mackey.

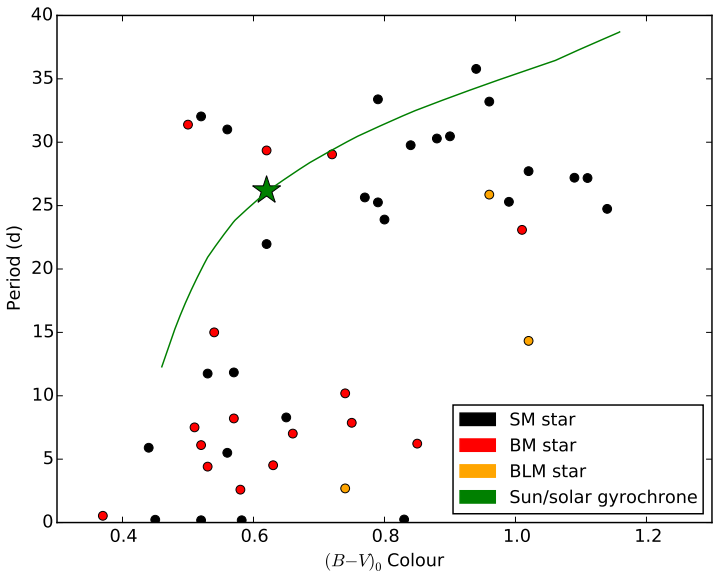

Figure 3.5: Preliminary CPD from *K2* Campaign 5 SS light curves calculated using the standard Lomb-Scargle periodogram and ACF. Binary members (BM) are in red, single members (SM) are in black, and binary likely members (BLM) are in gold.

or ACF result, or both. We only kept the results which appeared to be either reliable or plausible, and discarded the rest. If the two methods produced believable values and agreed with each other to within 5 d, we took the average period. We then filtered the remaining light curves for cluster membership status through the Mathieu catalog, plotting the members' periods and their associated $B-V$ colours in a colour-period diagram (CPD), shown in Figure 3.5. We used an $E(B-V)$ value of 0.04, as was done by Barnes et al. (2016). The membership classifications depicted in this figure include 'single members' (SM; in black), 'binary members' (BM; in red), and 'binary likely members' (BLM; in gold). Overlaid on the CPD is the Sun, represented as a green star, and a solar-age (4.6 Gyr) 'gyrochrone' — or gyrochronology relationship at a specific age — from Barnes (2010), using the convection turnover timescales from Barnes & Kim (2010).

The results in our CPD from Figure 3.5 generally follow the solar gyrochrone, but

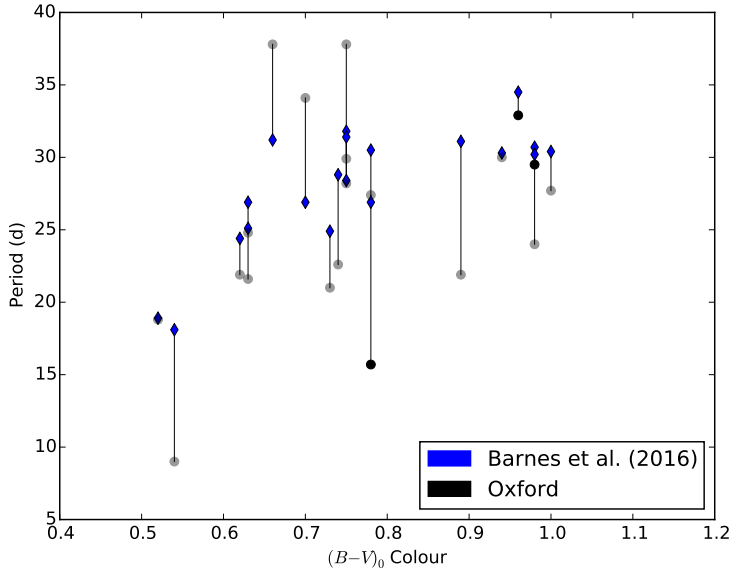

Figure 3.6: Comparison of Barnes et al. (2016) periods (blue diamonds) with our corresponding measurements (dark circles), connected by the gray lines. Black circles represent those measurements in which we had more (subjective) confidence, while the gray circles are those we did not trust as much.

they do deviate from the trend at the very blue and red ends, with the stars rotating faster than what the gyrochrone predicts. This could partially be due to the small age discrepancy between M67 and the Sun. On the surface, however, this appears to support the weakened magnetic braking theory of van Saders et al. (2016), especially for the more massive stars. Nonetheless, there is a lot of scatter in Figure 3.5; we did not have a satisfactory method for determining uncertainties when these values were computed; and we made no consideration regarding the amplitudes of the light curves.

We ran the SAP light curves through the Lomb-Scargle and ACF and compared measurements (decided upon in the same way as the SS) for the 20 stars published by Barnes et al. (2016). The results can be seen in Figure 3.6, where the periods from Barnes et al. (2016) are depicted as blue diamonds. These are connected via vertical lines to circles representing our corresponding measurements, the darkness of which

indicates how confident we are in our reported value (i.e. a gray circle represents less confidence based on checking the light curve by eye, while a black circle means we trust the result). A lot of discrepancy exists between the published periods and our own values. Not only do we not see a clear period in the majority of the versions of our light curves from Barnes et al. (2016), of the three where we do trust the result, one is drastically different from the published value. While this could be due to differences in the pipelines used to extract and correct the data (Barnes et al. 2016 use the PDC light curves from MAST; see Chapter 2), we have shown that our light curves are reasonably well-corrected, and thus are capable of producing a legitimate comparison with published results.

The scatter from our preliminary CPD, combined with the inconsistency in period measurements from our SAP set with those of Barnes et al. (2016), highlights the challenges of working with *K2* C05 data and emphasizes the need to quantitatively understand our limitations in finding rotation periods in M67. This includes further evaluating the pipelines used to extract and detrend the data, particularly with respect to the kinds of periods and amplitude ranges for which we have the most success. We also want to remove, as much as we can, the human element of deciding confidence levels in our measured periods. Now that we have presented our rotation detection techniques, we can begin to explore the absolute limits of period detection with the best-case scenario of un-evolving, sinusoidal signals in Chapter 4. In doing so, we make a more thorough comparison with the results from Barnes et al. (2016) and also Gonzalez (2016a), fully discussing the issues inherent to these studies with respect to establishing gyrochronology relations for older, main-sequence stars.

Chapter 4

Sinusoidal Injection Tests: Testing Sensitivity Limits in *K2* C05 M67 Data

The face of the Sun is not without expression,
but it tells us precious little of what is in its heart.

Armin J. Deutsch

4.1 Introduction

Chapter 2 was dedicated to the extraction and preparation of the *K2* light curves that we will use to look for rotation periods in M67, and Chapter 3 examined some common techniques for finding the periods themselves. However, as we briefly mentioned, Barnes et al. (2016) and Gonzalez (2016b,a) beat us to the punch in that regard, using C05 data to measure their own rotation periods and investigate their implications for gyrochronology. The main findings from Barnes et al. (2016) can be seen in Figure 4.1, which presents Figure 4 from that work. The colored lines are gyrochrones from Barnes (2010), the corresponding ages of which are provided. While it is apparent

This Chapter has been published as Esselstein et al. (2018).

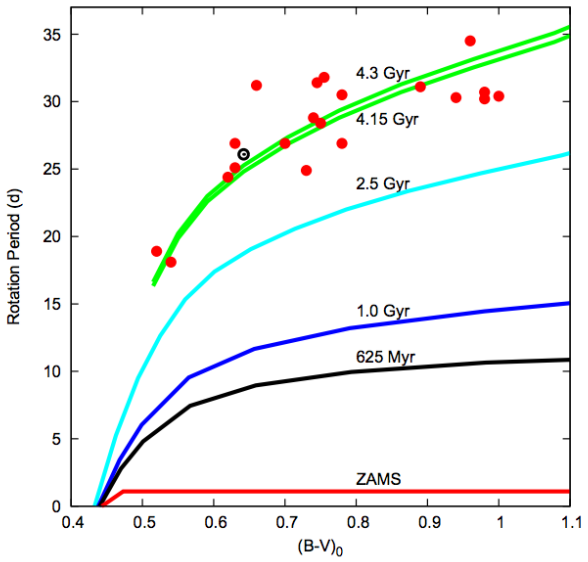

Figure 4.1: Figure 4 from Barnes et al. (2016) showing the measured rotation periods from that work and the gyrochronology relations from Barnes (2010) at different cluster ages.

from Figure 4.1 that Barnes et al. (2016) obtained a good match to pre-existing gyrochronology relations, this was based on a very small sample of 20 stars, with the majority of the reported periods not convincingly confirmed when the respective light curves are examined by eye. By contrast, the results from Gonzalez (2016a) show no dependence of rotation period on mass, but display significant scatter across all masses, as is evident in Figure 6 from that study, reproduced here in Figure 4.2. This figure shows all the rotation period measurements made by Gonzalez, the periods from Barnes et al. (2016), and a sample of Barnes (2010) gyrochrones at 5.5 Gyr, 4.5 Gyr, and 3.5 Gyr. A clear trend among the data does not exist, and none of the portrayed gyrochrones seems to be a good fit.

In addition, both Barnes et al. (2016) and Gonzalez (2016a) made specific choices about their extraction and detrending techniques without exploring other options, and, even more problematic, they both relied to a large degree on an unreproducible element of human judgment. Furthermore, the two studies are both inherently lim-

ited, working only with the individual postage stamps for stars on the outer edges of the cluster; they completely neglect the superstamp, a potentially rich source of representative rotation periods. Finally, there are even some discrepancies in measured period where stellar samples from each study overlap. Consequently, the two studies inferred mutually inconsistent gyrochronological ages for M67, with Barnes et al. (2016) (hereafter referred to as 'Barnes') reporting an age of 4.2 ± 0.2 Gyr and Gonzalez (2016a) (hereafter, 'Gonzalez') claiming 5.0 ± 0.2 Gyr.

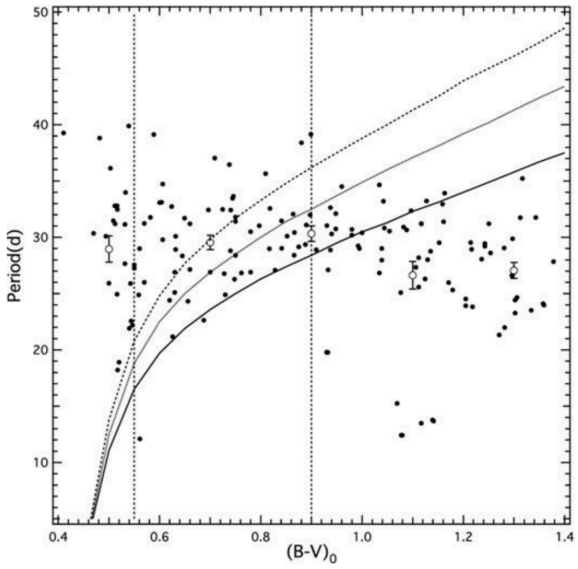

Figure 4.2: Figure 6 from Gonzalez (2016a) showing the measured rotation periods from that work combined with those from Barnes et al. (2016), with the average periods represented by white circles and the gyrochronology relations from Barnes (2010) for 5.5 Gyr (dashed), 4.5 Gyr (dotted), and 3.5 Gyr (solid).

The inconsistencies between Barnes and Gonzalez, and the issues with our own preliminary set of rotation periods from Chapter 3, should already alert us to the difficulty in finding reliable periods from M67 with *K2* data, but the challenges presented by the nature of the light curves themselves add yet another layer of uncertainty. Based on existing gyrochronology models, and on what we know about the Sun itself,

the majority of M67 members are expected to have rotation periods between 20 and 30 d with amplitudes of a few tenths of a percent. Even in the full *Kepler* field star sample of McQuillan et al. (2014), which is based on four years of continuous observations, there are relatively few detections in this area of parameter space. Whether this is a reflection of population demographics or merely sensitivity limits, the ∼75 d *K2* campaigns mean that we can only expect to see 2 – 3 rotation cycles for a typical M67 star, which makes finding long, low-amplitude rotation signals intrinsically problematic. Moreover, despite our best efforts to remove the systematic effects associated with the reduced precision of *K2* (as detailed in Chapter 2), the M67 light curves no doubt still suffer from lingering artificial features, which are compounded by the crowded field and relatively large *Kepler* pixels.

Indeed, a sample of 89 hot A and F stars from C05 highlighted troublesome features within the data, alerting us to the presence of non-astrophysical signals with significant power at 25 d and longer. While the selection of these hot stars is detailed in Section 4.2, it is enough to know for now that we should not expect to see periods much longer than about 5 d for these stars. However, this does not appear to be the case in the C05 data. Figure 4.3 shows three different period distributions for this sample of stars determined via the ACF, the Lomb-Scargle periodogram, and a modified version of the Lomb-Scargle, which we implement in this chapter. As common methods for rotation detection, the significant number of periods from the ACF and the standard Lomb-Scargle above 25 d implies that there is a substantial risk of making erroneous period measurements on the order of 25 – 30 d in M67. Neither of the published studies accounted for this possibility.

In light of these troubling circumstances, a thorough analysis of *K2* data becomes imperative. We must understand, in terms of signal period and amplitude, the sensitivity limits of the pipelines we use for light curve preparation and the reliability of a measurement when a detection has been made. To achieve these quantitative

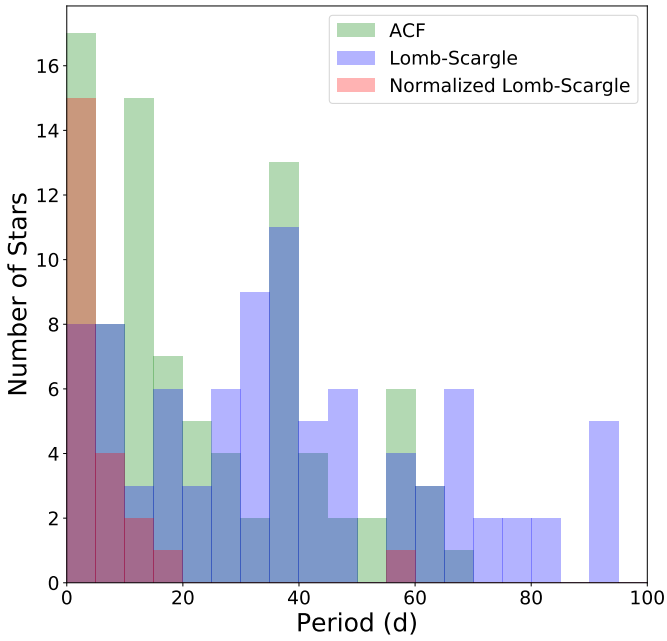

Figure 4.3: Periods acquired from a set of 89 K2 C05 A and F stars using the ACF (green) and the Lomb-Scargle periodogram (blue). We also include a normalized version of the Lomb-Scargle periodogram (red), which we implement later in this chapter, as a demonstration of how we can set detection thresholds and remove potentially anomalous measurements.

performance measures, we embarked on a comprehensive set of systematic tests, injecting over 120 000 simulated, sinusoidal signals into real, raw C05 M67 SAP and SS light curves, including those from the aforementioned set of A and F stars, before processing each dataset using both the Oxford and CfA pipelines (see Chapter 2). Our ability (or failure) to recover the injected signals, for which we know the correct period and phase, represents the best-case scenario for effective period detection from our processing techniques. Such information will guide us in the pursuit of a more accurate and complete list of periods from M67, which is the aim of Chapter 5.

This chapter details the injection tests we conducted, from test set-up to implications for rotation studies, past and future, of M67. We first relate the selection of the stellar samples used as the simulation basis light curves in Section 4.2, before describ-

ing the signals we injected into these light curves in Section 4.3. Next, Section 4.4 defines our detection algorithm for recovering the injected periods, which is based off the application of a normalized Lomb-Scargle periodogram. Section 4.5 explains how we analyze the test results before presenting them in Section 4.6. We discuss the results in-depth in Section 4.7, and, finally, summarize our findings in Section 4.8.

4.2 The Stellar Test Samples

Injection tests simulate real datasets, mimicking the noise and sampling of actual light curves with hypothetical astrophysical signals from planetary transits, flares, or rotational modulation, in an attempt to understand our ability to recover them. Because it is difficult to accurately reproduce the systematics of *K2* C05 light curves, we use raw light curves from that dataset as the basis for the injected signals. This has some problems, of course, the most obvious being that the real light curves may have a significant, astrophysical signal themselves, corrupting the results by interfering with the recovery of the injected signal; we discuss our procedure for minimizing the occurrence of this in Section 4.5. We use three different stellar samples from the C05 SAP and SS datasets, as well as a selection of hot stars taken from that campaign:

- *The SAP sample*: We use the 1877 SAP stars that fell on CCD module 6, which contains M67. The majority of these stars reside on the cluster's outer edges; 1319 of the 1877 have EPICs that match with the Mathieu catalog (see Section 2.2.2), and 236 are confirmed members from Geller et al. (2015).

- *The SS sample*: The SS sample contains 976 stars extracted from the M67 superstamp (using the Oxford pipeline) that match to the Mathieu catalog. Of the 976 SS stars, 359 are confirmed members from Geller et al. (2015), and 75 stars overlap with the SAP sample.

- *The hot star sample*: We define a hot star sample consisting of 89 main-sequence stars located on CCD modules 6, 11, and 16 from C05, extracted with *Kepler* simple aperture photometry. According to MAST, these stars have spectral types from A to F; effective temperatures ranging from 6300 K to 10715 K (the majority falling between 6300 and 7300 K); $B - V$ values of -1.0 to 0.45; and $\log g$ values greater than 4.0. They lack an outer convection zone, or have only a very thin one, and so are not able to support a large-scale magnetic field. Therefore, they do not spin-down quickly (Schatzman, 1962), and, if they do display periodic variability from either pulsations (many of these stars lie in the classical instability strip) or rotation (these hot stars are rapid rotators) (Nielsen et al., 2013b), it is expected to occur on timescales of $\sim$5 d or less. Thus, their light curves are expected to contain only noise and systematics on longer timescales. These are ideal injection test targets, since they can reveal where non-astrophysical signals dominate period searches, as we alluded to with Figure 4.3. Of the 89 hot stars, 22 overlap with the SAP sample.

Figure 4.4 shows the location of three samples on the C05 FOV, where the teal circles, filling up all of CCD module 6, represent the SAP and SS stars, and the scattering of orange diamonds represents the hot star dataset. We zoom in on channels 6.1 and 6.2 in Figure 4.5 to see the 1319 SAP and all 976 SS stars that comprise M67. This figure displays images from the ESO Online Digitized Sky Survey centered on each channel's respective pointing. The stars from the SAP sample are highlighted in blue, while the SS stars are marked in red.

We have now defined our three basis stellar samples to be used in the injection tests. We ultimately have six datasets, however, because we perform the tests using two different versions of each light curve: one version comes from the Oxford pipeline, while the other is processed by the CfA pipeline.

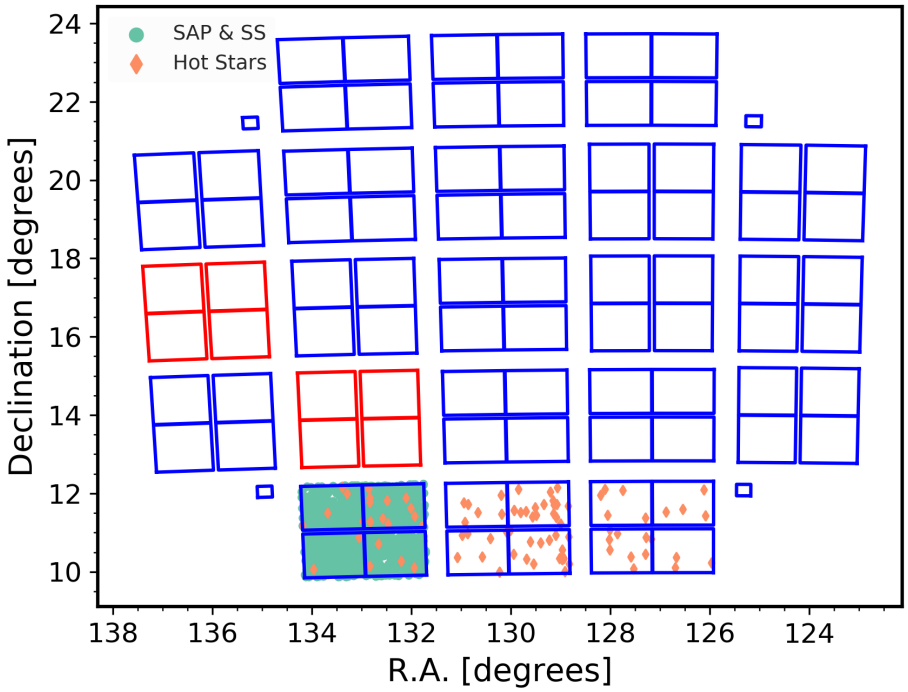

Figure 4.4: Location of the 1877 M67 SAP and 976 SS stars (teal circles) used in this study, along with an additional 89 hot stars (orange diamonds), on the *K2* C05 FOV.

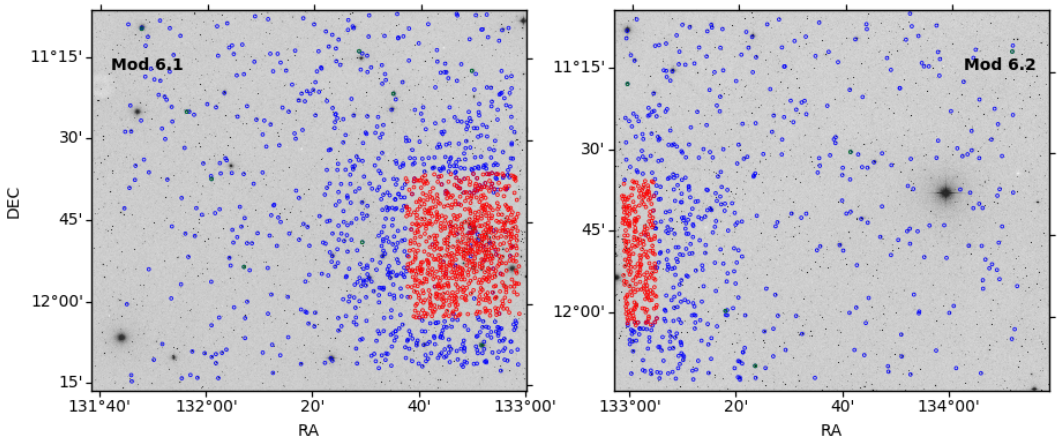

Figure 4.5: Zoomed in look at CCD channels 6.1 and 6.2, highlighting the M67 SAP (blue) and SS (red) stars using two images from the ESO Online Digitized Sky Survey.

4.3 The Injected Signals

We inject into each raw light curve in each of the datasets sinusoidal signals taking the following form:

$$f_{\rm inj} = \frac{a_{\rm inj}}{2} \sin(\frac{2\pi}{P_{\rm inj}} t + \phi_{\rm inj}) + 1 \tag{4.1}$$

where $f_{\rm inj}$ is the injected signal, $a_{\rm inj}$ is the injected amplitude, $P_{\rm inj}$ is the injected period, $\phi_{\rm inj}$ is the injected phase, and t is time in days. To inject $f_{\rm inj}$, we multiply it directly into the raw light curve. We vary $P_{\rm inj}$ from 5 to 35 d in intervals of 5 d. We vary $a_{\rm inj}$, as follows: 0.05%, 0.10%, 0.30%, 0.50%, 1.00%, and 3.00%. Each light curve, then, is injected with 42 different combinations of periods and amplitudes, leading to over 120 000 injections in total for each pipeline to then process. The phase, $\phi_{\rm inj}$, is selected at random for each injection, but we keep track of its value.

4.4 The Detection Algorithm

After we detrend the raw test light curves with the Oxford and CfA pipelines, we must determine our recovery method. Because our injections involve only sinusoidal signals, we use a modified version of the Lomb-Scargle periodogram (Scargle, 1982). As discussed in Chapter 3, the Lomb-Scargle is equivalent to least-squares fitting of sinusoids (Irwin et al., 2006), and, in principle, is optimal to recover stable sinusoidal signals with white Gaussian noise of known variance (which we assume).

Real stellar signals are not strictly sinusoidal, however; they contain significant power at harmonics of the true period due to spot distribution, evolve with the active regions, and may contain multiple periodic signals from differential rotation. Thus, rotation period searches in *Kepler* and *K2* data often use other methods that do not depend on the assumption of sinusoidal form or strict periodicity (McQuillan et al.,

2013; Angus et al., 2017). These methods have outperformed approaches based on least-squares sine-fitting in real and simulated datasets. However, if we know the signal of interest is sinusoidal, then a sine-fitting approach is likely to do at least as well as these alternative methods. We employ Equation 3.9 to search for 490 periods from 2 to 100 days, using an evenly-spaced grid in frequency space.

4.4.1 Periodogram Normalization

If the light curves consisted simply of a stable sinusoidal signal plus white Gaussian noise, locating the peak in the standard Lomb-Scargle periodogram would give us the best-fit period, and evaluating the significance of the detection would be relatively straightforward (see e.g. Horne & Baliunas, 1986; Nielsen et al., 2013b). However, this is not the case here, even after the systematics-correction steps of the Oxford and CfA pipelines. Residual systematics, which remain in the light curves despite our best efforts, often lead to broad peaks in the range of 25 – 60 d, and can overwhelm the peak from the injected signal. To address this, we perform a collective normalization of the periodograms before searching for the final peak.

To normalize the periodograms, we compute the median periodogram as a function of trial period for stars which we expect to share the same systematic noise properties (i.e. separately for the SAP and SS sets, and for the Oxford and CfA pipelines). Each star's periodogram is then divided by the median, thereby suppressing the excess power that is seen in many light curves. The normalized periodogram is thus given by $S'(P) = S(P)/\hat{S}(P)$, where $\hat{S}(P)$ is the median periodogram value for period P.

The median periodograms are evaluated from the non-injected versions of the light curves to avoid the induced power at fixed periods from their injected counterparts. They can be seen in Figure 4.6, with the Oxford SS and SAP median periodograms on the left and the CfA on the right. The SAP median periodograms for both datasets include the hot stars, because in both cases they were processed using the same

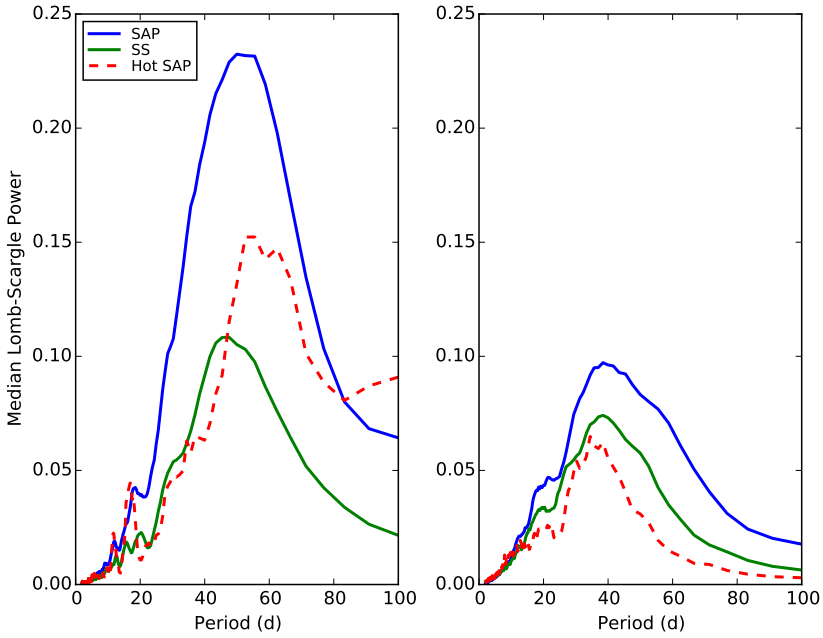

Figure 4.6: Median Lomb-Scargle periodogram for the non-injected SS (blue) and SAP (green) datasets for both pipelines. The non-injected hot star dataset for each pipeline separated from the SAP dataset is shown with red dashed lines. The Oxford pipeline is on the left, and the CfA pipeline is on the right. The presence of broad peaks around 30 d and longer in the hot star sample highlights the presence of long-term, non-astrophysical signals in the C05 light curves.

techniques, but Figure 4.6 also shows in red the hot star median periodograms separate from each SAP set. The broad peaks in the hot star periodograms of both pipelines emphasize that these trends are non-astrophysical; we should not expect periods longer than about 5 d for these stars. We also note that the median periodogram for the Oxford SAP set is higher overall, and peaks at longer periods, than the Oxford SS sample, hinting that the former contains systematics with larger amplitudes on greater timescales. This is consistent with the relative amplitudes of the PCA trends compared to noise for the two samples, which are smaller for the SS (see Chapter 2). It also means that long-period signals will be more heavily suppressed by normalization in the Oxford SAP sample.

Figure 4.7 illustrates the effects of normalization for an individual SAP star. The

top panel shows two light curves for EPIC 211355490, injected with a period of 20 d and amplitude of 0.1% and fully processed with the Oxford (gray) and CfA (blue) pipelines. The middle panel depicts the original periodograms prior to normalization for both pipelines, while the bottom panel gives the normalized versions. The respective periods are indicated by vertical lines. There is a relatively strong, long-period signal in the Oxford pipeline that is not present in the CfA (unsurprising given the differences in Figure 4.6), and this is what the Lomb-Scargle finds in the former, settling on a period of 62 d. On the other hand, the normalized Oxford periodogram has a peak at 19.2 d, which closely matches the injected period. The normalization of the periodogram thus allowed us to find the 'true' period of Oxford version of this light curve when otherwise it would have been lost by the systematic trend. The CfA, however, appears to have done a better job of cleaning up systematics in the light curve, and found peaks of 20.0 d in both the original and normalized periodograms.

4.4.2 Detection Threshold

Once we have identified the peak in each normalized periodogram, we must decide whether it is significant enough to count as a detection. The Lomb-Scargle always produces a result, but it would be imprudent to accept every measurement. After testing a number of possible schemes, we opted for the following detection threshold definition:

$$S'_{\mathrm{T}} = \mathrm{MAX}(S'_{90} \times C, S'_{\mathrm{min}}) \tag{4.2}$$

where S'_T is the threshold value, and S'_{90} is the 90^{th} percentile of the normalized peridogram for a given light curve. The terms C and S_{min} are tuning parameters which we can vary to alter the relative and absolute components of the threshold, respectively. For example, if $S'_{90} = 4$, and the value for C is set at 3, then the

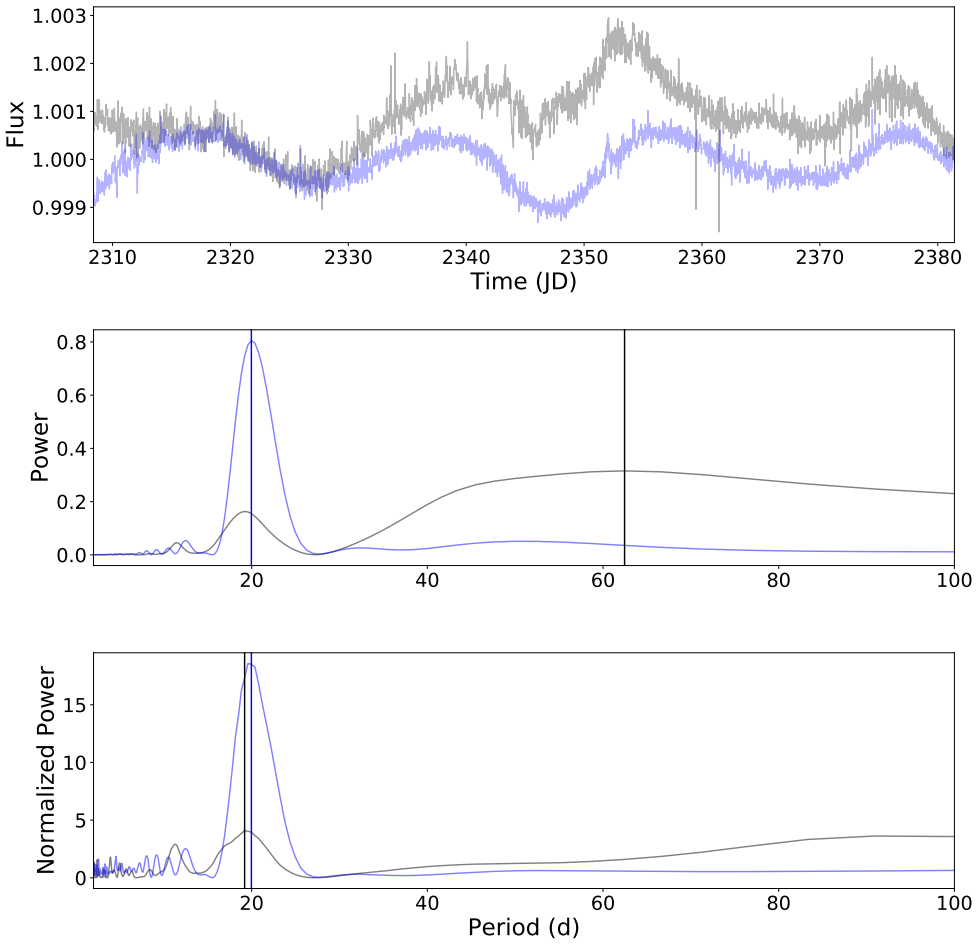

Figure 4.7: Example of the effect of periodogram normalization using EPIC 211355490 injected with a period of 20 d and amplitude of 0.1%. The top panel shows the systematics-corrected flux from the Oxford (gray) and CfA (blue) pipelines. The middle panel gives the original periodograms for both pipelines, while the bottom panel shows the normalized periodograms. The periods found in each periodogram are indicated by the vertical lines, with the black lines depicting the Oxford periods and the blue lines identifying the CfA periods. The CfA period in both cases is 20.0 d, while the Oxford period improves from about 62 d to 19.2 d.

maximum power of the normalized periodogram must be at 12 or greater for the associated period measurement to be considered a detection. The tuning parameter $S_{\min}$ comes into play when $S'_{90} \times C$ is so low that most peaks would qualify as a detection; it ensures that there is a minimum threshold value. Both C and $S_{\min}$ can then be varied to test their effects on sensitivity and reliability, which we discuss in the following section. If the highest peak in the normalized periodogram passes the threshold defined in Equation 4.2, we have a detection and record the corresponding period, best-fit amplitude, and phase. Otherwise, a result of 'no detection' is recorded.

4.5 Evaluating the Results

To evaluate the results of the injection tests, we need to quantify how sensitive the period search is, i.e. what fraction of the injected signals are successfully recovered, and how trustworthy the detections are, i.e. what fraction of the detections are 'valid', meaning that the measured period and phase are within some tolerance of the injected values. We must also deal with the problem of intrinsically variable stars and settle on values for C and $S_{\min}$. Here, we define key terms for interpreting the injection test results, discuss the identification and removal of stars with real variability from the test sample, and finalize our detection threshold based on the effects of C and $S_{\min}$.

4.5.1 Valid detections, completeness, and reliability

The important terms in understanding the statistics from this study are as follows:

- Validity: We consider a detection to be *valid* if the recorded period and phase are within 20% of the injected values.

- Completeness: For a given *injected* period and amplitude bin, we define *completeness* as the fraction of injected signals which led to a valid detection, i.e.

if we injected 100 stars with a period of 25 d and amplitude of 0.3%, what percentage were we able to recover? We also calculate a *threshold error* statistic, which records the fraction of cases where the period and phase corresponding to the highest peak in the normalized periodogram were within the valid range, but the peak was not high enough to pass the detection threshold.

- Reliability: For a given range of *measured* periods and amplitudes, we define the *reliability* as the fraction of valid recorded detections within that range.

Another way to understand completeness and reliability is to look ahead to Figure 4.10, which shows (for the hot star sample) the detected versus injected periods at each of the injected amplitudes. For completeness, we consider a vertical bin in one of these diagrams around one of the injected periods. The completeness is given by the number of detections (colored points) in that bin which are valid, divided by the total number of points in the bin. To be valid, a detection must lie within the gray shaded area, which indicates a $\leq 20\%$ period error. In addition, as defined above, a valid detection must also have a $\leq 20\%$ phase error (not shown on the figure). We can think of reliability as being similar, but considering a horizontal rather than vertical bin in the same kind of diagram. This is not quite correct, however, since reliability is computed for a given *detected* period and amplitude, whereas the figure has been made with respect to *injected* amplitude.

4.5.2 Calculating Uncertainties

To estimate the uncertainties, we assume a Poisson distribution with respect to both completeness and reliability and define the uncertainty as:

$$\sigma = \pm \frac{1}{\sqrt{N}} \tag{4.3}$$

where N is the number of injections per injected period and amplitude bin (i.e. no.

of injected amplitudes × no. of injected periods × no. of stars in each test sample) in the case of completeness. For reliability, N is the total number of detections in each measured period and amplitude range. Therefore, for each test set within each pipeline, the individual completeness values will have the same uncertainty while the reliability will vary from bin to bin. We recognize this is a little simplistic, but the more sophisticated approach would require repeating the injections many times, which would be too time-consuming. For our purposes, this is a good first approximation.

4.5.3 Intrinsically Variable Stars

We injected signals into real *K2* light curves to faithfully reproduce the noise properties of actual M67 light curves. Thus, we implicitly assumed that most do not already contain a detectable intrinsic periodic signal. However, of course, some do. In such cases, a detection might in fact be caused by the intrinsic, rather than the injected, signal. This can lead to detections which appear 'invalid', but are in fact correct, biasing the results. To avoid this, we run the period search on the non-injected versions of the light curves. If a detection occurs in any of these, the star is labelled as intrinsically variable, and all of the corresponding, injected versions of this star's light curves are excluded from the completeness and reliability statistics. This means that only a fraction of the total number of injections we performed is actually used in the final results. This is not entirely satisfactory, since we do not know whether the signals detected in the non-injected light curves are come from systematics or intrinsic stellar variability. Furthermore, the number of stars excluded as 'variables' depends on the detection threshold used. However, we were unable to devise a better solution. We note that, for reasonable threshold values, the variable stars represent a relatively small minority of the test light curves.

4.5.4 Varying the Threshold

While we have argued that a sine-fitting periodogram is the most appropriate approach for the recovery of the injected signals, the results of course depend on the fine details of normalization and the detection threshold. We have already alluded to the effects of the former. Regarding the latter, a lower threshold can be used to increase completeness slightly, but it also leads to a drop in reliability in the corresponding bins. If measured rotation periods in an actual period search are to be compared with theoretical models, it seems preferable to prioritize high reliability over slight gains in completeness — so long as the completeness itself is also well-measured, so we can account for missed detections when comparing the measured periods to theoretical expectations.

To see the effects of changing the tuning parameters of the detection threshold on completeness and reliability, for each injected light curve, we recorded the normalized periodogram peak S'; the corresponding period, phase, and amplitude; and the 90^{th} percentile of the normalized periodogram, S'_{90}. It was then trivial to vary the value of C and S_{min} in Equation 4.2 to examine the impact that these values have on completeness and reliability, as well as on the number of stars labelled as intrinsically variable and subsequently removed from the final quantitative assessments.

We varied $C = 0$ to $C = 6$ while holding S_{min} at 5, and tested S_{min} from 0 to 12 while holding C at 4, using the Oxford pipeline. A sample of the results can be seen in Figures 4.8 and 4.9. Each figure shows the effect of changing C on the top and S_{min} on the bottom. Figure 4.8 illustrates the effects on completeness for an injected period of 25 d across all injected amplitudes. In both panels of this figure, the number of stars in each injected period and amplitude bin is given. We can see that at $C = 0$ and $C = 1$, the results are dominated by the minimum threshold value, but they have relatively few stars per bin. Completeness then peaks at $C = 2$ before starting to decline again. There is an increase of $\sim$500 stars per bin at $C = 2$, followed by

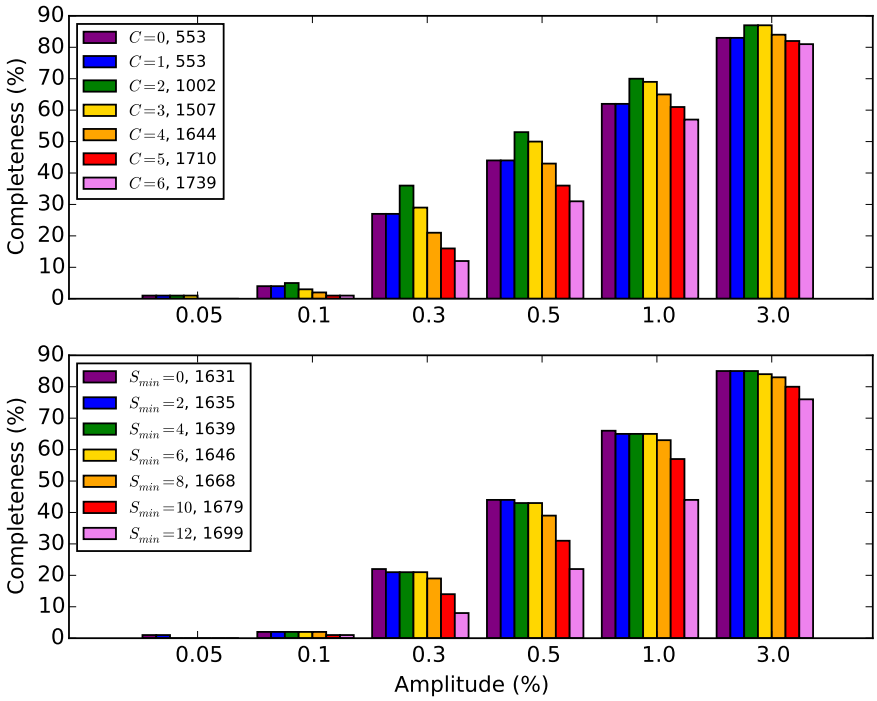

Figure 4.8: Comparison of completeness values for an injected period of 25d at all injected amplitudes for different values of C (top row) and S_{min} (bottom row). For the top row, S_{min} was fixed at 5. For the bottom row, C was fixed at 4. The legends are also marked with the number of stars in each injected period and amplitude bin for each value of C and S_{min}. It is worth noting that by $S_{min} = 12$, all sensitivity at periods greater than 25 d was gone. We used the Oxford pipeline for these tests.

another 500 stars at $C = 3$. Beyond $C = 3$, the number of stars per bin still grows, but less rapidly. For $S_{\rm min}$, the completeness essentially stays the same until about $S_{\rm min} = 8$. By $S_{\rm min} = 12$, the completeness drops to about half the values at $S_{\rm min} = 0$ at amplitudes of 0.5% and less. Not visible in Figure 4.8 is the fact that all sensitivity at periods greater than 25 d is lost. The number of stars per bin slightly increases with $S_{\rm min}$. Thus, as expected, C has a much greater effect on the number of stars per bin and, more importantly, completeness, than $S_{\rm min}$, as long as $S_{\rm min}$ is not too high.

Likewise, in Figure 4.9, we see how C and $S_{\rm min}$ affect reliability across the ranges of measured periods in this study. We have fixed the measured amplitude to the range

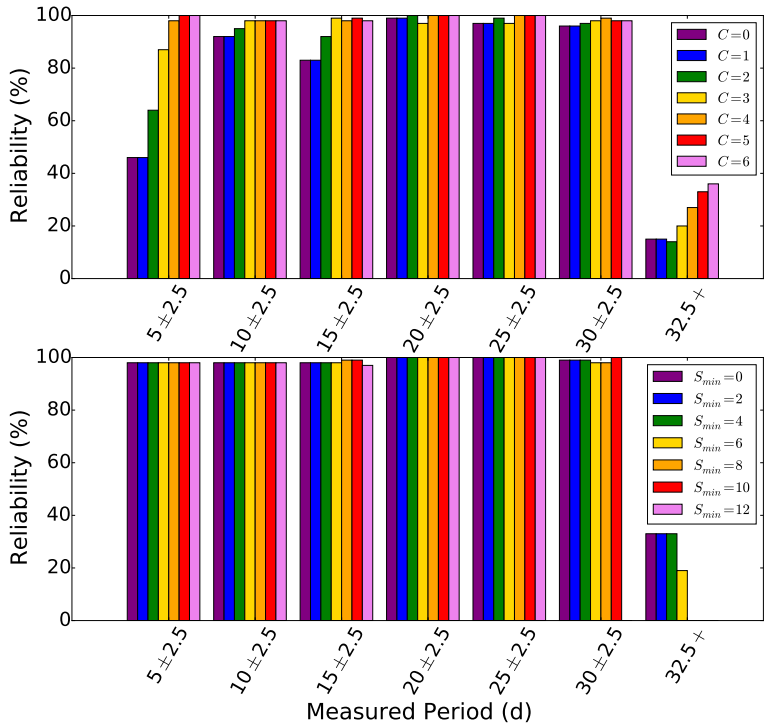

Figure 4.9: Comparison of reliability values for a measured amplitude between 0.25% and 0.45% across all detected periods for different values of C (top row) and S_{min} (bottom row). For the top row, S_{min} was fixed at 5. For the bottom row, we fixed C at 4. It is worth noting that we lost sensitivity for detections greater than 32.5 d at $S_{min} = 8$, and we lost sensitivity for detections greater than 27.5 d at $S_{min} = 12$. We used the Oxford pipeline for these tests.

of 0.25% to 0.45%, just above the solar range. As expected, reliability generally increases as C increases, noticeably so until about $C = 4$. The effect of changing $S_{\rm min}$, however, is negligible except at long periods, where reliability decreases until $S_{\rm min} = 8$. Here the reliability is zero, but with very few detections, and beyond, the number of detections drops to zero for periods longer than ∼30 d.

Figures 4.8 and 4.9 demonstrate the trade-off between completeness and reliability. Using large values for C and $S_{\rm min}$, i.e. a stringent detection threshold, leads to low completeness and large threshold error, but excellent reliability. A high threshold

also means that fewer stars are marked as intrinsically variable, so more injected light curves are used to compute the final statistics. As the threshold is gradually lowered, completeness increases and threshold error decreases, at the cost of reduced reliability. The number of variable stars also grows, and for very low detection thresholds almost all stars are excluded, leaving relatively few in the test samples. Therefore, we settled on $C = 4$ and $S_{\min} = 4$ as the best compromise. When using these values, 238 of the 1877 stars in the Oxford SAP were marked as intrinsically variable, as were 120 of the 976 SS stars and 23 of the 89 hot stars, leaving 1639, 856, and 66 stars in each set, respectively. Using the same tuning parameters for the CfA pipeline, we are left with 1587 SAP stars, 848 SS stars, and 70 hot stars.

4.6 Injection Test Results

With the injection tests set up and the detection threshold properly defined, we can compute completeness and reliability for each of the stellar samples from both pipelines. This section presents those results, though additional tables can be found in Appendix A. The results from the CfA pipeline come from the single-scale PDC-MAP, as opposed to multi-scale PDC-MAP. This is because, across the board, the former performed better for our purposes, as expected (see Section 2.5). Section 4.7 discusses the results in-depth.

4.6.1 Recovered versus Injected Periods

We present the initial results in Figures 4.10 through 4.15. Each of these figures is made up of six panels, corresponding to the injected amplitudes of 3.0, 1.0, and 0.50% (top row), and 0.3, 0.1, and 0.05% (bottom row). Within each panel, the colored circles represent detections, while those that did not pass the detection threshold are shown as smaller black dots. The gray shaded area in each plot shows the period

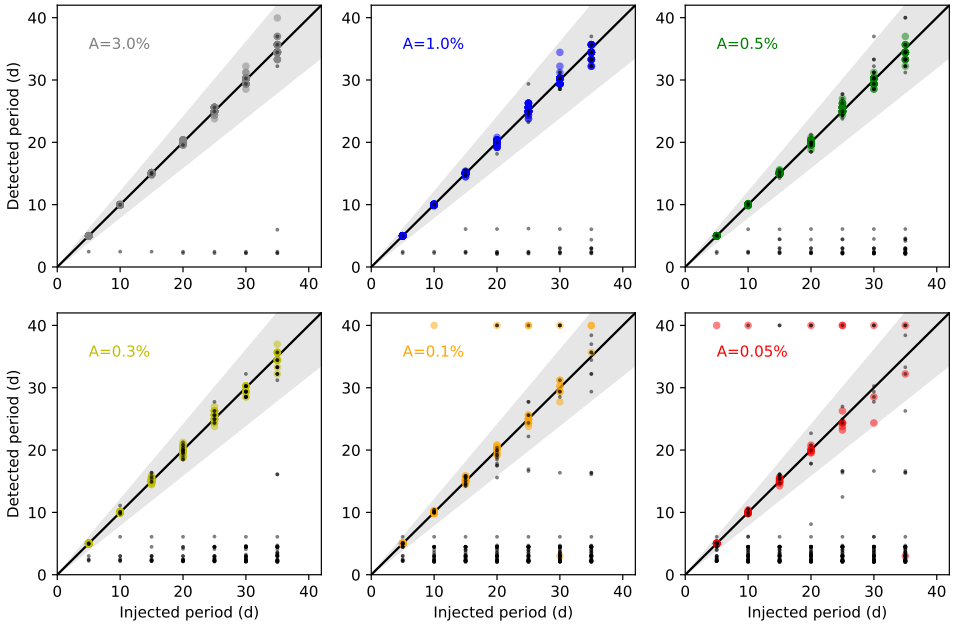

Figure 4.10: Detected versus injected period at each of the injected amplitudes for the hot star sample processed with the Oxford pipeline. Colored points represent cases which passed our detection threshold; those which did not are shown as smaller black points. The shaded grey area shows the region where the injected and detected periods are within 20% of each other.

validity range, though recall that a ±20% phase match is also required. Phase considerations aside, a black point in the shaded area is a missed valid detection, whereas a colored circle outside the shaded area is an invalid detection. We excluded stars marked as intrinsically variable. As expected, the number of both missed and invalid detections increases with longer periods and smaller amplitudes. While there are other interesting features from these plots to be discussed, some manifest themselves in the completeness and reliability, presented below. We therefore only present the results in this section, and defer a more detailed discussion to Section 4.7.

4.6.2 Completeness and Reliability

We now present the completeness and reliability results here in graphical form, although tables with actual values and uncertainties can be found in Appendix A. The

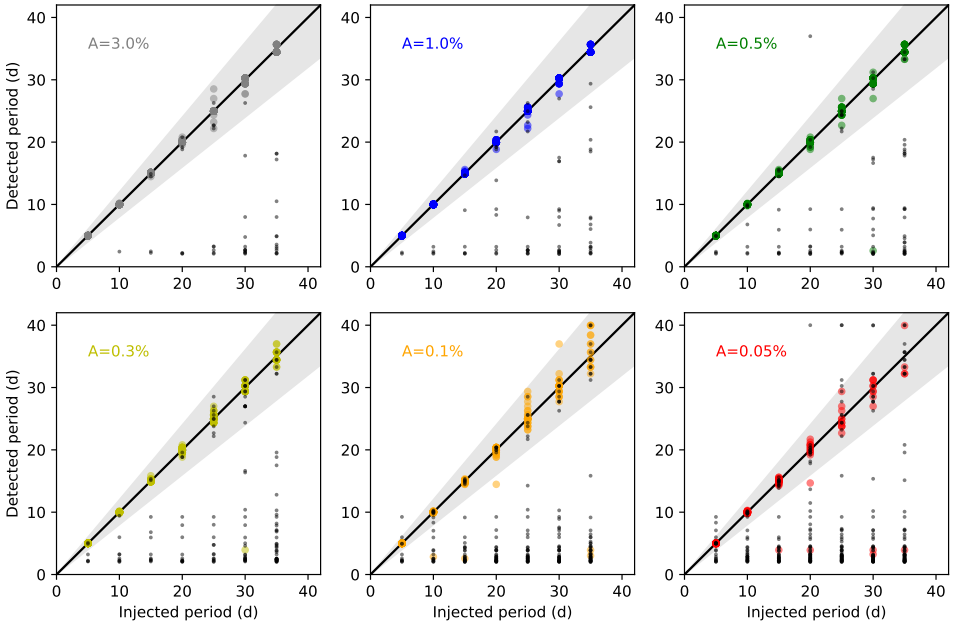

Figure 4.11: Same as Figure 4.10, but for the hot star sample processed with the CfA pipeline.

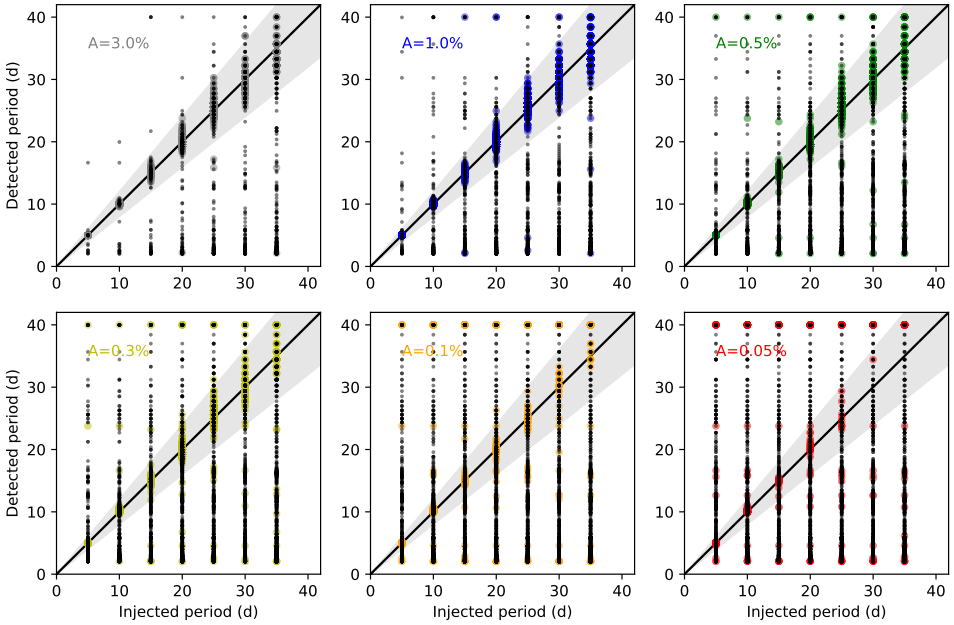

Figure 4.12: Same as Figure 4.10, but for the SAP sample processed with the Oxford pipeline.

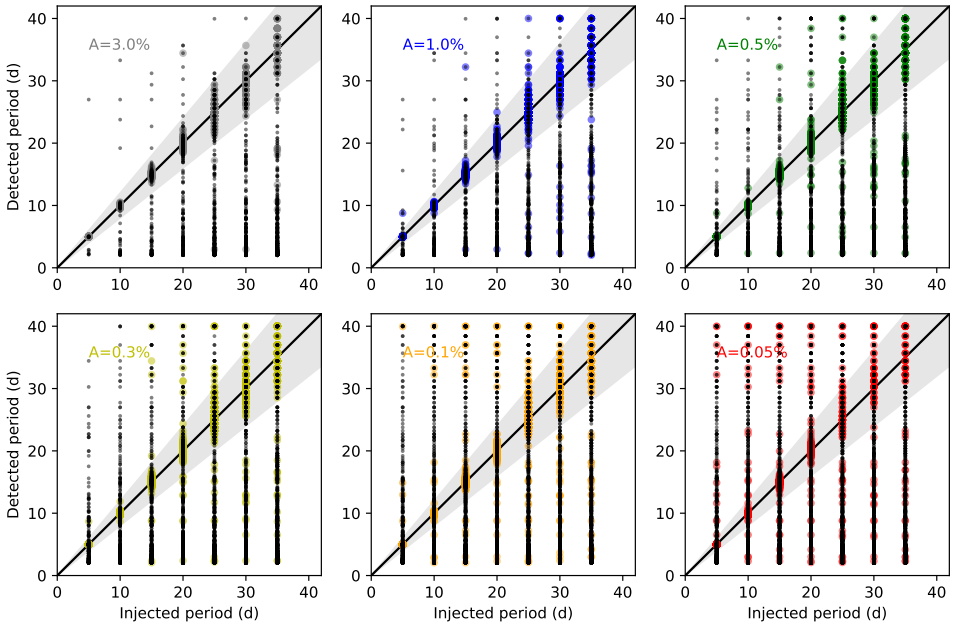

Figure 4.13: Same as Figure 4.10, but for the SAP sample processed with the CfA pipeline.

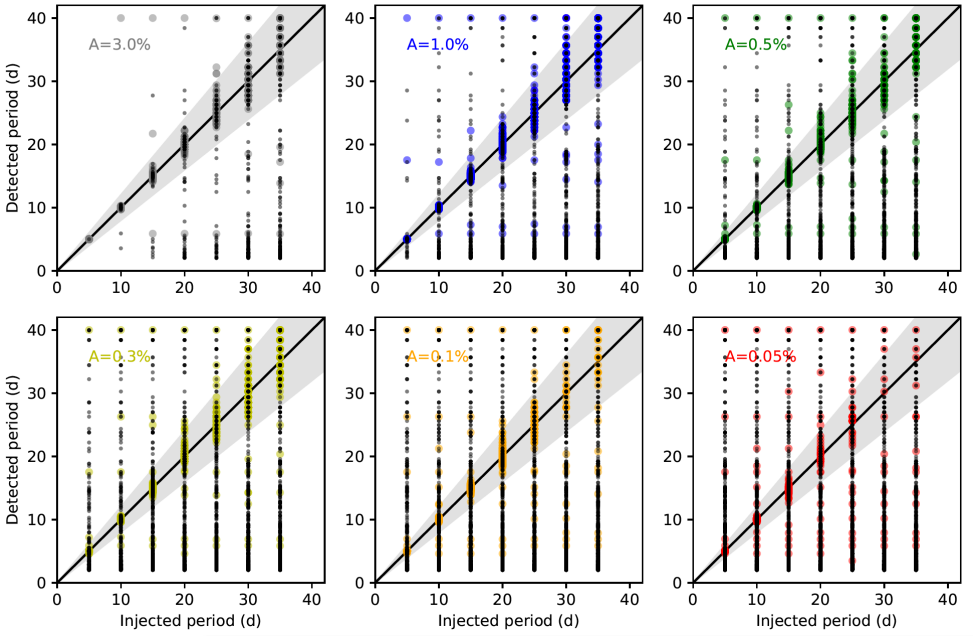

Figure 4.14: Same as Figure 4.10, but for the SS sample processed with the Oxford pipeline.

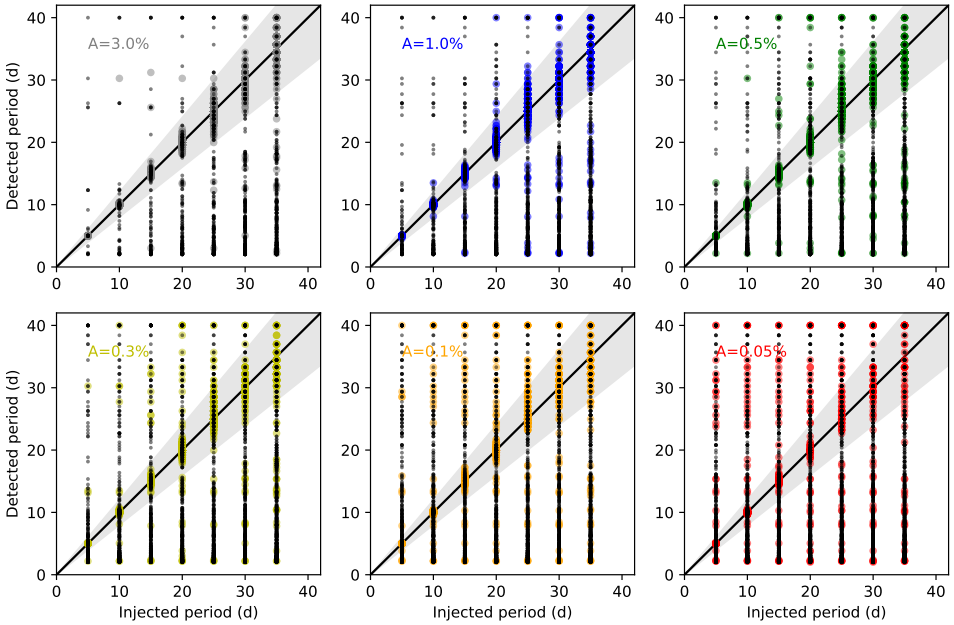

Figure 4.15: Same as Figure 4.10, but for the SS sample processed with the CfA pipeline.

completeness for the Oxford and CfA pipelines are shown in the top and bottom rows of Figure 4.16, respectively, and the columns, from left to right, belong to the hot star, SAP, and SS datasets. We have identified in blue the solar case, or where the injected period is 25 d and the amplitude is 0.1%.

Figure 4.17 presents the reliability for the Oxford and CfA pipelines in the top and bottom rows, respectively, and the columns again indicate the hot star, SAP, and SS samples. Each bin represents the percentage of valid detections within the measured period and amplitude range. The bins with red dots are those with relatively few detections. We consider SAP and SS bins with $\leq$100 detections and hot star bins with $\leq$30 detections as insignificant. All three samples, from both pipelines, have very few detections in the longest period, lowest amplitude bins. The corresponding (generally very high) reliability values therefore have large uncertainties and should not be treated as very meaningful.

Finally, Figure 4.18 shows the injected versus detected amplitudes for valid detec-

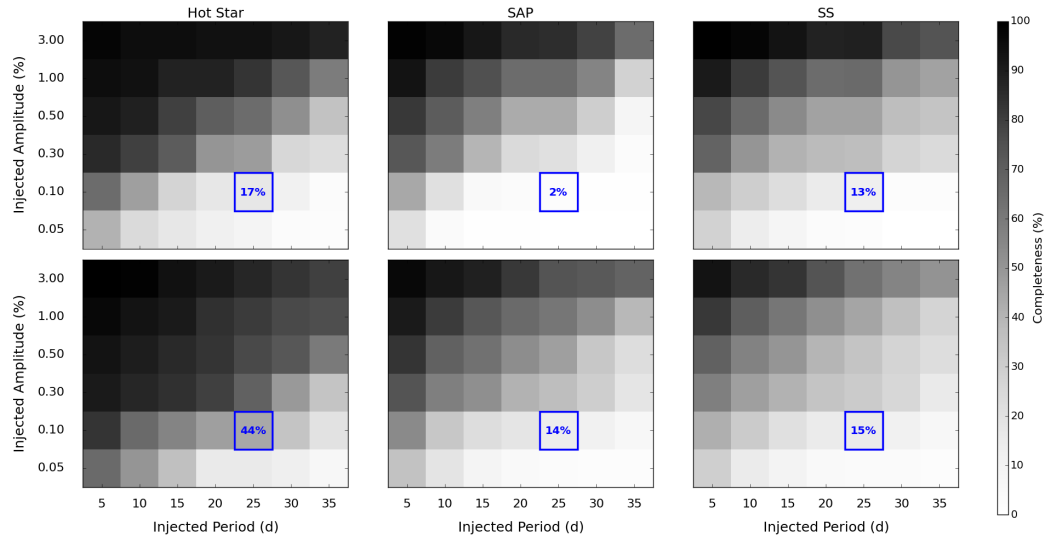

Figure 4.16: Completeness tables for the hot star (left), SAP (centre), and SS samples (right), detrended with the Oxford pipeline (top row) and the CfA pipeline (bottom row). The grids have the injected period bin along the x-axis and the injected amplitude along the y-axis. The completeness for the solar case is highlighted in blue for each dataset.

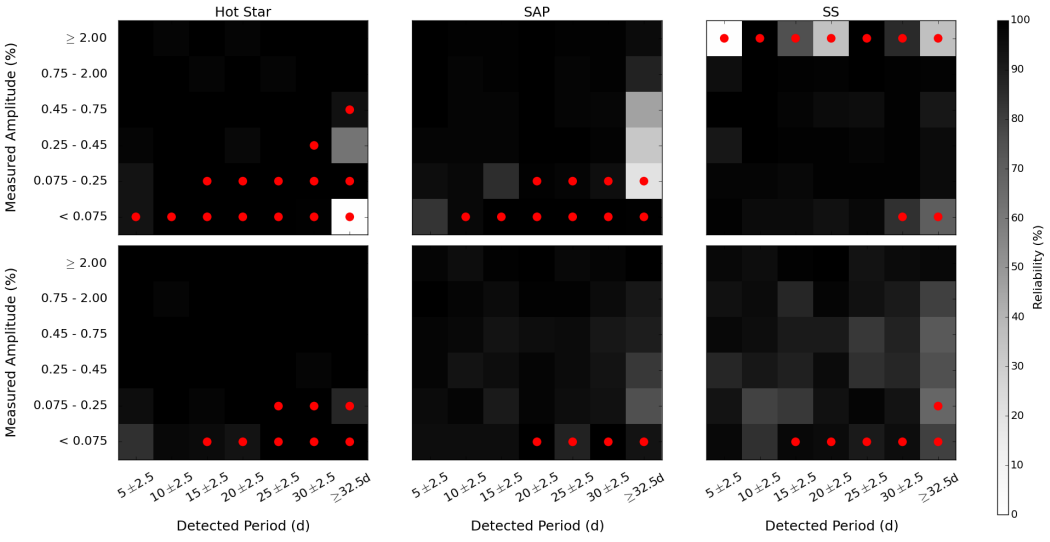

Figure 4.17: Reliability for the hot star (left), SAP (centre), and SS samples (right), detrended with the Oxford pipeline (top row) and the CfA pipeline (bottom row). The red circles represent where there were less than 30 detections in the hot star sample and less than 100 in the SAP and SS samples.

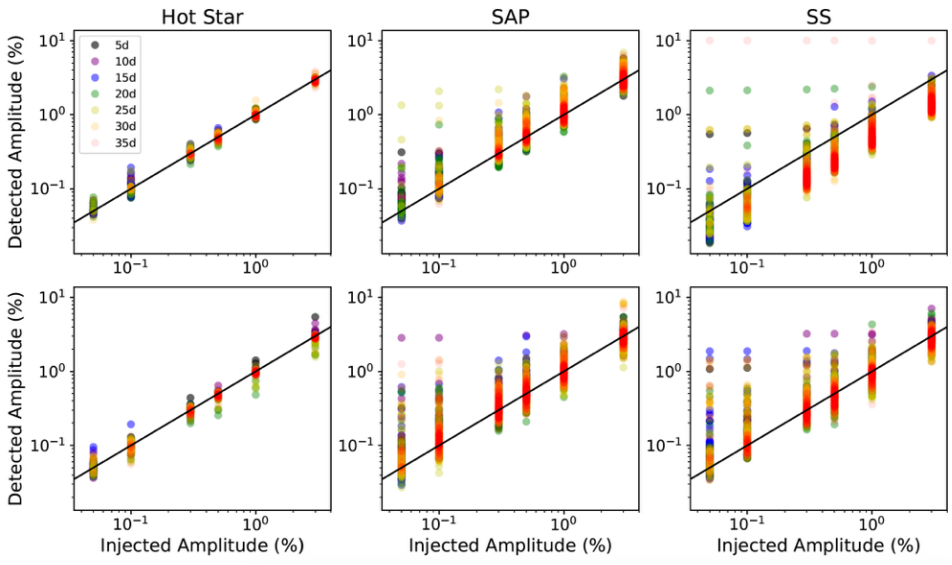

Figure 4.18: Injected vs. detected amplitude for the valid detections in the hot star (left), SAP (centre), and SS samples (right), detrended with the Oxford pipeline (top row) and CfA pipeline (bottom row). The associated injected periods are marked in different colors.

tions from the Oxford (top) and CfA (bottom) pipelines. The detected amplitudes can differ significantly from the injected ones for several reasons. First, the basis light curves may already contain some power at the corresponding period. Second, the intrinsic noise levels of the light curve will affect the amplitude of the flux as a whole. Lastly, the systematics correction steps can alter the injected signal, in some cases leading to measured amplitudes that are smaller than the injected ones (e.g. the Oxford SS).

4.7 Discussion

Here we dissect the injection test results, unveiling not only the sensitivity limits of two prominent light curve preparation pipelines, but also the challenges in conduct-

ing M67 rotation period searches with *K2* data and subsequent implications. We start with a brief discussion on the effects of periodogram normalization in light of completeness and reliability. Next, we look at the 'ideal case' of the hot star results before moving on to the SAP and SS results. We then provide an overall comparison of the samples and pipelines, commenting on the effectiveness of the latter. Finally, we will discuss the ramifications of our results on M67 rotation studies using only *K2* C05 data, particularly those of Barnes and Gonzalez.

4.7.1 Residual Long-term Trends

We now revisit the effects of periodogram normalization in light of the final results. As mentioned in Section 4.4.1, the median periodograms shown in Figure 4.6 tell us a lot about the residual trends present in the light curves after dretending by the Oxford and CfA pipelines. For the SAP and SS samples, the median periodogram rises steeply for periods above 20 d, peaking around $\sim$50 – 55 d and $\sim$40 – 45 d, respectively, before decreasing again and flattening off for periods $>$ 80 d (to which we expect little or no sensitivity in *K2* light curves, anyhow). While evident in both pipelines, this feature is much more dramatic in the Oxford pipeline. Regardless, the power present at periods relevant to a study of M67 in both hot star samples shows that this is non-astrophysical, despite our systematic corrections. Furthermore, the differences between the SAP and SS are significant: our *a priori* expectation was that the SS might be more problematic than the SAP due to increased crowding in the densest parts of M67. However, the median periodograms tell a different story, with considerably more residual power in the 30 – 70 d period range in the SAP than the SS light curves for both pipelines.

Normalizing the light curve periodograms has proven to be a critical step in recovering the injected signals. If the standard periodograms were used for period detection, the long-term residual trends would lead to numerous false detections at

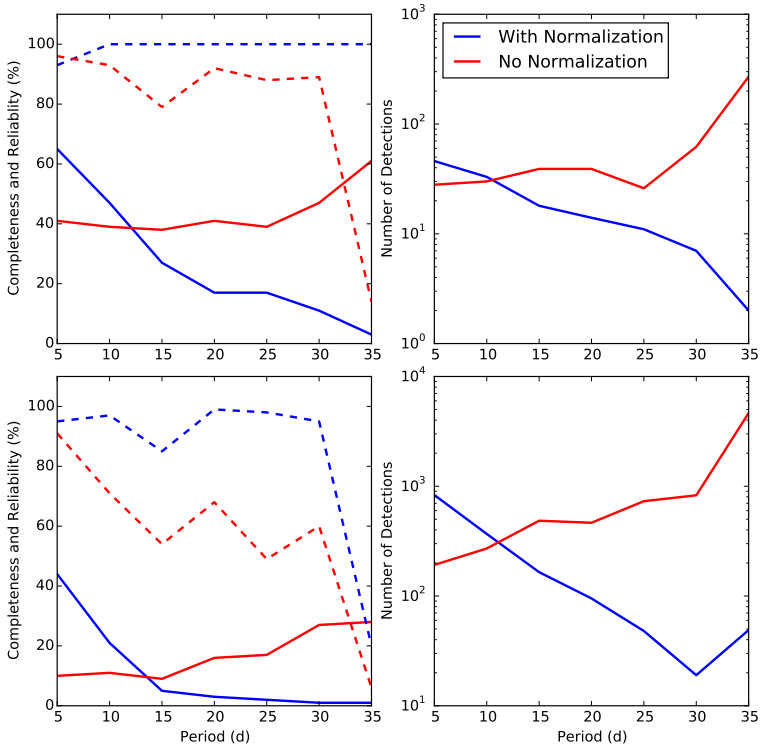

Figure 4.19: Comparison of completeness and reliability results for the Oxford hot star (top row) and SAP (bottom row) datasets with (blue) and without (red) normalization of the Lomb-Scargle periodogram for the solar amplitude (0.1% for completeness, 0.07 – 0.25% range for reliability). The left panels show the completeness (solid lines) and reliability (dashed lines) results, while the right panels show the number of detected periods with measured amplitudes of 0.07 – 0.25%.

mid-to-long periods. To see the exact effect of using the regular Lomb-Scargle versus our adaptation on completeness and reliability, we recovered the periods for the Oxford hot star and SAP injected datasets without normalizing the periodograms. For a detection threshold, we followed the example of Nielsen et al. (2013b) and set the threshold at four times the root mean square of the zero-mean time series, though we removed the same stars that had been marked as variables in the main test sets.

Figure 4.19 shows the completeness and reliability for the solar amplitude (0.1% injected amplitude for completeness, 0.07 – 0.25% measured amplitude for reliability),

along with the number of detections with measured amplitudes ranging from 0.07 to 0.25% at different periods (similar to the numbers in brackets in Tables A.7 through A.12). Results with normalization are in blue, while those without normalization are in red. Due to the lower detection threshold criteria and the long-term trends seen in the median periodograms, the number of detections for the un-normalized samples increases significantly compared to the normalized hot star and SAP samples. This allows for an increase in completeness, including at the solar case, which improved from 17% to 39% and 2% to 17% for the hot star and SAP samples, respectively. Completeness also begins to rise with increasing period starting around 25 d, countering the general trends of the normalized sample (which we will discuss below). However, as expected, the reliability at periods of 25 d and longer decreases drastically, and there is a disproportionate number of detections at these longer periods.

It is clear from Figure 4.19 that the normalization procedure we devised to avoid the lingering, long-term systematics is fairly successful, especially compared to the standard Lomb-Scargle periodogram. As further evidence for the justification of normalizing the periodograms, we record consistently high reliability wherever we have a significant number of detections (see Figure 4.17 and Tables A.7 to A.12 in Appendix A). However, this normalization is not a perfect solution, since it also suppresses the detection of real signals at longer periods, as apparent from Figure 4.16. Avoiding the trap of lingering systematics by normalizing the periodograms may sometimes come at the cost of real astrophysical signals.

4.7.2 The Hot Star Sample

The 89 hot stars should not show significant rotational modulation beyond about 5 d, making them ideal injection test targets. We can be confident that if we see a long period where we did not inject one, it is most likely the result of lingering systematics. For the Oxford pipeline, we were left with 66 stars after removing 23 variables (i.e.

those which have an astrophysical signal that could interfere with the results). Of these 23, 19 had detected periods of less than 10 d, and the rest had periods of less than ∼16 d, apart from one (see Figure 4.3). In the CfA pipeline, we used 70 stars in the final analysis. All 19 variables had periods under 12 d. These numbers again suggest that our normalization works reasonably well in both pipelines. The presence of flagged variables with periods longer than 5 d indicates that the hot star sample may be contaminated by background stars, or that it contains a number of cooler F stars, but it is good enough for our purposes.

As we can see in Figures 4.10 and 4.11, we do a good job recovering the injected periods from both pipelines in the hot star sample. Some of the invalid detections likely come from variables — possibly pulsators — not removed from the sample but with low amplitudes. Where these start to become detections at the lowest injected amplitudes, the injected signal may be 'boosting' (i.e. increasing the amplitude of the intrinsic signal) them just enough to be detected. Even for very regularly sampled data like *K2*, injecting a signal at a given period affects the periodogram at other frequencies in a complex way. A number of the invalid detections could also be the result of normalization, which promotes shorter periods at the expense of longer ones: when dividing out the median periodograms, the lower power seen at short periods in Figure 4.6 increases short-period significance relative to longer periods.

The hot star completeness for both pipelines can be found in the leftmost panels of Figure 4.16 and in Tables A.1 and A.2 in Appendix A. As expected from simple signal-to-noise arguments, we see completeness decline with increasing injected period and decreasing injected amplitude for both pipelines. We point out that the best-case scenario for recovering a solar-like signal of 25 d and 0.1% amplitude is ∼45% from the hot star dataset. As a whole, however, the limited size of the hot star sample means that the individual completeness values are somewhat uncertain (± ∼12%) for both pipelines.

The reliability in the hot star sample from either pipeline is consistently high (>90%). High reliability means that we can typically trust a detection made within a measured amplitude and period range. We can see from Figure 4.17 that where we have a significant number of detections (more than 30 for the hot star samples), we can be fairly confident in our results, though again, the uncertainties are relatively large for the hot star samples. The high reliability also indicates that normalization did not introduce low frequency signals into light curves that did not have a strong intrinsic signal in the first place, again reinforcing the validity of this step.

4.7.3 SAP and SS Completeness and Reliability

We have shown that the hot star sample is important for validating periodogram normalization and highlighting the presence of non-astrophysical power around 25 d and longer in the *K2* C05 light curves. We now discuss the results from the SAP and SS, which specifically illustrate the complexity of a period search in M67. Figures 4.12 to 4.15, which show the detected versus injected periods for the SAP and SS datasets from both pipelines, are a lot messier than their hot star counterparts due to the larger sample sizes and more diverse stellar populations within. However, like the hot stars, detections become sparser and less reliable as the injected period increases and the injected amplitude decreases. In addition, lingering power around 10 – 20 d seems to exist in the SAP and SS light curves. This power was either not originally strong enough to mark the light curves as variables until boosted by a lower-amplitude, injected signal, or it could be the result of half-period harmonic measurements from the Lomb-Scargle.

The completeness for the SAP and SS samples are in the middle and far right panels, respectively, in Figure 4.16. As with the hot stars, we see the same general trend of diminishing completeness with increasing injected period and decreasing amplitude, but it has been exacerbated. For both samples from either pipeline, col-

lapsing the figures onto either axis, the completeness falls around or below 50% for amplitudes $\leq$0.50% and periods $\geq$20 d, showing just how hard it is to detect long-period, low-amplitude signals in either dataset. Of particular importance is the solar case, highlighted in blue in Figure 4.16, where the injected period is 25 d and the amplitude is 0.10%. Critically, the completeness here is $\sim$15% or lower for both the SAP and SS in either pipeline. Even with the best-case scenario of perfect sinusoidal signals, solar variability, which we expect in M67, is clearly difficult to find with our detection criteria.

The middle and far right panels of Figure 4.17 present the reliability for the SAP and SS. Again, just like the hot stars, where there is a significant number of detections ($>$ 100 for these larger datasets), the reliability for the SAP and SS rarely drops below 90% for both pipelines. This is encouraging, as it shows that the procedure we have developed should lead to relatively few false alarms, i.e. where we do get a detection, we can generally trust the measurement.

There are a few striking features in Figure 4.17, however. Detecting long periods (particularly at $\sim$35 d) in the Oxford SAP sample appears to be not only more difficult than the CfA pipeline, but also less reliable. The low reliability in this period range could either be a result of periodogram normalization or a failure to correct the residual long-term trends in the data, which the CfA pipeline does better. The Oxford SAP sample also has lower reliability in the shortest period, lowest amplitude bin. This could be an effect of promoting short-period signals when dividing out the median periodogram. We experimented with adding a 'floor' to the Oxford median periodograms, by which we set any value below a given threshold to that floor in an attempt to reduce this effect. We tested floor values of 0.005 and 0.01. While these did improve reliability in the short period, low amplitude bin, the floors tended to reduce reliability overall in all three Oxford samples, particularly the hot star and SS sets, and especially around mid-range periods. Thus, we decided to exclude a floor

from the study to avoid further artificial effects.

One surprising feature in the SS reliability is the lack of detections across all periods at amplitudes of 2.0% and greater for the Oxford pipeline, even though many 3.0% signals were injected. This can be seen in both Figures 4.17 and 4.18. If we then compare the number of SS detections from one pipeline to another in the amplitude ranges of 0.75% – 2.00% and 0.075% – 0.25% in Tables A.11 and A.12 in Appendix A, there are systematically more detections in the Oxford pipeline than in the CfA pipeline for each range. This indicates that the amplitudes of the Oxford SS are suppressed, primarily after the PCA. Though the PCA may also suppress amplitudes in the Oxford SAP, it is more evident in the SS due to the high noise amplitude of the SS PCs compared to the SAP PCs (see Chapter 2). The amplitude suppression could also indicate that the Oxford pipeline removes some intrinsic variability in addition to systematics. Despite the suppression, however, the signals remain intact enough to be detected at a similar rate as the CfA SS, just at lower amplitudes.

4.7.4 Comparing the Samples and Pipelines

Now that we have examined all of the test samples, we can compare the relative performance of each, particularly regarding their respective light curve preparation methods. In both pipelines, the hot star sample has both the highest completeness and reliability across the injected and measured period-amplitude bins, but that is to be expected due to the sample's smaller size and less diversity in spectral type. In addition, the hot stars should be better at preserving the injected sinusoids, as they should be 'quieter' and have less rotational modulation or other competing signals in the original light curves. Finally, the average brightness of the hot star dataset is $K_p = 11.0$, while the combined average of the SAP and SS datasets is $K_p = 15.3$, and the number of valid detections generally decreases with increasing magnitude.

The Oxford SS completeness is slightly lower than the Oxford SAP at short pe-

riods and large amplitudes, but it is better for periods ≥ 15 d and amplitudes below about 0.50%. In addition, the SS sample is more reliable for both the longest and shortest detected periods. These differences are likely due to the separate light curve extraction methods in the Oxford pipeline. The SAP sample is extracted with pixellated apertures, which may not be very optimal for a crowded field, even in the outer regions of the cluster. The SS sample, however, uses deblended, circular apertures, making it better able to deal with crowding.

On the other hand, the CfA SAP completeness and reliability are very comparable (or slightly higher) across most bins when compared against the CfA SS sample. The slight advantage to the SAP sample is probably due to less crowding, as the two datasets are extracted and processed the same way in the CfA pipeline. In addition, the larger size of the SAP sample means that there is a bigger matrix from which to characterize and correct the common-mode trends via PDC-MAP (or PCA, in the case of the Oxford pipeline). This could partially help explain the generally higher completeness values from the SAP sample in either pipeline, as well as the higher reliability in the CfA case.

With respect to completeness, the CfA pipeline performs slightly better than the Oxford pipeline, particularly in the hot star and SAP samples. Thus, Figure 4.20 provides the average completeness (and associated reliability in smaller text) from the CfA SAP and SS samples as a summary of the best we can do with *K2* C05 M67 data. The solar case is highlighted in red. The differences between the Oxford and CfA pipelines are rooted in the approaches each takes to produce corrected light curves from raw *K2* data. The moving apertures and deblending procedures during light curve preparation give the Oxford pipeline an edge in certain cases, especially with the SS, but the larger, more optimized aperture selection from the CfA pipeline is superior elsewhere. While the Oxford pipeline typically better removes systematics from strongly variable stars (see Section 2.6), most M67 targets won't be sufficiently

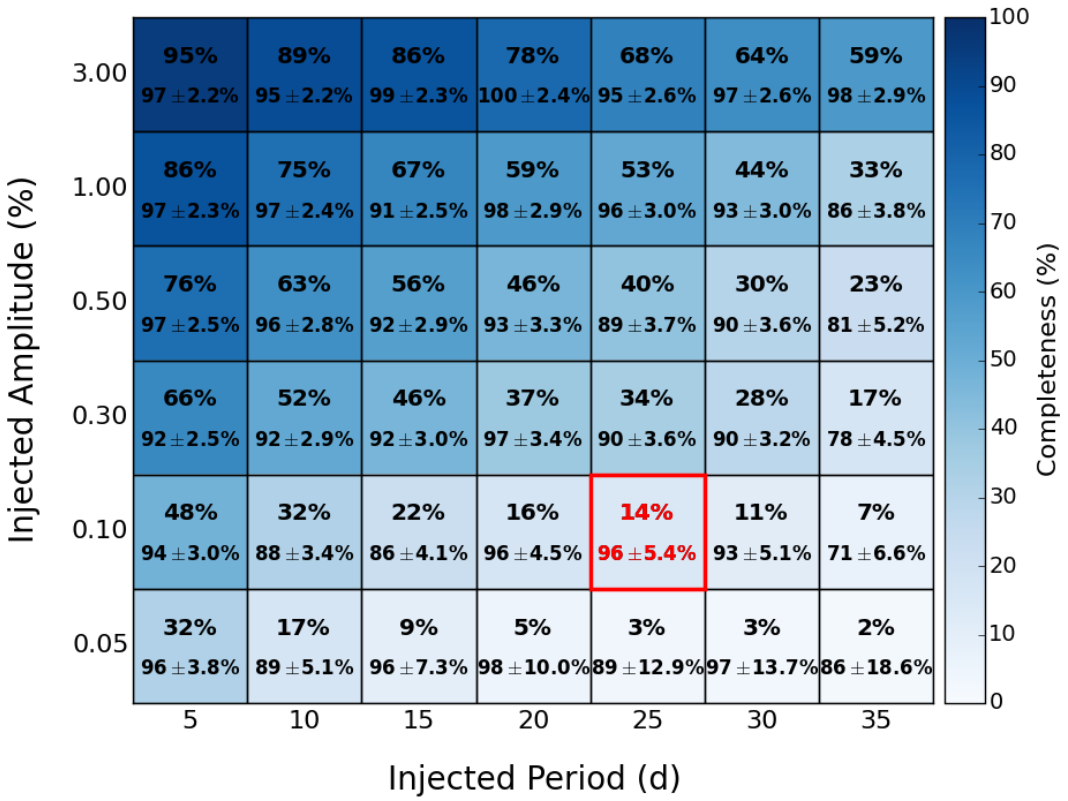

Figure 4.20: Average completeness (top number) and the roughly associated reliability (bottom number with uncertainty) for the CfA SAP and SS samples, with the solar case highlighted in red. The uncertainty for the completeness values is ±2.1%. Note that the reliability values do not perfectly match the injected amplitudes and periods but are representative of the ranges shown in Figure 4.17.

variable on short timescales, so the advantage is minimal. Finally, the more sophisticated PDC-MAP outperforms the relatively crude PCA in common-mode trend removal. While an ideal pipeline would combine the best elements of the the two, the performance of the existing pipelines is comparable, and both are valid options for an analysis of *K2* light curves. Most critically, however, for both pipelines, the solar case completenesss in the SAP and SS is at best ∼15%, illustrating just how difficult it is to detect 0.1% amplitude, 25 d signals in a single campaign of *K2* data.

4.7.5 Implications for *K2* M67 rotation studies

The injection test results indicate that measuring rotation periods for solar-like stars in M67 based on their *K2* light curves is challenging. Specifically, for the best case scenario of solar-like rotational variability — 0.1% amplitude, 25 d non-evolving sinusoidal signal — our completeness maxes out at 14% and 15% for the SAP and SS samples, respectively. Considering that detecting non-sinusoidal, evolving spot-modulation will be more difficult, these results suggest that both current and future rotation period measurements in M67, based solely on on campaign of *K2* data, must be carefully examined before they are used to guide stellar angular momentum evolution models and/or calibrate gyrochronology relations.

We consider the 20 stars with measured rotation periods from Barnes and those from Gonzalez where we had detections from either pipeline. Recall that all of these light curves come from the SAP sample. Since we do not have amplitude measurements for the versions of the light curves used in either paper, we estimated them by binning the flux of each light curve based on the reported period and taking the median of the difference between the 95^{th} and 5^{th} percentiles of each bin. We did this for both the Oxford and CfA versions of each light curve and averaged the values. We then estimated the completeness and reliability based on the corresponding SAP results from this study. We averaged the Oxford and CfA completeness for the injected period and amplitude bins closest to the determined values. If the calculated amplitude was halfway between the injected amplitudes, we used the higher amplitude bin. We also used the average Oxford and CfA reliability from the appropriately ranged bins into which the reported periods and estimated amplitudes fell.

The results are shown in Tables 4.1 and 4.2 at the end of this chapter. The completeness for the reported periods from Barnes is low, averaging at $\sim$27%, with only one period falling into a range above 50% (EPIC 211394185). The corresponding reliability is high, only dipping below 95% in one instance (EPIC 211397512). However,

these values are a bit misleading, since they only really apply to those cases where we would actually get a detection according to our criteria, i.e. using a threshold factor of $C = 4$. If we have a detection in an area with low completeness, then the result is generally trustworthy. Therefore, in Table 4.1, we also give the period for the corresponding, non-injected light curves from the Oxford and CfA pipelines where we had a detection based on our threshold (i.e. where the star was classified as a 'variable'). For this sample of stars, the Oxford pipeline only has 3 detections, while the CfA has 4. Almost all of these detections appear to be rough harmonics of the published result from Barnes, while the CfA period for EPIC 211423010 is close to the Barnes value.

Due to the low number of detections from either the Oxford or CfA pipelines, we wanted to see how much we would have to lower our detection threshold for the periods in the Barnes study to be counted as detections in both pipelines. The complete results from this test are given in Table A.13 in Appendix A. In most cases, the value of the threshold factor C had to be reduced to 2 or 1 for the measured period from either pipeline to be counted as a detection, which means the reliability falls considerably; the average Oxford reliability across the 20 stars is 65%, and the average CfA reliability is 61%. In addition, the Oxford and CfA periods still rarely match the published values (though in some cases they are harmonics), and they do not always match each other.

Returning to our results from using a threshold factor of $C = 4$, both the Oxford and CfA pipelines have detections for EPICs 211394185 and 211411621 from the Barnes sample. Figures 4.21 and 4.22 show the Oxford and CfA versions of these two light curves, respectively, along with the original and normalized periodograms in the middle and bottom panels, respectively. While obviously variable, a clear period is difficult to find by eye in either case, though it appears that the normalization suppressed any power at a period that would be comparable to the Barnes result.

The normalization step is important for avoiding false positives, however, as we have shown. We recognize that Barnes used several different period detection methods besides the standard Lomb-Scargle. However, the concern here is obviously the underlying signal, and the paucity of detections from the Oxford and CfA pipelines, as well as the lack of agreement with the Barnes result where we do have one, show just how challenging it is to measure solar-like signals in *K2* data.

In Table 4.2, we have a list of 18 EPICs from either the 'PDCSAP' or 'K2SC' samples given in Gonzalez where we had a detection from at least one of our pipelines. The average completeness is $\sim$60%, which is higher than the Barnes sample, and the reliability is $\geq$95% (except in one case, EPIC 211430648), but the stars listed here are only a small fraction of those published by Gonzalez. The PDCSAP sample in total has 98 reported periods; we detected 16 from this sample. The K2SC sample had 40 periods; we detected 9. In addition, notice that none of the stars in Table 4.1 show up in 4.2, meaning that of the 9 stars reported by Gonzalez that overlap with Barnes, neither the Oxford nor the CfA pipeline records a detection. However, as with the Barnes detections, the CfA and Oxford results agree with each other, and they are either in agreement with the Gonzalez value, or they are rough harmonics. The harmonics highlight ambiguity in the light curves, while the general lack of detections from the Gonzalez sample — especially where reported from Barnes — reinforces the conclusions we have already made about finding solar-like signals in M67.

We can use the completeness and reliability statistics from this work to guide future re-evaluations of M67 periods from *K2* data. Reliability establishes amplitude and period thresholds for detecting true signals in M67. We can probably trust detections in a measured period and amplitude bin with reliability of 80% or higher, suggesting that 1 or fewer out of every 5 measurements is likely to be unreliable. However, we need to take into account completeness, as we simply cannot say anything about the true number of stars with periods and amplitudes corresponding to a given

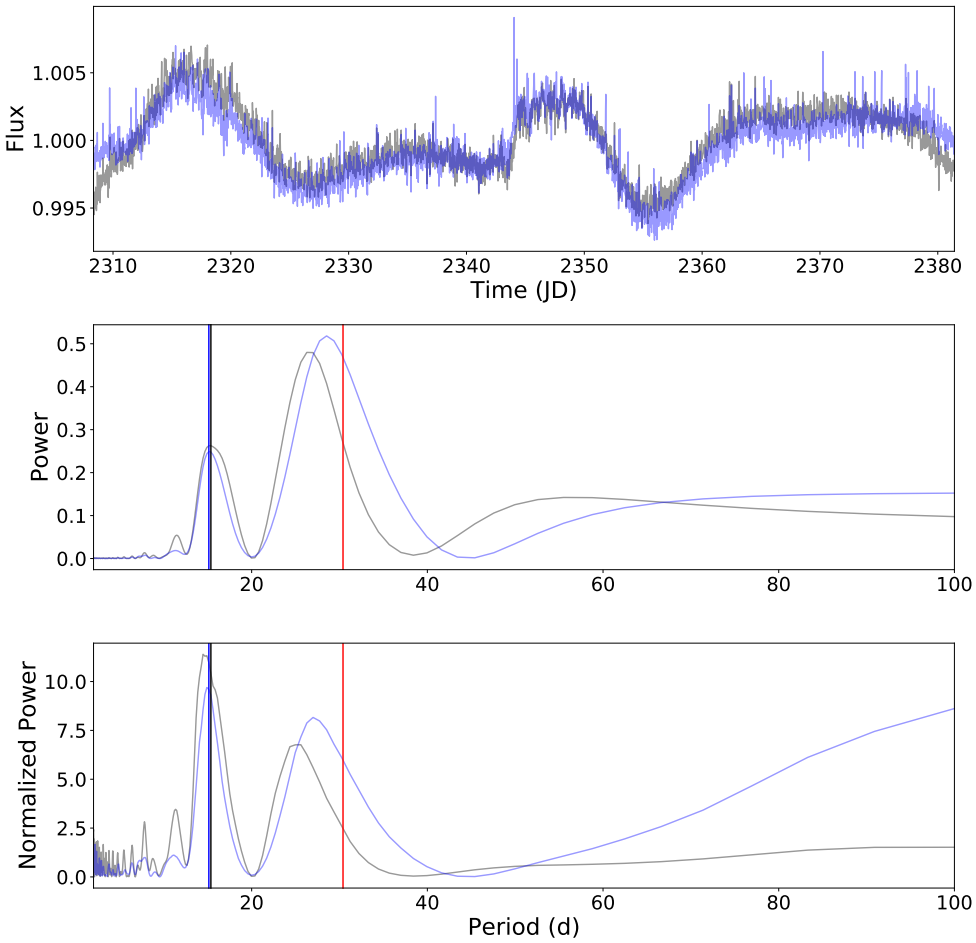

Figure 4.21: Light curves and periodograms for EPIC 211394185 from the Oxford (gray) and CfA (blue) pipelines. The top panel displays the light curves, while the middle panel gives the original periodogram power for both pipelines, and the bottom panel shows the normalized periodograms. In both periodogram panels, the black lines show the final Oxford period, the blue lines show the location of the final CfA period, and the red lines show the location of the period from the Barnes paper.

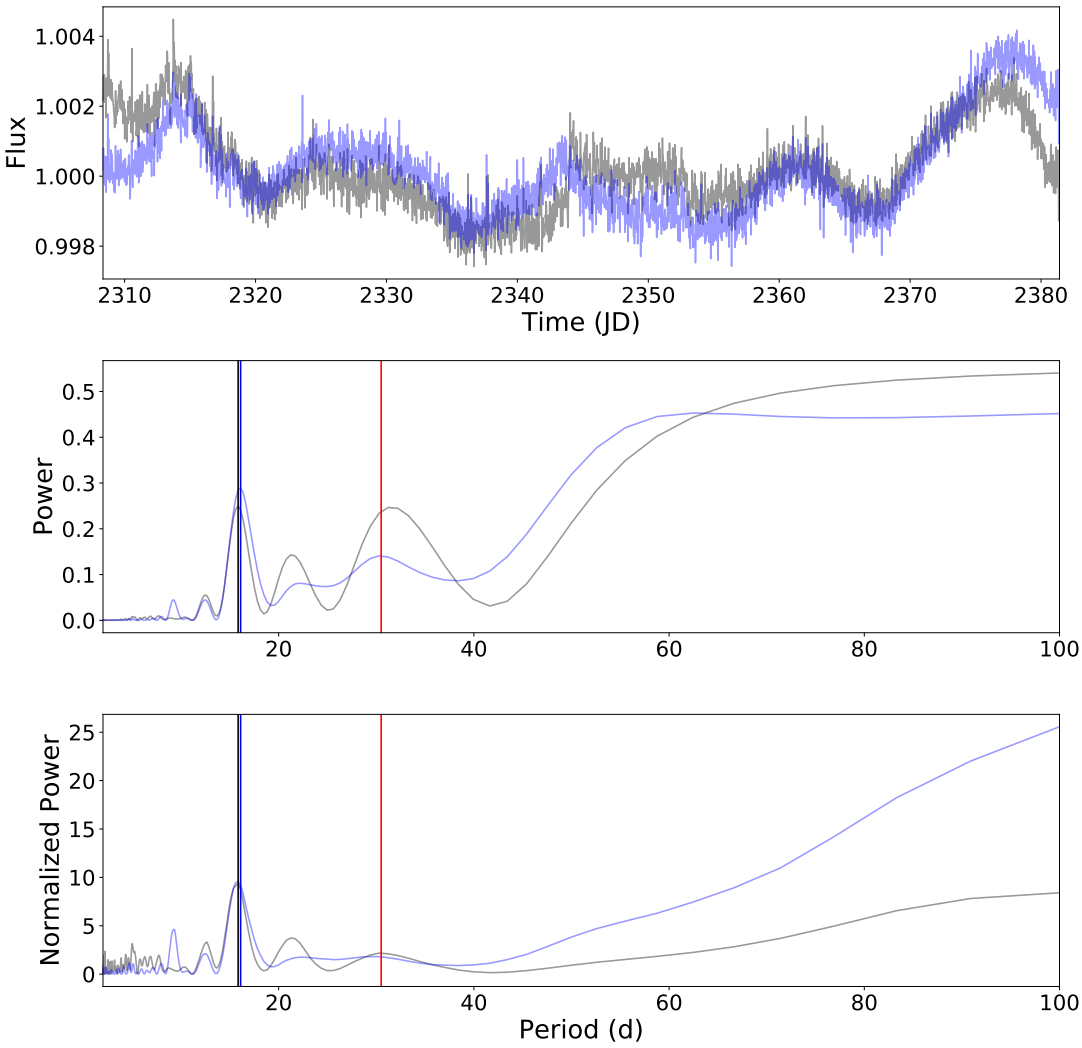

Figure 4.22: Same as Figure 4.21 except for EPIC 211411621.

bin without it; completeness tells us what fraction of potential detections we miss. For example, if we have three detections in a bin where the completeness was 50%, we know that we missed approximately 3 other stars in that range.

It is important to recall that these sinusoidal injection tests represent a 'best case' scenario: real rotation signals are non-sinusoidal and evolve over time, and both of these factors are likely to affect their detectability in a negative way. Therefore, although it is of course possible that better light curve extraction, detrending, and period search methods might be devised than those we have used here, it seems rather unlikely that the detectability of true rotation signals will improve much beyond what we have shown. In short, the *K2* C05 data may allow the measurement of some rotation periods for main-sequence stars in M67, but only if they are relatively active and display amplitudes somewhat larger than the active Sun.

4.8 Conclusions

Because of M67's immense scientific potential, we want to have a full understanding of the limits of the data we are using to measure this cluster's rotation periods. Though *K2* does have relatively high precision, especially compared to ground-based observations, the data still suffers from stubborn systematic features, and the $\sim$75 d observation window means that it will be challenging to identify periods of 25 d or longer, which we are expecting for a cluster the approximate age of the Sun. The crowded field will make this task even more difficult. It was the goal of this chapter to understand how these challenges manifest themselves so that we can ultimately acquire a set of M67 rotation periods in which we have confidence.

We devised a series of sinusoidal injection tests with real C05 data to determine our best-case sensitivity limits. We used the SAP light curves processed via the *Kepler* pipeline that fell on CCD module 6 (which encompassed M67), M67 mem-

bers contained in the superstamp, and a small set of hot A and F stars scattered throughout the C05 FOV as the three test samples. Into each raw light curve of each sample, we injected sinusoids with six different amplitudes ranging from 0.05% to 3.0% and seven periods ranging from 5 to 35 d. We separately processed the injected light curves using the Oxford and CfA pipelines. We defined a detection threshold and ran the Lomb-Scargle periodogram on the injected light curves and their non-injected counterparts, which we normalized by dividing out the median periodograms of the latter. Those non-injected light curves whose normalized periodograms met the detection threshold were marked as 'variable' and correspondingly removed from the injected samples. Finally, we analyzed the results of the period search on the remaining injected light curves in terms of completeness and reliability. Completeness describes our sensitivity in recovering the injected signals, while reliability quantifies how trustworthy a detected period is within a measured amplitude range.

The results of the injection tests shed light on the nature of the *K2* M67 data. The hot star samples from the Oxford and CfA pipelines highlighted the presence of non-astrophysical trends with power at ∼25 d and longer, a problematic feature given the periods we expect in M67, which necessitated periodogram normalization before the period search. In general, for three samples from both pipelines, completeness diminished as injected period increased and amplitude decreased. The hot star completeness was higher than the SAP and SS samples due to the brightness of the stars in the sample and the lack of rotational modulation beyond about 10 d for this particular dataset. However, for the SAP and SS from both pipelines, the completeness falls around or below 50% at injected periods of 20 d and amplitudes of 0.50%. Crucially, at the solar case — where the injected period is 25 d and the amplitude 0.10% — the maximum completeness is only ∼15% for the SAP and SS. Despite the generally low sensitivity, reliability is typically very high, consistently at values greater than 90%, except in the instance of very long periods (∼35 d) and a couple

cases at detected periods of around 15 d with moderately low measured amplitudes (0.075 – 0.25%). While it is very difficult to detect the kind of periods we expect to see in M67 given its age, if we do get a detection, we can generally trust the result.

The CfA completeness is generally greater than the Oxford pipeline in both the SAP and SS samples. Except at long periods and the ∼15 d range, the reliability for the SAP samples from both pipelines are comparable, but the Oxford reliability is slightly higher for the SS, despite amplitude suppression from the PCA. There is a slight trade-off between the two pipelines, and while the CfA performs marginally better overall, both are viable options.

It is important to understand how this study alters our understanding of both future and previously published studies regarding rotation periods in M67 from *K2* data. Overall, we urge caution when using the periods from Barnes et al. (2016) and Gonzalez (2016a) because we cannot reproduce the same results here without lowering our detection threshold and sacrificing reliability. However, we can use the injection tests as a basis for the re-evaluation of M67 periods. With completeness, we can quantify just how difficult it is to find even the best-case, long-period rotation signals in M67 data, or how many detections we may miss, while reliability gives us confidence in our measurement. To maintain some flexibility while still trusting the result, we decide on a reliability threshold of 80% for a given measured period and amplitude range.

We conducted this study specifically in the context of *K2* C05 M67 light curves, but the caution we have urged based on our conclusions can reasonably be extended to rotation studies with other *K2* campaigns and the upcoming, first data release from *TESS*. We have shown that long-term, systematic trends still exist in *K2* data which could skew low-amplitude period detections of about 25 d and longer, and these trends are likely to be present in other campaigns, especially in the crowded fields of clusters. Finally, while *TESS* will survey nearly the entire sky, the most coverage will

be along the Ecliptic poles as opposed to the Ecliptic itself, where observations will only last about 27 d (Ricker et al., 2014). While this will complement *K2* data, the short observation time and large pixel sizes (15 μm x 15 μm; Ricker et al. 2014) likely mean that the data will suffer from problems similar to those that we have seen in this study.

While we have gained in this chapter important insights into *K2* data, we have to remember that the sinusoidal injections present the best-case scenario. The rotational modulation in most stars does not usually take the form of a simple sinusoid. Therefore, in Chapter 5, we discuss applying some of the other approaches to detecting rotation periods beyond the Lomb-Scargle periodogoram, particularly the ACF and GP, which we described in Chapter 3. We also set out on smaller rounds of injection tests using more realistic signals, such as those generated from the star spot models of Aigrain et al. (2015b). Following this, we finally present our own rotation periods for M67 from C05 and the newly-released C16 data. In Chapter 6, we then apply — to the extent that we can — our periods to existing angular momentum evolution theory for main-sequence stars.

Table 4.1: Comparison with periods from Barnes et al. (2016)

EPIC	Barnes Per (d)	Amp (%)	Comp (%)	Rel (%)	Ox Per (d)	CfA Per (d)
211388204	31.8	0.32	21 ±1.8	96 ±3.9	–	–
211394185	30.4	0.78	55 ±1.8	98 ±2.3	15.4	15.1
211395620	30.7	0.47	32 ±1.8	95 ±3.1	–	–
211397319	25.1	0.31	29 ±1.8	98 ±3.2	–	–
211397512	34.5	0.73	34 ±1.8	68 ±4.1	16.4	–
211398025	28.8	0.29	21 ±1.8	96 ±3.9	–	–
211398541	30.3	0.51	32 ±1.8	95 ±3.1	–	–
211399458	30.2	0.66	32 ±1.8	95 ±3.1	–	–
211399819	28.4	0.31	21 ±1.8	96 ±3.9	–	–
211400500	26.9	0.30	29 ±1.8	98 ±3.2	–	–
211406596	26.9	0.36	29 ±1.8	98 ±3.2	–	–
211410757	18.9	0.14	11 ±1.8	99 ±5.8	–	–
211411477	31.2	0.20	21 ±1.8	95 ±11.9	–	–
211411621	30.5	0.30	21 ±1.8	96 ±3.9	15.8	16.1
211413212	24.4	0.22	29 ±1.8	97 ±8.0	–	–
211413961	31.4	0.26	21 ±1.8	96 ±3.9	–	–
211414799	18.1	0.17	11 ±1.8	99 ±5.8	–	9.0
211423010	24.9	0.29	29 ±1.8	98 ±3.2	–	22.2
211428580	26.9	0.33	29 ±1.8	98 ±3.2	–	–
211430274	31.1	0.40	32 ±1.8	96 ±3.9	–	–

The columns from left to right are EPIC, the associated period reported from Barnes et al. (2016), our estimate of the peak-to-peak amplitude for the light curve, the estimated completeness and reliability statistics based off the Barnes period and amplitude, and the Oxford and CfA periods where we have detections using $C = 4$.

Table 4.2: Comparison with detected periods from Gonzalez (2016a)

EPIC	Gonzalez Per (d)	Amp (%)	Comp (%)	Rel (%)	Ox Per (d)	CfA Per (d)
211387834	15.2	1.36	74 ±1.8	98 ±2.0	14.9	14.9
211390071	25.3	1.42	63 ±1.8	99 ±2.2	13.5	–
211393422	28.6	1.53	55 ±1.8	98 ±2.3	14.5	–
211397501	12.4, 12.4	1.19	81 ±1.8	98 ±1.9	12.2	12.5
211397955	29.0, 29.2	1.36	55 ±1.8	98 ±2.3	14.7	14.5
211400662	13.5	2.04	91 ±1.8	99 ±1.8	13.7	13.1
211403852	27.3	1.23	63 ±1.8	99 ±2.2	13.9	13.3
211404310	26.3	1.17	63 ±1.8	99 ±2.2	–	13.0
211405671	25.6, 28.2	2.06, 2.35	77, 76 ±1.8	98 ±2.0, 99 ±1.9	26.3	–
211407277	24.7	2.50	77 ±1.8	98 ±2.0	–	25.0
211408116	30.1	0.14	6 ±1.8	95 ±11.9	13.5	–
211408874	23.9, 24.5	2.12	80 ±1.8	98 ±2.0	–	23.8
211414974	26.8, 29.9	1.91, 1.92	63 ±1.8	97 ±2.1, 98 ±2.3	27.0	–
211424980	15.6, 31.2	1.26, 1.49	74 ±1.8	98 ±2.0, 98 ±2.3	15.6	15.6
211427666	28.8	1.20	55 ±1.8	98 ±2.3	14.1	–
211429354	25.9	0.19	8 ±1.8	97 ±8.0	–	26.3
211430648	32.6	0.67	16 ±1.8	68 ±4.1	–	17.2
211433352	13.7, 13.8	1.21	74 ±1.8	98 ±2.0	13.9	13.5

The columns from left to right are the EPICs from Gonzalez (2016a) where either of our two pipelines have detections, the associated periods reported from that paper, our estimate of the peak-to-peak amplitude for each light curve, the estimated completeness and reliability statistics based off the Gonzalez period and amplitude, and the Oxford and CfA periods where we have detections using $C = 4$. Where there is more than one reported value, the first number comes from the PDCSAP sample from Gonzalez (2016a), while the second number is from the K2SC sample.

Chapter 5

Finding M67 Rotation Periods with *K2* Data

Brewster Rockit by Tim Rickard

5.1 Introduction

The sinusoidal injection tests from Chapter 4 demonstrated just how difficult it is to find solar-like rotation signals from one campaign of *K2* data. In the best-case scenario where the stellar signal does not evolve and is roughly sinusoidal in shape, we can only detect, at a maximum, approximately 15% of the total number of stars with periods around 25 d and amplitudes of 0.1%. Nevertheless, we can utilize the lessons learned from the previous chapter to try to glean a list of rotation periods from M67,

both from C05 and the recent addition of C16 (released after we conducted the tests from Chapter 4). We have to be careful, however, because real, evolving signals will be much harder to accurately detect. This chapter is dedicated to the formulation of a procedure from which we can derive real *K2* M67 rotation periods. In Section 5.2, we perform a smaller round of injection tests with more realistic signals to compare the individual performance of the normalized Lomb-Scargle used in Chapter 4 with the implementations of the ACF and the GP discussed in Chapter 3. We then create an algorithm in Section 5.3 that combines all three rotation detection methods to produce periods from a single campaign of data; we apply this algorithm to C05 in Section 5.4. Section 5.5 describes the modification of this approach with the addition C16, an overview of which is given in Section 5.6. Finally, we delineate how we check for contamination in Section 5.7 before presenting our 'final' list of M67 periods in Section 5.8. These are the periods which we will take forward in our analysis of the angular momentum evolution of solar-age stars in Chapter 6.

5.2 Comparing the Lomb-Scargle, ACF, and GP

We employed a normalized version of the Lomb-Scargle in Chapter 4 to set a detection threshold and optimize the recovery of sinusoidal signals injected into *K2* C05 light curves. This was satisfactory for the purposes of those tests; by using un-evolving signals with known form, we revealed the best-case limits in rotation period detection from one campaign of *K2* data. While the normalized Lomb-Scargle, combined with a detection threshold, performs fairly well in this respect, it is worthwhile to explore both this technique and other rotation detection methods on more realistic signals.

We undertook a much smaller round of injection tests using a subset of the noise-free signals generated by the star spot model (SSM) from Aigrain et al. (2015b). These signals first model star spot emergence and distribution through parameters

for activity level (scaled to the Sun), activity cycle duration, and the minimum and maximum latitudes of spot formation (Aigrain et al., 2015b). The photometric signal, simulating 1000 d of observation, is then created by the flux modulation scheme of Aigrain et al. (2012), taking into account inclination, equatorial rotation period, rotational shear from differential rotation, and spot decay timescales (Aigrain et al., 2015b). Thus, they are much more realistic than the simple sinusoids from Chapter 4. We used SSM injections to compare the normalized Lomb-Scargle, ACF, and GP individually to uncover the strengths and weaknesses of each technique.

5.2.1 SSM Injection Test Set-up

The goal of this round of SSM tests is to compare rotation detection methods; we are not trying to find the absolute sensitivity limits like before. It would have been impractical at this stage to conduct these tests on the same scale as the sinusoidal ones because each SSM light curve is defined by many parameters, leading to a prohibitive amount of simulations. Therefore, we only use six stars from the Oxford SAP dataset as the basis for the injections: EPICs 211405988, 211425084, 211426069, 211428172, 211435338, and 211436917. These light curves have relatively low amplitudes (∼0.1–0.5%), and they are either 'flat' — meaning they do not exhibit strong variability, either from astrophysical or artificial sources — or they contain some bumps and wiggles which are more obviously systematic features but with not such large amplitudes that the injected signal would be completely overwhelmed.

Because we are most interested in solar-like signals, we restricted this round of SSM tests to periods of 20 d, 25 d, and 30 d and amplitudes of 0.1%, 0.2%, and 0.3%. The SSM light curves produced by Aigrain et al. (2015b) have fixed periods, however, and are not parameterized by amplitude but activity level. For each selected SSM signal, we first scaled the associated time array so that the period matched the one we wished to inject. To avoid distorting the original signal too much, we only looked

at those SSM light curves which had periods within ±5 d of the one we wanted to test. While this limited the number of usable SSM light curves, each 1,000 d signal is allowed to evolve quickly enough that one randomly selected ∼75 d segment (to roughly match the *K2* light curves; we interpolate the segment to the sampling of *K2* data) could look completely different from another randomly selected segment. Thus, we can use the same simulated light curve multiple times. We also had to scale the amplitudes by first estimating the 'raw' amplitude of each segment. Again, we binned the signal flux based on the period and took the median of the difference between the 95^{th} and 5^{th} percentiles of each bin. We then scaled the flux to the desired amplitude.

We also enforced criteria for spot evolution timescales and modeled differential rotation. With respect to the latter, we avoided those signals with differential rotation because the presence of multiple periods could skew the results of the tests, preventing us from properly comparing the normalized Lomb-Scargle (hereafter, simply referred to as 'the Lomb-Scargle'), ACF, and GP. In addition, we kept only those signals with spot decay factors of $\tau \geq 3$, which means that the spots evolve on timescales longer than three times the simulated period. This is not fully realistic, since the maximum observed sunspot lifetime is about a month, with the median falling on the order of days, and the Sun has a rotation period of about 25 d (Bradshaw & Hartigan, 2014). While not ideal, this is better than no evolution at all, and again, the purpose of these tests is to compare rotation period measurements, not find sensitivity limits. We injected each of the raw test EPICs 20 times for each test period and amplitude for a total of 1080 injections. An example of a light curve injected with a SSM signal is given in Figure 5.5, in Section 5.3. We detrended the test light curves with the Oxford pipeline because we do not have nominal access to the CfA pipeline, and the tests would not have gotten done in time.

5.2.2 Results and Discussion

We now present and discuss the results of this round of SSM injection tests. We did not utilize the MCMC at this stage. Figures 5.1 and 5.2 show the completeness and reliability for all three methods. In these figures, we have not enforced the detection threshold from Chapter 4 for the Lomb-Scargle; this decision will be discussed in more detail below. Figure 5.1 provides the completeness. Figure 5.2 merely illustrates reliability, though the actual values and their uncertainties can be found in Tables A.14 through A.17 in Appendix A. Here, the definition of completeness has slightly changed. Since we do not have a detection threshold, completeness states how often we get the correct period in a given injected period and amplitude bin; thus, it is now intrinsically linked with reliability.

With respect to completeness, both the Lomb-Scargle and the GP follow the same basic trend of decreasing sensitivity with increasing injected period and decreasing injected amplitude. The uncertainties on the completeness measurement for each bin ($\pm$9.1%) most likely account for where an individual bin does not follow the exact trend for these two methods, such as the Lomb-Scargle 25 d (11%) versus 30 d (17%) bin at an amplitude of 0.10%. While the overall Lomb-Scargle completeness is slightly higher than that of the GP across most period-amplitude bins, the GP has higher completeness for the solar case (25 d period, 0.1% amplitude) than the SSM Lomb-Scargle and either the Oxford (2 ± 2.5%) or CfA (18 ± 2.5%) SAP samples from the sinusoidal injection tests. The discrepancy between the SSM GP and the sinusoidal Oxford and SAP solar completeness probably arises from the limited number of basis light curves used for the SSM injections and the consequent lack of diversity relative to the sinusoidal samples. In addition, it should be noted that none of the methods in the SSM tests requires the phase match that was needed for a detected sinusoidal signal to be counted as valid. However, the difference in completeness between the GP and the SSM Lomb-Scargle highlights the potential of the GP for real signals.

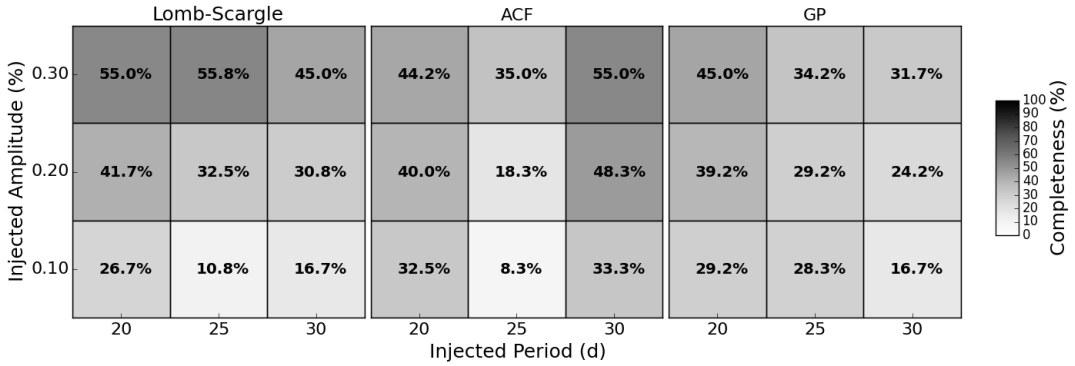

Figure 5.1: Completeness results for the Lomb-Scargle (left), ACF (middle), and GP (right) SSM injection tests without detection criteria. The uncertainties in all bins are ±9.1%.

Unlike the Lomb-Scargle and GP, the ACF produces very unexpected trends in completeness, at least at a first glance. While for a given injected period, the completeness decreases with decreasing amplitude, as expected, the ACF appears to have similar or even greater completeness across all amplitudes at injected periods of 30 d compared to the 20 d periods. An obvious drop in sensitivity also occurs at all three 25 d bins relative to the other two injected periods. The reason becomes apparent when looking at reliability in Figure 5.2: the ACF has the lowest average reliability and greatest number of measurements for periods ≥ 27.5 d. As seen in Table A.16, the ACF picks up 499 signals with periods longer than 32.5 d and amplitudes greater than 0.25%. The Lomb-Scargle, without detection criteria, has the next highest amount with only 71 measurements. Essentially, without a corresponding normalization step like the Lomb-Scargle or any sort of phase-matching criteria, the ACF is 'getting lucky' and really measuring long-term, systematic trends that happen to roughly match the period of the injected signal, making its completeness at longer periods appear to be greater than it actually is. Apart from the 30 d injected period bins, however, the ACF completeness is comparable to that of the GP except for injected periods of 25 d below 0.3% amplitude, where the GP performs better.

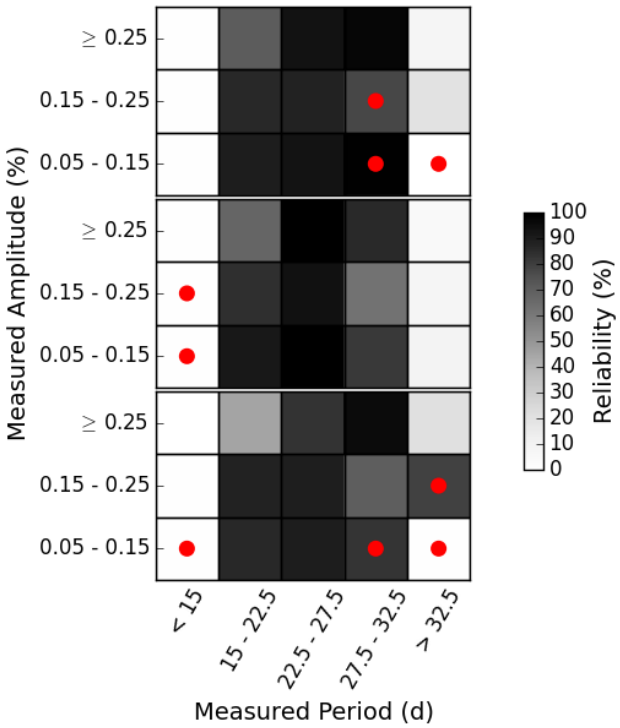

Figure 5.2: Reliability results for the Lomb-Scargle (top), ACF (middle), and GP (bottom) SSM injection tests without detection criteria. The red dots indicated measured period and amplitude bins where there were fewer than 10 detections.

Transitioning to reliability, we have already mentioned the untrustworthiness of the ACF at long periods. On the other hand, the GP and Lomb-Scargle are less reliable than the ACF for shorter periods. The GP and Lomb-Scargle, respectively, find 503 and 476 measurements with periods <15 d and amplitudes >0.25%, while the ACF only finds 76. For the Lomb-Scargle, this is likely due to harmonic measurements, and it is reasonable to believe that this may translate to the GP, since we also initialize the GP with the Lomb-Scargle result. However, the reliability of the three methods is roughly comparable, bin for bin, though the ACF has the highest average reliability for measured periods in the range of 22.5 – 27.5 d.

We now revisit the decision of excluding the Lomb-Scargle detection threshold. The effects of applying the detection threshold are shown in Figure 5.3, which provides the completeness for the Lomb-Scargle both with and without the threshold.

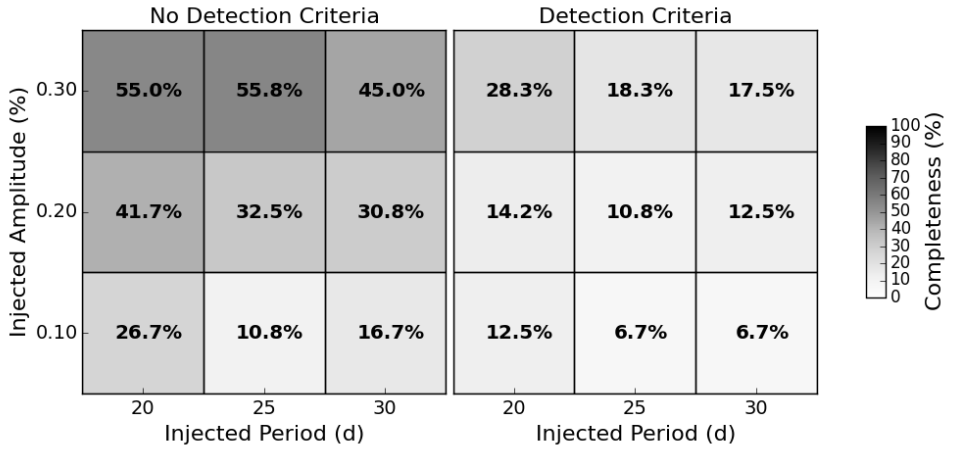

Figure 5.3: Comparison of completeness for the Lomb-Scargle without detection criteria (left) and with detection criteria (right).

Tables A.14 and A.15 in Appendix A provide the reliability for both cases, respectively. While reliability unsurprisingly increases almost across the board with the detection threshold, the completeness plummets. It is worth noting that while the uncertainty on the measured completeness is the same in each case at 9.1%, the uncertainties in the reliability values are very large due to the limited sample size. Therefore, it seems appropriate, in the case of realistic signals, to potentially sacrifice possible gains in reliability for a better chance at finding the signals in the first place. After all, the detection threshold is not optimal for non-sinusoidal signals, particularly in the presence of non-white noise. Throughout the period search, however, we can still keep track of whether or not a threshold applied to the Lomb-Scargle would have counted a specific measurement as a detection, without automatically discounting that measurement if the threshold is not met.

Yet, completely ignoring the detection threshold for the Lomb-Scargle is contradictory to the study conducted in Chapter 4. We judged the results from Barnes et al. (2016) and Gonzalez (2016a) on whether or not their measurements would have passed our detection threshold, and in many cases, we found that they would not.

The primary purpose of that study, though, was to demonstrate just how difficult it is to find rotation periods in a single campaign of *K2* data, and, in doing so, emphasize the need for caution and care when selecting a set of rotation periods for M67 from that data. Because the GP and the ACF sometimes perform better than even the Lomb-Scargle without any detection threshold, it makes sense to formulate an algorithm which takes into account all three methods in such a way that we can find periods with the appropriate amount of discretion.

5.3 Combining the Rotation Detection Methods

Using the results of the SSM tests, we developed an algorithm for finding rotation periods from one campaign of *K2* data. We first perform an initial period search with the Lomb-Scargle, ACF, and GP before filtering out more probable measurements to go through the MCMC and acquire uncertainties. Once we determine the initial measurements from all three methods, we filtered them with the following matching criteria, under the premise that a period is more likely to be accurate if different methods 'agree.' For a given period measurement:

1. If the ACF period is < 30 d:
   (a) the Lomb-Scargle and GP must both be within $\pm 20\%$ of the ACF, or
   (b) the Lomb-Scargle must be within $\pm 10\%$ of half the ACF, and the GP must be within $\pm 20\%$ of the ACF.
2. If the ACF period is > 30 d and there is a detection in the Lomb-Scargle:
   (a) the GP must be within $\pm 20\%$ of the Lomb-Scargle result, or
   (b) the GP must be within $\pm 10\%$ of half the Lomb-Scargle.

For the first set of criteria, we use the ACF as the basis for comparison due to its relatively high reliability in the 22.5 – 27.5 d period range combined with reasonable

completeness at 20 d periods. To avoid sensitivity dropping too low around the solar case, we do not enforce the Lomb-Scargle detection threshold in this case, but it still must match the ACF. In general, the Lomb-Scargle and GP must be within 20% of the ACF, but the Lomb-Scargle is particularly prone to harmonic measurements. Therefore, we accept those periods which are harmonics of the ACF, but put a small penalty on them by restricting the harmonic measurements to within only 10% of half the ACF. We do not include a harmonic measurement of the ACF with respect to the GP in this case because we are assuming that if the Lomb-Scargle produces a harmonic value of the ACF, the ACF is more likely to be correct, and the GP's flexibility in modeling will settle on the 'true' value.

We have shown, however, that the ACF is not very reliable beyond periods of about 30 d because it tends to pick up on long-term systematic features. In this case, we do not utilize the ACF result at all in selecting which measurements are run through the MCMC. Instead, we compare only the GP and the Lomb-Scargle. Because we have taken the ACF out of the matching process, we do enforce the Lomb-Scargle detection threshold. This increases the likelihood that a long-term period measurement from the Lomb-Scargle is legitimate. Again, the GP must be within 20% of the Lomb-Scargle. This time, we do accept those rare cases where the GP is half the Lomb-Scargle, still imposing the 10% penalty.

Once we have matched all the rotation periods, we run the measurements through the MCMC to obtain uncertainties. The MCMC often adjusts the GP period, sometimes by only a day or two and other times by a significant percentage, because the period found by the GP may be in a local minimum — and not the global — with respect to the likelihood. In practice, when applying our matching algorithm to real data, we accept those final periods that are within 20% of the original GP period. This means our approach is very conservative; it relies heavily on both the GP and final MCMC result both having a 'reasonable' value for the period, i.e. one that

matches the other two methods. The GP does not function here as an independent recovery method. We put a lot of emphasis on the ACF and Lomb-Scargle, but they are only useful if we obtain uncertainties from a GP output that roughly matches. Using the matching criteria on the SSM injection tests from above results in 186 periods out of 1080 to be fed into the MCMC.

A comparison of the 'matched' periods both pre- and post-MCMC can be seen in Figure 5.4. This figure plots the injected versus detected periods from both the GP (in blue) and the MCMC (in green). The shaded gray area represents the ±20% 'valid' region. We draw three main conclusions from this figure. First, in general, the reliability of our algorithm appears to be fairly high; most of the measurements fall within the valid region. Second, where the points are less reliable, they tend to cluster around 10 – 12 d for injected periods of 20 d and are scattered between about 10 d and 22.5 d for injected periods of 30 d. These features are most likely due to the characteristics of the basis light curves into which the signals were injected. Most of the erroneous short-period measurements come from low-amplitude (0.1%) injections into EPIC 211436917, where there is a noticeable break in the data, possibly exacerbated by the PCA. This is illustrated in Figure 5.5, where the Oxford-corrected, non-injected light curve is shown in blue, the injected SSM signal is in green, and the detrended, injected light curve is in orange. The break in the data, further distorted by the injected signal, fools the GP into thinking the period is shorter than it actually is. Finally, the MCMC does not appear to change the GP value too often (evidenced by the green points drowning out the blue near the one-to-one line), and if it does, the shift is minor. The cluster of green points between 10 d and 15 d at injected periods of 20 d is the exception. These measurements are probably caused by artificial features in the data, such as the break previously mentioned in EPIC 211436917.

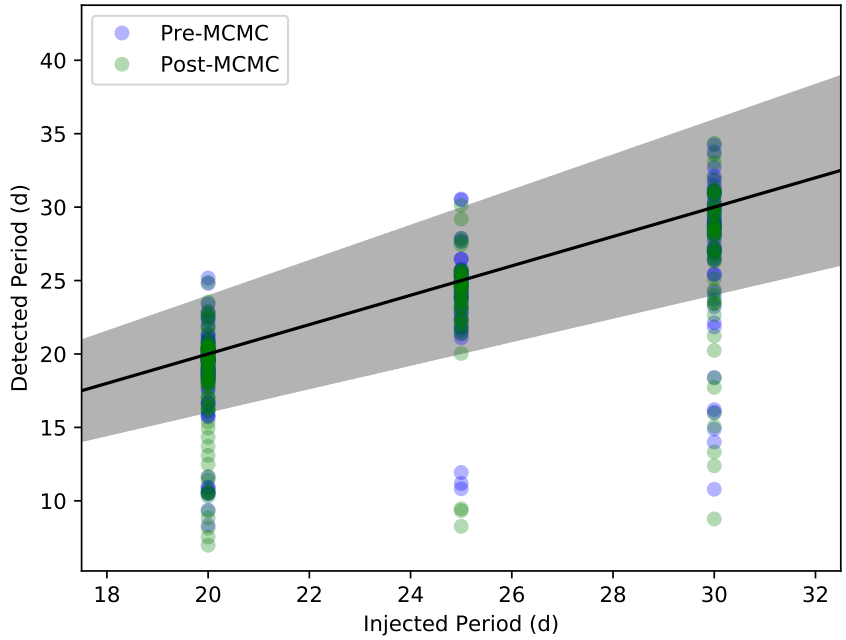

Figure 5.4: Injected versus detected SSM 'matched' periods from the GP pre-MCMC (blue) and post-MCMC (green). We do not show uncertainties in this plot because of the substantial overlap of datapoints.

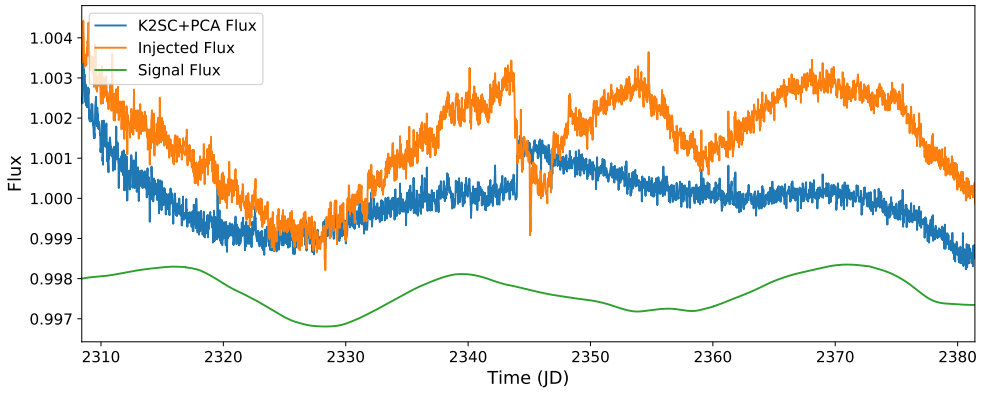

Figure 5.5: Example SSM injection for EPIC 211436917. The K2SC and PCA-corrected version of the non-injected light curve is given in blue. The injected 30 d, 0.1% amplitude signal is shown in green, and the fully-corrected injected light curve is in orange. This figure illustrates the break in the data — likely exacerbated by the PCA — which can lead to anomalous period measurements.

5.3.1 Evaluation of Combining Methods

There are clearly many issues with this combination method. As previously mentioned, this approach is very conservative. We removed the Lomb-Scargle detection requirement if the ACF period is less than 30 d to help preserve completeness, but generally requiring three of the methods (or their harmonics) to match is still very strict. Out of 1080 injections with known signals, we only recover about 17% across periods ranging from 20 – 30 d and amplitudes of 0.1 – 0.3%. This is discouraging, but the systematic difficulties combined with the intrinsically low-amplitude, evolving signals in the real light curves necessitate a strict approach when working with a single campaign of *K2* data, especially in light of M67's importance.

Another problem stems from the fact that the GP is completely dependent on the ACF and Lomb-Scargle, and we judge its final validity in relation to the other two methods. This seems circular, but for now we are using the GP to confirm the ACF and Lomb-Scargle periods and get uncertainties. Ideally, we want to separate the GP from the ACF and Lomb-Scargle so that it can independently arrive at the best-fit period. A possible solution is the creation of a 'GP periodogram,' by which we initialize the GP with a grid of periods spanning a given range. Each period is then 'frozen,' i.e. we fix the period at its input value and optimize the rest of the parameters to produce a likelihood for that period. The likelihood is the 'power,' and the period with the greatest likelihood can then be run through the MCMC to get uncertainties. This approach requires the use of `celerite` over other GP tools, such as `george`, due to the computational expense of testing a suitable range of periods.

We did attempt a GP periodogram on a set of SSM injections, but using the likelihood as the power proved to be unwise. The GP is so flexible that, even with fixed periods, it will find comparable likelihoods from optimizing the other parameters. This can be seen in Figure 5.6, where we computed the GP periodograms, shown in the bottom panel, for the two simulated light curves in the top panel. The example

light curves include one with a clear, 20 d SSM signal in blue and another with a less obvious, systematic-ridden, 30 d signal in orange. In both cases, the likelihood appears to plateau, with little variation at all test periods. The drop-off in likelihood at short periods in both periodograms indicates that the GP is conducting fewer independent tests in this region of parameter space. Therefore, in the future, we would like to test different ways of computing GP periodograms that do not rely on the likelihood as the power statistic.

More work on finding the optimum period detection method from a single set of *K2* campaign data clearly needs to be done. For example, we can probably relax some of the matching criteria, such as counting a GP measurement that is twice either the ACF or Lomb-Scargle result, or only requiring two of the three methods to match. We do not currently do the former because the GP is capped at a 40 d period, based on the 75 d observation window, to prevent it exploring periods which we will have no way of confirming by eye. Thus, this only becomes a problem if the ACF is less than 20 d, although we have shown that this method has fewer erroneous measurements in this regime (see Figure 5.2). In cases where the ACF is greater than 30 d and we are comparing the GP with the Lomb-Scargle, we put our trust in the Lomb-Scargle result because the detection threshold must have been passed. While it is true that the Lomb-Scargle, even where there is a detection, may be a harmonic, the GP is initialized with both the Lomb-Scargle and the ACF, and the greatest likelihood GP period may have been found using the less reliable, longer ACF result.

Finally, because we put so much emphasis on the (in)validity of the ACF, it would be prudent to either attempt an analogous normalization step that we use with the Lomb-Scargle, or implement a detection threshold specific to the ACF. This has already been explored by McQuillan et al. (2014), who based the selection of *Kepler* rotation periods off of relative peak heights and effective temperatures. We have not yet tried this due to time constraints. Using an ACF with a detection threshold,

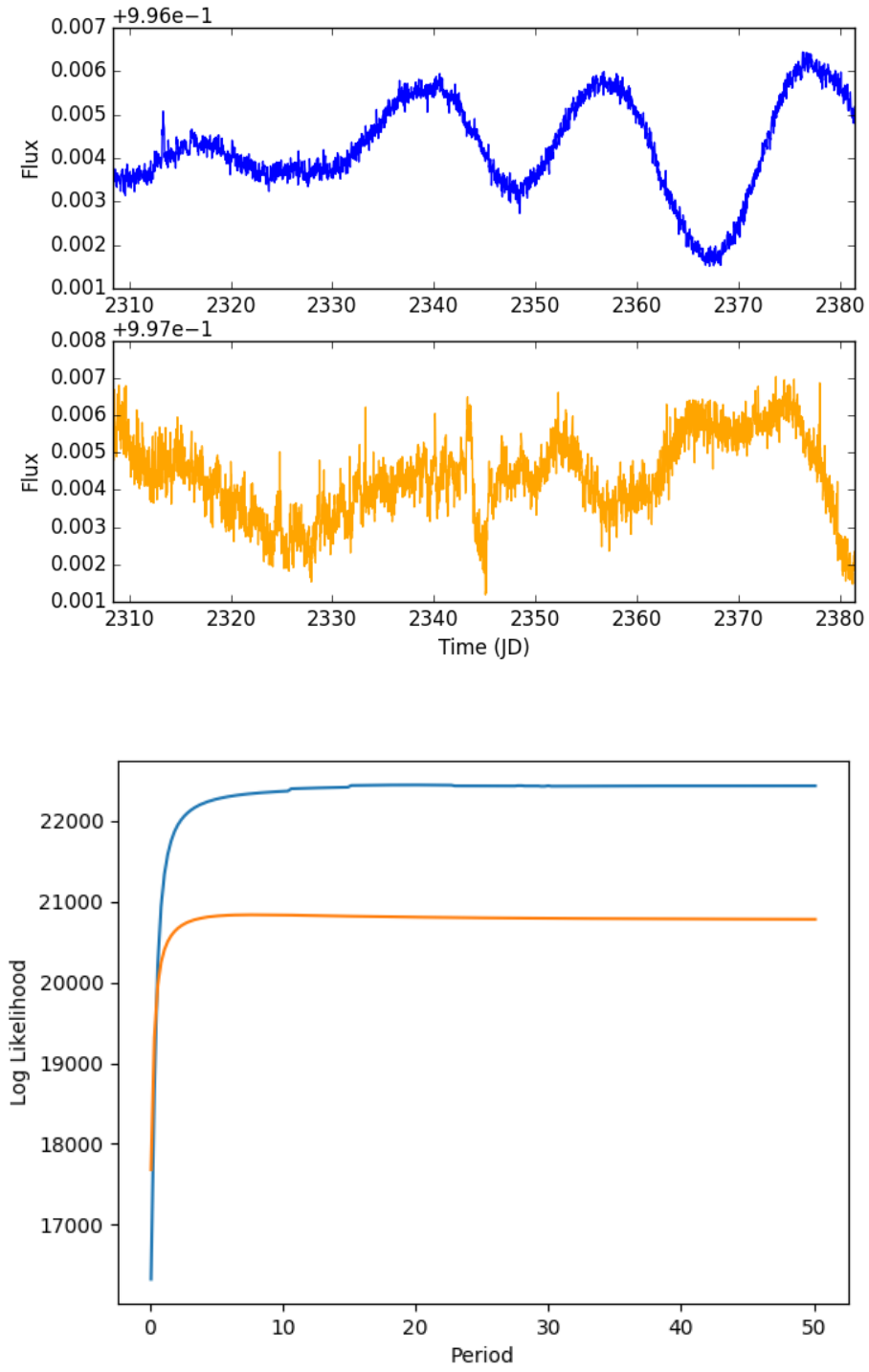

Figure 5.6: GP periodogram examples (bottom panel) for two simulated light curves (top panel): one with a clear 20 d injected SSM signal (in blue) and one with a less obvious 30 d injected signal (in orange).

however, would reduce the need to match with the Lomb-Scargle, since we would have more confidence in measured periods greater than 30 d.

5.4 C05 Rotation Periods

For the most part, we used the combination of methods outlined above to derive rotation periods for M67 from *K2* C05 data. After getting the final list of 'matched' periods following the MCMC, we further filtered the measurements based on M67 membership status, possible contamination from other stars (see Section 5.7), and whether or not we believed the final measurement when checking the light curve by eye. In an ideal world, we would not have to confirm by eye because this is not 100% reproducible, but the presence of systematic features in the *K2* data with power at periods we expect to find necessitates that we do. With respect to membership status, we keep those stars designated as single members (SM), binary members (BM), or binary likely members (BLM) in the Mathieu catalog. The determined periods and their uncertainties can be found in Table 5.1 in those rows where there is only a '5' under the campaign column. This table also indicates if the star to which each period belongs was from the SAP or SS dataset, what type of member it is in M67, and the output Lomb-Scargle and ACF periods. The associated light curves can be found in Appendix B.

For the majority of matched periods, we used the initial quality factor values given in Chapter 3, i.e. $Q_{1,0} = 7.5$ and $Q_{2,0} = 0$, when computing the GP. However, the GP sometimes missed obvious periods that the Lomb-Scargle and ACF easily found. We were often able to recover those periods using $Q_{1,0} = 4$ and $Q_{2,0} = 4$, though the exact cause of this is unclear. Putting the harmonic quality factor on par with the primary may allow the GP to better explore the parameter space; this could be related to the low likelihoods observed at short periods in the GP periodogram. In

the future, we will test the effects of initializing the GP iteratively with a range of values for each of the quality factors, or their ratios.

We compared our periods with those detected by the Lomb-Scargle in Barnes et al. (2016) and Gonzalez (2016a) in Chapter 4, as well as our preliminary list from Chapter 3. Most of the Gonzalez periods which we believed did not belong to confirmed members. We did miss a couple possible periods because our matching algorithm was too strict, but in most of these cases, the period was not particularly clear, anyway. Other times, the star in question appeared to be rotating so rapidly ($P < 1$ d), that either the GP modeled the signal merely as noise and found a long-term, systematic trend instead, or our algorithm missed it because of the Lomb-Scargle's period search limits. Sometimes, the GP output was simply wrong when either the Lomb-Scargle or ACF was likely correct. In these cases, we tried adjusting the initial quality factors, as above, or applying a low-pass filter in the cases where the GP may have been picking up on high-frequency systematics (on the order of $\sim$5 d) instead of the longer astrophysical signal. Finally, there were some light curves which appeared to have long-term variability, but the true period was too ambiguous when looking at just one campaign of data. We revisited these particular EPICs where there was overlap between C05 and C16 data (discussed below).

5.5 Testing the Addition of a New Campaign

Where the C16 (and eventually C18) overlaps with C05, we can be less stringent in conducting a period search under the assumption that more data will help remove some of the ambiguity surrounding long periods. This is where the GP really becomes important; we can run the Lomb-Scargle and ACF separately for each campaign and then fit the GP simultaneously to both campaigns, initializing it several times based on the different ACF and Lomb-Scargle results. If the Lomb-Scargle or ACF

from one campaign matches the corresponding measurement (or its harmonic) from the additional campaign, we do not initialize the GP separately for that particular method. Instead, in the case of the Lomb-Scargle, we add the periodograms together and use the top two peaks to initialize the GP. For the ACF, we interpolate the ACF of each campaign to the same grid (as there could be subtle differences in the lag array) before adding them together. Again, we initialize the GP using up to two of the greatest peaks. If the GP period for any of the initializations is considered periodic (recall that either Q_1 or Q_2 must be greater than $1/\sqrt{2}$), it is fed through the MCMC; otherwise, it is disregarded. The output MCMC period with the greatest likelihood after all realizations of the GP is then selected as the final period.

We tested this new method with another round of SSM injection tests using periods of 10 d, 20 d, and 30 d and amplitudes of 0.1%, 0.3%, and 0.5% to give a slightly broader scope for the period search. We created two 'campaigns' of data by copying the raw flux from one of the six basis light curves and creating a new time array beginning about 2.6 yr after the start of the first campaign (to match the separation between C05 and C16). We used the same selection criteria for the SSM light curves as before, but this time we cut two random segments from the same signal to inject separately into each campaign, simulating the evolution of star spots. For each period-amplitude combination, we injected each of the six test EPICs five times for a total of 270 injections. An example of EPIC 211405988 injected with a 20 d, 0.1% signal is given in Figure 5.7. The GP predictive model is given in red. These injection tests suffer from the same shortcomings as the single-campaign SSM tests, i.e. the small sample size and the limited number of basis light curves, but to a greater extent.

We ran the test light curves through two different versions of the GP. The first used $Q_{1,0} = 7.5$ and $Q_{2,0} = 0$, while the other used $Q_{1,0} = Q_{2,0} = 4$. Figure 5.8 shows the completeness for each scenario. Within each injected period bin, the completeness declines with decreasing amplitude, but we do not see completeness fall with increas-

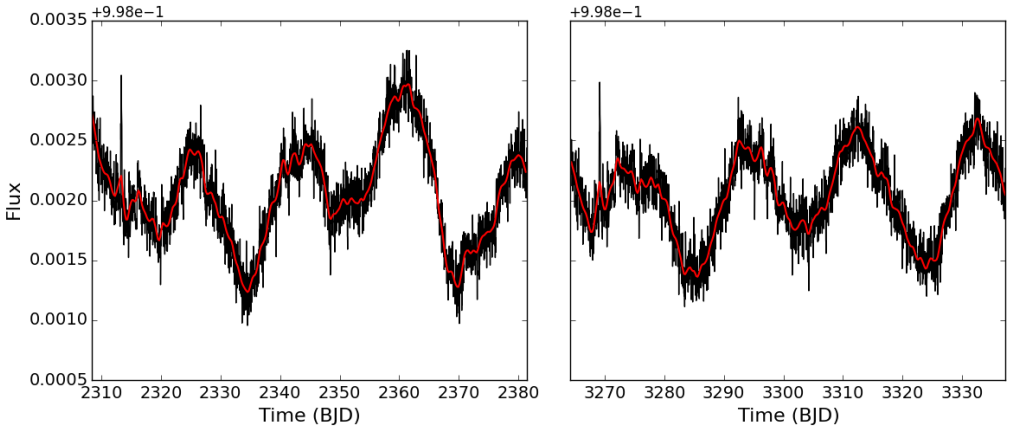

Figure 5.7: Example of EPIC 211405988 injected with a 20 d, 0.1% signal covering two 'campaigns' and modeled with a GP, shown in red.

ing period. Rather, the completeness peaks at 20 d, and while it drops again at 30 d, it remains greater at 30 d than 10 d across most amplitude bins. The uncertainty on the measured completeness in each bin is ∼18.3%, which could partially explain this result, especially in the second scenario. The peak at 20 d in the first scenario, however, may indicate something about the GP's performance with an additional campaign. If the two campaigns have similar systematic features, the GP may be pick up on those instead of the actual signal, analagous to how the ACF is prone to anomalous periods longer than 30 d. With two campaigns, the systematics may be reinforced and hold more weight. If this was the sole cause, however, we should see even higher completeness in the 30 d range. This may help explain why the completeness is higher at 30 d than 10 d, but the peak at 20 d suggests that features specific to the six basis light curves may be the most significant factor.

To understand what may be going on, Figure 5.9 shows the detected versus injected periods for the GP initialization at $Q_{1,0} = 7.5$ and $Q_{2,0} = 0$. From left to right (and blue to yellow), the plots show measurements for the 0.1%, 0.3%, and 0.5% injected amplitudes, respectively. The gray regions represent the ±20% valid region, while the light gray lines display the double and half-period harmonics. At

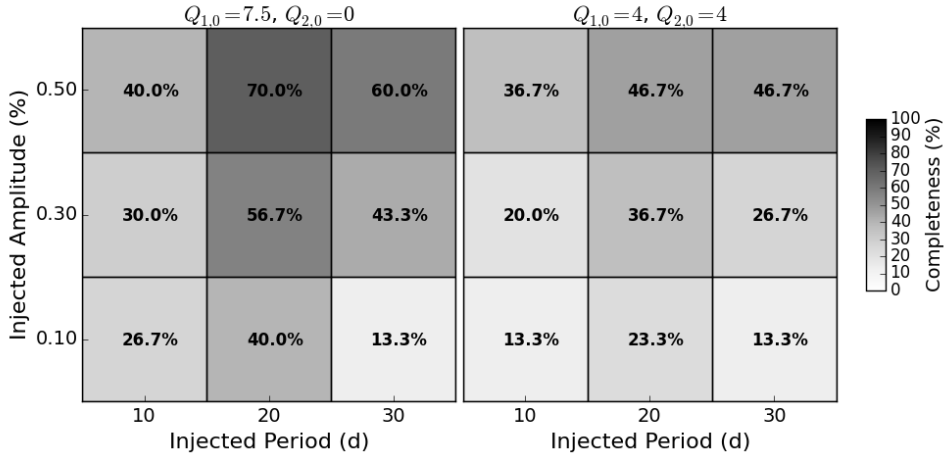

Figure 5.8: Completeness for SSM joined C05 and C16 simulations with GP initializations at $Q_{1,0} = 7.5$, $Q_{2,0} = 0$ (left), and $Q_{1,0} = 4$, $Q_{2,0} = 4$ (right). The uncertainty in each bin is $\pm 18.3\%$.

0.5%, our method works fairly well; the invalid points tend to be concentrated close to the harmonic values. The same is generally true of the 0.3% periods, though the invalid measurements show more scatter. Unsurprisingly, the number of invalid measurements and scatter is greatest at amplitudes of 0.1%. Concentrations between 11 d and 15 d in all three plots are likely due to EPIC 211436917, as before. The behavior at injected periods of 20 d is not too different from that of the other two injected periods. Therefore, if the GP is preferentially picking up on 20 d periods, it may be due to systematics in the basis light curves, as previously suggested. This effect is clearly not as strong in the second scenario, emphasizing the GP's sensitivity to the initial parameters.

At a glance, Figure 5.8 is encouraging because it shows that we can significantly increase our sensitivity to signals of $\sim$20 d and greater with the addition of another campaign. Our sinusoidal injection tests for a single campaign of data showed that, at best, we could only achieve 46%, 37%, and 16% completeness at 20 d for amplitudes of 0.5%, 0.3%, and 0.1%, respectively. Another campaign with realistic signals means we can potentially achieve up to 70%, 56.7%, and 40% for the same amplitudes.

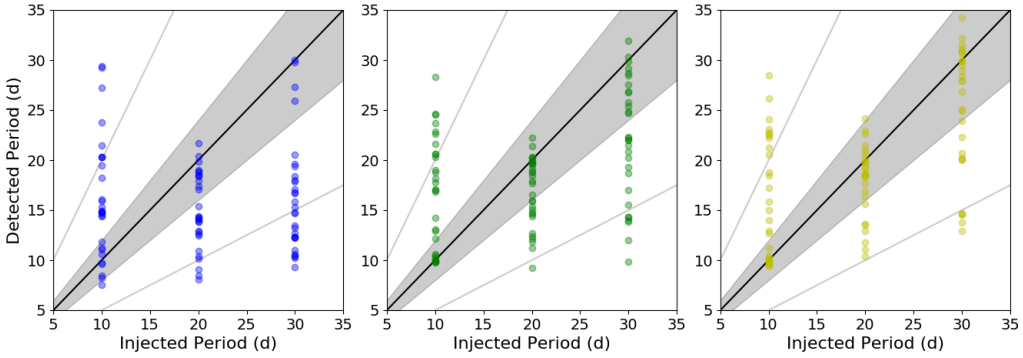

Figure 5.9: Injected versus detected MCMC periods for the two-campaign SSM injection tests. The blue points have injected amplitudes of 0.1%, the green have amplitudes of 0.3%, and the yellow have amplitudes of 0.5%. We do not show uncertainties in this plot due to the overlap of datapoints. The valid region is represented by the gray shaded area, while the light gray lines show the double and half-period harmonics.

Or, at worst, we may measure similar completeness, though with signals that are much harder to detect than sinusoids. However, we have discussed that this greater completeness could actually be the result of common, systematic trends in the light curves, which would be problematic. Furthermore, Figure 5.9 highlights the fact that periods found by this method should be double-checked by eye to ensure the GP is finding astrophysical variability instead of systematics. Finally, we need to keep in mind that these SSM tests are very limited in scope and are biased with respect to the basis light curves.

5.6 C16: A Quick Look

K2 C16 was conducted from 7 December 2017 to 25 February 2018.[1] The calibrated, raw C16 data was made publicly available from MAST on 29 May 2018. Thus, we did not have a lot of time to spend on processing and correcting the data to use in this thesis. However, we were able to fully process the C16 superstamp using the

[1] https://keplerscience.arc.nasa.gov/k2-fields.html

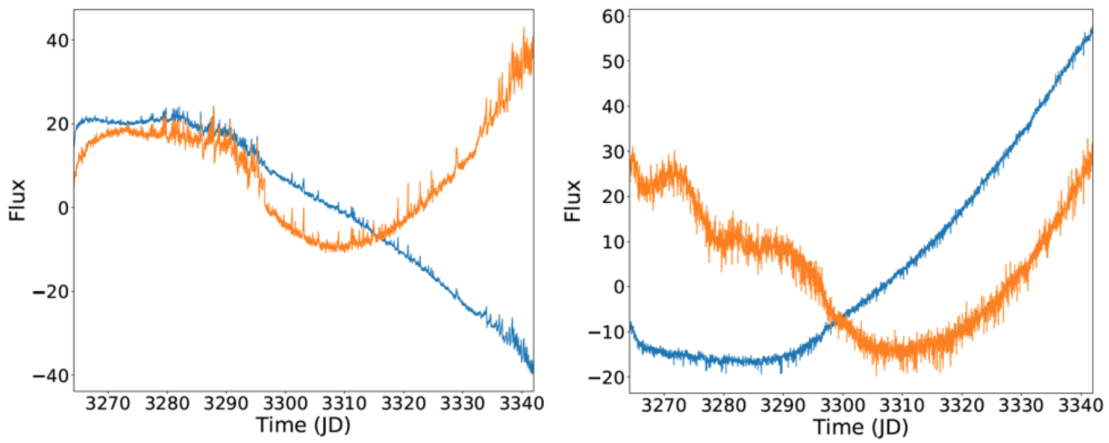

Figure 5.10: Principal components for the C16 SAP (left) and superstamp (right) datasets. The primary trends are in blue, while the secondary trends are in orange.

Oxford pipeline, and we used light curves processed by the CfA pipeline (courtesy of Andrew Vanderburg) for the SAP dataset, minus PDC-MAP (which needs to be done through NASA Ames and takes awhile to run). Instead, we used the PCA for long-term, common-mode corrections on the SAP sample. The PCAs for the C16 SAP and SS datasets can be seen in Figure 5.10; both used thresholds of 7.5% to produce two principal components. They are generally similar in shape to the C05 PCs, but they are less smooth, i.e. there are more artificial features in the C16 light PCs than the C05 ones, particularly in the first 30 d. There is not 100% overlap between C05 and C16, as M67 was monitored at the edge of the *Kepler* FOV in C16. The C16 SAP dataset contains 459 light curves, 404 of which were also observed in C05. In the superstamp, we extracted 928 light curves with astrometric solutions that matched the Mathieu catalog. Of these, 735 had matches in C05.

To calculate the scatter, we used the variation of MAD from Equation 2.3 in Chapter 2. The scatter for the extracted and fully-detrended light curves of each C16 dataset is plotted in red in Figure 5.11, with the SAP on the left and the SS on the right. The C16 SAP scatter is plotted over the final scatter from the C05 CfA

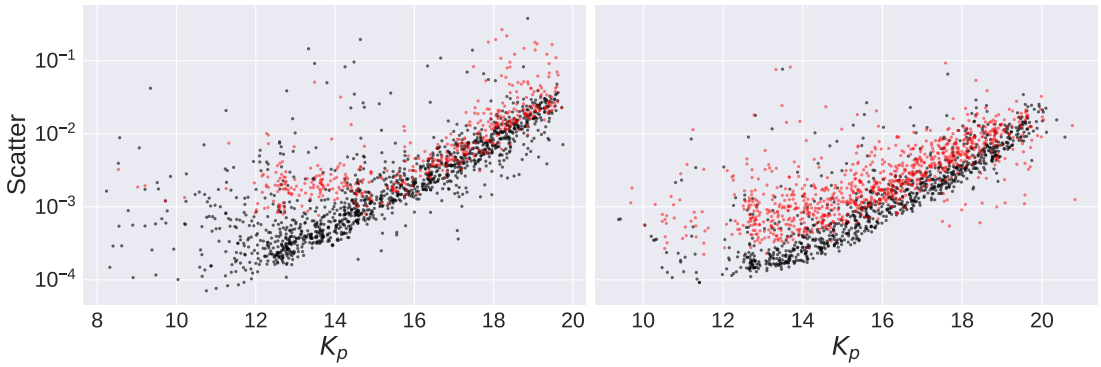

Figure 5.11: MAD scatter for the C16 SAP (left, red) and superstamp (right, red) datasets. The C05 scatter from the CfA SAP and Oxford SS are given in black in the left and right plots, respectively.

SAP dataset, in black, as a comparison, while the SS scatter is plotted over the final C05 Oxford SS scatter. We cannot make an exact comparison between the C05 and C16 scatter for the SAP, since the common-mode trend removal is different in each case, but we know that the PCA, in general, is worse than PDC-MAP. The SS data, however, was extracted and processed in the same way as the C05 Oxford SS, so the comparison is more direct. The final C16 SAP scatter at $K_p = 12$ is 1135 ppm, while the final SS scatter is 544 ppm.

Overall, the precision of the C16 light curves is about 2 – 3.5 times worse than C05. In the case of the SAP dataset, this could be due to the smaller sample size, but it is also likely that the systematics have gotten worse in C16. The mixture of the CfA pipeline with the less optimal PCA could play a role, but the increase in SS scatter is more indicative of systematics. Andrew Vanderburg removed a 5 d segment from the SAP light curves towards the end of the campaign due to the spacecraft drifting for an unusually long amount of time (i.e. beyond the 6 hr thruster firings), which the CfA pipeline is not designed to model. The PCs from C16 also indicate the presence of troublesome trends in the first 30 d of observation which may not be perfectly removed in each individual light curve. As an example, Figure 5.12 displays the C05 (left

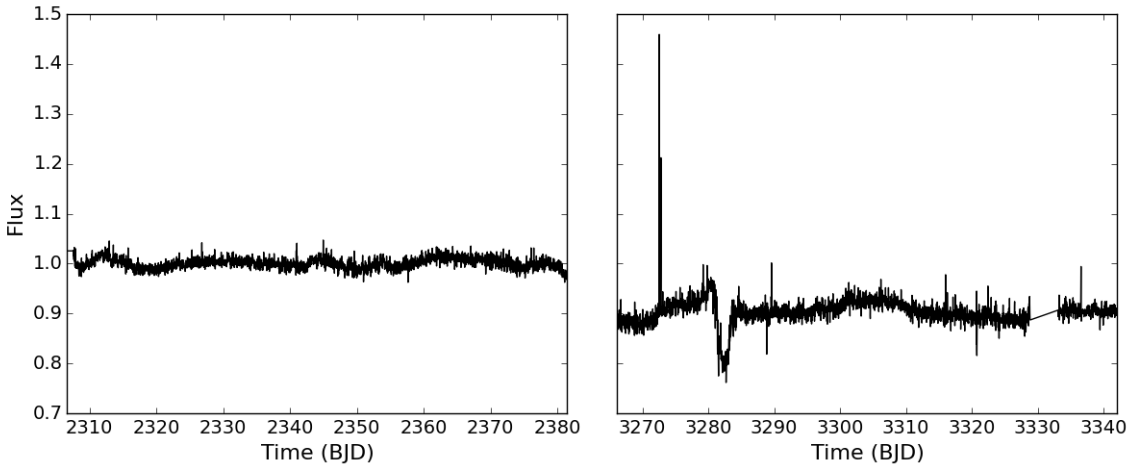

Figure 5.12: Light curves for EPIC 211402511 from C05 (left) and C16 (right).

panel) and C16 (right panel) light curves for SAP EPIC 211402511. It is clear that the systematics have changed since C05, evidenced by the large, non-astrophysical dip early in the C16 light curve. The C16 light curve is also slightly noisier overall than its C05 counterpart, and the outliers have not been as well-corrected.

Despite the decreased precision of the C16 light curves, two campaigns of data are still better than one, and we can use the techniques described above to add to the list of rotation periods gleaned from C05 alone. Since we found in Chapter 4 that the CfA pipeline is overall slightly better than the Oxford pipeline, it may be worthwhile to redo the period search when the final CfA SAP and SS light curves, both sets of which will have been corrected for long-term trends with PDC-MAP, become available. For now, though, our C16 light curves are good enough to try to get a list of M67 rotation periods which we can analyze in the context of angular momentum evolution.

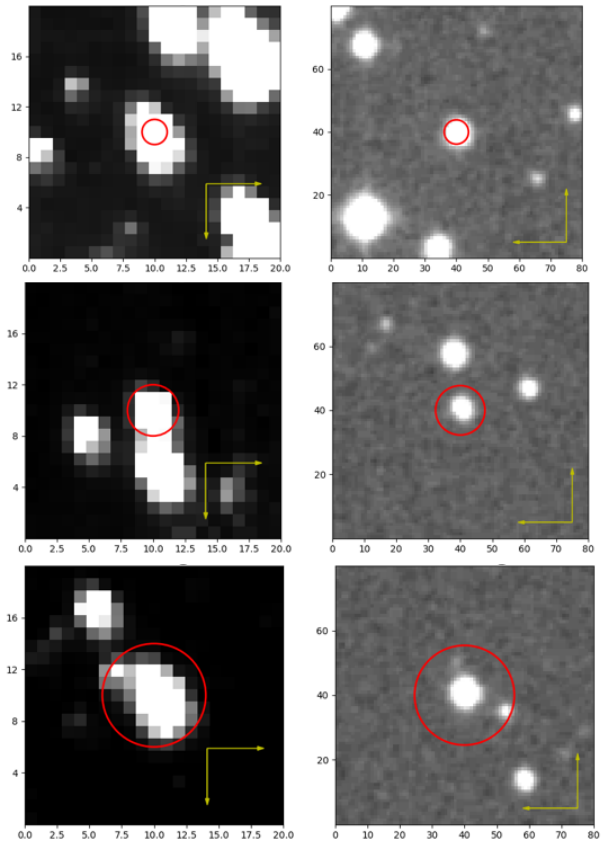

Figure 5.13: Examples of target stars without contamination (top row), likely contamination (middle row), and definite contamination (bottom row). The left column shows the *K2* images, while the right column gives the corresponding DSS images. Selected apertures are plotted in red, while the yellow arrows illustrate the orientation of *K2* images with respect to the DSS images.

5.7 Checking for Contamination

We have so far neglected how we handle the risk of contamination. The crowded field combined with the large pixel size of the *Kepler* CCDs necessitates checking if light from surrounding stars could be spilling into the selected aperture for a given target. We do this by simply looking at the *K2* image of a specific star plotted alongside a corresponding, high resolution image from the ESO Online Digital Sky Survey (DSS). In the case of the superstamp, we can directly over plot the apertures we used to extract the light curves. In Figure 5.13, we show examples of where there is no contamination (top row), likely contamination (middle row), and definite contamination (bottom row), using SS stars. The left-hand column provides the *K2* image, while the right-hand side displays the corresponding DSS image. Automatically-selected apertures are plotted in red, while the yellow arrows indicate the orientation of the *K2* images with respect to the DSS images. We check these plots for all targets in which we have measured periods, and we can either remove those periods where there is probable contamination, or, in the case of the SS, try a smaller aperture.

5.8 'Final' M67 Rotation Periods

We generally followed the procedures outlined above to find periods where C05 and C16 overlapped and for those EPICs unique to C16. After a last check for contamination, we plotted the M67 CMD with the stars for which we found periods highlighted in red. We identified and removed from the sample three red giants, three subgiants, and a few other stars clearly off the main sequence. The final CMD is given in Figure 5.14. A few of our stars (EPICs 211408078, 211411461, and 211420549) are on the turn-off, but instead of removing these, we make note of them for future reference. In blue are stars classified as SM in the Mathieu catalog, but which fall along or close to the binary sequence in the CMD; we have labeled these as 'possible binary members,'

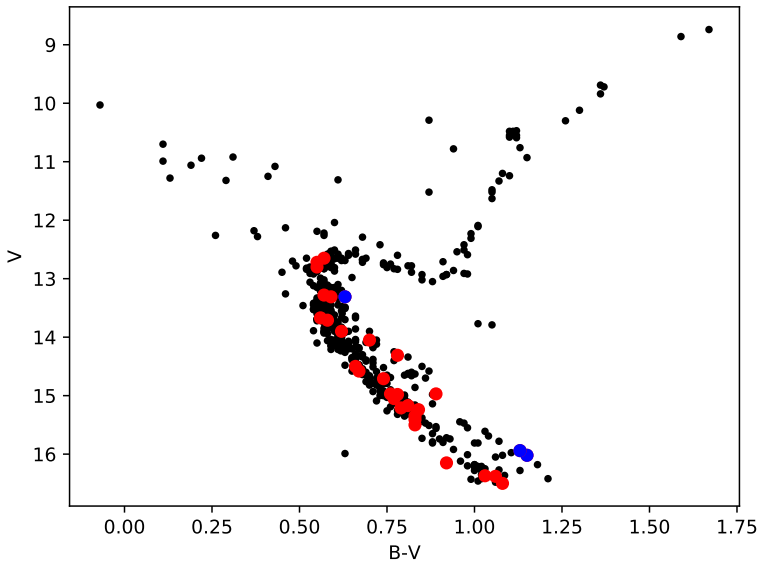

Figure 5.14: M67 CMD where the stars for which we have found rotation periods are highlighted in red, with 'PBM' stars in blue. All stars not on the main sequence have been removed from our period sample.

or 'PBM,' as there is a decent chance that these may actually be undetected binaries.

The final periods are in Table 5.1, and their associated light curves are in Appendix B. The addition of C16 data allowed us to recover 17 more periods for M67, 15 of which were based on the combination of both C05 and C16 light curves (shown as '5,16' in the campaign column of Table 5.1). However, notice that five of these cases have been highlighted with an asterisk. For two of these EPICs (211420549 and 211425493), we believed the result from the C05 data alone as opposed to the one resulting from a combination of the two campaigns, even though the C05 results do not strictly follow our matching algorithm (both have ACF periods just over 30 d). This is because either the C16 light curves for these particular stars are too noisy, or they do not show strong variability like their C05 counterparts. This is not altogether unexpected, as the stars could be at low points in their respective activity cycles during C16. The other highlighted stars are 211423010, 211411799,

Table 5.1: M67 Periods from *K2* Campaigns 5 and 16

EPIC	Campaign	Type	$B-V$	Per (d)	LS_5 (d)	LS_{16} (d)	ACF_5 (d)	ACF_{16} (d)
211402432	5,16	SS, SM	0.83	$29.5^{+1.1}_{-1.1}$	52.6	9.7	31.2	30.2
211402905	5,16	SS, SM	0.66	$23.6^{+1.0}_{-1.0}$	22.7	4.9	23.5	20.9
211404554	5	SS, BLM	1.060	$15.5^{+1.7}_{-1.1}$	12.8	–	12.9	–
211405776	5	SS, BM	0.70	$7.4^{+1.1}_{-1.0}$	7.1	–	7.0	–
211407470	5,16	SS, SM	0.76	$25.0^{+1.0}_{-1.0}$	12.80	8.53	24.6	25.8
211408078	5	SS, BM	0.57	$4.5^{+1.0}_{-1.0}$	4.3	–	4.1	–
211408909	5,16	SS, SM	0.83	$25.8^{+1.0}_{-1.0}$	29.4	8.5	25.8	24.5
211409139	5	SS, BM	0.89	$6.4^{+1.0}_{-1.0}$	6.1	–	6.5	–
211409515	5,16	SS, BM	0.78	$30.5^{+1.0}_{-1.0}$	27.0	2.5	28.9	36.7
211410014	5,16	SS, BM	0.57	$22.0^{+1.2}_{-1.0}$	5.5	3.4	21.4	14.9
211410278	5	SS, BM	0.67	$4.3^{+1.1}_{-1.1}$	4.5	–	4.7	–
211410402	5	SS, BM	0.56	$6.3^{+1.0}_{-1.0}$	6.2	–	6.2	–
211410700	16	SS, SM	0.74	$26.9^{+1.1}_{-1.1}$	–	27.7	–	27.6
211411461	5	SS, BM	0.55	$8.1^{+1.1}_{-1.1}$	3.4	–	7.5	–
211411698	16	SS, BM	0.59	$6.1^{+1.0}_{-1.0}$	–	5.9	–	6.1
211411716	5	SS, BM	0.79	$8.0^{+1.0}_{-1.0}$	7.9	–	7.8	–
211413688	5	SS, SM	1.08	$29.8^{+1.1}_{-1.1}$	13.1	–	27.7	–
211414799	5,16*	SAP, BM	0.58	$19.8^{+1.2}_{-1.1}$	9.0	–	8.6	–
211415154	5	SS, BM	0.62	$2.6^{+1.0}_{-1.0}$	2.6	–	2.4	–
211415239	5,16	SS, SM	0.84	$28.5^{+1.1}_{-1.0}$	27.0	3.4	54.1	23.6
211416940	5	SS, SM	0.81	$25.3^{+1.0}_{-1.0}$	14.3	–	26.1	–
211417843	5	SS, SM	1.03	$26.8^{+1.3}_{-1.0}$	28.5	–	28.8	–
211419114	5,16	SS, PBM	0.63	$26.8^{+1.1}_{-1.1}$	13.2	9.8	27.2	31.0
211419629	5,16	SS, PBM	1.15	$27.5^{+1.0}_{-1.0}$	13.7	13.9	27.3	27.1
211420549	5,16*	SS, BM	0.55	$31.4^{+1.0}_{-1.0}$	33.3	15.6	32.9	56.5
211423010	5,16*	SAP, SM	0.77	$25.3^{+1.4}_{-1.2}$	22.2	–	43.1	–
211424811	5,16	SS, SM	0.83	$33.9^{+1.1}_{-1.1}$	16.4	16.1	16.6	31.3
211425493	5,16*	SS, SM	0.92	$31.2^{+1.0}_{-1.0}$	15.4	2.3	32.3	47.14
211425620	5	SS, BLM	0.78	$2.7^{+1.0}_{-1.0}$	2.7	–	2.3	–
211431607	5,16*	SAP, PBM	1.13	$34.2^{+1.1}_{-1.3}$	14.1	45.4	13.1	44.9

The columns from left to right are EPIC identification number; the campaign(s) from which we got the period; the light curve type, with respect to both the dataset from which it was extracted and its membership status from the Mathieu catalog; the $B-V$ colour from the Mathieu catalog; the final period post-MCMC with uncertainties, in days; the Lomb-Scargle outputs in days for each campaign, where available; and the ACF result for each campaign, also in days. Periods highlighted in blue are where the Lomb-Scargle measurements passed the detection threshold and matched our final result (or are rough harmonics).

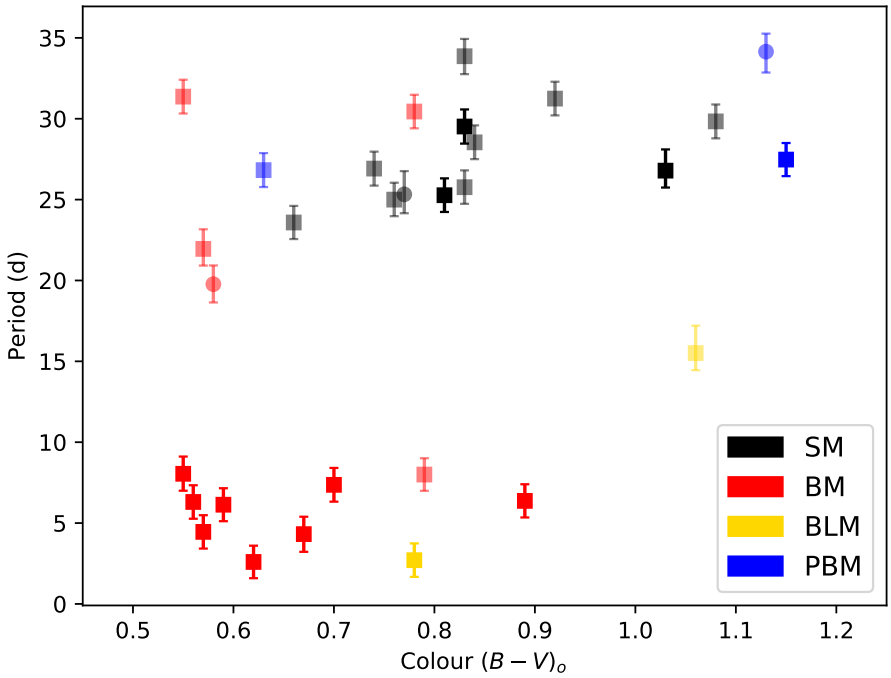

Figure 5.15: M67 CPD of the stars for which we have found rotation periods. Stars from the superstamp are shown as squares, while circles represent stars from the SAP. Black points are SM stars, red points are BM stars, yellow points are BLM stars, and blue points are 'PBM' stars. The shading on the data points illustrates our subjective confidence in the rotation period, i.e. darker points indicate more confidence, and lighter points less.

and 211431607. The C05 periods from these stars were verified by eye when looking at the C16 light curves, but when the light curves from the two campaigns were processed simultaneously, the GP output the incorrect period. Therefore, we took the C05 period for the former two and the C16 period for the latter, even if they did not pass our matching criteria.

Our final CPD for M67 is illustrated in Figure 5.15. Here, stars from the superstamp are represented as squares, and those from the SAP dataset are shown as circles; SM stars are in black, BM stars are in red, BLM stars are in yellow, and PBM stars are in blue. Darker points are where we have more faith in the measure-

ment, while lighter points indicate less subjective confidence (a detection from the Lomb-Scargle often correlates with this; periods with a detection are highlighted in blue in Table 5.1). The $B - V$ values come from the Mathieu catalog, and we use $E(B - V) = 0.04$, as was done by Barnes et al. (2016).

Several features are immediately apparent in Figure 5.15. First, the vast majority of the measurements come from the superstamp. This makes sense, since the SS light curves typically have higher precision than those from the SAP. In addition, because the SS stars make up the densest parts of the cluster, more of them are likely to be confirmed members. Second, we have a fair amount of binaries, most of which are rotating relatively rapidly. A few, however, are not, and the synchronization timescales for all the binaries in our sample will be interesting to determine. Third, there does appear to be a trend in rotation periods for single member stars, though there is still more scatter in the plot than we would like to see. We will explore whether this scatter is real or not in the following chapter.

Furthermore, we acknowledge that our selection criteria may bias our sample towards short-period systems. A third of our M67 stars have periods of < 10 d and a median amplitude of 0.75%, and of the 12 periods in the final sample that have passed the detection threshold defined in Chapter 4, nine belong to this group. This is not wholly unexpected, since we found in the sinusoidal injection tests that we have high completeness at short periods and large amplitudes. We would also expect that the error bars for the short-period systems would be much smaller than their longer-period counterparts. From Table 5.1 and Figure 5.15, however, this is not evidently the case; all periods have error bars roughly on the order of 1 d. We need to more fully investigate this, as it indicates that there could be a systematic limitation or bias in how the MCMC explores the parameter space, especially given the input period from the GP. In the meantime, we are testing nested sampling as a possible alternative to both the GP periodogram and MCMC, and in a small test set, the error bars seem to

correlate with the discrepancy between the known, 'true' period and the maximum likelihood value. This work is very premature, though, and outside the scope of this thesis.

Finally, despite our best efforts, we still have a very small sample of periods. We have brought considerable attention to the shortcomings and problems of the methods we have described in this chapter to measure M67 rotation periods from *K2* data, and a lot of work is still to be done. It is highly unlikely that the set of rotation periods presented here is what future development and testing of stellar evolutionary models will be built upon. However, they are the 'final' rotation periods for this thesis, and we will use them to attempt to draw what preliminary conclusions we can regarding the angular momentum evolution of solar-age stars.

5.8.1 A Few Remarks

We would like to emphasize that we ourselves are not fully satisfied with the methods developed here. They do not adequately incorporate the careful work from Chapter 4, and they are very ad hoc. Furthermore, it is hard to make the claim that our procedure and these 'final' periods are any better than those from Barnes et al. (2016) and Gonzalez (2016a). However, we believe that we have done the best we could given the tight timeline for thesis completion. In addition, we described our method in much more detail — including all weaknesses — than either of the published works. And while we plan to do a large-scale round of SSM tests to revamp our method following thesis submission and make our periods publishable, the tests we have done, both in this chapter and the last, have given us a better eye for differentiating between real and systematic features in the light curves. Finally, given what we have learned, we do not expect the results to change that much, even if we are able to get a more refined list of *K2* M67 rotation periods. Thus, we can proceed with a preliminary analysis of the periods presented here.

Chapter 6

The Role of M67 in Angular Momentum Evolution Theory

The stars are the jewels of the night, and perchance surpass anything which day has to show.

Henry David Thoreau

6.1 Introduction

Now that we have obtained a list of M67 rotation periods from *K2* C05 and C16, we can begin to analyze them in the context of angular momentum evolution. While this will be challenging, given the small sample size and inherent scatter of our data points, our set of periods may be able to give us some insight into the nature of the angular momentum of solar-age stars. As we saw from Figure 5.15 in the preceding chapter, almost half of our sample comes from binary systems, most of which are rotating rapidly. This gives us the chance to explore in Section 6.2 tidal synchronization timescales while also separating out those binary components which may have effectively evolved as single-member stars. We can then use the un-synchronized binaries in conjunction with the single members to look at how M67 fits with standard gy-

rochronology models and angular momentum evolution theory. We accomplish this to the extent that we can in Section 6.3, comparing and commenting on the implications of the empirical versus theoretical models in light of the observed scatter.

6.2 Binary Tidal Synchronization Timescales

While measuring the rotation periods of cool, solar-age stars is not easy, it is clear from Figure 5.15 that our method has little trouble confidently determining the periods for binary systems in M67, at least for periods below 10 d (assuming no binary photometric effects, e.g. ellipsoidal variations, which we discuss later). Thus, we can extend our analysis of the angular momentum evolution of solar-age stars to that of whole binary systems. Here, we apply tidal evolution theory to our binary sample in an attempt to constrain working models as well as isolate those systems whose primaries likely evolved separately from their secondaries, in essence making them additional candidates for testing gyrochronology.

6.2.1 Tidal Evolution Theory

The cornerstone work in tidal evolution theory comes from Zahn (1977), who discusses various mechanisms responsible for the tidal dissipation of close binary systems, for stars both with and without convective envelopes, leading to the derivations of synchronization and circularization timescales. Synchronization is achieved when the rotation period of both stars in a binary equals that of the system's orbital period, while circularization refers to the reduction in eccentricity over time as tides affect the system's total orbital energy. All of the stars in our sample are later than F5, meaning they should all have convective envelopes (albeit with varying sizes). Therefore, we will only focus on the formulisms for these types of stars.

The two most prominent tides at work in stellar systems are the equilibrium

tide and dynamical tide, but we are primarily concerned here with the former, as it has the most dominant role in stars with convective envelopes (Zahn, 1977). The equilibrium tide describes the internal response of one star to the gravitational effects of its companion (Zahn, 1989). Tidal torques arise from the offset between the force of gravity of one body and the bulge it produces on its companion (and vice versa). The offset, in turn, results from the rotation of both bodies combined with the time required, and mechanisms responsible for, stellar material to form into a bulge as gravity acts upon it (Zahn, 1989). If the rotation period of one star is shorter than the orbital period of the system, the gravity acting on the misaligned bulge will act as a brake, lengthening the star's rotation period. In doing so, angular momentum is transferred from the slowing star to the whole system, adding rotational energy to the orbit and increasing its size. On the other hand, if a body is rotating slower than the orbital period, the equilibrium tide will speed up its rotation, decreasing the size of the orbit as rotational energy is transferred into that body.

Over time, the tidal interactions between the stars in a close binary system will cause the two components to synchronize. Zahn (1977) cites turbulent friction arising from convection as the primary mechanism in the dissipation of tidal energy for cool stars. Taking into account the effects of angular momentum transfer, perturbations from gravitational potential energy, and tidal dissipation from turbulent friction, Zahn (1977) derives the following equation for the tidal synchronization timescale, t_{sync}, in years, for stars with convective envelopes:

$$t_{sync} = \frac{1}{6q^2k_2}\left(\frac{MR^2}{L}\right)^{\frac{1}{3}}\frac{I}{MR^2}\left(\frac{a}{R}\right)^6 \tag{6.1}$$

where q is the mass ratio of the secondary to the primary; M, R, L, and I are the mass, radius, luminosity, and moment of inertia of the primary, respectively; a is the semi-major axis; and k_2 is the constant for apsidal motion of the system computed to the second order. However, Zahn (1977) then simplifies this equation to:

$$t_{sync} \sim q^{-2}\Big(\frac{a}{R}\Big)^6 \sim 10^4\Big(\frac{1+q}{2q}\Big)^2 P^4 \tag{6.2}$$

where P is the orbital period in days. Zahn (1977) makes these simplifications under the acknowledgement that the various coefficients in Equation 6.1 are not exact and the assumption that even with the reduced complexity, Equation 6.2 falls within the error bars of Equation 6.1. Based on Equation 6.2, if $a/R \leq 40$, binaries with members similar in age and composition to the Sun should be synchronized (Zahn, 1977). Therefore, we should expect binaries in M67 falling within a scaled separation of 40 to be synchronized, as well.

Discrepancies between observations and theory, however, soon became apparent, and further attempts were made to refine the latter (Zahn, 1989). Zahn (1989), for example, tried to modify theory with a better treatment of how turbulent friction is affected by the convective mixing length, while others simply made adjustments that fit observations. Falling into the latter category, Albrecht et al. (2012) invoked tidal evolution theory to help explain the alignment between the orbits of hot Jupiters (exoplanets roughly the size of Jupiter orbiting close to their parent star) and their host star equators. In doing so, they developed equations for tidal synchronization timescales based on Zahn (1977), but with modifications made in light of empirical evidence as opposed to theory. For stars with convective envelopes, Albrecht et al. (2012) present the following equation for the synchronization timescales:

$$\frac{1}{t_{sync}} = \frac{1}{10 \times 10^9\,\mathrm{yr}} q^{-2}\Big(\frac{a/R}{40}\Big)^{-6} \tag{6.3}$$

Here, q is the ratio of the mass of primary, M_1, to the secondary, M_2, and R is the radius of the secondary. The switch between the primary and secondary is doable because the two companions both exert tidal forces on each other, and the change in the definition of R is consistent with that of q. The scaling of a/R by 40 hearkens

back to the separation scaling from Equation 6.2, while dividing by 10 Gyr reflects the main-sequence lifetime of a solar-like star, or the total time in which tidal dissipation in the form of turbulent friction is the most relevant (i.e. before a star evolves off the main sequence and its internal structure changes dramatically) (Albrecht et al., 2012). We use Equation 6.3, primarily grounded in theory but scaled empirically, to calculate the synchronization timescales for the binaries in M67.

6.2.2 Observations and Analysis

Dave Latham of the Harvard Center for Astrophysics provided us with the orbital solutions for our sample of M67 binaries, derived from spectroscopic and radial velocity data obtained through long-term monitoring of M67 members as described by Geller et al. (2015). To calculate the synchronization timescales, we only focused on those binaries labeled as confirmed binary members from that work. Of these, EPIC 211408078 is actually a part of a triple star system. To keep the analysis simple, we did not include EPIC 211408078 in the study at this stage, though we hope to return to it at some point in the future. We also excluded EPIC 211409139, because we did not have a complete orbital solution for this binary (i.e. mass, separation, eccentricity, orbital period, etc.). This left 11 M67 binaries for us to analyze.

EPICs 211411461 and 211415154 are double-lined spectroscopic binaries, with the masses of the primary and secondary in each system dependent only upon the inclination of the respective systems. The majority of the M67 binaries in our sample, however, are single-lined. They have minimum constraints on the mass of the secondary in each system but no information regarding the primary. We assumed that both stars in this category contributed to the observed V magnitudes from Geller et al. (2015), with negligible bolometric correction. We converted these to absolute magnitudes and luminosities, applying the distance modulus from Sarajedini et al. (2009), which corresponds to approximately 880 pc. We then used the solar isochrone

Table 6.1: Tidal Synchronization Timescales for M67 Binaries

EPIC	P_{rot} (d)	P_{orb} (d)	$t_{i=90^\circ}$ (Gyr)	$t_{i=65^\circ}$ (Gyr)	$t_{i=45^\circ}$ (Gyr)
211405776	7.4	6.3	7.5e-5	1.1e-4	3.3e-4
211409515	30.5	53.0	3.1	4.4	10.7
211410014	22.0	959.5	147018	223110	536411
211410278	4.3	358.5	70.5	160.6	707.4
211410402	6.3	6.0	6.9e-5	1.0e-4	2.4e-4
211411461	8.1	7.2	2.2e-2	–	–
211411698	6.1	5.8	5.6e-4	8.1e-4	2.6e-3
211411716	8.0	139.8	155.0	225.3	596.0
211414799	19.8	9.1	9.3e-5	1.6e-4	3.6e-4
211415154	2.6	2.7	6.9e-4	1.34e-4	–
211420549	31.4	583.4	6022	9478	22987

The columns from left to right indicate the EPIC number; stellar rotation period (presumably of the primary), in days; orbital period, in days; and the synchronization timescales assuming $i = 90^\circ$, $i = 65^\circ$, and $i = 45^\circ$, all in Gyr.

with $Z = 0.0162$ from the Yale-Potsdam Solar Isochrones (or YaPSI, Spada et al. 2017), as was done for an analysis of another M67 binary by Sandquist et al. (2018), to obtain total mass estimates for each system. For all the binaries, including the double-lined ones, we then solved for the masses of the primary and secondary using inclination angles of $i = 90^\circ$, $i = 65^\circ$, and $i = 45^\circ$. We again utilized the isochrones to get estimates for the radii of the secondaries at each inclination before computing the corresponding separation, a. The uncertainties in mass and separation from the orbital solutions are typically on the order of a couple percent.

We obtained the synchronization timescales for each binary in our sample. The orbital periods, determined rotation periods, and computed timescales are presented in Table 6.1, while Figure 6.1 graphically illustrates these results. In Figure 6.1, each circle represents a binary system, the timescale for synchronization expressed through the circle's color. Cooler, bluer points should fall on or near the dotted one-to-one line that indicates synchronization of the rotation period with the orbital period. In the top row, the sizes of the circles symbolize the ratio between the mass of the primary and the secondary, while in the bottom row, the sizes are representative of the

ratio between the separation and the radius of the secondary. In the top and bottom panels of the first column ($i = 90°$), we provide reference sizes for $q = 1$ and $a/R = 40$, respectively, with an unfilled circle drawn in the top left-hand corner of each plot. The circles in the first column of Figure 6.1 are also transparent to reveal underlying binary systems along the one-to-one line that are otherwise obscured by overlapping data points. We did not include timescales for EPICs 211411461 and 211415154 at $i = 45°$ and EPIC 211411461 at $i = 65°$ because the masses became too large to extract reasonable values for the radii from our choice of isochrone. Regardless, EPIC 211415154 should almost definitely be synchronized, and its rotation period is indicative of this. EPIC 211411461 is also likely to have synchronized within the first billion years, and the orbital period is within the error bars of the rotation period.

6.2.3 Discussion

According to Table 6.1, all binaries should be synchronized by the age of M67 except for EPICs 211410014, 211410278, 211411716, and 211420549. Figure 6.1 reinforces these results; almost all of the binaries that should be synchronized fall along the one-to-one line. Depending on the inclination angle, EPIC 211409515 (represented as the green circle just under the one-to-one line) should either already be synchronized, or it will achieve synchronization near the end of its main sequence life. Indeed, the difference between the rotation and orbital periods suggests that the inclination angle is lower than $\sim 60°$, producing a synchronization timescale greater than the age of the system. The exception to the rule is EPIC 211414799, for which we have a measured period of about 19 d. This system should have synchronized well within the first million years after formation, regardless of the inclination angle used. Therefore, the period we have measured is likely a harmonic, and the true period is probably closer to 9 d. Once again, this highlights the ambiguity in rotation period often present in light curves.

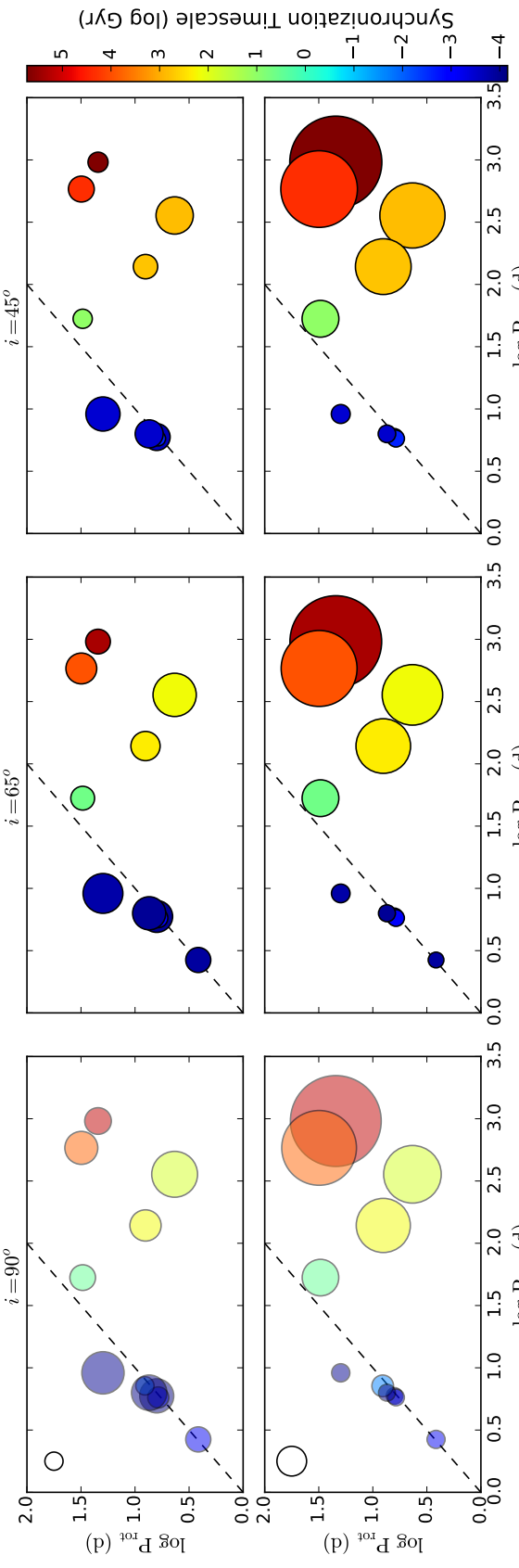

Figure 6.1: Synchronization timescales plotted with rotation versus orbital period for our sample of M67 binaries at inclinations of $i = 90°$ (left column), $i = 65°$ (center), and $i = 45°$ (right). In the top row, the sizes of the circles represent the mass ratio M_1/M_2, while in the bottom row, the sizes of the circles are illustrate a/R_2. The blank circles in the top and bottom panels of the first column specify the scaling of $M_1/M_2 = 1$ and $a/R_2 = 40$, respectively. The colors of the data points display the synchronization timescales. The points in the first column are transparent to reveal binary systems otherwise obscured by overlapping data.

Our results appear to support the prescription for tidal synchronization provided by Albrecht et al. (2012). The ratio between the separation and the radius of the secondary in each of the synchronized binaries is under 40, as was predicted by Zahn (1977). While we could be seeing ellipsoidal variation as opposed to star spot modulation for these binaries, the evolution apparent in the light curves in Appendix B points to the latter (although ellipsoidal variation is still likely present to some degree in the synchronized systems). For EPIC 211409515, we find $a/R \sim 61$, again suggesting that this system should not be synchronized, although it explains this binary's proximity to the one-to-one line in Figure 6.1 compared to the un-synchronized binaries. All of the other binaries have values of $a/R > 100$. The separation between the two stars in a binary is by far the biggest contributing factor in the tidal synchronization timescale, since it is raised to the sixth power. It is unsurprising, then, that the points larger than our reference circle in the bottom row of Figure 6.1 — especially relative to their counterparts in the top row — have synchronization timescales much greater than the age of M67. Even if we assume that the primary star in the single-lined binaries is the sole contributor to the observed $B - V$, the timescales overall become shorter, but the conclusions do not change. The only binary that would synchronize under this assumption is EPIC 211409515, with a timescale of about 1.1 – 1.3 Gyr, depending on the inclination. However, given the data and the agreement between our synchronization timescale and the separation for EPIC 211409515, our treatment of the single-lined binaries seems reasonable.

The synchronization timescales for EPICs 211410014, 211410278, 211411716, and 211420549 are so long, and the separations are so large, that the components of these four binary system likely evolved independently. Therefore, we can potentially use the binaries in these systems in our analysis of how M67 fits into gyrochronology and angular momentum evolution theory. The most promising of these are EPICs 211410014 and 211420549, although we have to keep in mind that the latter is right

along the main-sequence turnoff. EPICs 211410278 and 211411716 are a little more puzzling, however; these systems have large separations and are not particularly hot (their total $B - V$ values are 0.67 and 0.79, respectively), so we would expect to see periods similar to that of the Sun. Nonetheless, we have found rotation periods of less than 10 d for both binaries. There could potentially be some contamination from background stars, particularly with respect to EPIC 211411716, or the $B - V$ values may have been misattributed as a result of the crowded field. Another possible explanation could be that these stars are actually a part of a hierarchal triple system, and we have not yet resolved the third member.

The next step in our analysis of tidal theory with M67 binaries is to look at circularization timescales for stars with convective envelopes. It would be interesting to see if those binaries in our sample that are synchronized have achieved circular orbits. We also need to perform a more in-depth comparison of our results using Equation 6.3 from Albrecht et al. (2012) with timescale prescriptions based more on theory than empirical evidence, as well as other observations. In doing so, we can help constrain theory and possibly gain better understanding of the mechanisms responsible for tidal dissipation.

6.3 Testing Gyrochronology and Angular Momentum Evolution Theory

We can now take a look at the extent to which M67 falls in line with standard gyrochronology models and existing angular momentum theory. Recall that the 'standard' gyrochronology models typically contain mass and age dependencies fit to observational data primarily obtained from young open clusters. Until M67 was observed by *K2*, the oldest cluster to have been used to calibrate gyrochronology had an age of 2.5 Gyr. Gyrochronology holds up well for these younger clusters, but its

validity becomes more ambiguous for older main-sequence stars. Angular momentum evolution theory, on the other hand, attempts to invoke understanding of the physical processes at work both on the surface and within the interiors of stars to predict observed rotation periods. The theory put forward by van Saders et al. (2016) explains well observations for older stars, particularly those evolving off the main sequence and onto the subgiant branch, but M67 gives us the opportunity to potentially test it at solar age. Here, we compare our sample of rotation periods first with gyrochronology models and then those developed by theory. While we may be able to glean some insight from these comparisons, we must keep in mind the limited scope of our set of rotation periods and the apparent scatter within.

6.3.1 Comparison with Standard Gyrochronology Models

We now plot the rotation periods of our single member stars and the four binaries identified as having evolved independently against several standard gyrochronology models. From here on out, we treat the 'possible binary members' identified in Chapter 5 as single member stars, since we do not know for certain whether or not they are undetected binaries (in which case we do not have orbital solutions, anyway). The models include those of Barnes (2007) (B2007), Mamajek & Hillenbrand (2008) (MH2008), Meibom et al. (2009) (M2009), Barnes (2010) (B2010), and Angus et al. (2015) (A2015). The parameters for each of these models, except that of B2010, are given in Table 1.1 in Chapter 1; the formula for B2010 is given in Equation 1.8 in that chapter. For each of these models, we assumed an age of 4.3 Gyr.

Figure 6.2 shows our rotation periods plotted with the gyrochrones from B2007, MH2008, M2009, B2010, and A2015. The rotation periods of the single members are given in black, except for where we have identified them as coming from possible binary members, in which case they are shown in blue. For the known binaries, shown in red, we assume that the $B - V$ from Geller et al. (2015) is that of the

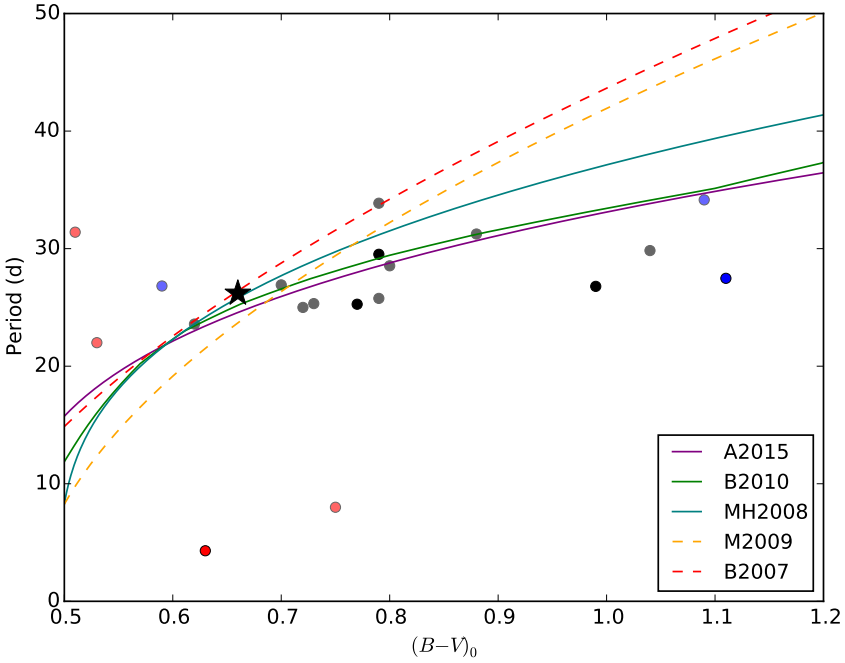

Figure 6.2: Comparison of standard gyrochronology models with rotation periods for M67 stars that likely evolved independently. Red points represent binary members, black points are single members, and blue points are 'possible binary members' classified as single members. Darker points express more subjective confidence in our measurements. The Sun is illustrated as a black star.

primary, since these stars are widely-separated, single-lined binaries. Those periods for which we have more confidence in the measurement are emboldened. We do not show uncertainties in the period measurements on this plot for the sake of clarity, but they are generally ± 1 d. As a point of reference, the Sun is shown as a black star, although we do need to keep in mind that the Sun is likely to be a couple hundred million years older than the members of M67.

It is immediately apparent from Figure 6.2 that the standard gyrochronology models, in general, do not describe the data very well. While the Sun appears to fall right along B2007, both this gyrochrone and M2009 fail to account for the bulk of data points beyond $(B-V)_0 \sim 0.75$. The MH2008 gyrochrone also reproduces the Sun, and while it begins to curve towards the rotation periods of later stars, it still greatly

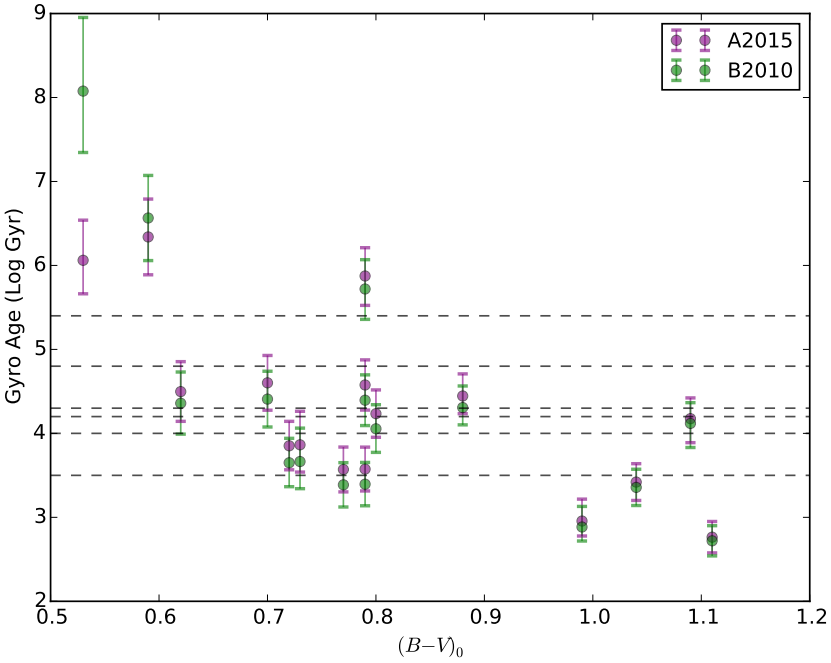

Figure 6.3: Gyro ages from B2010 (green) and A2015 (purple) for our sample of single member stars, along with EPIC 211410014. The horizontal dashed lines represent ages for M67 from the literature.

overestimates them (which, alternatively, means that the model would underestimate the cluster's age based on our sample). Of the standard gyrochronology models, B2010 and A2015 are the best. Regarding the former, this may be the result of attempting to incorporate convective turnover timescales, adding more physics to an otherwise empirical formulism. However, the convective turnover timescales themselves are uncertain, which may explain why the gyrochrone appears to erroneously predict longer periods than what we see. With respect to A2015, the Bayesian approach to calibrating the parameters for the mass and age dependencies may have made this particular model more accurate than other models that use the same basic structure, most notably those of B2007 and M2009.

We used the prescriptions of B2010 and A2015 to determine what ages we would back out for M67 from the individual periods in our sample. In Figure 6.3, we have

plotted the 'gyro ages' computed from A2015 (in purple) and B2010 (in green) for each of the periods in Figure 6.2. The uncertainties are propagated from the errors in the rotation period measurements. The dashed horizontal lines indicate M67 age estimates: 3.5 Gyr, 4.0 Gyr (Sarajedini et al. 2009), 4.2 Gyr (Balaguer-Núñez et al. 2007), 4.3 Gyr (Carraro et al. 1994; Barnes et al. 2016), 4.8 Gyr (Carraro et al. 1994), and 5.4 Gyr (Gonzalez 2016a). There appears to be a general trend of decreasing age with increasing $B - V$. The standard models, then, tend to underestimate rotation periods for M67 at the bluer end of our sample and overestimate them at the red end. Despite this, the average gyro ages for B2010 and A2015 are $\sim$4.3 Gyr with standard deviations on the order of about 1.0 – 1.4 Gyr. An age of 4.3 Gyr is consistent with the literature, although we excluded the extreme outlier periods from EPICs 211410278, 211411716, and 211420549 for this estimate. If we include them, the gyro ages become 4.9 Gyr and 4.4 Gyr for B2010 and A2015, respectively, but with standard deviations of 4.8 Gyr and 2.7 Gyr. While the average gyro ages from both models are fairly reasonable, the scatter in our sample means that, for any individual star, an age determination based on rotation period alone from either B2010 or A2015 would be very uncertain.

6.3.2 Application of Angular Momentum Evolution Theory

We will now compare our rotation periods to models derived from angular momentum evolution theory. We begin with the models developed by Van Saders & Pinsonneault (2013), which take into account angular momentum transport and loss in addition to changes in stellar structure. These models are grounded in physics, incorporating convective mixing length, nuclear reaction rates, opacity, atmospheric conditions, and the changing moment of inertia. Assuming the efficient transfer of angular momentum through rigid-body rotation, Van Saders & Pinsonneault (2013) use the prescriptions of Matt et al. (2012) to describe the angular momentum loss in stars over time. The

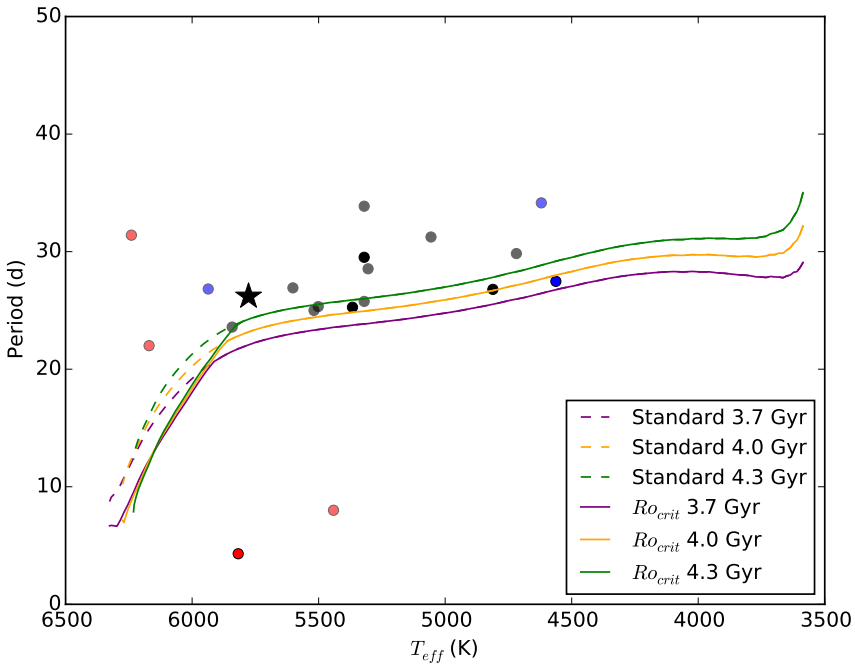

Figure 6.4: Comparison of theoretical angular momentum evolution models from Van Saders & Pinsonneault (2013) and van Saders et al. (2016) with our periods from M67. Red points represent binary members, black points are single members, and blue points are 'possible binary members.' Darker points express more subjective confidence in our measurements. The Sun is illustrated as a black star.

models of Van Saders & Pinsonneault (2013) were used as the basis for van Saders et al. (2016), the difference between the two works being the incorporation of a critical Rossby number above which the magnetic braking of the rotational velocity of stars weakens, particularly for hotter stars. Therefore, for this section, we will refer to the Van Saders & Pinsonneault (2013) models as the 'standard' angular momentum evolution (SAME) models and those of van Saders et al. (2016) as 'Ro_{crit}.'

Figure 6.4 plots SAME and Ro_{crit} models for ages of 3.7 Gyr, 4.0 Gyr, and 4.3 Gyr with the periods from our M67 single member stars and independently-evolved binaries. Again, the Sun is displayed as a black star. At a glance, both the SAME and Ro_{crit} models appear to do a better job of describing the data than the standard gyrochronology models, particularly for cooler stars. We will discuss in-depth

the relative performances and implications of both the gyrochronology and angular momentum evolution models below. It should be noted now, however, that there is some uncertainty involved in the conversion of $B-V$ to effective temperature, which we based off the work of Pecaut & Mamajek (2013). We unfortunately do not have enough data points beyond temperatures greater than 6000 K to properly test the weakened magnetic breaking theory from van Saders et al. (2016). This could be due to an unmet detection threshold in the Rossby number similar to that of Ro_{crit}, as suggested by van Saders et al. (2018), who predict that rotation periods will be unmeasurable by 1.5 Gyr for stars hotter than 6500 K or for solar-like stars by about 4.2 Gyr. Because we do have several measurements around solar temperatures, our lack of data points is probably due to the difficulty in working with *K2* data. We do note that neither the SAME models, nor those from gyrochronology, fit the binaries very well: two are rotating too fast for their temperature, while the remaining are too slow. We have already discussed possible causes for the former, but with respect to the latter, particularly EPIC 211420549 ($P \sim 30$ d), we may be seeing the signal from the secondary. We estimate the $B-V$ for this star to range from 1.44 – 1.47, with an average T_{eff} of ∼3750 K. This would fit the 4.3 Gyr SAME model very well, but the period would be too short for any of the gyrochronology models.

6.3.3 Discussion

While the angular momentum evolution theory models in Figure 6.4 appear to fit the data better than the gyrochronology models in Figure 6.2, we can conduct a crude determination of the χ^2 statistic to make a more quantitative comparison. To do this, we only include those rotation periods from single member stars and the binary EPIC 211410014. Again, we assumed the $B-V$ value of EPIC 211410014 is associated with the primary. The gyrochronology model from A2015 produced the minimum χ^2 with a value of 7.6. The next best models were the 4.3 Gyr SAME model at $\chi^2 = 8.1$,

followed by B2010 at 10.4. If we remove the binary, we achieve χ^2 values of 6.3, 6.8, and 6.0 for A2015, B2010, and the 4.3 Gyr SAME model, respectively. None of these values for χ^2 are particularly convincing, but, at the very least, they support an age of the cluster close to 4.0 Gyr.

Notwithstanding, the discrepancy between the χ^2 values of the different models is almost meaningless due to the scatter inherent in our data points. We may achieve a better 'fit' with the SAME models computed at an age older than 4.3 Gyr, for example, but we could do the same by *decreasing* the age in the gyrochronology models. Without knowing whether or not the observed scatter is real, we simply cannot make any conclusive statements regarding the true age of M67 based on our sample of rotation periods. We can speculate on the nature of the scatter, however. Looking at Figures 6.2 and 6.4, we can see that of the 19 M67 rotation periods plotted, we have designated only five as 'confident' measurements. One of these belongs to EPIC 211410287, a binary with an unexpectedly short period given its mass and synchronization timescale. We have already suggested how this anomalous measurement could be the result of a misattributed $B - V$ value. It is possible that this may be the case for some of the less confident data points, as well, explaining in part some of the scatter. Of the remaining four 'confident' measurements, three do generally fall along the angular momentum evolution models, both at ages of 4.0 Gyr and 4.3 Gyr, suggesting that less scatter is observed in higher quality measurements. Therefore, it is more likely that the scatter is due to the difficulties in extracting rotation periods from *K2* light curves as opposed to the true rotation period distribution.

If we look at the 'confident' measurements and exclude the binaries, the 4.3 Gyr SAME model slightly outperforms A2015 and B2010. If we count the period of EPIC 211420549 as that coming from the secondary, the 4.3 Gyr SAME model does even better. Because the SAME model is based on physical principles, we are more likely to use it to explain the data than either of the gyrochronology models. Despite

this, it is worth reiterating that we cannot, at this stage, make any definitive claims regarding the validity of either the SAME models or A2015 and B2010. Furthermore, our 'final' set of rotation periods did not afford us the chance to test the weakened magnetic braking law of van Saders et al. (2016). We cannot properly test either gyrochronology or angular momentum evolution theory from *K2* C05 and C16 data. The addition of C18, which will almost completely overlap with C05, may help us detect more rotation periods, removing some of the ambiguity in the observed scatter and allowing us to gain a better understanding of how the angular momentum of solar-age stars changes over time. This campaign is only limited to an observation window of about 50 d, though, so we may have to look to other upcoming missions, such as those from the Large Synoptic Space Telescope (LSST), to achieve the high photometric precision required to accomplish the difficult task of measuring rotation periods within M67. We will discuss this in more detail in the next chapter.

6.4 Conclusions and Future Work

The goal of this chapter was to demonstrate, to whatever extent possible, the state of angular momentum evolution of solar-age stars using the rotation periods of members from the old open cluster M67. While our sample of rotation periods as a whole is small, we have a sizable set of binaries with confident period measurements for which we could compute tidal synchronization timescales, exploring the angular momentum of stellar systems as opposed to that of single members alone. We found our data to be in good agreement with the prescription of Albrecht et al. (2012), which is based both on empirical evidence and theory; those binaries with scaled separations greater than 40 have not yet synchronized, while the remainder have synchronized well within the first billion years. In a later work, we can also compute circularization timescales for M67 binaries, which, in conjunction with synchronization and other observational

evidence, can ultimately help constrain tidal evolution theory.

The limited sample size and scatter from our set of *K2* M67 rotation periods, however, means that we cannot conclusively comment on the validity of either gyrochronology or angular momentum evolution models. While these models do appear to support an age for the cluster around 4.0 – 4.3 Gyr, the inherent scatter makes it difficult to constrain this estimate. In order to gain a better understanding of the angular momentum of solar-age stars, we need a more complete list of rotation periods which we trust. To obtain this, more work clearly needs to be done on how we can extract rotation periods from *K2* data, and it seems worthwhile to complement *K2* data with that of future missions.

Chapter 7

Conclusions and Future Work

It is reasonable to hope that in the not too distant future,
we shall be competent to understand so simple a thing as a star.

Arthur Eddington

At the start of this thesis, we introduced gyrochronology, which seeks to establish the relationships among stellar age, mass, and rotation period. By calibrating these relationships with young open clusters, gyrochronology offers the chance to divulge a star's age through a directly observable parameter, i.e. the rotational modulation of its light curve, measurable through high-precision monitoring. By the age of the Hyades, stars later than about F5 are found to show increasing period with age, generally following the Skumanich relation of $P \propto t^{1/2}$. The mechanisms responsible are thought to be torques produced from stellar wind co-rotating with surface magnetic fields, combined with the mass loss that occurs when stellar matter is subsequently extended to large radii, carrying away a disproportionate amount of angular momentum. Largely empirical, gyrochronology does a good job of modeling the observed spin-down of stars up to cluster ages of approximately 2.5 Gyr (Meibom et al., 2015).

Predictions from gyrochronology, however, are in disagreement with older asteroseismic samples (Angus et al., 2015), and they cannot explain the observed rapid rotation of old, main-sequence stars more massive than the Sun (van Saders et al.,

2016). Furthermore, van Saders et al. (2016) have suggested that magnetic fields weaken in middle-aged stars, decreasing the efficiency of the braking mechanism. The old open cluster M67, containing stars of comparable age and composition to the Sun, is an ideal test case for both gyrochronology and angular momentum evolution theory. Recently observed by the *Kepler* spacecraft as part of the *K2* mission, we now have access to light curves with potentially high enough precision to attempt such a study. The goal of this thesis, therefore, was to shed light on the angular momentum evolution of solar-age stars through *K2* observations M67. While Barnes et al. (2016) and Gonzalez (2016a) have previously endeavored to do just that, discrepancies in their results have prompted a more critical approach. We now present a summary of our work in pursuit of that goal, as well as the conclusions we have made thus far. We then outline a plan for future work before providing a few, final remarks.

7.1 Summary and Conclusions

Before we could embark upon an analysis of the *K2* M67 light curves, we had to extract them from the raw data and then remove any artificial features, or systematics. This formed the basis of Chapter 2. For each campaign of *K2* data, we worked with two different sets of light curves: those produced using simple aperture photometry in the *Kepler* pipeline, and those falling within the data region known as the superstamp, encompassing the densest portions of the cluster and for which we had to implement our own extraction technique. We refer to the former as the 'SAP' light curves, and the latter as the 'SS' dataset. Both samples undergo pixel-level calibration via the *Kepler* pipeline before extraction. The SAP light curves are then created by optimizing the sum of the pixels falling within a given 'postage stamp,' or individual target image. The SS light curves, on the other hand, are extracted following the technique of Aigrain et al. (2015a), modified to include variable background subtraction. After

performing an astrometric solution and identifying each source using what we have described as the 'Mathieu catalog,' we produce six different versions of each light curve using circular apertures of varying radii.

The *K2* mission, while still managing higher precision than ground-based telescopes, suffers from unique systematics due to the loss of two reaction wheels in 2013. Therefore, following extraction, we had to correct for star-by-star systematics and common-mode trends to prepare the light curves for rotation period detection. The first we accomplished with K2SC (Aigrain et al., 2016), designed to model and remove the characteristic *K2* sawtooth pattern arising from thruster firings every 6 hrs. After running each star individually through K2SC, we conducted a principle component analysis (PCA) on each set of light curves to remove long-term, common-mode trends. In doing so, we achieved median precisions of 544 ppm and 203 ppm at $K_p = 12$ for the fully-processed Campaign 5 (C05) SAP and SS light curves, respectively.

We have dubbed our combination of extraction and preparation techniques the 'Oxford' pipeline. In this thesis, we compared the Oxford pipeline with another implemented by Andrew Vanderburg, formerly of the Harvard Center for Astrophysics, and Jeff Smith of NASA Ames, referred to here as the 'CfA' pipeline. This alternative pipeline involves light curve extraction and correction following the prescription of Vanderburg & Johnson (2014) and Vanderburg et al. (2016). This is followed-up by the implementation of the *Kepler* PDC-MAP, courtesy of Jeff Smith, to remove the common-mode trends. The CfA pipeline produces precisions of 321 ppm and 275 ppm for the C05 SAP and SS datasets, respectively. Here, we have our first indication that the CfA pipeline, using the more sophisticated PDC-MAP, produces slightly higher quality light curves for the SAP sample. However, it is comparable to the Oxford pipeline with respect to the SS.

In Chapter 3, we described several rotation detection methods before undertaking our own preliminary period search with *K2* C05 light curves. We briefly acknowledged

some techniques utilized by other studies but not incorporated in this thesis, such as the wavelet power spectrum, phase dispersion minimization, minimum string length, and general Bayesian period signal detection. While these are all viable options, we pursued the more traditional Lomb-Scargle periodogram and autocorrelation function, or ACF. The Lomb-Scargle has the advantage of not requiring evenly-sampled data, while the ACF does not assume that the data takes a specific form, allowing it to better account for light curve evolution. We then used the Lomb-Scargle and ACF to produce an initial set of rotation periods, which we compared with Barnes et al. (2016). The lack of agreement between our results and those that had been published, combined with a conspicuous amount of scatter in the period-colour relation, prompted us to undertake a more careful, systematic approach to *K2* data.

We also provided in Chapter 3 an introduction to Gaussian processes, or GPs. In practice, we employed `celerite` (Foreman-Mackey et al., 2017), which drastically reduces the computation time otherwise required for the standard GP. Dan Foreman-Mackey provided us with a covariance function describing a mixture of simple harmonic oscillators (SHOs) with five free parameters, including period, P, and quality factors Q_1 and Q_2, representing an oscillator with period P and its harmonic, $P/2$, respectively. The GP is initialized with guesses for P acquired from the Lomb-Scargle and ACF, and it searches for the set of parameters which maximizes the probability of being observed in light of the data. In theory, if either quality factor is greater than $1/\sqrt{2}$, the data exhibits some degree of periodicity, which we enforced to count a result from the GP as legitimate. We did not, at this stage in the thesis, incorporate this version of the GP in our determination of the initial C05 rotation periods because `celerite` was not yet available.

As previously mentioned, our preliminary rotation period search motivated a more comprehensive look at the nature of the *K2* C05 light curves and our ability to detect reliable rotation periods from them. We accomplished this in Chapter 4, conducting a

comprehensive set of sinusoidal injection tests to uncover our best-case limits in period detection. We injected over 120 000 sinusoidal signals with periods ranging from 5 – 35 d and amplitudes of 0.05 – 3.0% into real, raw *K2* M67 light curves. After processing the injected light curves separately using the Oxford and CfA pipelines, we attempted to recover the signals using a normalized version of the Lomb-Scargle periodogram, which served two purposes. The first was to identify and remove from each test sample those stars whose non-injected light curves likely had astrophysical variability which could contaminate the results. The second was to suppress power at long periods, discovered in a set of C05 hot stars, arising from lingering systematics in the data. We could also define a detection threshold based on the normalized power of each test light curve that balanced completeness, or detection sensitivity, with reliability, or a quantification of how much trust we put in a given measurement which passed the detection threshold.

We drew several important conclusions from the sinusoidal injection tests. The first is that the CfA pipeline appears to perform slightly better than the Oxford pipeline, notably with respect to the SAP, but both are viable options in producing usable light curves. Next, and most importantly, we found that detecting solar-like signals from one campaign of *K2* data is intrinsically difficult. At best, we were only able to recover approximately 15% of injected signals with periods of 25 d and amplitudes of 0.1%. However, reliability was generally very high, often greater than 90% for any given measured period and amplitude bin. Using the detection method we presented in Chapter 4, we suggest a minimum reliability of 80% to retain a detection, but we have to keep in mind that this is based on un-evolving, sinusoidal signals with known form; real data will be even more challenging and may require more flexibility. We also compared our results with those of Barnes et al. (2016) and Gonzalez (2016a). Very few of the measurements in these studies passed as detections using our threshold, but when they did, our periods either agreed with

theirs or were rough harmonics, a common effect of the Lomb-Scargle. Rather than invalidating the results present in these papers, our study highlights the need for caution in applying them to gyrochronology or angular momentum evolution theory, especially since they did not make allowances for the lingering, long-term systematics. Finally, the sinusoidal injection tests illustrated that care must be taken in other *K2* rotation studies, particularly involving clusters, and those that will soon be underway as a part of *TESS*.

Chapter 4 demonstrated the difficulty in detecting solar-like signals in *K2* data, but we were still left with the task of doing just that. In Chapter 5, therefore, we attempted to develop our own rotation detection procedure which incorporated lessons learned from the sinusoidal injection tests but also utilized other techniques which could complement the normalized Lomb-Scargle, namely the ACF and the GP implemented through `celerite`. We first focused on optimizing rotation detection from a single campaign of *K2* data. Utilizing smaller injection tests with realistic signals based on the star spot models of Aigrain et al. (2015b), we developed an algorithm which required the results of all three methods to agree with each other, or 'match' to a certain extent, in order to accept a measurement. For each light curve that passed our matching criteria, we then used a Markov Chain Monte Carlo (MCMC) sampler to explore the parameter space of the GP model and derive period uncertainties. We put a lot of faith in the ACF, and the GP functioned more as a confirmation of the Lomb-Scargle and ACF than as an independent method. With the addition of another campaign, however, we could relax the matching requirements and process both versions of a light curve simultaneously through the GP; we demonstrated this with another round of SSM injections, simulating both C05 and C16 data. Due to time constraints, our approach ended up being both very ad hoc and conservative. We will fully address the improvements that need to be made in the following section, but we do not expect the results to substantially change.

While not fully satisfactory, we were able to recover 30 rotation periods for M67 from *K2* data using the algorithms developed from the SSM injections. Of these, 17 were found due to the addition of C16, released at the end of May 2018. Andrew Vanderburg provided us with C16 SAP light curves prepared with the CfA pipeline. These did not yet have time to be corrected with PDC-MAP, however, so we instead applied the PCA. We processed the SS light curves with the full Oxford pipeline. With median precisions of 1135 ppm and 544 ppm at $K_p = 12$ for the C16 SAP and SS light curves, respectively, it is apparent that the systematics have worsened from C05 to C16. Despite this, the additional campaign doubled the number of rotation periods we were able to measure in M67, most of which come from the superstamp.

Plotting our 'final' set of M67 rotation periods versus their $B-V$ from Geller et al. (2015), a couple features become obvious. The first is that we have a fair amount of binaries in our sample with short rotation periods. We can use these binaries to test tidal evolution theory, specifically in the form of synchronization timescales, to explore the angular momentum of stellar systems as opposed to just single stars. Furthermore, these timescales can separate out those binaries whose components most likely evolved independently of each other, making them suitable test cases for gyrochronology. Second, despite our best efforts, there is still a large amount of scatter in our data, which is also relatively sparse. As a result, any conclusions regarding the angular momentum evolution of solar-like stars will be loosely constrained.

We conducted our analysis of the *K2* M67 rotation periods in Chapter 6, starting with the calculation of binary synchronization timescales through the prescription of Albrecht et al. (2012) for stars with convective envelopes. Using orbital solutions provided by Dave Latham of the Harvard Center for Astrophysics, we found that our sample of binaries supports the theory developed by Zahn (1977), upon which Albrecht et al. (2012) is based. Albrecht et al. (2012) have adjusted the derivation from Zahn (1977), however, to fit observations, most notably the lack of synchro-

nization from binaries with scaled separations of 40. By comparing our results with other observations and computing circularization timescales, we may be able to help constrain tidal theory so that it better matches empirical evidence; this will be discussed in more detail in the next section. We also found from our synchronization analysis that four of our binaries likely evolved independently, and we carried these forward with the single member stars in our examination of how our sample fits in with standard gyrochronology models and angular momentum evolution theory.

We plotted our sample of M67 rotation periods with standard gyrochronology models from Barnes (2007), Mamajek & Hillenbrand (2008), Meibom et al. (2009), Barnes (2010), and Angus et al. (2015). We did the same with the angular momentum evolution (AME) models from Van Saders & Pinsonneault (2013) and van Saders et al. (2016). The gyrochrones from Barnes (2010) and Angus et al. (2015) fit the data best on the gyrochronology side, and each produced an average age of $\sim$4.3 Gyr for the cluster from the periods. However, using any individual star to estimate the cluster's age from either model is very uncertain. With respect to the AME models, the 4.3 Gyr model from Van Saders & Pinsonneault (2013) best describes the data. We unfortunately do not have enough data points in the appropriate regime to test the weakened magnetic braking model of van Saders et al. (2016); it is unclear if the reason for this is due to our conservative approach or real sensitivity limits (see van Saders et al. 2018).

Regardless, while we could potentially achieve a better fit with the AME model by recomputing it at an older age, we could also do the same by generating *younger* gyrochrones. This ambiguity is a result of the scatter in the data. Out of the single-member stars in our sample, the few for which we have more confidence in our final period fit the models of Van Saders & Pinsonneault (2013) and van Saders et al. (2016) better than those from gyrochronology. This suggests that the scatter is a result of the difficulty with the data as opposed to real variation. Overall, while

the AME models appear to do a slightly better job at physically representing the behavior of M67 members, it is encouraging that, together with gyrochronology, we can back out ages around 4.0 Gyr, consistent with the literature. We cannot, however, comment much more on the angular momentum evolution of solar-age stars due to the limitations of our sample.

7.2 Future Work

Because we did not succeed in gaining substantial insight into how M67 fits into angular momentum evolution theory, it is clear that more work needs to be done to fully take advantage of this important cluster. In terms of optimizing our product light curves, we can extend our comparison of the Oxford and CfA pipelines to those of Libralato et al. (2016) and Cody et al. (2018), for example. In addition, the recent release of C16 meant that we had to use a hybrid version of the SAP light curves as opposed to the full CfA, which we have demonstrated does a better job of correcting this type of dataset than the Oxford pipeline. It may be worthwhile, then, redoing the rotation period search using C16 SAP light curves that have been corrected with PDC-MAP. The use of the Oxford pipeline for the SS, however, probably does not make as much of a difference, since it performed similarly to the CfA pipeline in the sinusoidal injection tests and even had a slightly better precision for the C05 light curves. Nonetheless, we may still see some gains from the CfA SS light curves when they become available.

The biggest room for improvement comes from how we determine our rotation periods from *K2* data. We need to refine our approach, making it more streamlined and less strict while still remaining true to the spirit of our sinusoidal injection tests in Chapter 4. The first step would be to conduct a larger round of SSM injection tests than we did in Chapter 5, similar in scale to the sinusoidal ones. In doing so, we can

gain a better understanding of the advantages and disadvantages of the Lomb-Scargle, ACF, and GP, and how they work together. Such tests may also shed light on how the initial guesses for the quality factors affect the GP result. We could accomplish this by initializing the GP for each period several times, either using a range of quality factor ratios or randomizing their selection, and then choosing the final output which maximizes the likelihood. Applying a detection threshold or normalization step for the ACF, analogous to that of the Lomb-Scargle, may also lead to improvements in reliable detections without having to enforce any matching criteria among the three methods, and we can further explore the concept of a GP periodogram. Overall, a larger set of SSM injections will help us optimize period detection for light curves with more realistic signals than those from the sinusoidal tests, leading to a more polished set of rotation periods which meet the standards for publication.

We emphasize, however, that we do not expect the results to substantially change. Even with the addition of C18, which will add another $\sim$50 d of observation, the systematics inherent in *K2* data — with power on timescales similar to that of the periods we expect to see — will still make establishing a quality set of M67 rotation periods very challenging. We can, therefore, begin looking towards future missions which may produce complementary or even better data than that from *K2*. The first of these is the Large Synoptic Survey Telescope, or LSST. While ground-based, LSST is expected to reach photometric magnitudes up to 25 within exposures of 10 – 15 s, with discontinuous time sampling at both short and long cadences (Tyson, 2002; LSST Science Collaboration et al., 2017). The LSST Collaboration have proposed a modified extension of the standard observation strategy to incorporate M67, taking advantage of short-cadence monitoring to avoid saturation from stars brighter than about $V = 16$ (LSST Science Collaboration et al., 2017). In addition, the upcoming, space-based *PLATO* ('PLAnetary Transits and Oscillations of stars') mission, with a magnitude range of $V = 4$ to 16 and wide field-of-view, is designed to characterize

exoplanets and determine stellar ages and masses through asteroseismology (Rauer et al., 2014). At the same time, it will produce light curves ideally-suited for variability studies (Rauer et al., 2014). While its magnitude range is not optimized for M67, *PLATO* may provide valuable complementary data to that of both *K2* and LSST.

Finally, despite the problems we have had in determining rotation periods for the single-member stars in M67, we have had moderate success with the binaries, particularly those with periods of less than 10 d. We have already conducted a preliminary analysis of how our M67 binaries fit into tidal synchronization theory adjusted for empirical evidence; the next step is to determine the circularization timescales. We can then compare our synchronization and circularization timescales with those derived from theory alone, as well as other observations. This may allow us to constrain tidal evolution theory for binaries whose components contain convective envelopes.

7.3 Final Remarks

My restrictive timeline, combined with the difficulty of working with *K2* data to measure the rotation periods of solar-like stars, has left this thesis with an incomplete air about it. We have not made any conclusive claims regarding the angular momentum of stars in M67, which is disappointing, and we have acknowledged that more work needs to be done. However, we have performed the first extensive study of the limits of rotation period detection with *K2* data, highlighting troublesome systematic features that two prominent correction pipelines have been unable to remove. This work is applicable not only to M67 and C05, but all other rotation studies utilizing *K2* data, and even future observations from *TESS*. And while we have seen only a small glimpse of how M67 fits into angular momentum evolution theory, it is my hope that the preliminary analysis conducted here will lead to enhanced detection algorithms which can fully unlock the secrets of this old open cluster.

Appendix A

Result Tables from Injection Tests

Tables A.1 through A.6 present the Chapter 4 sinusoidal injection test completeness from the Oxford and CfA hot star, SAP, and SS samples. Tables A.7 through A.12 provide the sinusoidal reliability, including the number of detections made in each measured period and amplitude range, shown in brackets. The last table in this appendix dealing with the sinusoidal injection tests, Table A.13, illustrates the minimum values of the detection threshold factor C needed to count the measurements for the non-injected light curves reported in Barnes et al. (2016) from the Oxford and CfA pipelines as detections, along with the associated reliability.

The Chapter 5 SSM reliability results are presented in Tables A.16 through A.17. These tables include the completeness both with and without detection criteria for the normalized Lomb-Scargle, used throughout. The SSM tables follow the same general format as the sinusoidal reliability tables, i.e. the number of detections in each measured period and amplitude bin are marked by brackets. The exception is that the measured amplitude is displayed as a_{meas} as opposed to $2\alpha_{peak}$ because the amplitudes were determined differently in the SSM injection tests than they were in the sinusoidal tests.

Table A.1: Oxford Hot Star Completeness (%)

$a_{\rm inj} \setminus P_{\rm inj}$	5d	10d	15d	20d	25d	30d	35d
3.00%	98	95	95	94	94	92	88
1.00%	95	94	88	88	83	73	59
0.50%	92	89	80	70	65	52	35
0.30%	86	80	71	50	48	26	23
0.10%	65	47	27	17	17	11	3
0.05%	41	24	17	12	9	3	2

Total number of injections per period-amplitude bin: 66; $\sigma = \pm 12.3\%$

Table A.2: CfA Hot Star Completeness (%)

$a_{\rm inj} \setminus P_{\rm inj}$	5d	10d	15d	20d	25d	30d	35d
3.00%	100	99	94	91	87	83	80
1.00%	97	93	91	84	81	77	76
0.50%	93	90	86	83	77	73	60
0.30%	91	87	84	80	69	49	34
0.10%	83	66	56	47	44	34	20
0.05%	66	50	36	16	16	13	6

Total number of injections per period-amplitude bin: 70; $\sigma = \pm 12.0\%$

Table A.3: Oxford SAP Completeness (%)

$a_{\rm inj} \setminus P_{\rm inj}$	5d	10d	15d	20d	25d	30d	35d
3.00%	99	97	92	86	85	79	65
1.00%	93	81	75	65	65	56	28
0.50%	82	71	58	43	43	30	8
0.30%	73	59	40	24	21	12	3
0.10%	44	21	5	3	2	1	1
0.05%	21	4	1	1	0	0	0

Total number of injections per period-amplitude bin: 1639; $\sigma = \pm 2.5\%$

Table A.4: CfA SAP Completeness (%)

$a_{\rm inj} \setminus P_{\rm inj}$	5d	10d	15d	20d	25d	30d	35d
3.00%	97	92	89	82	74	72	68
1.00%	91	81	73	66	61	53	39
0.50%	83	69	63	53	47	33	23
0.30%	74	58	52	41	37	30	18
0.10%	54	33	23	18	14	11	7
0.05%	35	19	9	5	3	2	2

Total number of injections per period-amplitude bin: 1587; $\sigma = \pm 2.5\%$

Table A.5: Oxford SS Completeness (%)

$a_{\rm inj} \setminus P_{\rm inj}$	5d	10d	15d	20d	25d	30d	35d
3.00%	100	98	93	88	89	77	74
1.00%	91	81	74	65	66	50	46
0.50%	78	66	54	46	46	37	34
0.30%	68	50	41	38	37	27	24
0.10%	39	30	23	15	13	2	2
0.05%	28	14	8	3	2	0	0

Total number of injections per period-amplitude bin: 843; $\sigma = \pm 3.4\%$

Table A.6: CfA SS Completeness (%)

$a_{\rm inj} \setminus P_{\rm inj}$	5d	10d	15d	20d	25d	30d	35d
3.00%	93	86	83	74	63	56	51
1.00%	82	70	61	52	45	36	27
0.50%	69	57	50	40	34	27	23
0.30%	58	47	41	34	31	26	16
0.10%	42	31	21	15	15	11	7
0.05%	29	15	10	5	4	4	2

Total number of injections per period-amplitude bin: 844; $\sigma = \pm 3.4\%$

Table A.7: Oxford Hot Star Reliability (%)

$2\alpha_{peak}/p_{peak}$	5±2.5d	10±2.5d	15±2.5d	20±2.5d	25±2.5d	30±2.5d	32.5d+
≥2.00%	100 ±12.4 [65]	98 ±12.5 [64]	100 ±12.6 [63]	98 ±12.6 [63]	100 ±12.7 [62]	100 ±12.8 [61]	100 ±13.1 [58]
0.75-2.00%	100 ±12.6 [63]	100 ±12.7 [62]	98 ±13.0 [59]	100 ±13.1 [58]	98 ±13.4 [56]	100 ±14.1 [50]	100 ±16.4 [37]
0.45-0.75%	100 ±13.0 [59]	100 ±13.5 [55]	100 ±13.9 [52]	100 ±16.0 [39]	100 ±16.7 [36]	100 ±17.1 [34]	94 ±24.3 [17]
0.25-0.45%	98 ±12.9 [60]	100 ±13.5 [55]	100 ±14.4 [48]	97 ±16.0 [39]	100 ±16.0 [39]	100 ±22.9 [19]	62 ±17.7 [32]
0.075-0.25%	93 ±14.7 [46]	100 ±17.4 [33]	100 ±23.6 [18]	100 ±26.7 [14]	100 ±30.2 [11]	100 ±37.8 [7]	100 ±70.7 [2]
<0.075%	93 ±18.6 [29]	100 ±25.0 [16]	100 ±30.2 [11]	100 ±37.8 [7]	100 ±37.8 [7]	100 ±70.7 [2]	– [0]

Table A.8: CfA Hot Star Reliability (%)

$2\alpha_{peak}/p_{peak}$	5±2.5d	10±2.5d	15±2.5d	20±2.5d	25±2.5d	30±2.5d	32.5d+
≥2.00%	100 ±12.0 [70]	100 ±12.0 [69]	100 ±12.3 [66]	100 ±12.7 [62]	100 ±13. [59]	100 ±13.4 [56]	100 ±13.4 [56]
0.75-2.00%	100 ±12.1 [68]	98 ±12.3 [66]	100 ±12.5 [64]	100 ±13.0 [59]	100 ±13.6 [54]	100 ±13.2 [57]	100 ±13.7 [53]
0.45-0.75%	100 ±12.5 [64]	100 ±12.7 [62]	100 ±13.0 [59]	100 ±13.2 [57]	100 ±13.9 [52]	100 ±15.1 [44]	100 ±17.1 [34]
0.25-0.45%	100 ±12.4 [65]	100 ±12.9 [60]	100 ±13.0 [59]	100 ±13.1 [58]	100 ±14.1 [50]	98 ±15.6 [41]	100 ±18.0 [31]
0.075-0.25%	95 ±12.8 [61]	100 ±14.3 [49]	98 ±15.2 [43]	100 ±17.4 [33]	100 ±18.9 [28]	100 ±18.9 [28]	87 ±25.8 [15]
<0.075%	84 ±13.5 [55]	97 ±16.9 [35]	96 ±20.4 [24]	93 ±25.8 [15]	100 ±27.7 [13]	100 ±28.9 [12]	100 ±57.7 [3]

Table A.9: Oxford SAP Reliability (%)

$2\alpha_{peak}/p_{peak}$	5±2.5d	10±2.5d	15±2.5d	20±2.5d	25±2.5d	30±2.5d	32.5d+
≥2.00%	100 ±2.5	99 ±2.5	99 ±2.6	100 ±2.7	99 ±2.7	99 ±2.6	96 ±3.2
	[1620]	[1598]	[1525]	[1414]	[1405]	[1440]	[996]
0.75-2.00%	100 ±2.6	98 ±2.7	99 ±2.8	100 ±3.0	98 ±3.0	99 ±3.1	88 ±4.7
	[1523]	[1364]	[1250]	[1076]	[1095]	[1025]	[456]
0.45-0.75%	100 ±2.8	98 ±3.1	98 ±3.5	100 ±4.3	98 ±4.0	98 ±4.5	46 ±6.2
	[1267]	[1065]	[812]	[534]	[623]	[495]	[261]
0.25-0.45%	98 ±2.8	98 ±3.1	98 ±3.6	100 ±4.4	100 ±5.1	99 ±6.8	33 ±7.4
	[1278]	[1074]	[768]	[519]	[391]	[214]	[184]
0.075-0.25%	95 ±3.5	97 ±5.1	85 ±7.8	99 ±10.3	98 ±14.4	95 ±22.9	20 ±14.3
	[832]	[386]	[165]	[95]	[48]	[19]	[49]
<0.075%	83 ±5.3	97 ±12.4	100 ±22.4	100 ±25.0	100 ±44.7	100 ±100.0	100 ±100.0
	[358]	[65]	[20]	[16]	[5]	[1]	[1]

Table A.10: CfA SAP Reliability (%)

$2\alpha_{peak}/p_{peak}$	5±2.5d	10±2.5d	15±2.5d	20±2.5d	25±2.5d	30±2.5d	32.5d+
≥2.00%	98 ±2.5	95 ±2.5	99 ±2.6	100 ±2.8	97 ±2.9	98 ±2.9	100 ±3.1
	[1567]	[1539]	[1426]	[1293]	[1194]	[1172]	[1070]
0.75-2.00%	100 ±2.6	98 ±2.8	96 ±2.8	99 ±3.0	99 ±3.2	96 ±3.3	92 ±3.9
	[1470]	[1316]	[1245]	[1078]	[954]	[903]	[667]
0.45-0.75%	98 ±2.8	97 ±3.1	93 ±3.1	95 ±3.5	96 ±3.8	92 ±4.2	90 ±5.5
	[1313]	[1057]	[1011]	[797]	[677]	[567]	[333]
0.25-0.45%	98 ±2.9	93 ±3.1	95 ±3.3	98 ±3.7	96 ±4.0	93 ±4.0	82 ±5.2
	[1213]	[1050]	[896]	[721]	[640]	[618]	[365]
0.075-0.25%	96 ±3.3	98 ±4.2	91 ±4.8	98 ±5.5	95 ±6.8	94 ±6.5	75 ±7.8
	[915]	[575]	[426]	[329]	[217]	[237]	[165]
<0.075%	95 ±4.2	95 ±5.9	95 ±8.6	100 ±13.4	88 ±15.2	100 ±16.7	93 ±26.7
	[572]	[291]	[134]	[56]	[43]	[36]	[14]

Table A.11: Oxford SS Reliability (%)

$2\alpha_{peak}/p_{peak}$	5±2.5d	10±2.5d	15±2.5d	20±2.5d	25±2.5d	30±2.5d	32.5d+
≥2.00%	–	100 ±100.0	75 ±25.0	35 ±15.8	100 ±27.7	86 ±37.8	36 ±13.4
	[0]	[1]	[16]	[40]	[13]	[7]	[56]
0.75-2.00%	95 ±3.4	100 ±3.5	99 ±3.5	99 ±3.6	100 ±3.6	99 ±3.9	99 ±4.0
	[886]	[826]	[797]	[752]	[760]	[657]	[620]
0.45-0.75%	100 ±3.7	100 ±3.9	98 ±4.1	96 ±4.5	95 ±4.5	99 ±6.8	92 ±7.2
	[739]	[652]	[584]	[497]	[501]	[215]	[191]
0.25-0.45%	92 ±4.9	100 ±5.7	99 ±6.0	99 ±6.6	98 ±6.4	99 ±6.0	96 ±6.2
	[421]	[311]	[279]	[227]	[246]	[274]	[262]
0.075-0.25%	98 ±3.3	98 ±3.7	97 ±4.1	99 ±4.2	99 ±4.2	99 ±4.6	96 ±4.8
	[898]	[713]	[601]	[558]	[563]	[478]	[442]
<0.075%	99 ±4.2	96 ±5.1	96 ±6.3	94 ±8.3	97 ±9.4	84 ±20.0	70 ±22.4
	[557]	[388]	[253]	[145]	[114]	[25]	[20]

Table A.12: CfA SS Reliability (%)

$2\alpha_{peak}/p_{peak}$	5±2.5d	10±2.5d	15±2.5d	20±2.5d	25±2.5d	30±2.5d	32.5d+
≥2.00%	97 ±3.5	95 ±3.6	99 ±3.8	100 ±4.0	93 ±4.3	96 ±4.4	97 ±4.9
	[810]	[768]	[703]	[620]	[545]	[513]	[411]
0.75-2.00%	94 ±3.7	96 ±4.0	87 ±4.0	98 ±4.8	94 ±5.0	91 ±5.0	80 ±6.4
	[740]	[619]	[613]	[428]	[394]	[405]	[241]
0.45-0.75%	97 ±4.2	95 ±4.6	91 ±4.9	91 ±5.5	82 ±6.3	88 ±5.8	72 ±8.8
	[568]	[477]	[418]	[329]	[256]	[302]	[128]
0.25-0.45%	87 ±4.1	92 ±4.8	89 ±4.9	96 ±5.7	84 ±6.0	87 ±5.0	75 ±7.4
	[587]	[434]	[418]	[312]	[278]	[396]	[183]
0.075-0.25%	93 ±5.0	79 ±5.3	82 ±6.6	94 ±7.1	98 ±8.5	93 ±8.0	67 ±10.6
	[400]	[356]	[232]	[199]	[139]	[158]	[89]
<0.075%	97 ±6.4	84 ±8.4	97 ±11.9	96 ±14.9	91 ±20.9	95 ±21.8	80 ±25.8
	[241]	[141]	[71]	[45]	[23]	[21]	[15]

Table A.13: Minimum Detection Threshold Factors for Barnes et al. (2016)

EPIC	Barnes Per (d)	Ox Per (d)	Ox C	Ox Rel (%)	CfA Per (d)	CfA C	CfA Rel (%)
211388204	31.8	2.2	1	6 ±3.2	2.1	1	26 ±8.0
211394185	30.4	15.4	4	98 ±3.6	15.1	4	95 ±3.3
211395620	30.7	28.5	2	98 ±4.5	3.5	2	38 ±3.3
211397319	25.1	7.9	2	96 ±12.0	47.6	1	54 ±16.0
211397512	34.5	16.4	4	98 ±3.6	38.4	3	85 ±5.7
211398025	28.8	22.2	2	100 ±28.9	10.4	2	78 ±4.5
211398541	30.3	5.3	–	–	16.9	2	77 ±5.0
211399458	30.2	7.9	2	86 ±4.5	4.32	1	17 ±5.2
211399819	28.4	13.9	2	36 ±2.4	2.1	1	17 ±5.2
211400500	26.9	13.5	3	82 ±6.6	2.0	2	38 ±3.3
211406596	26.9	31.2	2	85 ±6.9	2.4	1	26 ±8.0
211410757	18.9	18.8	–	–	9.4	3	93 ±5.6
211411477	31.2	5.7	1	6 ±3.2	5.7	1	26 ±8.0
211411621	30.5	15.8	4	85 ±7.8	16.1	4	91 ±4.8
211413212	24.4	5.3	1	6 ±3.2	7.5	1	61 ±14.7
211413961	31.4	2.9	1	6 ±3.2	15.4	3	88 ±4.5
211414799	18.1	4.6	3	100 ±20.9	9.0	4	98 ±4.2
211423010	24.9	20.8	2	92 ±7.8	22.2	4	98 ±5.5
211428580	26.9	5.1	1	6 ±3.2	2.4	1	26 ±8.0
211430274	31.1	23.2	2	89 ±11.2	27.0	2	93 ±6.8

The columns from left to right are EPIC, the associated period reported from Barnes et al. (2016), the period from the Oxford pipeline, the Oxford threshold factor C that results in a detection, the corresponding value for reliability, the period from the CfA pipeline, the CfA detection value for C, and the CfA reliability.

Table A.14: SSM Lomb-Scargle Reliability without Detections (%)

$a_{\mathrm{meas}}/p_{peak}$	<15 d	15–22.5 d	22.5–27.5 d	27.5–32.5 d	≥32.5 d
≥0.25%	0 ±4.4	71 ±7.2	93 ±12.8	98 ±10.5	8 ±11.9
	[503]	[192]	[61]	[90]	[71]
0.15-0.25%	0 ±15.4	87 ±18.3	88 ±24.3	78 ±33.3	20 ±31.6
	[42]	[30]	[17]	[9]	[10]
0.05-0.15%	0 ±30.2	90 ±22.4	93 ±25.8	100 ±33.3	–
	[11]	[20]	[15]	[9]	[0]

Table A.15: SSM Lomb-Scargle Reliability with Detections (%)

$a_{\mathrm{meas}}/p_{peak}$	<15 d	15–22.5 d	22.5–27.5 d	27.5–32.5 d	≥32.5 d
≥0.25%	0 ±27.7	85 ±16.0	91 ±20.9	100 ±18.6	33 ±57.7
	[13]	[39]	[23]	[29]	[3]
0.15-0.25%	0 ±44.7	95 ±21.3	92 ±28.9	78 ±33.3	–
	[5]	[22]	[12]	[9]	[0]
0.05-0.15%	–	94 ±23.6	100 ±31.6	100 ±57.7	–
	[0]	[18]	[10]	[3]	[0]

Table A.16: SSM ACF Reliability (%)

$a_{\mathrm{meas}}/p_{peak}$	<15 d	15–22.5 d	22.5–27.5 d	27.5–32.5 d	≥32.5 d
≥0.25%	0 ±11.5	67 ±7.6	100 ±16.4	86 ±8.7	4 ±4.5
	[76]	[172]	[37]	[133]	[499]
0.15-0.25%	0 ±37.8	84 ±17.7	94 ±25.0	63 ±25.0	8±16.4
	[7]	[32]	[16]	[16]	[37]
0.05-0.15%	–	92 ±28.9	100 ±30.2	82 ±30.2	10 ±21.8
	[0]	[12]	[11]	[11]	[21]

Table A.17: SSM GP Reliability (%)

$a_{\mathrm{meas}}/p_{peak}$	<15 d	15–22.5 d	22.5–27.5 d	27.5–32.5 d	≥32.5 d
≥0.25%	0 ±5.6	48 ±5.9	83 ±14.4	96 ±13.9	44 ±33.3
	[320]	[286]	[48]	[52]	[9]
0.15-0.25%	0 ±14.9	88 ±20.0	89 ±22.9	70 ±31.6	80 ±44.7
	[45]	[25]	[19]	[10]	[5]
0.05-0.15%	0 ±57.7	86 ±21.3	90 ±22.4	83 ±40.8	0 ±50.0
	[3]	[22]	[20]	[6]	[4]

Appendix B

M67 Light Curves

We present in the following two pages the light curves of those M67 stars for which we have rotation periods. We display them in two groups. The first are those from stars which did not overlap in the C05 and C16 samples, plotted in blue with the GP predictive mean shown in red. The second group is comprised of the light curves of those stars which do overlap in both campaigns. Here, the flux is plotted in black, but the GP predictive mean is again in red. A vertical, dashed blue line indicates the break between the C05 and C16, although the two campaigns are in reality separated by $\sim$2.6 yr. For all light curves, we plot flux versus total observation time rather than Julian date.

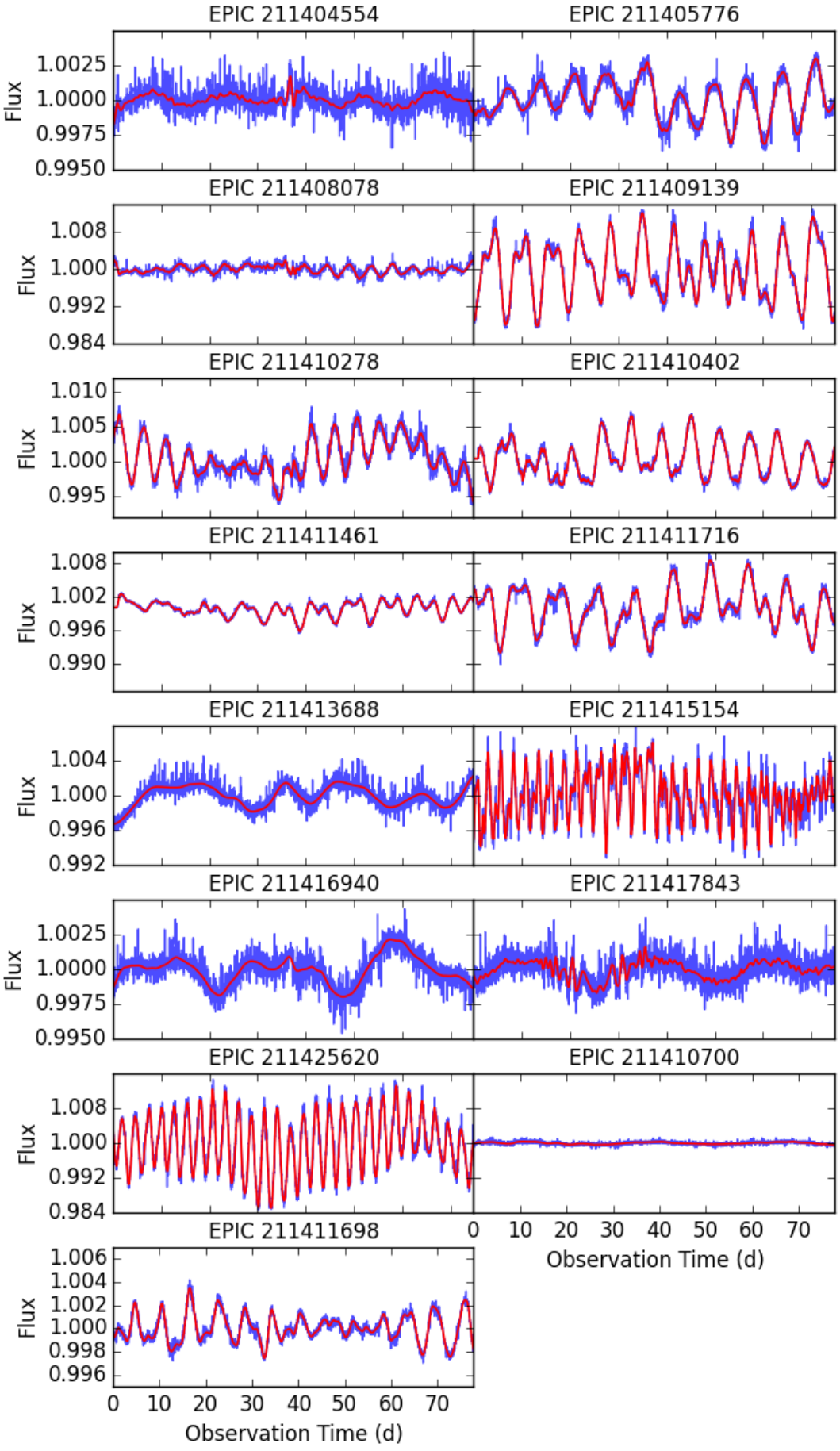
EPIC 211404554
EPIC 211405776
EPIC 211408078
EPIC 211409139
EPIC 211410278
EPIC 211410402
EPIC 211411461
EPIC 211411716
EPIC 211413688
EPIC 211415154
EPIC 211416940
EPIC 211417843
EPIC 211425620
EPIC 211410700
EPIC 211411698
Flux
Observation Time (d)

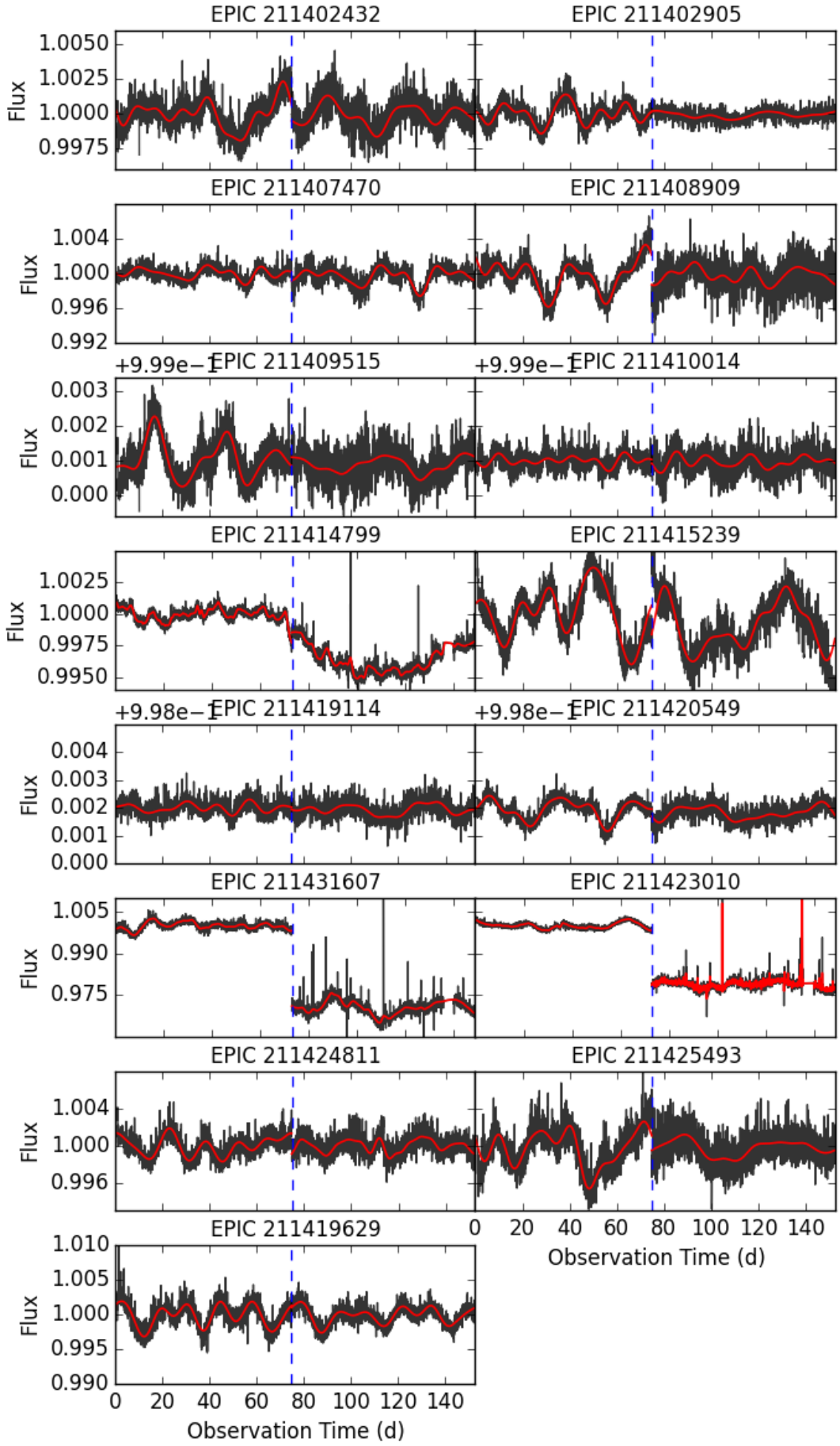
EPIC 211402432
EPIC 211402905
EPIC 211407470
EPIC 211408909
+9.99e−1
EPIC 211409515
+9.99e−1
EPIC 211410014
EPIC 211414799
EPIC 211415239
+9.98e−1
EPIC 211419114
+9.98e−1
EPIC 211420549
EPIC 211431607
EPIC 211423010
EPIC 211424811
EPIC 211425493
EPIC 211419629
Flux
Observation Time (d)

Bibliography

Abt, H. A., 1970. Catalog of Individual Radial Velocities, 0h-12h, Measured by Astronomers of the Mount Wilson Observatory. *The Astrophysical Journal Supplement Series*, **19**, 387.

Abt, H. A., 1973. Catalog of Individual Radial Velocities, 12ˆ{h}-24ˆ{h}, Measured by Astronomers of the Mount Wilson Observatory. *The Astrophysical Journal Supplement Series*, **26**, 365.

Abt, H. A. & Hunter Jr, J. H., 1962. Stellar Rotation in Galactic Clusters. *The Astrophysical Journal*, **136**, 381.

Aerts, C., Christensen-Dalsgaard, J. & Kurtz, D. W., 2010. *Asteroseismology*. Springer Science & Business Media.

Affer, L., Micela, G., Favata, F., Flaccomio, E. & Bouvier, J., 2013. Rotation in NGC 2264: a study based on CoRoT photometric observations. *Monthly Notices of the Royal Astronomical Society*, **430**(2), 1433–1446.

Aigrain, S., Cameron, A. C., Ollivier, M., Pont, F., Jorda, L., Almenara, J., Alonso, R., Barge, P., Bordé, P., Bouchy, F. et al., 2008. Transiting exoplanets from the CoRoT space mission-IV. CoRoT-Exo-4b: a transiting planet in a 9.2 day synchronous orbit. *Astronomy & Astrophysics*, **488**(2), L43–L46.

Aigrain, S., Hodgkin, S., Irwin, J., Hebb, L., Irwin, M., Favata, F., Moraux, E. & Pont, F., 2007. The Monitor project: searching for occultations in young open clusters. *Monthly Notices of the Royal Astronomical Society*, **375**(1), 29–52.

Aigrain, S., Hodgkin, S. T., Irwin, M. J., Lewis, J. R. & Roberts, S. J., 2015a. Precise time series photometry for the Kepler-2.0 mission. *MNRAS*, **447**, 2880–2893.

Aigrain, S., Llama, J., Ceillier, T., Chagas, M. L. d., Davenport, J. R. A., García, R. A., Hay, K. L., Lanza, A. F., McQuillan, A., Mazeh, T., de Medeiros, J. R., Nielsen, M. B. & Reinhold, T., 2015b. Testing the recovery of stellar rotation signals from Kepler light curves using a blind hare-and-hounds exercise. *MNRAS*, **450**, 3211–3226.

Aigrain, S., Parviainen, H. & Pope, B. J. S., 2016. K2SC: flexible systematics correction and detrending of K2 light curves using Gaussian process regression. *MNRAS*, **459**, 2408–2419.

Aigrain, S., Parviainen, H., Roberts, S., Reece, S. & Evans, T., 2017. Robust, open-source removal of systematics in Kepler data. *Monthly Notices of the Royal Astronomical Society*, **471**(1), 759–769.

Aigrain, S., Pont, F. & Zucker, S., 2012. A simple method to estimate radial velocity variations due to stellar activity using photometry. *Monthly notices of the royal astronomical society*, **419**(4), 3147–3158.

Alard, C. & Lupton, R. H., 1998. A method for optimal image subtraction. *The Astrophysical*

Journal, **503**(1), 325.

Albrecht, S., Winn, J. N., Johnson, J. A., Howard, A. W., Marcy, G. W., Butler, R. P., Arriagada, P., Crane, J. D., Shectman, S. A., Thompson, I. B. et al., 2012. Obliquities of hot Jupiter host stars: Evidence for tidal interactions and primordial misalignments. *The Astrophysical Journal*, **757**(1), 18.

Albrow, M., Beaulieu, J.-P., Birch, P., Caldwell, J., Kane, S., Martin, R., Menzies, J., Naber, R., Pel, J.-W., Pollard, K. et al., 1998. The 1995 pilot campaign of PLANET: searching for microlensing anomalies through precise, rapid, round-the-clock monitoring. *The Astrophysical Journal*, **509**(2), 687.

Albrow, M., Horne, K., Bramich, D., Fouqué, P., Miller, V., Beaulieu, J.-P., Coutures, C., Menzies, J., Williams, A., Batista, V. et al., 2009. Difference imaging photometry of blended gravitational microlensing events with a numerical kernel. *Monthly Notices of the Royal Astronomical Society*, **397**(4), 2099–2105.

Alonso, R., Auvergne, M., Baglin, A., Ollivier, M., Moutou, C., Rouan, D., Deeg, H., Aigrain, S., Almenara, J., Barbieri, M. et al., 2008. Transiting exoplanets from the CoRoT space mission-II. CoRoT-Exo-2b: a transiting planet around an active G star. *Astronomy & Astrophysics*, **482**(3), L21–L24.

Ambikasaran, S., Foreman-Mackey, D., Greengard, L., Hogg, D. W. & O'Neil, M., 2016. Fast Direct Methods for Gaussian Processes. *IEEE transactions on pattern analysis and machine intelligence*, **38**(2), 252–265.

Anderson, E. R., Duvall, Jr., T. L. & Jefferies, S. M., 1990. Modeling of solar oscillation power spectra. *ApJ*, **364**, 699–705.

Anderson, J., Bedin, L. R., Piotto, G., Yadav, R. S. & Bellini, A., 2006. Ground-based CCD astrometry with wide field imagers-I. Observations just a few years apart allow decontamination of field objects from members in two globular clusters. *Astronomy & Astrophysics*, **454**(3), 1029–1045.

Anderson, J. & King, I. R., 2000. Toward high-precision astrometry with WFPC2. I. deriving an accurate point-spread function. *Publications of the Astronomical Society of the Pacific*, **112**(776), 1360.

Angus, R., Aigrain, S., Foreman-Mackey, D. & McQuillan, A., 2015. Calibrating gyrochronology using Kepler asteroseismic targets. *MNRAS*, **450**, 1787–1798.

Angus, R., Morton, T., Aigrain, S., Foreman-Mackey, D. & Rajpaul, V., 2017. Inferring probabilistic stellar rotation periods using Gaussian processes. *ArXiv e-prints*.

Appourchaux, T., Michel, E., Auvergne, M., Baglin, A., Toutain, T., Baudin, F., Benomar, O., Chaplin, W. J., Deheuvels, S., Samadi, R. et al., 2008. CoRoT sounds the stars: p-mode parameters of Sun-like oscillations on HD 49933. *Astronomy & Astrophysics*, **488**(2), 705–714.

Armstrong, D. J., Kirk, J., Lam, K. W. F., McCormac, J., Osborn, H. P., Spake, J., Walker, S., Brown, D. J. A., Kristiansen, M. H., Pollacco, D., West, R. & Wheatley, P. J., 2016. K2 variable catalogue - II. Machine learning classification of variable stars and eclipsing binaries in K2 fields 0-4. *MNRAS*, **456**, 2260–2272.

Armstrong, D. J., Osborn, H. P., Brown, D. J. A., Kirk, J., Lam, K. W. F., Pollacco, D. L., Spake, J. & Walker, S. R., 2014. K2 Variable Catalogue I: A Catalogue of Variable

Stars from K2 Field 0. *ArXiv e-prints*.

Auer, L. & Van Altena, W., 1978. Digital image centering. II. *The Astronomical Journal*, **83**, 531–537.

Baglinl, A., Auvergne, M., Barge, P. & Deleuil, M., 2009. CoRoT: Description of the Mission and Early Results. *Transiting Planets (IAU S253)*, **253**(253), 71.

Bakos, G., Kovács, G., Torres, G., Fischer, D., Latham, D., Noyes, R., Sasselov, D., Mazeh, T., Shporer, A., Butler, R. et al., 2007. HD 147506b: a supermassive planet in an eccentric orbit transiting a bright star. *The Astrophysical Journal*, **670**(1), 826.

Bakos, G., Noyes, R. W., Kovács, G., Stanek, K. Z., Sasselov, D. D. & Domsa, I., 2004. Wide-Field Millimagnitude Photometry with the HAT: A Tool for Extrasolar Planet Detection. *PASP*, **116**, 266–277.

Bakos, G., Torres, G., Pál, A., Hartman, J., Kovács, G., Noyes, R., Latham, D., Sasselov, D., Sipőcz, B., Esquerdo, G. et al., 2010. HAT-P-11b: a super-Neptune planet transiting a bright K star in the Kepler field. *The Astrophysical Journal*, **710**(2), 1724.

Balaguer-Núñez, L., Galadí-Enríquez, D. & Jordi, C., 2007. uvby - H_{beta} CCD photometry and membership segregation of the open cluster NGC 2682 (M 67). *A&A*, **470**, 585–596.

Baliunas, S. L., Donahue, R. A., Soon, W. & Henry, G. W., 1998. Activity Cycles in Lower Main Sequence and POST Main Sequence Stars: The HK Project. In R. A. Donahue & J. A. Bookbinder, eds., *Cool Stars, Stellar Systems, and the Sun*, vol. 154 of *Astronomical Society of the Pacific Conference Series*, 153.

Baliunas, S. L., Nesme-Ribes, E., Sokoloff, D. & Soon, W. H., 1996. A Dynamo Interpretation of Stellar Activity Cycles. *ApJ*, **460**, 848.

Ballard, S., Charbonneau, D., Deming, D., Knutson, H. A., Christiansen, J. L., Holman, M. J., Fabrycky, D., Seager, S. & A?Hearn, M. F., 2010. A search for a sub-Earth-sized companion to GJ 436 and a novel method to calibrate warm Spitzer IRAC observations. *Publications of the Astronomical Society of the Pacific*, **122**(897), 1341.

Barge, P., Baglin, A., Auvergne, M., Rauer, H., Léger, A., Schneider, J., Pont, F., Aigrain, S., Almenara, J.-M., Alonso, R. et al., 2008. Transiting exoplanets from the CoRoT space mission-I. CoRoT-Exo-1b: a low-density short-period planet around a G0V star. *Astronomy & Astrophysics*, **482**(3), L17–L20.

Barnes, S. A., 2003. On the Rotational Evolution of Solar- and Late-Type Stars, Its Magnetic Origins, and the Possibility of Stellar Gyrochronology. *ApJ*, **586**, 464–479.

Barnes, S. A., 2007. Ages for Illustrative Field Stars Using Gyrochronology: Viability, Limitations, and Errors. *ApJ*, **669**, 1167–1189.

Barnes, S. A., 2010. A simple nonlinear model for the rotation of main-sequence cool stars. I. Introduction, implications for gyrochronology, and color-period diagrams. *The Astrophysical Journal*, **722**(1), 222.

Barnes, S. A. & Kim, Y.-C., 2010. Angular Momentum Loss from Cool Stars: An Empirical Expression and Connection to Stellar Activity. *ApJ*, **721**, 675–685.

Barnes, S. A., Weingrill, J., Fritzewski, D., Strassmeier, K. G. & Platais, I., 2016. Rotation Periods for Cool Stars in the 4 Gyr old Open Cluster M67, The Solar–Stellar Connection, and the Applicability of Gyrochronology to at least Solar Age. *ApJ*, **823**, 16.

Belcher, J. & MacGregor, K., 1976. Magnetic acceleration of winds from solar-type stars. *The*

Astrophysical Journal, **210**, 498–507.

Berta-Thompson, Z. K., Irwin, J., Charbonneau, D., Newton, E. R., Dittmann, J. A. et al., 2015. A rocky planet transiting a nearby low-mass star. *Nature*, **527**, 204–207.

Bertelli, G., Bressan, A., Chiosi, C., Fagotto, F. & Nasi, E., 1994. Theoretical isochrones from models with new radiative opacities. *A&AS*, **106**, 275–302.

Bildsten, L., Brown, E. F., Matzner, C. D. & Ushomirsky, G., 1997. Lithium Depletion in Fully Convective Pre-Main-Sequence Stars. *The Astrophysical Journal*, **482**(1), 442.

Binks, A. S. & Jeffries, R. D., 2014. A lithium depletion boundary age of 21 Myr for the Beta Pictoris moving group. *MNRAS*, **438**, L11–L15.

Blaauw, A., 1964. The O Associations in the Solar Neighborhood. *ARA&A*, **2**, 213.

Borucki, W. J., Koch, D., Basri, G., Batalha, N., Brown, T. et al., 2010. Kepler Planet-Detection Mission: Introduction and First Results. *Science*, **327**(5968), 977–980. ISSN 0036-8075.

Bouchy, F., Queloz, D., Deleuil, M., Loeillet, B., Hatzes, A., Aigrain, S., Alonso, R., Auvergne, M., Baglin, A., Barge, P. et al., 2008. Transiting exoplanets from the CoRoT space mission-III. The spectroscopic transit of CoRoT-Exo-2b with SOPHIE and HARPS. *Astronomy & Astrophysics*, **482**(3), L25–L28.

Bradshaw, S. J. & Hartigan, P., 2014. On sunspot and starspot lifetimes. *The Astrophysical Journal*, **795**(1), 79.

Bressan, A., Fagotto, F., Bertelli, G. & Chiosi, C., 1993. Evolutionary sequences of stellar models with new radiative opacities. II - Z = 0.02. *A&AS*, **100**, 647–664.

Bressan, A., Marigo, P., Girardi, L., Salasnich, B., Dal Cero, C., Rubele, S. & Nanni, A., 2012. PARSEC: stellar tracks and isochrones with the PAdova and TRieste Stellar Evolution Code. *Monthly Notices of the Royal Astronomical Society*, **427**(1), 127–145.

Brown, T. M., Christensen-Dalsgaard, J., Weibel-Mihalas, B. & Gilliland, R. L., 1994. The effectiveness of oscillation frequencies in constraining stellar model parameters. *ApJ*, **427**, 1013–1034.

Brown, T. M. & Gilliland, R. L., 1994. Asteroseismology. *Annual Review of Astronomy and Astrophysics*, **32**(1), 37–82.

Bruntt, H., 2009. Accurate fundamental parameters of CoRoT asteroseismic targets-The solar-like stars HD 49933, HD 175726, HD 181420, and HD 181906. *Astronomy & Astrophysics*, **506**(1), 235–244.

Bryson, S. T., Tenenbaum, P., Jenkins, J. M., Chandrasekaran, H., Klaus, T., Caldwell, D. A., Gilliland, R. L., Haas, M. R., Dotson, J. L., Koch, D. G. & Borucki, W. J., 2010. The Kepler Pixel Response Function. *ApJ*, **713**, L97–L102.

Burbidge, E. M., Burbidge, G. R., Fowler, W. A. & Hoyle, F., 1957. Synthesis of the Elements in Stars. *Rev. Mod. Phys.*, **29**, 547–650.

Burke, C. J., Pinsonneault, M. H. & Sills, A., 2004. Theoretical Examination of the Lithium Depletion Boundary. *ApJ*, **604**, 272–283.

Burke, Jr., E. W., Rolland, W. W. & Boy, W. R., 1970. A Photoelectric Study of Magnetic Variable Stars. *JRASC*, **64**, 353.

Carraro, G., Chiosi, C., Bressan, A. & Bertelli, G., 1994. Five old open clusters: NGC 2682, NGC 2243, Berkeley 39, NGC 188 and NGC 6791. *A&AS*, **103**.

Ceillier, T., García, R. A., Salabert, D. & Mathur, S., 2014. Surface rotation of solar-like oscillating stars. In J. Ballet, F. Martins, F. Bournaud, R. Monier & C. Reylé, eds., *SF2A-2014: Proceedings of the Annual meeting of the French Society of Astronomy and Astrophysics*, 467–469.

Chaboyer, B., Demarque, P. & Pinsonneault, M. H., 1995a. Stellar models with microscopic diffusion and rotational mixing. 1: Application to the Sun. *ApJ*, **441**, 865–875.

Chaboyer, B., Demarque, P. & Pinsonneault, M. H., 1995b. Stellar models with microscopic diffusion and rotational mixing. 2: Application to open clusters. *ApJ*, **441**, 876–885.

Chaplin, W. J., Basu, S., Huber, D., Serenelli, A., Casagrande, L. et al., 2014. Asteroseismic Fundamental Properties of Solar-type Stars Observed by the NASA Kepler Mission. *The Astrophysical Journal Supplement Series*, **210**(1), 1.

Chaplin, W. J., Lund, M. N., Handberg, R., Basu, S., Buchhave, L. A. et al., 2015. Asteroseismology of Solar-Type Stars with K2: Detection of Oscillations in C1 Data. *PASP*, **127**, 1038.

Charbonneau, D., Allen, L. E., Megeath, S. T., Torres, G., Alonso, R., Brown, T. M., Gilliland, R. L., Latham, D. W., Mandushev, G., O'Donovan, F. T. et al., 2005. Detection of thermal emission from an extrasolar planet. *The Astrophysical Journal*, **626**(1), 523.

Charbonneau, D., Brown, T. M., Latham, D. W. & Mayor, M., 2000. Detection of Planetary Transits Across a Sun-like Star. *ApJ*, **529**, L45–L48.

Charbonneau, P. & MacGregor, K., 1992. Angular momentum transport in magnetized stellar radiative zones. I-Numerical solutions to the core spin-up model problem. *The Astrophysical Journal*, **387**, 639–661.

Charbonneau, P. & MacGregor, K., 1993. Angular momentum transport in magnetized stellar radiative zones. II. The solar spin-down. *The Astrophysical Journal*, **417**, 762.

Charbonnel, C., Decressin, T., Amard, L., Palacios, A. & Talon, S., 2013. Impact of internal gravity waves on the rotation profile inside pre-main sequence low-mass stars. *Astronomy & Astrophysics*, **554**, A40.

Charbonnel, C. & Talon, S., 2005. Influence of gravity waves on the internal rotation and Li abundance of solar-type stars. *Science*, **309**(5744), 2189–2191.

Choi, J., Dotter, A., Conroy, C., Cantiello, M., Paxton, B. & Johnson, B. D., 2016. Mesa isochrones and stellar tracks (MIST). I. Solar-scaled models. *The Astrophysical Journal*, **823**(2), 102.

Christensen-Dalsgaard, J., 1988. A Hertzsprung-Russell Diagram for Stellar Oscillations. In J. Christensen-Dalsgaard & S. Frandsen, eds., *Advances in Helio- and Asteroseismology*, vol. 123 of *IAU Symposium*, 295.

Christiansen, J. L., Jenkins, J. M., Caldwell, D. A., Burke, C. J., Tenenbaum, P., Seader, S., Thompson, S. E., Barclay, T. S., Clarke, B. D., Li, J., Smith, J. C., Stumpe, M. C., Twicken, J. D. & Van Cleve, J., 2012. The Derivation, Properties, and Value of Kepler's Combined Differential Photometric Precision. *PASP*, **124**, 1279–1287.

Cody, A. M., Barentsen, G., Hedges, C., Gully-Santiago, M. & de Miranda Cardoso, J. V., 2018. K2SUPERSTAMP: The Release of Calibrated Mosaics for the Kepler / K2 Mission. *Research Notes of the AAS*, **2**(1), 25.

Collier Cameron, A., Davidson, V. A., Hebb, L., Skinner, G., Anderson, D. R. et al., 2009. The main-sequence rotation-colour relation in the Coma Berenices open cluster. *MNRAS*,

400, 451–462.

Cowan, J. J., Thielemann, F.-K. & Truran, J. W., 1987. Nuclear chronometers from the r-process and the age of the galaxy. *ApJ*, **323**, 543–552.

Cowan, J. J., Thielemann, F.-K. & Truran, J. W., 1991. Radioactive Dating of the Elements. *Annual Review of Astronomy and Astrophysics*, **29**(1), 447–497.

Cowan, N. B., Machalek, P., Croll, B., Shekhtman, L. M., Burrows, A., Deming, D., Greene, T. & Hora, J. L., 2012. Thermal phase variations of WASP-12b: Defying predictions. *The Astrophysical Journal*, **747**(1), 82.

Cox, J., 1980. Theory of stellar pulsation, Research supported by the National Science Foundation Princeton.

Crotts, A. P., 1992. M31-A unique laboratory for gravitational microlensing. *The Astrophysical Journal*, **399**, L43–L46.

Da Costa, G. S., 1992. Basic Photometry Techniques. In S. B. Howell, ed., *Astronomical CCD Observing and Reduction Techniques*, vol. 23 of *Astronomical Society of the Pacific Conference Series*, 90.

Deleuil, M., Deeg, H., Alonso, R., Bouchy, F., Rouan, D., Auvergne, M., Baglin, A., Aigrain, S., Almenara, J., Barbieri, M. et al., 2008. Transiting exoplanets from the CoRoT space mission-VI. CoRoT-Exo-3b: the first secure inhabitant of the brown-dwarf desert. *Astronomy & Astrophysics*, **491**(3), 889–897.

Delorme, P., Collier Cameron, A., Hebb, L., Rostron, J., Lister, T. A., Norton, A. J., Pollacco, D. & West, R. G., 2011. Stellar rotation in the Hyades and Praesepe: gyrochronology and braking time-scale. *MNRAS*, **413**, 2218–2234.

Deming, D., Knutson, H., Kammer, J., Fulton, B. J., Ingalls, J., Carey, S., Burrows, A., Fortney, J. J., Todorov, K., Agol, E. et al., 2015. Spitzer Secondary Eclipses of the Dense, Modestly-irradiated, Giant Exoplanet HAT-P Using Pixel-level Decorrelation. *The Astrophysical Journal*, **805**(2), 132.

Denissenkov, P. A., 2010. A Model of Magnetic Braking of Solar Rotation That Satisfies Observational Constraints. *The Astrophysical Journal*, **719**(1), 28.

Denissenkov, P. A. & Pinsonneault, M., 2007. A revised prescription for the Tayler-Spruit dynamo: magnetic angular momentum transport in stars. *The Astrophysical Journal*, **655**(2), 1157.

Domingo, V., Fleck, B. & Poland, A. I., 1995. The SOHO mission: an overview. *Solar Physics*, **162**(1-2), 1–37.

Dorren, J. D. & Guinan, E. F., 1982. Evidence for starspots on single solar-like stars. *AJ*, **87**, 1546–1557.

Dotter, A., 2016. MESA Isochrones and Stellar Tracks (MIST) 0: Methods for the Construction of Stellar Isochrones. *The Astrophysical Journal Supplement Series*, **222**(1), 8.

Douglas, S. T., Agüeros, M. A., Covey, K. R., Cargile, P. A., Barclay, T., Cody, A., Howell, S. B. & Kopytova, T., 2016. K2 Rotation Periods for Low-mass Hyads and the Implications for Gyrochronology. *ApJ*, **822**, 47.

Dworetsky, M. M., 1983. A period-finding method for sparse randomly spaced observations of 'How long is a piece of string?'. *MNRAS*, **203**, 917–924.

Edvardsson, B., Andersen, J., Gustafsson, B., Lambert, D. L., Nissen, P. E. & Tomkin,

J., 1993. The Chemical Evolution of the Galactic Disk - Part One - Analysis and Results. *A&A*, **275**, 101.

Edwards, S., Strom, S. E., Hartigan, P., Strom, K. M., Hillenbrand, L. A., Herbst, W., Attridge, J., Merrill, K. M., Probst, R. & Gatley, I., 1993. Angular momentum regulation in low-mass young stars surrounded by accretion disks. *AJ*, **106**, 372–382.

Eggen, O. J. & Sandage, A. R., 1964. New photoelectric observations of stars in the old galactic cluster M67. *ApJ*, **140**, 130.

Elvey, C., 1930. The rotation of stars and the contours of Mg+ 4481. *The Astrophysical Journal*, **71**.

Endal, A. & Sofia, S., 1979. The evolution of rotating stars. III-Predicted surface rotation velocities for stars which conserve total angular momentum. *The Astrophysical Journal*, **232**, 531–540.

Endal, A. S. & Sofia, S., 1981. Rotation in solar-type stars. I - Evolutionary models for the spin-down of the sun. *ApJ*, **243**, 625–640.

Epstein, C. R. & Pinsonneault, M. H., 2014. How Good a Clock is Rotation? The Stellar Rotation-Mass-Age Relationship for Old Field Stars. *The Astrophysical Journal*, **780**(2), 159.

Esselstein, R., Aigrain, S., Vanderburg, A., Smith, J. C., Meibom, S., Van Saders, J. & Mathieu, R., 2018. The K2 M67 Study: Establishing the Limits of Stellar Rotation Period Measurements in M67 with K2 Campaign 5 Data. *The Astrophysical Journal*, **859**(2), 167.

Fagotto, F., Bressan, A., Bertelli, G. & Chiosi, C., 1994a. Evolutionary sequences of stellar models with new radiative opacities. III. Z=0.0004 and Z=0.05. *A&AS*, **104**, 365–376.

Fagotto, F., Bressan, A., Bertelli, G. & Chiosi, C., 1994b. Evolutionary sequences of stellar models with new radiative opacities. IV. Z=0.004 and Z=0.008. *A&AS*, **105**, 29–38.

Fan, X., Burstein, D., Chen, J.-S., Zhu, J., Jiang, Z. et al., 1996. Deep Wide-Field Spectrophotometry of the Open Cluster M67. *AJ*, **112**, 628.

Feltzing, S., Holmberg, J. & Hurley, J. R., 2001. The solar neighbourhood age-metallicity relation - Does it exist? *A&A*, **377**, 911–924.

Fitch, W. S., 1967. Evidence of Tidal Effects in Some Pulsating Stars. I. CC Andromedae and Sigma Scorpii. *ApJ*, **148**, 481.

Foreman-Mackey, D., Agol, E., Ambikasaran, S. & Angus, R., 2017. Fast and Scalable Gaussian Process Modeling with Applications to Astronomical Time Series. *AJ*, **154**, 220.

Foreman-Mackey, D., Hogg, D. W., Lang, D. & Goodman, J., 2013. emcee: The MCMC Hammer. *PASP*, **125**, 306.

Fricke, K. J. & Kippenhahn, R., 1972. Evolution of rotating stars. *Annual Review of Astronomy and Astrophysics*, **10**(1), 45–72.

Fröhlich, C., 2000. Observations of irradiance variations. *Space Science Reviews*, **94**(1-2), 15–24.

Fröhlich, C., 2006. Solar irradiance variability since 1978. In *Solar Variability and Planetary Climates*, 53–65. Springer.

Fröhlich, C. & Lean, J., 1998. The Sun's total irradiance: Cycles, trends and related climate change uncertainties since 1976. *Geophysical Research Letters*, **25**(23), 4377–4380.

Gaia Collaboration, Babusiaux, C., van Leeuwen, F., Barstow, M. A., Jordi, C., Vallenari, A., Bossini, D., Bressan, A., Cantat-Gaudin, T., van Leeuwen, M. & et al., 2018. Gaia Data Release 2: Observational Hertzsprung-Russell diagrams. *ArXiv e-prints*.

Gaia Collaboration, Prusti, T., de Bruijne, J. H. J., Brown, A. G. A., Vallenari, A., Babusiaux, C., Bailer-Jones, C. A. L., Bastian, U., Biermann, M., Evans, D. W. & et al., 2016. The Gaia mission. *A&A*, **595**, A1.

Gallet, F. & Bouvier, J., 2015. Improved angular momentum evolution model for solar-like stars-II. Exploring the mass dependence. *Astronomy & Astrophysics*, **577**, A98.

García, R. A., Ceillier, T., Salabert, D., Mathur, S., van Saders, J. L. et al., 2014. Rotation and magnetism of Kepler pulsating solar-like stars. Towards asteroseismically calibrated age-rotation relations. *A&A*, **572**, A34.

Geller, A. M., Latham, D. W. & Mathieu, R. D., 2015. Stellar Radial Velocities in the Old Open Cluster M67 (NGC 2682). I. Memberships, Binaries, and Kinematics. *AJ*, **150**, 97.

Gillen, E., Hillenbrand, L. A., David, T. J., Aigrain, S., Rebull, L., Stauffer, J., Cody, A. M. & Queloz, D., 2017. New Low-mass Eclipsing Binary Systems in Praesepe Discovered by K 2. *The Astrophysical Journal*, **849**(1), 11.

Gilliland, R. L., 1985. The relation of chromospheric activity to convection, rotation, and evolution off the main sequence. *ApJ*, **299**, 286–294.

Gilliland, R. L. & Brown, T. M., 1988. Time-Resolved CCD Photometry of an Ensemble of Stars. *Publications of the Astronomical Society of the Pacific*, **100**(628), 754.

Gilliland, R. L. & Brown, T. M., 1992. The oscillating blue stragglers in the open cluster M67. *AJ*, **103**, 1945–1954.

Gilliland, R. L., Brown, T. M., Christensen-Dalsgaard, J., Kjeldsen, H., Aerts, C. et al., 2010. Kepler Asteroseismology Program: Introduction and First Results. *PASP*, **122**, 131.

Gilliland, R. L., Brown, T. M., Kjeldsen, H., McCarthy, J. K., Peri, M. L., Belmonte, J. A., Vidal, I., Cram, L. E., Palmer, J., Frandsen, S., Parthasarathy, M., Petro, L., Schneider, H., Stetson, P. B. & Weiss, W. W., 1993. A search for solar-like oscillations in the stars of M67 with CCD ensemble photometry on a network of 4 M telescopes. *AJ*, **106**, 2441–2476.

Gilliland, R. L., Chaplin, W. J., Jenkins, J. M., Ramsey, L. W. & Smith, J. C., 2015. Kepler Mission Stellar and Instrument Noise Properties Revisited. *The Astronomical Journal*, **150**(4), 133.

Girardi, L., Bressan, A., Bertelli, G. & Chiosi, C., 2000. Evolutionary tracks and isochrones for low- and intermediate-mass stars: From 0.15 to 7 M_{sun}, and from Z=0.0004 to 0.03. *A&AS*, **141**, 371–383.

Gizis, J. E., Reid, I. N. & Hawley, S. L., 2002. The Palomar/MSU Nearby Star Spectroscopic Survey. III. Chromospheric Activity, M Dwarf Ages, and the Local Star Formation History. *The Astronomical Journal*, **123**(6), 3356.

Gonzalez, G., 2016a. A revised gyro-age for M67 from Kepler/K2-Campaign-5 light curves. *MNRAS*, **463**, 3513–3519.

Gonzalez, G., 2016b. Variability among stars in the M 67 field from Kepler/K2-Campaign-5 light curves. *MNRAS*, **459**, 1060–1068.

Gough, D., 1987. Seismological measurement of stellar ages. *Nature*, **326**, 257–259.

Gough, D. O., 1990. The internal structure of late-type main-sequence stars. In B. Gustafsson & P. E. Nissen, eds., *Astrophysics: Recent Progress and Future Possibilities*, 13–50.

Gregory, P. C. & Loredo, T. J., 1992. A new method for the detection of a periodic signal of unknown shape and period. *ApJ*, **398**, 146–168.

Hartman, J. D., Bakos, G. Á., Kovács, G. & Noyes, R. W., 2010. A Large Sample of Photometric Rotation Periods for FGK Pleiades Stars. *ArXiv e-prints*.

Hartman, J. D., Gaudi, B. S., Holman, M. J., McLeod, B. A., Stanek, K. Z., Barranco, J. A., Pinsonneault, M. H., Meibom, S. & Kalirai, J. S., 2009. Deep MMT Transit Survey of the Open Cluster M37 IV: Limit on the Fraction of Stars with Planets as Small as 0.3RJ. *The Astrophysical Journal*, **695**(1), 336.

Hempelmann, A., Schmitt, J. H. M. M. & Stępień, K., 1996. Coronal X-ray emission of cool stars in relation to chromospheric activity and magnetic cycles. *A&A*, **305**, 284.

Herbig, G. H. & Spalding, Jr., J. F., 1955. Axial Rotation and Line Broadening in Stars of Spectral Types F0-K5. *ApJ*, **121**, 118.

Hernández, A. G., Moya, A., Michel, E., Garrido, R., Suárez, J., Rodríguez, E., Amado, P., Martín-Ruiz, S., Rolland, A., Poretti, E. et al., 2009. Asteroseismic analysis of the CoRoT δ Scuti star HD 174936. *Astronomy & Astrophysics*, **506**(1), 79–83.

Hoaglin, D. C., Mosteller, F. & Tukey, J. W., 1983. *Understanding Robust and Exploratory Data analysis*. Wiley.

Horne, J. H. & Baliunas, S. L., 1986. A prescription for period analysis of unevenly sampled time series. *ApJ*, **302**, 757–763.

Howard, R. & Harvey, J., 1970. Spectroscopic determinations of solar rotation. *Solar Physics*, **12**(1), 23–51.

Howell, S. B., Sobeck, C., Haas, M., Still, M., Barclay, T. et al., 2014. The K2 Mission: Characterization and Early Results. *PASP*, **126**, 398–408.

Hoyle, F. & Fowler, W. A., 1960. Nucleosynthesis in Supernovae. *ApJ*, **132**, 565.

Huang, C., Penev, K., Hartman, J., Bakos, G., Bhatti, W., Domsa, I. & de Val-Borro, M., 2015. High-precision photometry for K2 Campaign 1. *Monthly Notices of the Royal Astronomical Society*, **454**, 4159–4171.

Ibukiyama, A. & Arimoto, N., 2002. HIPPARCOS age-metallicity relation of the solar neighbourhood disc stars. *A&A*, **394**, 927–941.

Irwin, J., Aigrain, S., Bouvier, J., Hebb, L., Hodgkin, S., Irwin, M. & Moraux, E., 2009. The Monitor project: rotation periods of low-mass stars in M50. *MNRAS*, **392**, 1456–1466.

Irwin, J., Aigrain, S., Hodgkin, S., Irwin, M., Bouvier, J., Clarke, C., Hebb, L. & Moraux, E., 2006. The Monitor project: rotation of low-mass stars in the open cluster M34. *MNRAS*, **370**, 954–974.

Irwin, J., Hodgkin, S., Aigrain, S., Bouvier, J., Hebb, L., Irwin, M. & Moraux, E., 2008a. The Monitor project: rotation of low-mass stars in NGC 2362 - testing the disc regulation paradigm at 5 Myr. *MNRAS*, **384**, 675–686.

Irwin, J., Hodgkin, S., Aigrain, S., Bouvier, J., Hebb, L. & Moraux, E., 2008b. The Monitor project: rotation of low-mass stars in the open cluster NGC 2547. *MNRAS*, **383**, 1588–1602.

Irwin, J., Hodgkin, S., Aigrain, S., Hebb, L., Bouvier, J., Clarke, C., Moraux, E. & Bramich, D., 2007a. The Monitor project: rotation of low-mass stars in the open cluster NGC 2516. *Monthly Notices of the Royal Astronomical Society*, **377**(2), 741–758.

Irwin, J., Irwin, M., Aigrain, S., Hodgkin, S., Hebb, L. & Moraux, E., 2007b. The Monitor project: data processing and light curve production. *Monthly Notices of the Royal Astronomical Society*, **375**(4), 1449–1462.

Irwin, J., Irwin, M., Aigrain, S., Hodgkin, S., Hebb, L. & Moraux, E., 2007. The Monitor project: data processing and light curve production. *MNRAS*, **375**, 1449–1462.

Irwin, M. J., Lewis, J., Hodgkin, S., Bunclark, P., Evans, D., McMahon, R., Emerson, J. P., Stewart, M. & Beard, S., 2004. VISTA data flow system: pipeline processing for WFCAM and VISTA. In *Optimizing scientific return for astronomy through information technologies*, vol. 5493, 411–423. International Society for Optics and Photonics.

Jacobson, H. R., Pilachowski, C. A. & Friel, E. D., 2011. A Chemical Abundance Study of 10 Open Clusters Based on WIYN-Hydra Spectroscopy. *AJ*, **142**, 59.

Janes, K. A. & Smith, G. H., 1984. The giant branch of the old open cluster M67. *AJ*, **89**, 487–495.

Jeffries, R. D., Naylor, T., Mayne, N. J., Bell, C. P. M. & Littlefair, S. P., 2013. A lithium depletion boundary age of 22 Myr for NGC 1960. *MNRAS*, **434**, 2438–2450.

Jeffries, R. D. & Oliveira, J. M., 2005. The lithium depletion boundary in NGC 2547 as a test of pre-main-sequence evolutionary models. *MNRAS*, **358**, 13–29.

Jenkins, J. M., Caldwell, D. A., Chandrasekaran, H., Twicken, J. D., Bryson, S. T., Quintana, E. V., Clarke, B. D., Li, J., Allen, C., Tenenbaum, P. et al., 2010. Overview of the Kepler science processing pipeline. *The Astrophysical Journal Letters*, **713**(2), L87.

Johnson, H. L. & Sandage, A. R., 1955. The galactic cluster M67 and its significance for stellar evolution. *ApJ*, **121**, 616.

Jørgensen, B. R. & Lindegren, L., 2005. Determination of stellar ages from isochrones: Bayesian estimation versus isochrone fitting. *A&A*, **436**, 127–143.

Kaehler, H., 1978. The Vogt-Russell theorem, and new results on an old problem. In A. G. D. Philip & D. S. Hayes, eds., *The HR Diagram - The 100th Anniversary of Henry Norris Russell*, vol. 80 of *IAU Symposium*, 303–311.

Kallinger, T., Weiss, W. W., Barban, C., Baudin, F., Cameron, C., Carrier, F., De Ridder, J., Goupil, M.-J., Gruberbauer, M., Hatzes, A. et al., 2010. Oscillating red giants in the CoRoT exofield: asteroseismic mass and radius determination. *Astronomy & Astrophysics*, **509**, A77.

Katz, D., Munari, U., Cropper, M., Zwitter, T., Thévenin, F., David, M., Viala, Y., Crifo, F., Gomboc, A., Royer, F. et al., 2004. Spectroscopic survey of the Galaxy with Gaia–I. Design and performance of the Radial Velocity Spectrometer. *Monthly Notices of the Royal Astronomical Society*, **354**(4), 1223–1238.

Kawaler, S. D., 1988. Angular momentum loss in low-mass stars. *ApJ*, **333**, 236–247.

Kawaler, S. D., 1989. Rotational dating of middle-aged stars. *ApJ*, **343**, L65–L68.

Knutson, H. A., Charbonneau, D., Allen, L. E., Burrows, A. & Megeath, S. T., 2008. The 3.6-8.0 μm broadband emission spectrum of HD 209458b: Evidence for an atmospheric temperature inversion. *The Astrophysical Journal*, **673**(1), 526.

Koch, D. G., Borucki, W. J., Basri, G., Batalha, N. M., Brown, T. M., Caldwell, D., Christensen-Dalsgaard, J., Cochran, W. D., DeVore, E., Dunham, E. W. et al., 2010. Kepler mission design, realized photometric performance, and early science. *The Astrophysical*

Journal Letters, **713**(2), L79.

Kovács, G., Bakos, G. & Noyes, R. W., 2005. A trend filtering algorithm for wide-field variability surveys. *Monthly Notices of the Royal Astronomical Society*, **356**(2), 557–567.

Kraft, R. P., 1967. Studies of Stellar Rotation. V. The Dependence of Rotation on Age among Solar-Type Stars. *ApJ*, **150**, 551.

Krishnamurthi, A., Pinsonneault, M., Barnes, S. & Sofia, S., 1997. Theoretical models of the angular momentum evolution of solar-type stars. *The Astrophysical Journal*, **480**(1), 303.

Lachaume, R., Dominik, C., Lanz, T. & Habing, H. J., 1999. Age determinations of main-sequence stars: combining different methods. *A&A*, **348**, 897–909.

Lafler, J. & Kinman, T., 1965. An RR Lyrae Star Survey with Ihe Lick 20-INCH Astrograph II. The Calculation of RR Lyrae Periods by Electronic Computer. *The Astrophysical Journal Supplement Series*, **11**, 216.

Lang, D., Hogg, D. W., Mierle, K., Blanton, M. & Roweis, S., 2010. Astrometry.net: Blind astrometric calibration of arbitrary astronomical images. *AJ*, **137**, 1782–2800. ArXiv:0910.2233.

Lanotte, A., Gillon, M., Demory, B.-O., Fortney, J., Astudillo, N., Bonfils, X., Magain, P., Delfosse, X., Forveille, T., Lovis, C. et al., 2014. A global analysis of Spitzer and new HARPS data confirms the loneliness and metal-richness of GJ 436 b. *Astronomy & Astrophysics*, **572**, A73.

Lanzafame, A. C., Distefano, E., Messina, S., Pagano, I., Lanza, A. F., Eyer, L., Guy, L. P., Rimoldini, L., Lecoeur-Taibi, I., Holl, B., de Fombelle, M. A. G. J., Nienartowicz, K., Marchal, O. & Mowlavi, N., 2018. Gaia Data Release 2: Rotational modulation in late-type dwarfs. *ArXiv e-prints*.

Laws, C., Gonzalez, G., Walker, K. M., Tyagi, S., Dodsworth, J., Snider, K. & Suntzeff, N. B., 2003. Parent Stars of Extrasolar Planets. VII. New Abundance Analyses of 30 Systems. *The Astronomical Journal*, **125**(5), 2664.

Leiner, E., Mathieu, R. D., Stello, D., Vanderburg, A. & Sandquist, E., 2016. The K2 M67 Study: An Evolved Blue Straggler in M67 from K2 Mission Asteroseismology. *The Astrophysical Journal Letters*, **832**(1), L13.

Lewis, N. K., Knutson, H. A., Showman, A. P., Cowan, N. B., Laughlin, G., Burrows, A., Deming, D., Crepp, J. R., Mighell, K. J., Agol, E. et al., 2013. Orbital phase variations of the eccentric giant planet HAT-P-2b. *The Astrophysical Journal*, **766**(2), 95.

Libralato, M., Bedin, L. R., Nardiello, D. & Piotto, G., 2016. A PSF-based approach to Kepler/K2 data - I. Variability within the K2 Campaign 0 star clusters M 35 and NGC 2158. *MNRAS*, **456**, 1137–1162.

Liu, W. M. & Chaboyer, B., 2000. The Relative Age of the Thin and Thick Galactic Disks. *The Astrophysical Journal*, **544**(2), 818.

Lockwood, G. W., Thompson, D. T., Radick, R. R., Osborn, W. H., Baggett, W. E., Duncan, D. K. & Hartmann, L. W., 1984. The photometric variability of solar-type stars. IV. Detection of rotational modulation among Hyades stars. *Publications of the Astronomical Society of the Pacific*, **96**(583), 714.

Loktin, A. V., 2005. Kinematics of Stars in the Old Open Cluster M67. *Astronomy Reports*, **49**, 693–700.

Lomb, N. R., 1976. Least-squares frequency analysis of unequally spaced data. *Ap&SS*, **39**, 447–

462.

LSST Science Collaboration, Marshall, P., Anguita, T., Bianco, F. B., Bellm, E. C. et al., 2017. Science-Driven Optimization of the LSST Observing Strategy. *ArXiv e-prints*.

Ludwig, H.-G., Caffau, E., Steffen, M., Bonifacio, P. & Sbordone, L., 2010. Accuracy of spectroscopy-based radioactive dating of stars. *Astronomy & Astrophysics*, **509**, A84.

Luger, R., Agol, E., Kruse, E., Barnes, R., Becker, A., Foreman-Mackey, D. & Deming, D., 2016. EVEREST: Pixel Level Decorrelation of K2 Light Curves. *AJ*, **152**, 100.

Luger, R., Kruse, E., Foreman-Mackey, D., Agol, E. & Saunders, N., 2017. An update to the EVEREST K2 pipeline: Short cadence, saturated stars, and Kepler-like photometry down to Kp = 15. *ArXiv e-prints*.

Lund, M. N., Handberg, R., Davies, G. R., Chaplin, W. J. & Jones, C. D., 2015. K2P2: A Photometry Pipeline for The K2 Mission. *The Astrophysical Journal*, **806**(1), 30.

Lyra, W. & Porto de Mello, G. F., 2005. Fine structure of the chromospheric activity in Solar-type stars - The Hα line. *A&A*, **431**, 329–338.

MacGregor, K. B. & Brenner, M., 1991. Rotational evolution of solar-type stars. I - Main-sequence evolution. *ApJ*, **376**, 204–213.

Machalek, P., McCullough, P. R., Burke, C. J., Valenti, J. A., Burrows, A. & Hora, J. L., 2008. Thermal emission of exoplanet XO-1b. *The Astrophysical Journal*, **684**(2), 1427.

Maeder, A., 1972. The Nuclear and Kinematic Age of Stellar Associations. In G. Cayrel de Strobel & A. M. Delplace, eds., *IAU Colloq. 17: Age des Etoiles*, 24.

Maeder, A. & Meynet, G., 2000. The evolution of rotating stars. *Annual Review of Astronomy and Astrophysics*, **38**(1), 143–190.

Magic, Z., Serenelli, A., Weiss, A. & Chaboyer, B., 2010. On using the color-magnitude diagram morphology of M67 to test solar abundances. *The Astrophysical Journal*, **718**(2), 1378.

Mamajek, E. E. & Hillenbrand, L. A., 2008. Improved Age Estimation for Solar-Type Dwarfs Using Activity-Rotation Diagnostics. *ApJ*, **687**, 1264–1293.

Mancini, L., Giacobbe, P., Littlefair, S. P., Southworth, J., Bozza, V. et al., 2015. Rotation periods and astrometric motions of the Luhman 16AB brown dwarfs by high-resolution lucky-imaging monitoring. *A&A*, **584**.

Manzi, S., Randich, S., de Wit, W. J. & Palla, F., 2008. Detection of the lithium depletion boundary in the young open cluster IC 4665. *A&A*, **479**, 141–148.

Marigo, P., Girardi, L., Bressan, A., Groenewegen, M. A., Silva, L. & Granato, G. L., 2008. Evolution of asymptotic giant branch stars-II. Optical to far-infrared isochrones with improved TP-AGB models. *Astronomy & Astrophysics*, **482**(3), 883–905.

Mateo, M. & Schechter, P. L., 1989. The DoPHOT two-dimensional photometry program. In *ESO/ST-ECF Data Analysis Workshop*, vol. 31, 69–83.

Mathieu, R. D. & Latham, D. W., 1986. The spatial distribution of spectroscopic binaries and blue stragglers in the open cluster M67. *AJ*, **92**, 1364–1371.

Mathieu, R. D., Latham, D. W., Griffin, R. & Gunn, J. E., 1986. Precise radial velocities of late-type stars in the open clusters M11 and M67. *The Astronomical Journal*, **92**, 1100–1117.

Mathieu, R. D. & Mazeh, T., 1988. The circularized binaries in open clusters - A new clock for age determination. *ApJ*, **326**, 256–264.

Mathur, S., García, R. A., Catala, C., Bruntt, H., Mosser, B. et al., 2010a. The

solar-like CoRoT target HD 170987: spectroscopic and seismic observations. *A&A*, **518**, A53.

Mathur, S., García, R. A., Régulo, C., Creevey, O. L., Ballot, J., Salabert, D., Arentoft, T., Quirion, P.-O., Chaplin, W. J. & Kjeldsen, H., 2010b. Determining global parameters of the oscillations of solar-like stars. *A&A*, **511**, A46.

Mathur, S., Metcalfe, T., Woitaszek, M., Bruntt, H., Verner, G., Christensen-Dalsgaard, J., Creevey, O., Doğan, G., Basu, S., Karoff, C. et al., 2012. A uniform asteroseismic analysis of 22 solar-type stars observed by Kepler. *The Astrophysical Journal*, **749**(2), 152.

Matt, S. P., Brun, A. S., Baraffe, I., Bouvier, J. & Chabrier, G., 2015. The Mass-dependence of Angular Momentum Evolution in Sun-like Stars. *The Astrophysical Journal Letters*, **799**(2), L23.

Matt, S. P., MacGregor, K. B., Pinsonneault, M. H. & Greene, T. P., 2012. Magnetic Braking Formulation for Sun-like Stars: Dependence on Dipole Field Strength and Rotation Rate. *The Astrophysical Journal Letters*, **754**(2), L26.

Matthews, J. M., 2007. One small satellite, so many light curves: Examples of delta Scuti asteroseismology from the MOST space mission^ 1. *Communications in Asteroseismology*, **150**, 333.

Mayor, M., 1974. Kinematics and Age of Stars. *A&A*, **32**, 321.

McQuillan, A., Aigrain, S. & Mazeh, T., 2013. Measuring the rotation period distribution of field M dwarfs with Kepler. *MNRAS*, **432**, 1203–1216.

McQuillan, A., Mazeh, T. & Aigrain, S., 2013. Stellar Rotation Periods of the Kepler Objects of Interest: A Dearth of Close-in Planets around Fast Rotators. *The Astrophysical Journal Letters*, **775**(1), L11.

McQuillan, A., Mazeh, T. & Aigrain, S., 2014. Rotation Periods of 34,030 Kepler Main-sequence Stars: The Full Autocorrelation Sample. *ApJS*, **211**, 24.

Meibom, S., Barnes, S. A., Latham, D. W., Batalha, N., Borucki, W. J. et al., 2011. The Kepler Cluster Study: Stellar Rotation in NGC 6811. *ApJ*, **733**, L9.

Meibom, S., Barnes, S. A., Platais, I., Gilliland, R. L., Latham, D. W. & Mathieu, R. D., 2015. A spin-down clock for cool stars from observations of a 2.5-billion-year-old cluster. *Nature*, **517**, 589–591.

Meibom, S., Mathieu, R. D. & Stassun, K. G., 2009. Stellar Rotation in M35: Mass-Period Relations, Spin-Down Rates, and Gyrochronology. *ApJ*, **695**, 679–694.

Meibom, S., Mathieu, R. D., Stassun, K. G., Liebesny, P. & Saar, S. H., 2011. The color-period diagram and stellar rotational evolution?new rotation period measurements in the open cluster M34. *The Astrophysical Journal*, **733**(2), 115.

Mestel, L., 1953. Rotation and stellar evolution. *Monthly Notices of the Royal Astronomical Society*, **113**(6), 716–745.

Metcalfe, T. S., Monteiro, M. J. P. F. G., Thompson, M. J., Molenda-Żakowicz, J., Appourchaux, T. et al., 2010. A Precise Asteroseismic Age and Radius for the Evolved Sun-like Star KIC 11026764. *The Astrophysical Journal*, **723**(2), 1583.

Michel, E., Baglin, A., Auvergne, M., Catala, C., Samadi, R., Baudin, F., Appourchaux, T., Barban, C., Weiss, W. W., Berthomieu, G. et al., 2008. CoRoT measures solar-like oscillations and granulation in stars hotter than the Sun. *Science*, **322**(5901), 558–560.

Mighell, K. J., 1999. CCD Aperture Photometry. In E. R. Craine, D. L. Crawford & R. A. Tucker, eds., *Precision CCD Photometry*, vol. 189 of *Astronomical Society of the Pacific Conference Series*, 50.

Miller-Ricci, E., Rowe, J. F., Sasselov, D., Matthews, J. M., Guenther, D. B., Kuschnig, R., Moffat, A. F., Rucinski, S. M., Walker, G. A. & Weiss, W. W., 2008a. MOST Space-based Photometry of the Transiting Exoplanet System HD 209458: Transit Timing to Search for Additional Planets. *The Astrophysical Journal*, **682**(1), 586.

Miller-Ricci, E., Rowe, J. F., Sasselov, D., Matthews, J. M., Kuschnig, R., Croll, B., Guenther, D. B., Moffat, A. F., Rucinski, S. M., Walker, G. A. et al., 2008b. MOST* Space-based Photometry of the Transiting Exoplanet System HD 189733: Precise Timing Measurements for Transits across an Active Star. *The Astrophysical Journal*, **682**(1), 593.

Monteiro, H., Dias, W. S. & Caetano, T. C., 2010. Fitting isochrones to open cluster photometric data. A new global optimization tool. *A&A*, **516**, A2.

Montgomery, K. A., Marschall, L. A. & Janes, K. A., 1993. CCD photometry of the old open cluster M67. *AJ*, **106**, 181–219.

Moutou, C., Bruntt, H., Guillot, T., Shporer, A., Guenther, E., Aigrain, S., Almenara, J., Alonso, R., Auvergne, M., Baglin, A. et al., 2008. Transiting exoplanets from the CoRoT space mission-V. CoRoT-Exo-4b: stellar and planetary parameters. *Astronomy & Astrophysics*, **488**(2), L47–L50.

Nardiello, D., Libralato, M., Bedin, L. R., Piotto, G., Borsato, L., Granata, V., Malavolta, L. & Nascimbeni, V., 2016. A PSF-based approach to Kepler/K2 data - III. Search for exoplanets and variable stars within the open cluster M 67 (NGC 2682). *MNRAS*, **463**, 1831–1843.

Naylor, T. & Jeffries, R., 2006. A maximum-likelihood method for fitting colour–magnitude diagrams. *Monthly Notices of the Royal Astronomical Society*, **373**(3), 1251–1263.

Nielsen, M. B., Gizon, L., Schunker, H. & Karoff, C., 2013a. Measuring Stellar Rotation Periods with Kepler. In H. Shibahashi & A. E. Lynas-Gray, eds., *Progress in Physics of the Sun and Stars: A New Era in Helio- and Asteroseismology*, vol. 479 of *Astronomical Society of the Pacific Conference Series*, 137.

Nielsen, M. B., Gizon, L., Schunker, H. & Karoff, C., 2013b. Rotation periods of 12 000 main-sequence Kepler stars: Dependence on stellar spectral type and comparison with v sin i observations. *A&A*, **557**, L10.

Nielsen, M. B., Gizon, L., Schunker, H. & Schou, J., 2014. Rotational splitting as a function of mode frequency for six Sun-like stars. *A&A*, **568**, L12.

Noyes, R. W., 1983. The relation between rotation and magnetic activity on lower main sequence stars as derived from chromospheric indicators. In J. O. Stenflo, ed., *Solar and Stellar Magnetic Fields: Origins and Coronal Effects*, vol. 102 of *IAU Symposium*, 133–146.

Noyes, R. W., Hartmann, L. W., Baliunas, S. L., Duncan, D. K. & Vaughan, A. H., 1984. Rotation, convection, and magnetic activity in lower main-sequence stars. *ApJ*, **279**, 763–777.

Oliveira, A. F., Monteiro, H., Dias, W. S. & Caetano, T. C., 2013. Fitting isochrones to open cluster photometric data. III. Estimating metallicities from UBV photometry. *A&A*, **557**, A14.

Pace, G., 2013. Chromospheric activity as age indicator-An L-shaped chromospheric-activity versus

age diagram. *Astronomy & Astrophysics*, **551**, L8.

Pace, G. & Pasquini, L., 2004. The age-activity-rotation relationship in solar-type stars. *A&A*, **426**, 1021–1034.

Parker, E. N., 1979. Cosmical magnetic fields: Their origin and their activity. *Oxford, Clarendon Press; New York, Oxford University Press, 1979, 858 p.*.

Pasquini, L., Biazzo, K., Bonifacio, P., Randich, S. & Bedin, L. R., 2008. Solar twins in M 67. *A&A*, **489**, 677–684.

Pecaut, M. J. & Mamajek, E. E., 2013. Intrinsic colors, temperatures, and bolometric corrections of pre-main-sequence stars. *The Astrophysical Journal Supplement Series*, **208**(1), 9.

Penny, A. & Dickens, R., 1986. CCD photometry of the globular cluster NGC 6752. *Monthly Notices of the Royal Astronomical Society*, **220**(4), 845–867.

Pepper, J., Gillen, E., Parviainen, H., Hillenbrand, L. A., Cody, A. M., Aigrain, S., Stauffer, J., Vrba, F. J., David, T., Lillo-Box, J., Stassun, K. G., Conroy, K. E., Pope, B. J. S. & Barrado, D., 2017. A Low-mass Exoplanet Candidate Detected by K2 Transiting the Praesepe M Dwarf JS 183. *The Astronomical Journal*, **153**(4), 177.

Perryman, M. A. C., Lindegren, L., Kovalevsky, J., Hoeg, E., Bastian, U. et al., 1997. The HIPPARCOS Catalogue. *A&A*, **323**, L49–L52.

Pollacco, D. L., Skillen, I., Cameron, A. C., Christian, D. J., Hellier, C., Irwin, J., Lister, T., Street, R., West, R. G., Anderson, D. et al., 2006. The WASP project and the SuperWASP cameras. *Publications of the Astronomical Society of the Pacific*, **118**(848), 1407.

Pont, F. & Eyer, L., 2004. Isochrone ages for field dwarfs: method and application to the age–metallicity relation. *Monthly Notices of the Royal Astronomical Society*, **351**(2), 487–504.

Press, W. H., Teukolsky, S. A., Vetterling, W. T. & Flannery, B. P., 1992. Numerical Recipes in C: The Art of Scientific Computing (; Cambridge.

Prosser, C. F., Schild, R. E., Stauffer, J. R. & Jones, B. F., 1993a. Photometric Light Curves for Ten Rapidly Rotating Stars in Alpha Persei, the Pleiades, and the Field. *Publications of the Astronomical Society of the Pacific*, **105**(685), 269.

Prosser, C. F., Shetrone, M. D., Dasgupta, A., Backman, D. E., Laaksonen, B. D., Baker, S. W., Marschall, L. A., Whitney, B. A., Kuijken, K. & Stauffer, J. R., 1995. Rotation Periods of Open-Cluster Stars. III. *Publications of the Astronomical Society of the Pacific*, **107**(709), 211.

Prosser, C. F., Shetrone, M. D., Marilli, E., Catalano, S., Williams, S. D., Backman, D. E., Laaksonen, B. D., Adige, V., Marschall, L. A. & Stauffer, J. R., 1993b. Rotation Periods of Open Cluster Stars. II. *Publications of the Astronomical Society of the Pacific*, **105**(694), 1407.

Quintana, E. V., Jenkins, J. M., Clarke, B. D., Chandrasekaran, H., Twicken, J. D., McCauliff, S. D., Cote, M. T., Klaus, T. C., Allen, C., Caldwell, D. A. & Bryson, S. T., 2010. Pixel-level calibration in the Kepler Science Operations Center pipeline. In *Software and Cyberinfrastructure for Astronomy*, vol. 7740 of *Proc. SPIE*, 77401X.

Racine, R., 1971. Photometry of M67 to $M_v = +12$. *ApJ*, **168**, 393.

Radick, R. R., Lockwood, G. W., Skiff, B. A. & Baliunas, S. L., 1998. Patterns of Variation among Sun-like Stars. *ApJS*, **118**, 239–258.

Radick, R. R., Lockwood, G. W., Skiff, B. A. & Thompson, D. T., 1995. A 12 Year Photometric Study of Lower Main-Sequence Hyades Stars. *ApJ*, **452**, 332.

Radick, R. R., Mihalas, D., Hartmann, L., Worden, S. P., Africano, J. L., Klimke, A. & Tyson, E. T., 1982. The photometric variability of solar-type stars. I. Preliminary results for the Pleiades, Hyades and the Malmquist field. *Publications of the Astronomical Society of the Pacific*, **94**(562), 934.

Radick, R. R., Mihalas, D., Lockwood, G. W., Thompson, D. T., Warnock, III, A., Hartmann, L. W., Worden, S. P., Henry, G. W. & Sherlin, J. M., 1983a. The photometric variability of solar-type stars. III - Results from 1981-82, including parallel observations of thirty-six Hyades stars. *PASP*, **95**, 621–634.

Radick, R. R., Thompson, D. T., Lockwood, G. W., Duncan, D. K. & Baggett, W. E., 1987. The activity, variability, and rotation of lower main-sequence Hyades stars. *ApJ*, **321**, 459–472.

Radick, R. R., Wilkerson, M. S., Worden, S. P., Africano, J. L., Klimke, A., Ruden, S., Rogers, W., Armandroff, T. E. & Giampapa, M. S., 1983b. The photometric variability of solar-type stars. II - Stars selected from Wilson's chromospheric activity survey. *PASP*, **95**, 300–310.

Rajpaul, V., Aigrain, S., Osborne, M. A., Reece, S. & Roberts, S., 2015. A Gaussian process framework for modelling stellar activity signals in radial velocity data. *MNRAS*, **452**, 2269–2291.

Rasmussen, C. E. & Williams, C. K., 2006. *Gaussian process for machine learning*. MIT press.

Rauer, H., Catala, C., Aerts, C., Appourchaux, T., Benz, W., Brandeker, A., Christensen-Dalsgaard, J., Deleuil, M., Gizon, L., Goupil, M.-J. et al., 2014. The PLATO 2.0 mission. *Experimental Astronomy*, **38**(1-2), 249–330.

Rauer, H., Queloz, D., Csizmadia, S., Deleuil, M., Alonso, R., Aigrain, S., Almenara, J., Auvergne, M., Baglin, A., Barge, P. et al., 2009. Transiting exoplanets from the CoRoT space mission-VII. The ?hot-Jupiter?-type planet CoRoT-5b. *Astronomy & Astrophysics*, **506**(1), 281–286.

Rebull, L. M., Stauffer, J. R., Bouvier, J., Cody, A. M., Hillenbrand, L. A. et al., 2016a. Rotation in the Pleiades with K2. I. Data and First Results. *AJ*, **152**, 113.

Rebull, L. M., Stauffer, J. R., Bouvier, J., Cody, A. M., Hillenbrand, L. A. et al., 2016b. Rotation in the Pleiades with K2. II. Multiperiod Stars. *AJ*, **152**, 114.

Reinhold, T. & Gizon, L., 2015. Rotation, differential rotation, and gyrochronology of active Kepler stars. *A&A*, **583**, A65.

Reinhold, T., Reiners, A. & Basri, G., 2013. Rotation and differential rotation of active Kepler stars. *A&A*, **560**, A4.

Ricker, G. R., Winn, J. N., Vanderspek, R., Latham, D. W., Bakos, G. Á. et al., 2014. Transiting Exoplanet Survey Satellite (TESS). In *Space Telescopes and Instrumentation 2014: Optical, Infrared, and Millimeter Wave*, vol. 9143 of *Proc. SPIE*, 914320.

Roberts, S., McQuillan, A., Reece, S. & Aigrain, S., 2013. Astrophysically robust systematics removal using variational inference: application to the first month of Kepler data. *Monthly Notices of the Royal Astronomical Society*, **435**(4), 3639–3653.

Sanders, W. L., 1977. Membership of the open cluster M67. *A&AS*, **27**, 89–116.

Sandquist, E. L., Mathieu, R. D., Quinn, S. N., Pollack, M. L., Latham, D. W. et al., 2018. The K2 M67 Study: A Curiously Young Star in an Eclipsing Binary in an Old Open Cluster. *The Astronomical Journal*, **155**(4), 152.

Sarajedini, A., Dotter, A. & Kirkpatrick, A., 2009. Deep 2MASS Photometry of M67 and Calibration of the Main-Sequence J - K_S Color Difference as an Age Indicator. *ApJ*, **698**, 1872–1878.

Scargle, J. D., 1982. Studies in astronomical time series analysis. II - Statistical aspects of spectral analysis of unevenly spaced data. *ApJ*, **263**, 835–853.

Schatzman, E., 1962. A theory of the role of magnetic activity during star formation. *Annales d'Astrophysique*, **25**, 18.

Schou, J., Antia, H., Basu, S., Bogart, R., Bush, R., Chitre, S., Christensen-Dalsgaard, J., Di Mauro, M., Dziembowski, W., Eff-Darwich, A. et al., 1998. Helioseismic studies of differential rotation in the solar envelope by the solar oscillations investigation using the Michelson Doppler Imager. *The Astrophysical Journal*, **505**(1), 390.

Shajn, G. & Struve, O., 1929. On the rotation of the stars. *MNRAS*, **89**, 222–239.

Shporer, A., O'Rourke, J. G., Knutson, H. A., Szabó, G. M., Zhao, M., Burrows, A., Fortney, J., Agol, E., Cowan, N. B., Desert, J.-M. et al., 2014. Atmospheric characterization of the hot Jupiter Kepler-13Ab. *The Astrophysical Journal*, **788**(1), 92.

Silva Aguirre, V., Davies, G. R., Basu, S., Christensen-Dalsgaard, J., Creevey, O. et al., 2015. Ages and fundamental properties of Kepler exoplanet host stars from asteroseismology. *MNRAS*, **452**, 2127–2148.

Skumanich, A., 1972. Time Scales for CA II Emission Decay, Rotational Braking, and Lithium Depletion. *ApJ*, **171**, 565.

Slettebak, A., 1954. The Spectra and Rotational Velocities of the Bright Stars of Draper Types B8-A2. *The Astrophysical Journal*, **119**, 146.

Slettebak, A., 1955. The Spectra and Rotational Velocities of the Bright Stars of Draper Types A3-G0. *ApJ*, **121**, 653.

Slettebak, A. & Howard, R. F., 1955. Axial Rotation in the Brighter Stars of Draper Types B2-B5. *The Astrophysical Journal*, **121**, 102.

Smith, J. C., Morris, R. L., Jenkins, J. M., Bryson, S. T., Caldwell, D. A. & Girouard, F. R., 2016. Finding optimal apertures in kepler data. *Publications of the Astronomical Society of the Pacific*, **128**(970), 124501.

Smith, J. C., Stumpe, M. C., Cleve, J. E. V., Jenkins, J. M., Barclay, T. S., Fanelli, M. N., Girouard, F. R., Kolodziejczak, J. J., McCauliff, S. D., Morris, R. L. & Twicken, J. D., 2012. Kepler Presearch Data Conditioning II - A Bayesian Approach to Systematic Error Correction. *Publications of the Astronomical Society of the Pacific*, **124**(919), 1000.

Soderblom, D. R., 2010. The Ages of Stars. *ARA&A*, **48**, 581–629.

Soderblom, D. R., Duncan, D. K. & Johnson, D. R. H., 1991. The chromospheric emission-age relation for stars of the lower main sequence and its implications for the star formation rate. *ApJ*, **375**, 722–739.

Soderblom, D. R., Stauffer, J. R., Hudon, J. D. & Jones, B. F., 1993a. Rotation and chromospheric emission among F, G, and K dwarfs of the Pleiades. *ApJS*, **85**, 315–346.

Soderblom, D. R., Stauffer, J. R., MacGregor, K. B. & Jones, B. F., 1993b. The evolution of angular momentum among zero-age main-sequence solar-type stars. *ApJ*, **409**, 624–634.

Spada, F., Demarque, P., Kim, Y.-C., Boyajian, T. & Brewer, J., 2017. The Yale–Potsdam Stellar Isochrones. *The Astrophysical Journal*, **838**(2), 161.

Spruit, H., 2002. Dynamo action by differential rotation in a stably stratified stellar interior. *Astronomy & Astrophysics*, **381**(3), 923–932.

Spruit, H. C., 1999. Differential rotation and magnetic fields in stellar interiors. *A&A*, **349**, 189–202.

Stauffer, J., Cody, A. M., Baglin, A., Alencar, S., Rebull, L., Hillenbrand, L. A., Venuti, L., Turner, N. J., Carpenter, J., Plavchan, P. et al., 2014. CSI 2264: Characterizing accretion-burst dominated light curves for young stars in NGC 2264. *The Astronomical Journal*, **147**(4), 83.

Stauffer, J., Rebull, L., Bouvier, J., Hillenbrand, L. A., Collier-Cameron, A. et al., 2016. Rotation in the Pleiades with K2. III. Speculations on Origins and Evolution. *AJ*, **152**, 115.

Stauffer, J. R., Hartmann, L., Soderblom, D. R. & Burnham, N., 1984. Rotational velocities of low-mass stars in the Pleiades. *ApJ*, **280**, 202–212.

Stauffer, J. R. & Hartmann, L. W., 1986. The rotational velocities of low-mass stars. *Publications of the Astronomical Society of the Pacific*, 1233–1251.

Stellingwerf, R. F., 1978. Period determination using phase dispersion minimization. *ApJ*, **224**, 953–960.

Stello, D., Vanderburg, A., Casagrande, L., Gilliland, R., Aguirre, V. S., Sandquist, E., Leiner, E., Mathieu, R. & Soderblom, D. R., 2016. The K2 M67 Study: Revisiting Old Friends with K2 Reveals Oscillating Red Giants in the Open Cluster M67. *The Astrophysical Journal*, **832**(2), 133.

Stetson, P., 1979. Photographic stellar photometry with the PDS microdensitometer. *The Astronomical Journal*, **84**, 1056–1066.

Stetson, P. B., 1987. DAOPHOT: A computer program for crowded-field stellar photometry. *Publications of the Astronomical Society of the Pacific*, **99**(613), 191.

Stevenson, K. B., Bean, J. L., Seifahrt, A., Gilbert, G. J., Line, M. R., Désert, J.-M. & Fortney, J. J., 2016. A Search for Water in the Atmosphere of HAT-P-26b Using LDSS-3C. *The Astrophysical Journal*, **817**(2), 141.

Stevenson, K. B., Harrington, J., Fortney, J. J., Loredo, T. J., Hardy, R. A., Nymeyer, S., Bowman, W. C., Cubillos, P., Bowman, M. O. & Hardin, M., 2012. Transit and eclipse analyses of the exoplanet HD 149026b using BLISS mapping. *The Astrophysical Journal*, **754**(2), 136.

Stumpe, M. C., Smith, J. C., Catanzarite, J. H., Van Cleve, J. E., Jenkins, J. M., Twicken, J. D. & Girouard, F. R., 2014. Multiscale Systematic Error Correction via Wavelet-Based Bandsplitting in Kepler Data. *PASP*, **126**, 100.

Stumpe, M. C., Smith, J. C., Van Cleve, J. E., Twicken, J. D., Barclay, T. S., Fanelli, M. N., Girouard, F. R., Jenkins, J. M., Kolodziejczak, J. J., McCauliff, S. D. et al., 2012. Kepler Presearch Data Conditioning I?Architecture and algorithms for error correction in Kepler light curves. *Publications of the Astronomical Society of the Pacific*, **124**(919), 985.

Taylor, B. J., 2007. The Benchmark Cluster Reddening Project. II. A Reddening Value for M67. *AJ*, **133**, 370–386.

Tchernyshyov, K., Meixner, M., Seale, J., Fox, A., Friedman, S. D., Dwek, E. & Galliano, F., 2015. Elemental Depletions in the Magellanic Clouds and the Evolution of Depletions with Metallicity. *The Astrophysical Journal*, **811**(2), 78.

Thompson, S. E., Coughlin, J. L., Hoffman, K., Mullally, F., Christiansen, J. L. et al., 2017. Planetary Candidates Observed by Kepler. VIII. A Fully Automated Catalog With Measured Completeness and Reliability Based on Data Release 25. *ArXiv e-prints*.

Tomaney, A. B. & Crotts, A. P. S., 1996. Expanding the Realm of Microlensing Surveys with Difference Image Photometry. *AJ*, **112**, 2872.

Torrence, C. & Compo, G. P., 1998. A Practical Guide to Wavelet Analysis. *Bulletin of the American Meteorological Society*, **79**, 61–78.

Twicken, J. D., Clarke, B. D., Bryson, S. T., Tenenbaum, P., Wu, H., Jenkins, J. M., Girouard, F. & Klaus, T. C., 2010. Photometric analysis in the Kepler Science Operations Center pipeline. In *Software and Cyberinfrastructure for Astronomy*, vol. 7740 of *Proc. SPIE*, 774023.

Tyson, J. A., 2002. Large synoptic survey telescope: overview. In *Survey and Other Telescope Technologies and Discoveries*, vol. 4836, 10–21. International Society for Optics and Photonics.

Ulrich, R. K., 1986. Determination of stellar ages from asteroseismology. *ApJ*, **306**, L37–L40.

Van Cleve, J. E., Howell, S. B., Smith, J. C., Clarke, B. D., Thompson, S. E., Bryson, S. T., Lund, M. N., Handberg, R. & Chaplin, W. J., 2016. That's How We Roll: The NASA K2 Mission Science Products and Their Performance Metrics. *PASP*, **128**(7), 075002.

van Saders, J. L., Ceillier, T., Metcalfe, T. S., Silva Aguirre, V., Pinsonneault, M. H., García, R. A., Mathur, S. & Davies, G. R., 2016. Weakened magnetic braking as the origin of anomalously rapid rotation in old field stars. *Nature*, **529**, 181–184.

Van Saders, J. L. & Pinsonneault, M. H., 2013. Fast star, slow star; old star, young star: subgiant rotation as a population and stellar physics diagnostic. *The Astrophysical Journal*, **776**(2), 67.

van Saders, J. L., Pinsonneault, M. H. & Barbieri, M., 2018. Forward Modeling of the Kepler Stellar Rotation Period Distribution: Interpreting Periods from Mixed and Biased Stellar Populations. *ArXiv e-prints*.

Vandenberg, D. A., 1985. Evolution of 0.7-3.0 solar masses stars having Fe/H between -1.0 and 0.0. *ApJS*, **58**, 711–769.

VandenBerg, D. A., Gustafsson, B., Edvardsson, B., Eriksson, K. & Ferguson, J., 2007. A Constraint on Z? from Fits of Isochrones to the Color-Magnitude Diagram of M67. *The Astrophysical Journal Letters*, **666**(2), L105.

Vanderburg, A. & Johnson, J. A., 2014. A Technique for Extracting Highly Precise Photometry for the Two-Wheeled Kepler Mission. *PASP*, **126**, 948–958.

Vanderburg, A., Latham, D. W., Buchhave, L. A., Bieryla, A., Berlind, P., Calkins, M. L., Esquerdo, G. A., Welsh, S. & Johnson, J. A., 2016. Planetary Candidates from the First Year of the K2 Mission. *ApJS*, **222**, 14.

Vanderburg, A., Montet, B. T., Johnson, J. A., Buchhave, L. A., Zeng, L. et al., 2015. Characterizing K2 Planet Discoveries: A Super-Earth Transiting the Bright K Dwarf HIP 116454.

ApJ, **800**, 59.

Vaughan, A. H. & Preston, G. W., 1980. A Survey of Chromospheric CA II H and K Emission in Field Stars of the Solar Neighborhood. *Publications of the Astronomical Society of the Pacific*, **92**(548), 385.

Vaughan, A. H., Preston, G. W. & Wilson, O. C., 1978. Flux Measurements of CA II H and K Emission. *Publications of the Astronomical Society of the Pacific*, **90**(535), 267.

von Hoerner, S., 1960. Die zeitliche Rate der Sternentstehung. *Fortschritte der Physik*, **8**.

Walker, G., Matthews, J., Kuschnig, R., Johnson, R., Rucinski, S., Pazder, J., Burley, G., Walker, A., Skaret, K., Zee, R. et al., 2003. The MOST asteroseismology mission: Ultraprecise photometry from space. *Publications of the Astronomical Society of the Pacific*, **115**(811), 1023.

Weber, E. J. & Davis, Jr., L., 1967. The Angular Momentum of the Solar Wind. *ApJ*, **148**, 217–227.

Wehlau, W. & Leung, K.-C., 1964. The Multiple Periodicity of Delta Delphini. *ApJ*, **139**, 843.

Wilson, O., 1968. Flux measurements at the centers of stellar H-and K-lines. *ApJ*, **153**, 221.

Wilson, O. & Skumanich, A., 1964. Dependence of Chromospheric Activity upon Age in Main-Sequence Stars: Additional Evidence. *The Astrophysical Journal*, **140**, 1401.

Wilson, O. C., 1963. A Probable Correlation Between Chromospheric Activity and Age in Main-Sequence Stars. *ApJ*, **138**, 832.

Wilson, O. C., 1978. Chromospheric variations in main-sequence stars. *ApJ*, **226**, 379–396.

Yadav, R. K. S., Bedin, L. R., Piotto, G., Anderson, J., Cassisi, S., Villanova, S., Platais, I., Pasquini, L., Momany, Y. & Sagar, R., 2008. Ground-based CCD astrometry with wide-field imagers. II. A star catalog for M 67: WFI@2.2 m MPG/ESO astrometry, FLAMES@VLT radial velocities. *A&A*, **484**, 609–620.

Yi, S., Demarque, P., Kim, Y.-C., Lee, Y.-W., Ree, C. H., Lejeune, T. & Barnes, S., 2001. Toward better age estimates for stellar populations: The Y2 isochrones for solar mixture. *The Astrophysical Journal Supplement Series*, **136**(2), 417.

Yi, S., Demarque, P., Kim, Y.-C., Lee, Y.-W., Ree, C. H., Lejeune, T. & Barnes, S., 2001. Toward Better Age Estimates for Stellar Populations: The Y^2 Isochrones for Solar Mixture. *ApJS*, **136**, 417–437.

Zahn, J.-P., 1977. Tidal friction in close binary stars. *Astronomy and Astrophysics*, **57**, 383–394.

Zahn, J.-P., 1989. Tidal evolution of close binary stars. I-Revisiting the theory of the equilibrium tide. *Astronomy and Astrophysics*, **220**, 112–116.

Zahn, J.-P., 1992. Circulation and turbulence in rotating stars. *Astronomy and Astrophysics*, **265**, 115–132.

Zechmeister, M. & Kürster, M., 2009. The generalised Lomb-Scargle periodogram. A new formalism for the floating-mean and Keplerian periodograms. *A&A*, **496**, 577–584.

Zellem, R. T., Lewis, N. K., Knutson, H. A., Griffith, C. A., Showman, A. P., Fortney, J. J., Cowan, N. B., Agol, E., Burrows, A., Charbonneau, D. et al., 2014. The 4.5 μm full-orbit phase curve of the hot Jupiter HD 209458b. *The Astrophysical Journal*, **790**(1), 53.

Zhao, J. K., Oswalt, T. D., Rudkin, M., Zhao, G. & Chen, Y. Q., 2011. The Chromospheric Activity, Age, Metallicity, and Space Motions of 36 Wide Binaries. *The Astronomical Journal*, **141**(4), 107.